論文 / 著書情報
Article / Book Information

題目(和文)	
Title(English)	Systematic Survey of Short X-ray Transients by MAXI
著者(和文)	薄井 竜一
Author(English)	Ryuichi Usui
出典(和文)	学位:博士(理学), 学位授与機関:東京工業大学, 報告番号:甲第9377号, 授与年月日:2014年3月26日, 学位の種別:課程博士, 審査員:河合　誠之,垣本　史雄,堂谷　忠靖,松原　英雄,陣内　修
Citation(English)	Degree:Doctor (Science), Conferring organization: Tokyo Institute of Technology, Report number:甲第9377号, Conferred date:2014/3/26, Degree Type:Course doctor, Examiner:,,,,
学位種別(和文)	博士論文
Type(English)	Doctoral Thesis

TOKYO INSTITUTE OF TECHNOLOGY

DOCTORAL THESIS

Systematic Survey of Short X-ray Transients by MAXI

Author:
Ryuichi USUI

Supervisor:
Prof. Nobuyuki KAWAI

A thesis submitted in fulfilment of the requirements
for the degree of Doctor of Physics

in the

Kawai Grp.
Department of Physics

March 2014

Abstract

We present the systematic search of short X-ray transients for the 1327-day data obtained with MAXI (Monitor of All-sky X-ray Image). Short X-ray transients have been detected by past X-ray/γ-ray satellites in large-sky surveys, and their temporal, spectral and spatial characteristics have been studied. They include Gamma-Ray Bursts (GRBs), X-ray bursts from neutron-star binaries, X-ray flares of active stars and X-ray short activities of blazars. In addition shock breakouts of supernovae and tidal disruption events at the center of a nearby galaxy have been also reported recently. Discovery of new class of transients should also benefit astrophysics. To perform the search we used the data obtained by the Gas Slit Camera (GSC) of MAXI, an X-ray detector that monitors almost the whole sky with the arc-like field of view every 92-min orbital period of the International space station. While the search of transients using the GSC data has been already performed in the past, its method required detailed modeling of the instrument and the background, and the propagation of errors and the evaluation of significance was not trivial. In addition, the used data covered only the first 15-month of operation. Thus, we newly develop a simple and versatile analysis program, and conducted the search for short X-ray transients from the MAXI-GSC data obtained since October 2009 until May 2013.

The search consists of two main processes; global search and localization. First we prepare a dataset which excludes data from the galactic plane and the vicinity of 30 bright X-ray sources in order to prevent false detections. Next, as the global search, we extracted candidate transient events which have significant excess X-ray counts over the background assuming the Poisson statistics. Third, the localization process determines the accurate position, X-ray flux and refined detection significance of these candidates. The significance is evaluated by the probability for the observed excess assuming the null hypothesis that it is consistent with the background, which is sampled in the regions surrounding the candidate in the time-vs-detector coordinate plane. Since these excesses include false detections originating from X-rays of solar flares and increasing of background, we carefully removed them and finally obtained 146 short X-ray transient with sufficiently high significance.

First we performed cross matching of the detected short X-ray transients with the reported GRBs and some optical/X-ray/γ-ray source catalogs. This study resulted in associations with 11 prompt emissions of GRBs, one GRB's afterglow, several X-ray bursts from neutron-star X-ray binaries, and flares of active stars. On the other hand, we cannot find significant associations with active galactic nuclei partly because the localization error is not so small considering the source density on the sky.

In addition we studied spectral characteristics and investigate positional and spatial distributions of the detected short X-ray transients. Their hardness ratio of 8-20 keV to 2-8 keV energy bands is larger on average than those of stellar flares, and comparable to those of X-ray bursts and prompt emission of GRBs. The dipole and quadruple moment of the transients imply their positional distribution is isotropic, which is consistent with the expectation of the previous studies. However, $V/V_{\rm max}$ test reveals that the spatial distribution is not consistent with a uniform distribution in space. This distribution indicates the detected transients include too many faint events near thresholds. In addition, the $\log N$-$\log S$ plot shows excess of the faint transients, and is also inconsistent with the uniform spatial distribution. The excess of short X-ray transients at large distance implies a distribution astrophysically implausible.

To investigate possible origins of such false detections, we examined their correlations with the detected time, detector coordinate and detected position on earth. However, we found no significant dependence on them, meaning that solar flares or variation of charged particles at high latitudes and around the South Atlantic anomaly is not responsible for the false detections. The variations of anti-coincident signal count are confirmed not to significantly affect the false detections except for one case. We found, however, one anomaly. One of the GSC (camera 7) had significantly larger number of transients detections than another (Camera 1) while these two cameras share the same field of view. This indicates that one of the origins of false detections in intrinsic to the camera, probably noise in the detector or readout electronics.

Acknowledgements

For the five year of my graduate course, I have been supported and encouraged by many people. I would like to express deep gratitude to my supervisor associate professor N. Kawai who has provided the scientific facts, the way of thinking and the discussion based on his deep knowledges and experiences. I want to thank assistant professor Y. Yatsu, Dr. Y. Saito and Dr. M. Arimoto who have encouraged me and talked about not only scientific discussion but also dairy topics. The members of our laboratory and friends also have uplifted me, so I thank them.

In this thesis, I used the scientific data obtained by MAXI. This mission is operated by the collaboration of the agency, institutes and universities. I am grateful to the all MAXI operation and scientific team who gives me the opportunity for analyzing the valuable and notable data. Especially, I have greatly benefited form the scientific members; Prof. M. Matsuoka, Prof. H. Negro, Dr. T. Mihara, Dr. M. Serino, Dr. M. Sugizaki, Dr. M. Morii and Dr. M. Kimura. This thesis mostly reflects their wide-ranging discussions and constructive suggestions for data analysis and physical interpretations.

Finally, I owe my deepest gratitude to my family. My father, mother and grandmother mentally and financially care about me. I hope they will enjoy their life after the childcare about me and brothers. I also thank to my brothers who are my best encouraging sympathizers.

This work has been financially supported by Global-COE “Nanoscience and Quantum Physics”. In addition, I thank to developed technologies and cultures which support and encourage me. The template of this thesis is provided by `www.latextemplates.com`.

Contents

List of Figures

List of Tables

Abbreviations

MAXI	**M**onitor of **A**ll-sky **X**-ray **I**mage
ISS	**I**nternational **S**pace **S**tation
GSC	**G**as **S**lit **C**amera
SSC	**S**olid state **S**lit **C**amera
SXT	**S**hort **X**-ray **T**ransient
GRB	**G**amma-**R**ay **B**urst
XRR	**X**-**R**ay **R**ich GRB
XRF	**X**-**R**ay **F**lash
LMXB	**L**ow **M**ass **X**-ray **B**inary
XRB	**X**-**R**ay **B**urst
YSO	**Y**oung **S**tellar **O**bject
AGN	**A**ctive **G**alactic **N**uclei
TDE	**T**idal **D**isruption **E**vent
NXB	**N**on **X**-ray **B**ackground
CXB	**C**osmic **X**-ray **B**ackground
SAA	**S**outh **A**tlantic **A**nomaly
FoV	**F**ield **o**f **V**iew
FWHM	**F**ull **W**idth of **H**alf **M**aximum

Chapter 1

Introduction

For decades, X-ray/γ-ray observational satellites have been performed all-sky survey missions. One of their main purposes is an investigation of short X-ray transients which have duration time from one-second to one day. Since the early era of the X-ray astronomy, several types of such short transient phenomena have been reported. For example, X-ray bursts which have fast-rise and slow-decay shaped temporal X-ray activities within a few hundred-seconds have been observed from binary systems consisting of neutron stars and ordinary stars. Another short transients are X-ray flares from active stars which have the strong magnetospheric energy release and are emitted from RS CVn type sources (which are binaries of low-mass main sequence stars) and young stellar objects (which are primordially constructed stars).

The most notable category of short X-ray/γ-ray transient is the Gamma-Ray burst (GRB) which was first detected by the Vela nuclear experiment satellites in 1960's (Klebesadel et al. [36]). Following the detection, more than ten missions have reported numerous GRBs. In particular, since the discovery of afterglow phenomena of GRB by the BeppoSAX satellite in 1997, advanced satellites such as HETE-2, *Swift* and *Fermi* have performed multi-wavelength observations aimed to reveal the temporal, spectral and cosmological characteristics of GRBs. Furthermore, theoretical investigations with numerical simulations have been performed; nevertheless, the progenitor and mechanism of the extremely bright γ-ray/X-ray emission are still mystery to astronomers.

In 2009, a new X-ray monitoring mission started operation on the International Space Station (ISS), that is Monitor of All-sky X-ray Image (MAXI). The high sensitive gas proportional counters and charge-coupled detectors (CCDs) have already discovered new X-ray sources, such as binaries comprising black holes or neutron stars, super soft source associated with a white dwarf binary, classical short X-ray transients and GRBs. Toizumi [75] performed the first short X-ray transient survey to this valuable survey data and reported 29 transients including some known GRBs. In this study they searched the transients with variable detection sensitivity due to large fluctuation of background and positional dependency on the detector and then estimated the significance of detection based on unbinned ligklihood analysis assuming a locally constant background. This method has limitations in two aspects; one is the assumption on the locally flat background, the other is the assumption on the gaussian PSF (point spread function) used in the image fitting. In order to overcome their limitations we use a simple square aperture to evaluate the significance of source detection. Following the criteria, we will systematically perform the second short X-ray transient survey. In addition to the technical developments, our survey will be performed to the data provided by the longer monitoring observation than that of the previous study.

The first chapter in this thesis (Chapter 2) will review astrophysical background information of various kinds of short X-ray transients which will be discovered in our analysis. In addition, past surveys to search short transient phenomena with several X-ray/γ-ray astronomical observatories will be introduced to understand the whole context of systematic investigation in the chapter. Next, in Chapter 3, we will show the mission of MAXI and observational characteristic of the X-ray detector, GSC, which provides the data analyzed in our analysis. Thirdly, we will describe method of the transient source search and investigate detection threshold, position determination accuracy and possible fake detections in Chapter 4. Then, results of the analysis and discussions will be reported in Chapter 5. We will discuss cross matching of detected transients with known GRBs, comparison of hardness ratio, statistical test to study positional and spatial distributions, and interpretation to the origin of the detections. Finally, we show the conclusion of our transient search analysis in Chapter 6.

Chapter 2

Background information of short X-ray transient

For the last several decades, numerous all-sky surveys for X-ray and gamma-ray transients have been performed and attempted to reveal their astrophysical characteristics. In the first part of this chapter, we will introduce physical properties of short X-ray transients (SXTs) which can be detected in our transient search study. Next, we will review the historical surveys especially focusing on the result in the soft (< 50 keV) X-ray energy band. Finally, we will overview statistical study to test isotropy of SXT spatial distribution for the results of the all-sky surveys.

2.1 Observable transient phenomena with MAXI

2.1.1 Gamma-ray burst

Gamma-Ray Bursts (GRBs) are bright γ-ray flashes first detected by the Vela satellites in 1960's (Klebesadel et al. [36]). The main observational features of GRB are isotropic angular distribution in the sky, short duration time in the order of 10^{-1}–10^{2} sec, greatest amount of the emitted energy about 10^{52} erg and afterglow phenomena subsequently appearing the main prompt emission.

Great contribution was made to the GRB study in the early era by the Burst And Transient Source Experiment (BATSE) instrument mounted on the Compton Gamma Ray Observatory

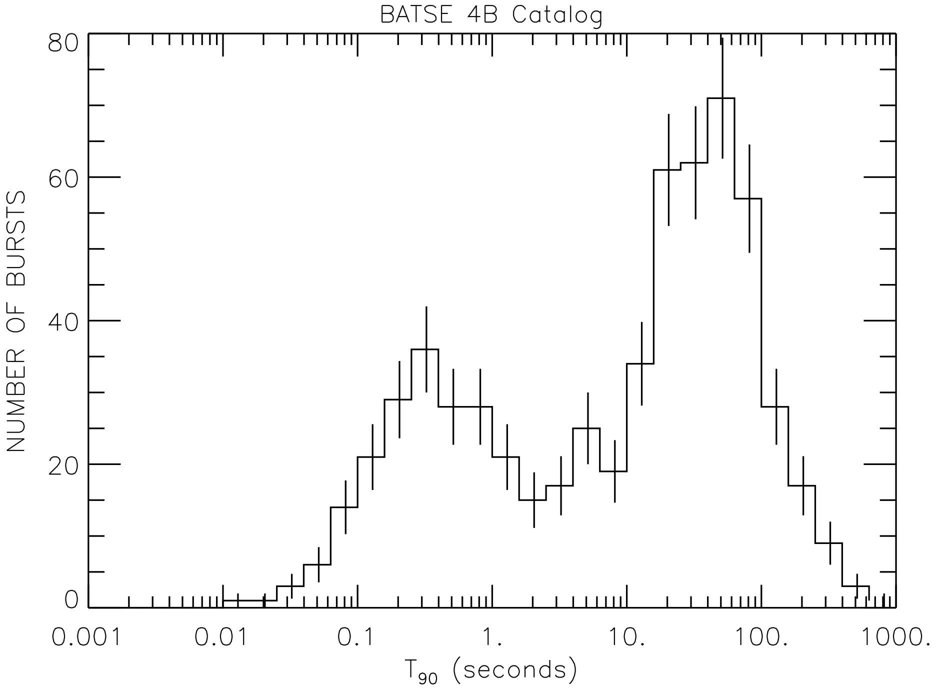

FIGURE 2.1: Distribution of duration time of GRBs observed by BATSE. Two populations are shown; one peaks at ~ 0.3 sec and the other at a few ten second.

(CGRO) satellite. The BATSE Large Area Detector is a NaI scintillation counter mounted on each corner of the satellite sensitive to 20 keV – 2 MeV photons. With the $\gtrsim 60\%$ sky coverage, BATSE detected 2704 GRB in the four year observation (Paciesas et al. [55]). These GRBs have isotropic spatial distribution as demonstrated in Figure 2.2 (Paciesas et al. [55]). This feature suggested the GRBs are originated from the cosmological distance rather than our galaxy or nearby galaxies. In addition, Kouveliotou et al. [40] shows the distribution of duration time T_{90} of the GRBs and indicates two distributions; short GRB with the duration of < 2 sec and long GRB with > 2 sec. The distribution of T_{90} which is the time taken to accumulate 90% of a burst fluence starting at the 5% level is shown in Figure 2.1[1].

Following the launch of the CGRO satellite, *BeppoSAX* started observation in the X-ray to γ-ray energy bands. The satellite has two wide field detectors, Gamma-Ray Burst Monitor (GRBM) and Wide Field Camera (WFC), and the Narrow Field Instruments (NFIs) that observe X-ray and γ-ray sources with the high angular resolution using focusing X-ray telescopes. In 1997, quick follow-up observations with telescopes of the NFIs were performed by a GRB event (GRB970228)[2] and revealed decaying X-ray emission in the 2–10 keV band (Costa et al. [11]). This emission was name "afterglow" and provided much more accurate localization than the

---

[1] `http://www.batse.msfc.nasa.gov/batse/grb/`

[2] GRB events are named after the date on which they are discovered.

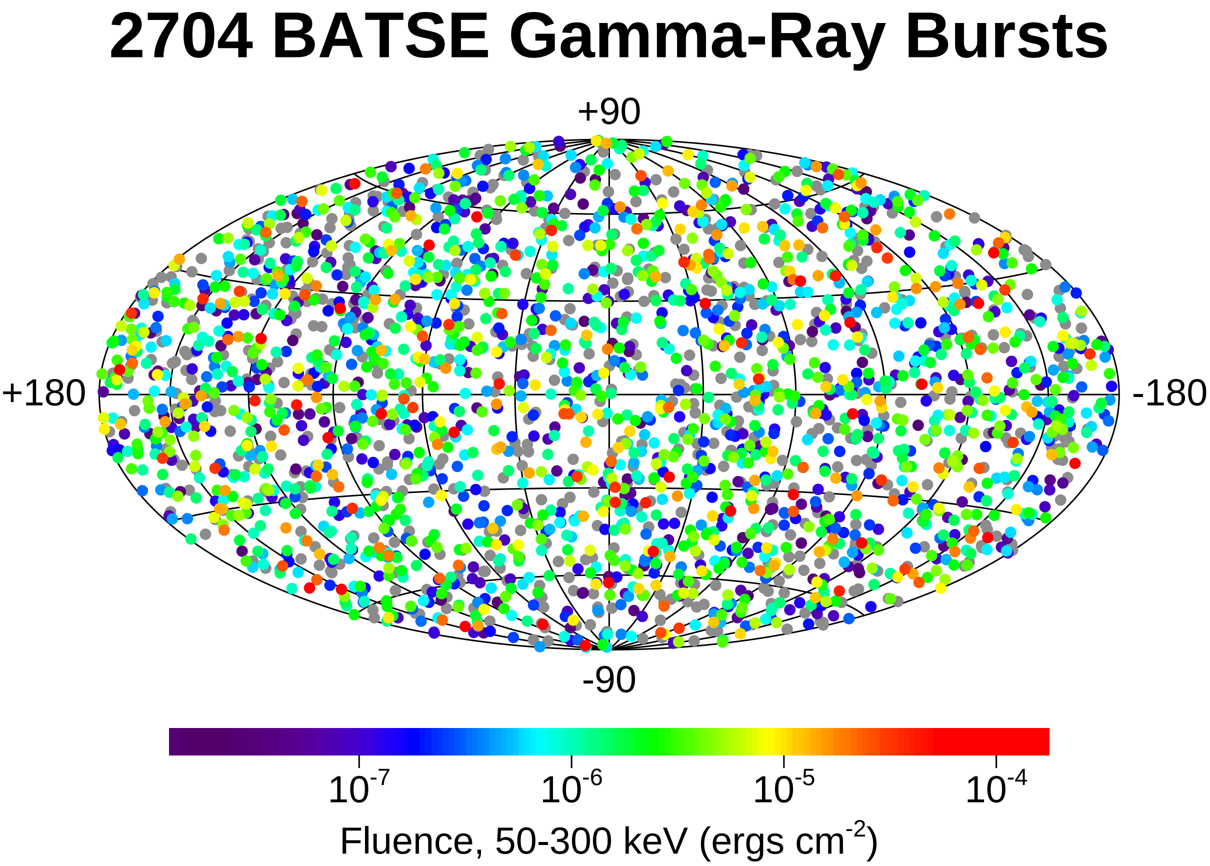

FIGURE 2.2: Spatial distribution of GRBs observed by BATSE in the Galactic coordinate. The colors means fluences of GRBs corresponding to the lower bar.

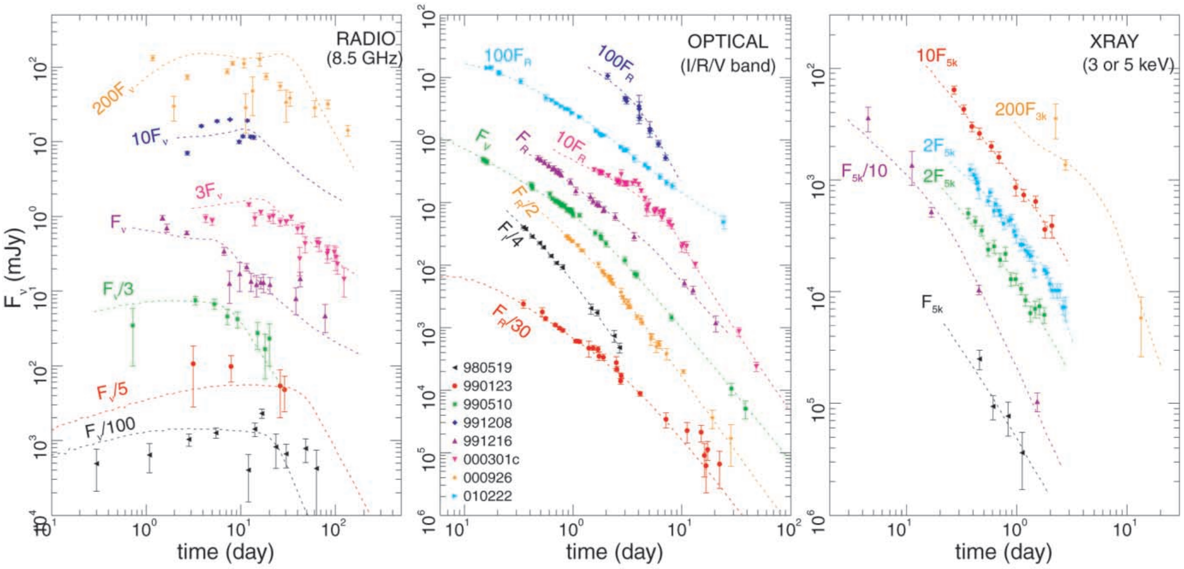

FIGURE 2.3: Light curves of GRB afterglows obtained in the radio, optical and X-ray wavelengths. The dashed lines are results of numerical calculation, whose parameters are listed in Panaitescu & Kumar [57].

result using traditional γ-ray detectors. Owing to the accurate localization, van Paradijs et al. [80] discovered the optical counterpart of GRB970228 using a ground-based telescope. After the remarkable discovery, another GRB (GRB970508) accompanied with X-ray and optical afterglow emissions was discovered (Djorgovski et al. [12]). Optical spectroscopic observations revealed that the GRB was associated with a galaxy whose redshift is ~ 0.835 and had the total emitted γ-ray energy of $\sim 10^{52}$ erg assuming the isotropic emission (Metzger et al. [48]). Since the discovery of afterglow, γ-ray emission of GRB has been called as "prompt emission".

The detections of afterglow phenomena and development of observational technology in the γ-ray and X-ray bands have greatly contributed to the study of GRB. The highlight of the result is suggestion of the GRB's progenitors as supernova. The supernova-GRB association were suggested from observations of SN1998bw/GRB980425 and confirmed with SN2003dh/SN030329 since the positional coincidence and the supernova-like temporally and spectroscopically behaviors of the optical counterparts of the GRBs (Galama et al. [17], Hjorth et al. [29]). This indicates that GRB phenomena are probably originated from supernova explosions.

Another investigation with developed observatories is determination of the distance of GRBs by observations of the spectra in optical wavelength. As the result, the typical energy released from a GRB is known as 10^{52}–10^{54} erg assuming the isotropic emissivity. In order to explain the energetics and high γ-ray luminosity within a short time, narrowlly-collimated explosion and mass ejection traveling with the speed exceeding $> 99\%$ of the speed of light, "jet", was introduced. If such jet aligns into our line of sight, brightness of radiation from the jet is enhanced with the relativistic beaming effect, that is derived from the special relativity as time dilation. In addition to the distance estimation, observations of afterglows show temporal evolutions mostly in the X-ray, optical and radio wavelengths which are well represented with power-law function with "break" at the elapsed time of 10^3–10^5 sec after the detections of the prompt emission. Figure 2.3 demonstrate the samples of afterglow light curves. This is explained that the deceleration of the relativistic jet due to interaction in circumstellar medium surrounding the progenitor, which is a prediction of the fireball model (Wijers et al. [82]). In conclusion, the typical agreement of GRB emission mechanism is the focused explosion from the relativistically-traveling jet which is driven by a central engine of a supernova.

The GRB prompt emission is one of the SXT candidates for MAXI-GSC. According to the distribution of X-ray fluence[3] of prompt emission obtained with the HETE-2 satellite (Sakamoto

---

[3] The flux integrated over time.

et al. [63]), the typical fluence in the 2–30 keV energy band is 10^{-7}–10^{-5} erg cm^{-2}. Assuming typical time duration of GRB as 100 sec, the peak X-ray flux of 10^{-9}–10^{-7} erg cm^{-2} s^{-1} is large enough to detect with GSC. In fact, since the first light in August 2009 until May 2013, GSC has discovered 35 probable GRBs (or short X-ray transients), which are summarized in Serino [68]. Almost one third of them (13 events) were confirmed with other observatories such a *Swift*, *Fermi*, and Konus-Wind; however 22 events were detected with only MAXI.

X-ray afterglows are also possible SXTs which will be detected by MAXI-GSC. The typical fluxes of afterglow are 10^{-8} erg cm^{-2} s^{-1} at the peak level (the elapsed time $\sim$ 100 sec after the GRB detection) and 10^{-12}–10^{-14} erg cm^{-2} s^{-1} during the late phase ($\sim 10^5$ sec after) in the *Swift*-XRT 0.3–10 keV energy band. MAXI-GSC can detect such afterglow in the bright time. In addition, late-time (10^3–10^5 sec after the prompt emission) X-ray afterglow associated with nearby GRB, e.g., GRB130427A with the redshift of 0.34 (Maselli et al. [46]), may be also detectable with GSC.

2.1.2 X-ray flash

In the traditional study of GRB, some classifications have been introduced; whether the duration time is short or long, type of its host galaxy and whether it accompanies supernova or not. Focusing to the spectral feature, GRBs are identified into *classical* GRBs, X-ray rich GRBs (XRRs) and X-ray flashes (XRFs). The first suggestion of XRF is Heise et al. [27] which reported peculiar GRBs detected with the BeppoSAX satellite. They selected 17 transients which were detected by Wide Field Camera (covering $2-25$ keV) but were not by Gammay-Ray Burst Monitor ($40-700$ keV) and classified them into XRFs.

The HETE-2 satellite which was launched in 2000 also observed short transients with the X-ray/γ-ray detectors, whose specifications will be described in Section 2.2.3. Using ratios between fluences of the GRBs in X-ray (2–30 keV) and γ-ray (30–400 keV) obtained with HETE-2, Sakamoto et al. [63] classified 45 burst events into 10 GRBs, 19 XRRs and 16 XRFs with the distribution of Figure 2.4. Although various temporal and spectral characteristics were investigated, Sakamoto et al. [63] finally concluded that all three kinds of bursts will arise from the same phenomenon. Sakamoto et al. [65] sophisticated the phenomenalistic study with the bursts obtained with the *Swift* satellite. *Swift* has Burst Alert Telescope (BAT) detecting 15–150 keV photons, which are different from the case of HETE-2. They performed similar analysis to the *Swift* detected bursts (10 XRFs, 17 XRRs and 14 GRBs) under the re-defined threshold

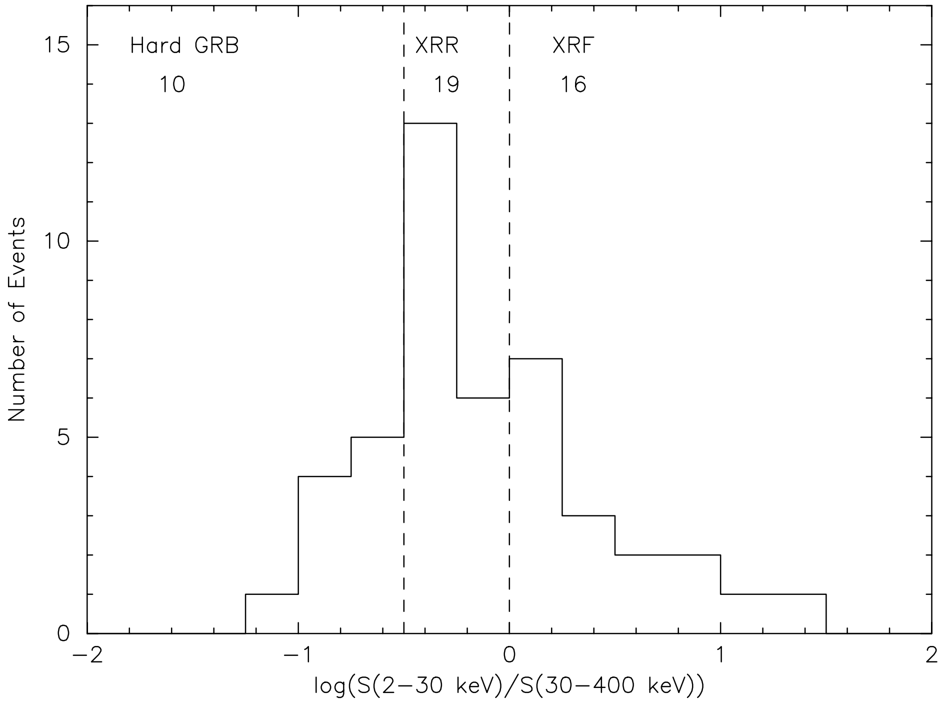

FIGURE 2.4: Distribution of hardness ratio of GRBs obtained by the HETE-2 satellite. The dashed lines divide the hard GRBs, XRRs and XRFs.

of fluence ratio in 25–50 keV and 50–100 keV and also concluded the spectral features of GRB, XRR and XRF are similar. However, since *Swift* provided light curves of X-ray afterglow with its X-ray Telescope (XRT; 0.3–10 keV), the difference of temporal properties were discovered; the break of the GRB light curves appeared at much earlier times than that of the XRF ones.

2.1.3 X-ray burst from neutron star binary

A binary system consisting of a neutron star, which is a compact star supported by quantum degeneracy pressure and having the typical radii of 10 km and the mass of 1.4 times solar-mass ($M_\odot$), and a star, which is a normal star and not compact, is another SXT candidate. Such system with the low-mass ($\lesssim 1M_\odot$) star is called as low-mass X-ray binary (LMXB) and that with the massive ($\gtrsim 10M_\odot$) star is high-mass X-ray binary (HMXB). X-ray bursts are characteristic phenomena of LMXBs which have fast-rise and slow-decay temporal activities of the X-ray flux in a few 1–10 sec as shown in Figure 2.5 and spectra which represented with blackbody radiation whose the temperature is a few keV. Observationally, such bursts have two categories labeled Type I and Type II, however only two sources have shown the Type II burst. Hereafter, we means the Type I bursts as X-ray bursts (XRB) of LMXB.

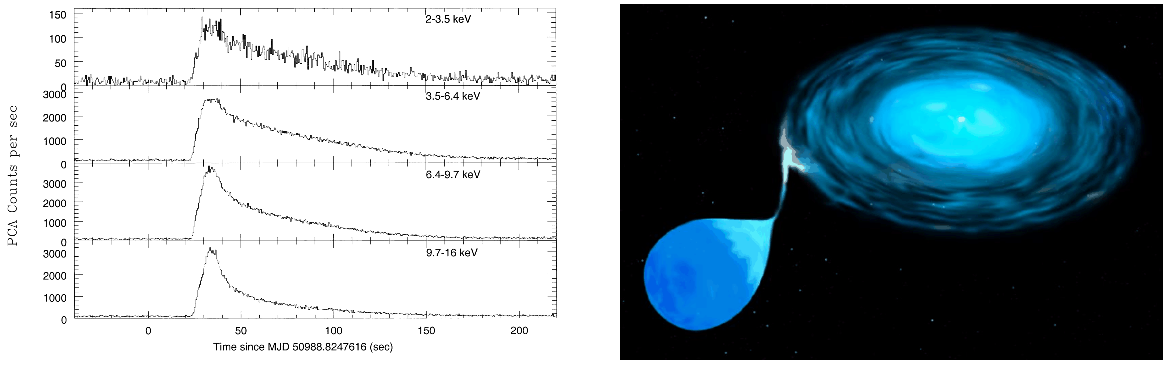

FIGURE 2.5: Left: The light curve of an X-ray burst from GS 1826−24 obtained with the RXTE satellite by Kong et al. [39]. Right: Illustration of X-ray binary system. The star at the left side is ordinary star which provides gas to the compact star located at the right side. Although neutron star, white dwarf or black hole will be located at the center of accretion disk, the former two objects show X-ray bursts.

The physical mechanism of X-ray burst is explained with mass accretion and nuclear fusion of the accreted matter as shown in the right panel of Figure 2.5. Gas which mainly consists of hydrogen and helium is transferred from the star to the neutron star with forming an accretion disk around the neutron star at the Lagrange point in the LMXB system. The gas travels in the accretion disk and cumulates on the surface, compressed with strong gravitational field of the neutron star. When the pressure and temperature reached at the limit, nuclear fusion starts. This reaction burns up and heat the material on the whole surface with emitting a bright X-ray burst.

The luminosity of XRBs is limited by the Eddington limit, which is 3.8×10^{38} erg s^{-1} with a neutron star whose mass is 1.4 times of the Sun and which has hydrogen-poor atmosphere (Strohmayer & Bildsten [73]). Based on the one-scan detection limit, GSC can detect XRBs which are located at less than $\sim$ 100 kpc.[4] This distance includes the radius of our galaxy, however does not reach other nearby galaxies. Since a neutron star, which is a part of LMXB, is an old star remained after the supernova explosion, the binary often found in globular clusters. A globular cluster is a clump of stars that orbits a galactic core. Globular clusters typically include older stars, white dwarfs and neutron stars. Thus, many LMXBs are discovered in the clusters, such as 4U 0517−40 in NGC 1851 and EXO 1745-248 in Terzan 5.

---

[4] One pc (pronounced as “parsec”) is $\sim 3 \times 10^{18}$ cm.

2.1.4 Active star flare

Stars in an early phase of its evolution or a complex environment such as binary systems will show flares which are observed with wide wavelength band. One of such system is RS CVn (Canum Venaticorum) type variable star. It is a class of close binary systems consisting of late-type stars, such as G-M type stars (Hall [23]). These systems show luminous X-ray emissions which will be driven by the chromospherically activity of the stars. The origin of the coronal activity is interpreted as cool large stellar spots (in analogy to sunspots). The flares have fast-rise and slow-decay X-ray light curves and the anomalous luminosity with the orders of magnitude to the solar flares.

An X-ray flare of M dwarf is also driven with the energy release of the magnetic field. The star is a very-low-mass ($\lesssim 0.1$ M$_\odot$) star with the spectral class of M (the effective temperature of 2000–3000 K) showing the Hα emission line. The surface magnetic field is strong and releases the energy as flares with the large luminosity in the radio-to-X-ray band. The mechanism powering the magnetic field is not fully understood.

The young stellar object (YSO) is a generic name of newly born stars from interstellar molecular clouds. Based on the spectra in infrared and optical wavelengths, the YSOs are classified into sub-classes. The spectral features reflect evolution stage of the YSO; whether the core is surrounded by the clouds, whether the accretion flow and disk is dense or not. The evolved YSOs are named as T Tauri stars after the first identified source. The fast-rise and slow-decay X-ray activities observed from the stars are characterized with the surprisingly luminosity which is brighter than the solar flare by a several order of magnitude. The progenitors of the flares are interpreted as strong magnetic activities on the surface of the star and/or between the star and the accretion disk.

The typical luminosity of these flares is $> 10^{30}$ erg s^{-1}. Thus, we estimate that flares from nearby stars with 100 pc ($\sim 10^{19}$ cm) are detectable, assuming the typical detection limit of GSC with one-scan transit ($\sim 10^{-9}$ erg cm^{-2} s^{-1}). Since the distance is comparable to the thickness of the galactic plane, GSC will observe X-ray flares from the stars which are isotropically distributed around the solar system.

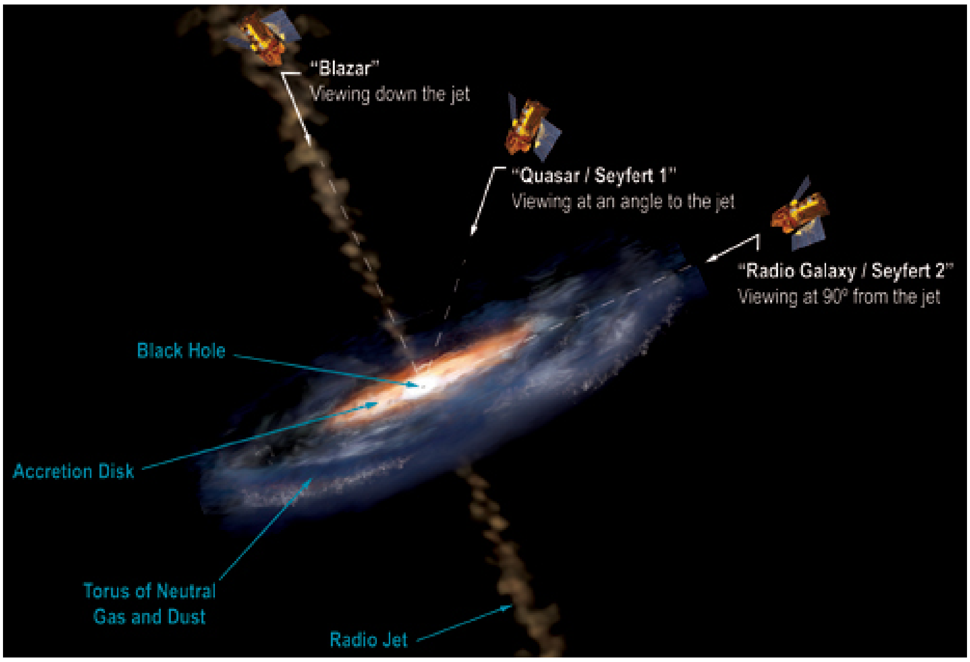

FIGURE 2.6: Illustration of AGN system. Around the massive black hole located at the center bright region, the accretion disk, truss structure and relativistic jet are generated. The three white allows indicate difference of our viewing angle. Seeing the AGN with the on-axis directions, we will observe the system as a blazar.

2.1.5 Flare of blazar

Active galactic nucleus (AGN) is a super massive black hole located at the center of galaxy and shows high luminosity in wide waveband from radio to γ-ray. The black hole with the mass of 10^6–10^{10} $M_\odot$ has an accretion disk and often a narrowly-collimated outflow, called as jet. Figure 2.6 shows the schematic picture of the AGN system[5]. From the aspect of viewing angle, AGNs are classified into sub groups. Blazar is a group of AGNs which have a jet oriented to our line of sight. The apparent luminosity of the blazar's jet is enhanced with the relativistic beaming since the plasma in the jet is accelerated into sub light-speed ($\gg 99\%$) and is observed with face-on. A type of blazars with rapid temporal variation of the luminosity is called as BL Lac object after its prototype. In the case of representative BL Lac examples, such as Markarian 421 (Mrk 421), the peak luminosity of the X-ray flare is the order of 10^{-9} erg cm^{-2} s^{-1} (Isobe et al. [31]) that is comparable to or larger than the detection limit of one-scan GSC transit. The time duration of the flares, from sub-day to day (Bartoli et al. [3], Kataoka et al. [33]), is long enough to detect with a scan. The long flares may be continuously detected during several scans of GSC.

---

[5] `http://www.nasa.gov/centers/goddard/images/content/182566main2_1agn_LO.jpg`

2.1.6 Tidal disruption event

One of the surprising phenomena is anomalous X-ray and γ-ray emission associated with a tidal disruption event. When a star pass through close to a massive object (e.g., black hole), its strong gravitational field destroys the star via the tidal force. The debris fall into the massive star making an accretion disk and emitting radiation in multi wavelengths. As the result this phenomena are observed as tidal disruption events (TDEs). The long-term temporal evolution of TDEs was theoretically predicted as a power-law function with the index of $-5/3$ (Evans & Kochanek [14], Lodato et al. [43]). Classical TDEs have been reported by some observatories that the light curve followed the theory and the spectra were represented as blackbody with the temperature of much less than 1 keV and the peak luminosity of 10^{42}–10^{44} erg s^{-1} (Halpern et al. [24], Komossa & Bade [38]).

In 2011 a new type of TDE candidate Swift J164449.3+573451 was discovered by *Swift* and MAXI with the peak X-ray flux of 7×10^{-9} erg cm^{-2} s^{-1}. Figure 2.7 shows the long-term light curve obtained by *Swift* (Burrows et al. [7]). In contrary to the classical TDEs, the source associated with a 10^8 $M_\odot$ supermassive black hole has shown bright X-ray emission with the flux of $> 10^{-10}$ erg cm^{-2} s^{-1} for more than ten days. The observations performed in radio to γ-ray wavelength revealed the relativistic jet which may be driven by the TDE aligned into our line of sight and originated anomalous emission by synchrotron and/or inverse Compton processes (Bloom et al. [5], Burrows et al. [7], Zauderer et al. [85]). The lower panel of Figure 2.7 demonstrates the story of the TDE associated with the jet[6]. Since the event rate of the TDE was estimated as 0.08–3.9 $year^{-1}$ (Burrows et al. [7]), additional candidates may be discovered in our analysis.

2.1.7 Supernova shock breakout

Supernovae (SNe) are luminous stellar explosions associated with the death of stars. Based on the spectral features in optical wavelength, SNe are classified into four main types; Ia, Ib, Ic and II. Here, progenitors of the type Ia SNe are white dwarfs are provided mass from stars in the binaries. When the mass reaches at the Chandrasekhar limit, the dwarf is gravitationally collapsed and drives an explosion following violent nuclear fusion in its core. On the other hand, the other types are triggered in the ending of the evolution by the core collapse of massive star

---

[6] `http://www.nasa.gov/mission_pages/swift/bursts/devoured-star.html`

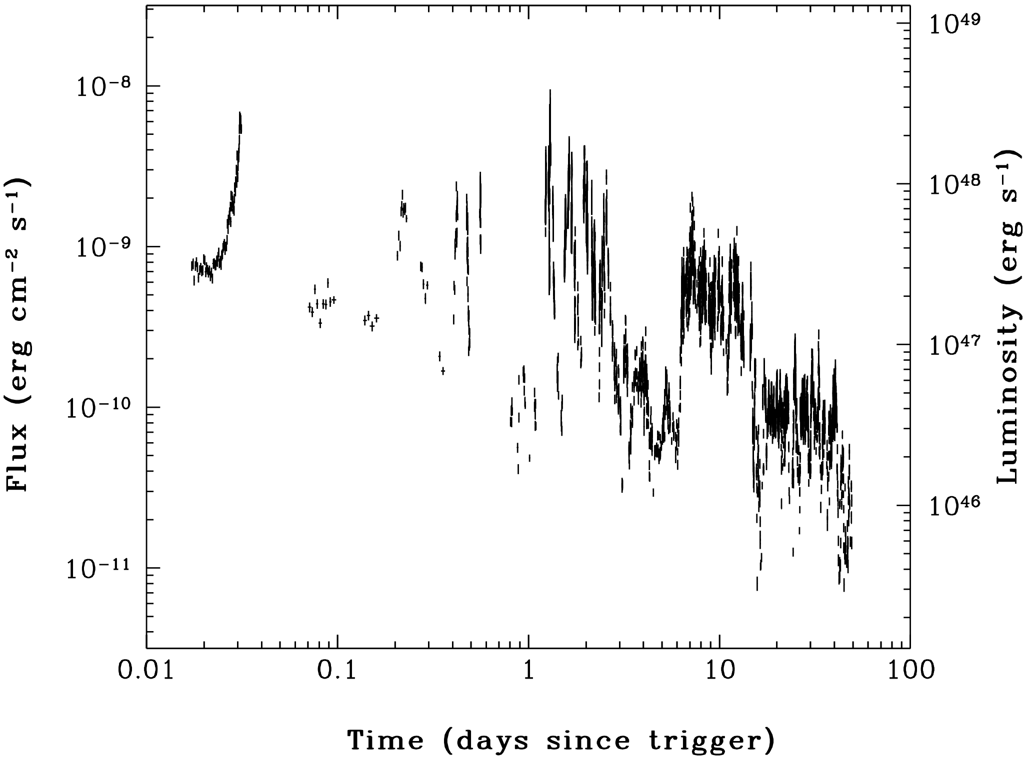

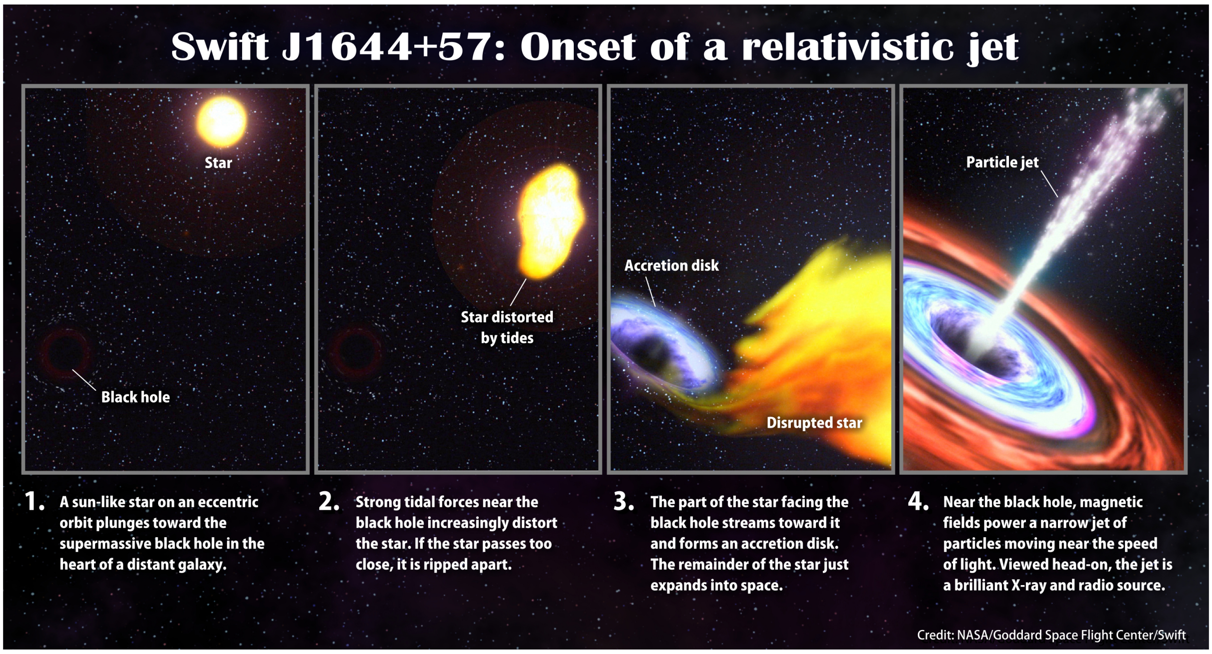

FIGURE 2.7: Up: The light curve of Swift J1644+57 obtained by *Swift*-XRT. Low: The illustration of how to generate the relativistic jet with the tidal disruption event of Swift J1644+57. The black hole at the left side of each panel swallows the distorted star and powers the narrow jet. We observed this phenomenon in face-on.

whose mass is several times larger than the stelar mass. Observationally, SNe are discovered a few day after its ignition when the accompanied neutrinos will be detected. Colgate [9] and Klein & Chevalier [37] theorized early X-ray and/or ultraviolet emission when shock wave originated from the core breaks out through the stellar surface.

The prompt X-ray emission from a break-out of super nova shock wave was detected in 2008 as the X-ray outburst XRO080109 which associated with the super nova SN2008D (Soderberg et al. [72]). The X-ray light curve was characterized fast-rise with the rise time of 63 sec and exponential decay. The spectral analysis reported the peak flux is 6.9×10^{-10} erg cm^{-2} s^{-1} in the 0.3–10 keV band. Since the luminosity is 6.1×10^{43} erg s^{-1} assuming the host galaxy as NGC2770 (the distance is 27 Mpc), MAXI-GSC will be detectable such shock break outs accompanying SNe in a few Mpc distance.

2.2 Information of past transient event surveys

2.2.1 Early history of all-sky X-ray surveys

In the early era of X-ray astronomy, in 1970s and 1980s, several observatories performed X-ray all-sky surveys. They discovered many X-ray sources that are now well known and short X-ray transients (SXTs) with detecters which were mainly sensitive to soft X-rays ($<$ a few 10 keV). Some of these observatories such as the Uhuru satellite (launched in 1970), the third small astronomy satellite SAS-3 (launched in 1972) have reported discoveries of SXTs (Forman et al. [16], Hoffman et al. [30]).

Ariel V, which is an X-ray astronomical observation satellite launched in 1974, performed all-sky survey for 5.5 year and reported 27 SXTs (Pye & McHardy [60]). A detector onboard the satellite is a set of collimated proportional counters with a field of view $0.75° \times 10.6°$ as called Sky Survey Instrument (SSI). These SXTs were detected with a significance of $> 5.5\sigma$, or a threshold flux of > 8 SSI count s^{-1} $= 20$ mCrab. Eleven of them were identified as flare stars and known X-ray sources including blazars, X-ray binaries and globular clusters. Pye & McHardy [60] reported that possible counterparts of other unidentified SXTs were gamma-ray bursts and/or yet unknown classes of object.

A systematic all-sky survey were also performed by High Energy Astronomy Observatory 1 (HEAO-1) which was launched in 1977. This observatory had four types of X-ray and soft γ-ray detectors consisting of proportional counters with collimators and scintillator detectors. One of the detectors, Large Area Sky Survey experiment (LASS or called as A-1), had performed observations for six month in the 0.5–20 keV band and discovered ten SXTs (Ambruster & Wood [1]). Although four of them were identified as flare stars, other six transients were unidentified, which may have been gamma-ray bursts. The survey data of another detector, Cosmic X-ray Experiment (CXE or called as A-2), provided five new ones and three sources which were previously found flare stars (Connors et al. [10]).

The *Einstein* observatory (i.e., HEAO-2 Giacconi et al. [20]) was the first imaging X-ray telescope launched in 1978. Detection of SXTs with the Imaging Proportional Counter (IPC) on the observatory was reported in Gotthelf et al. [21]. They discovered 42 SXTs with the limiting sensitivity of 10^{-11} erg cm^{-2} s^{-1} in the 0.2–3.5 keV band. Gotthelf et al. [21] concluded 18 of the transients have harder spectra and slow decaying light curves and were originated from common source like as GRBs.

In addition to the mission by Europe and the United States, Japan and Soviet Union also performed X-ray survey in 1970s and 1980s, From Japan, three mission of X-ray observatories were launched; Hakucho in 1979, Tenma in 1983 and Ginga in 1987. The Gamma-ray Burst Detector (GBD) onboard Ginga have observed 24 SXTs in 1.5–370 keV for about a year (Yoshida et al. [84]). Since GBD had no position sensitivity without any collimators, any counterpart of the SXTs has not been confirmed. In 1989 a Soviet space observatory Granat were launched. The all-sky X-ray instrument WATCH monitored approximately 75% sky in the 8–100 keV and energy band. Castro-Tirado et al. [8] reported six SXT detections, of which three were possible GRBs and two were associated with known sources.

2.2.2 All-sky surveys in 1990s

In 1990s, another developed all-sky survey missions have been launched, such as the CGRO, ROSAT, BeppoSAX and RXTE satellites. The CGRO and BeppoSAX performed surveys in the hard X-ray bands, 20–600 keV of CGRO and 40–700 keV of BeppoSAX, whose results focusing to GRB will be described in Section 2.1.1. One of the remarkable contributors of the soft X-ray survey was ROSAT (the *Röntgen* Satellite), which was launched in 1990. In the first six months, ROSAT observed the all sky with the Position Sensitive Proportional Counter (PSPC) in the 0.1–2.4 keV. The telescope provided data with $\sim 10^{-12}$ erg cm^{-2} s^{-1} detective sensitivity and detected 27 X-ray transients (Greiner et al. [22]). Although most of them were identified to flare stars, the small detection rate of ROSAT all-sky survey is consistent with the rate of afterglows expected from the BATSE data.

In 1995, the *Rossi* X-ray Timing Explorer (RXTE) satellite was launched into low-Earth orbit. The satellite had two instrument which observed soft X-rays, the Proportional Counter Array (PCA) and the All-Sky Monitor (ASM) which detected photons in the 2–20 keV and 2–12 keV energy bands. The PCA is a pointing observable instrument consisting of gas proportional counters and observing in the 2–60 keV. On the other hand, the ASM consists of three set of position sensitive proportional counters and slit masks (Levine et al. [42]). Using the ASM, Smith et al. [71] reported light curves of 15 GRBs. They represented the difference of temporal variability detected by the ASM and other instrument, such as BATSE, observing in the hard energy bands. One year after the RXTE launch, in 1996, the BeppoSAX satellite started observation with the telescope instruments, the Wide Field Camera (WFC) and Gamma-Ray Burst Monitor (GRBM). The sensitive energy bands of the WFC and GRBM are 2–28 keV and 40–700 keV, respectively. The main achievement of the BeppoSAX focusing to the soft X-ray transient is the discovery of GRB's afterglow and X-ray Flashes (XRFs).

2.2.3 Recent surveys

The High Energy Transient Explorer (HETE-2) was a satellite aimed to observe GRBs launched in 2000. HETE-2 has FREGATE (NaI scintillation counters), WXM (proportional counters and coded masks) and SXC (X-ray CCDs with corded mask). A burst detected with the FREGATE and/or WXM is localized by the WXM and performed fine localization with SXC. The detection and localization result are immediately reported to the GRB Coordinate Network (GCN)[7]. Number of the detected GRB with HETE-2 is 250 events in about six year operation (Pélangeon et al. [58]). With the HETE-2 data in the first three years, Sakamoto et al. [63] revealed the temporal and spectral properties of the XRFs and X-ray-rich GRBs. The 45 HETE-2 detected GRBs are characterized by its fluence ratio between the 2–30 keV and 30–400 keV into GRB, X-ray-rich GRB and XRF.

The *Swift*sattelite, which was launched in 2004, is the largest contibutor of rapid localization of GRBs. As same as HETE-2, the satellite is specified to observe GRBs and report information (position, flux and significance) of the bursts to the GCN via the Internet. *Swift* has three observational instruments; Burst Alert Telescope (BAT), X-ray telescope (XRT) and UV/Optical

---

[7] `http://gcn.gsfc.nasa.gov/`

Telescope (UVOT). The BAT detector detects GRBs within the 1.4 steradian FoV and roughly localizes them with their accuracy of sub-degree. When the BAT detects a GRB, the satellite is quickly oriented into the burst and starts observation with the XRT and UVOT. In the five year operation *Swift* detected 476 bursts by BAT (Sakamoto et al. [66]). Additional XRF samples detected by *Swift* revealed similarities and differences of the temporal and spectral properties between GRBs and XRFs (see Section 2.1.2 and Sakamoto et al. [65]). Moreover, *Swift* discovered new type SXTs such as the unexpected X-ray flare associated with tidal disruption event (see Section 2.1.6) and the shock break out of the super nova (see Section 2.1.7).

2.2.4 Systematic SXT search with MAXI

Since 2009, MAXI has been performing all-sky continuous monitoring with $\sim 80\%$ sky coverage in one orbit period of the International Space Station (ISS). With two kinds of X-ray counters, Gas Slit Camera (GSC) and Solid-state Slit Camera (SSC), SXTs including GRBs have been reported by the MAXI observation (The specifications of MAXI and these detectors will be described in the next chapter).

A systematic search for SXTs has been already performed by Toizumi [75] for the first 15-month observation data of GSC. The method of the search consists of two main processes; rough extraction of SXT candidates and local analysis for the candidates. The former process selects excesses against fluctuation of GSC background which is represented by its simplified model. This selections were sequentially performed to the observation data which were temporally partitioned with every short duration of GSC's one-scan transit. The partitioned data were represented with the background model which consists of non-X-ray background and cosmic X-ray background as shown in Figure 2.8. On the data, SXTs will appear as excesses with the significant signal to noise ratio against the background supposing that its fluctuation is the Poisson distribution. Next, they performed local analysis to determine accurate positions on the sky and X-ray fluxes of the selected candidates, statistically fitting with point spread function (PSF) of the GSC counter. The PSF of GSC is approximately duplicated by a product of triangular function and Gaussian function, which will be describe in Section 3.2.4.1. The local analysis fitted the X-ray event data of the selected candidates with the function using the un-binned likelihood method instead of the chi-square test so as to estimate the goodness of fit. Finally, the previous systematic search found 29 SXT candidates with the detection threshold

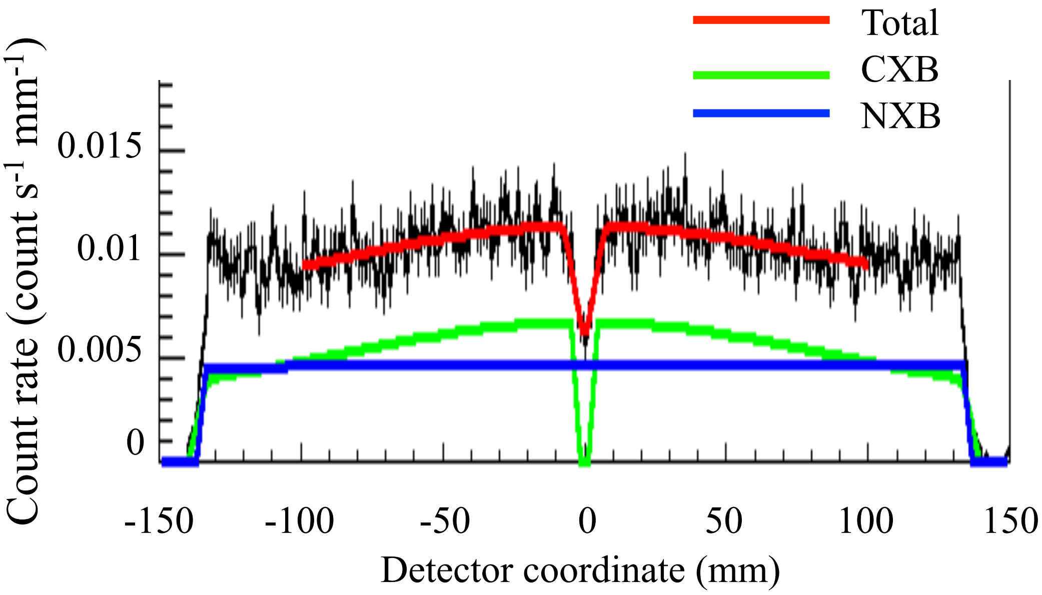

FIGURE 2.8: Distribution of X-ray events along the MAXI-GSC detector coordinate and result of model fitting provided by Toizumi [75]. The blue and green lines are model functions of non X-ray background (NXB) and cosmic X-ray background (CXB). The red one is sum of these contributions.

probability of 10^{-8}. Four known GRBs and five possible GRBs were associated with the found SXTs.

Although the previous transient search study seems as success, it possesses complex estimation of propagation of errors. The searching method consists of two processes, selection of excess base on the Poisson-distributed background and local analysis with the PSF-fitting. Here, we note that determination of the detection threshold and estimation of fake detection in the later process depend on whether the former selection process detects these SXT candidates or does not. Furthermore, the analysis has the complicated dependency, nevertheless, the detection significances were estimated independently. Thus, the holistically propagation of errors cannot be simply interpreted. To avoid such complicated situations, we develop new simple and straightforward method to search SXTs from the MAXI-GSC long observational data. The method which will be explained in Chapter 4 supposes the Poisson-fluctuated background of the GSC counter and estimates only significance of excesses originated from SXTs; however it does not apply such fitting analysis with the background model and the PSF of X-ray sources. In Chapter 5 and 6, we will discuss an explicitly determined detection threshold and the estimation of fake detections using the simple method.

2.3 statistical test of survey study

2.3.1 Test of isotropy

If celestial objects distribute randomly, the positional distribution on the celestial sphere will be isotropic. To verify the isotropic/anisotropic positional distribution of celestial objects, two statistics $\langle \cos\theta \rangle$ (Hartmann & Epstein [26]) and $\langle \sin^2 b - 1/3 \rangle$ (Briggs et al. [6]) have been appreciated. The former is the dipole moment toward the Galactic center is the mean of the $\cos\theta_i$, where θ_i is an angle between the ith SXT candidate and the Galactic center. Another statistics, $\langle \sin^2 b - 1/3 \rangle$, the quadruple moment which tests a concentration in the Galactic plane or at the Galactic poles, where b is galactic latitude. If observation has even exposure and effective area, an isotropic distribution provides both statistics of zero.

Using these statistics, the isotropic distribution of GRBs has been confirmed by several studies. For example, Briggs et al. [6] investigated positional distribution with the 1005 GRBs obtained by the BATSE satellite. The result estimated the difference of these statistics by $< 1\sigma$ and concluded the isotropic distribution of GRBs. In the past transient source survey with MAXI also suggested isotropic distribution with the $\langle \cos\theta \rangle = 0.02 \pm 0.17$ (Toizumi [75]).

2.3.2 $V/V_{\max}$ test

To investigate uniformity of radial distribution of celestial objects, $V/V_{\max}$ test was introduced by Schmidt et al. [67]. First we suppose that a source with its luminosity of L and flux $F > F_{\rm lim}$ at a distance r is detectable with an instrument in the Euclidean space. Here, the distance r and the maximum distance at which the same source is detectable $r_{\max}$ is estimated from

$$r = \left(\frac{L}{4\pi F}\right)^{1/2} \tag{2.1}$$

$$r_{\max} = \left(\frac{L}{4\pi F_{\rm lim}}\right)^{1/2}. \tag{2.2}$$

Next, we define two spherical volumes;

$$V = \frac{4\pi r^3}{3} \tag{2.3}$$

$$V_{\max} = \frac{4\pi r_{\max}^3}{3}. \tag{2.4}$$

If we consider the uniform distribution of the sources, half of the source will be detected in the inner half of the volume $V_{\rm max}$ and the other half in the outer half. Thus, the average of $V/V_{\rm max}$ is expected as $V/V_{\rm max} = 0.5$.

Since in the actual observation we obtained number of X-ray/γ-ray photons using a detector, the $V/V_{\rm max}$ value is converted to

$$\frac{V}{V_{\rm max}} = \left(\frac{C}{C_{\rm lim}}\right)^{-3/2}. \tag{2.5}$$

Here, C and $C_{\rm lim}$ are the detected photon count of a source and the detection limit estimated by the signal to noise ratio of the instrument R, respectively. Supposing Poison distributed fluctuation of the background count $N_{\rm b}$, the $C_{\rm lim}$ is defined as $R\sqrt{N_{\rm b}}$. Pendleton et al. [59] reported $V/V_{\rm max} = 0.329 \pm 0.011$, which is not equal to 0.5, base on the BATSE's GRB catalog. Following the work, Paciesas et al. [55] also reported the non-half value with the revised 4th BATSE GRB catalog. These results support that GRBs are cosmologically distanced sources and the space is not flat but distorted.

2.3.3 Log$N$-log S plot

Another leading mark to study the spatial distribution is log N-log S plot. Here, S means a photon or energy fluence observed in any wavelength range and decreases inversely with square of the source distance r, i.e., $S \propto r^{-2}$. The N is cumulative number of sources whose fluxes are larger than the corresponding flux S. If objects uniformly distribute in the flat Euclidean space, number of objects within the radius r is proportional to the volume of the space, $N \propto r^3$. Therefore, the cumulative number of the objects will have relation with the observed flux as $N \propto S^{-3/2}$.

The first log N-log S plot of transient X-ray sources is obtained by the HEAO-1 satellite as shown in Figure 2.9 (Ambruster & Wood [1]). It is visually suitable to the S^{-1} relation rather than $S^{-3/2}$. The following transient X-ray surveys (Arefiev et al. [2]) provided wide fluence band log N-log S plot which was assembled with archival data of the Ariel V, HEAO-1, WATCH, *ROSAT* and *Einstein*satellites. The plot Figure 2.10 is globally represented by the single power-law function with the index of −1. The previous study of short transient search with MAXI-GSC provided the similar log N-log S plot as shown in Figure 2.11 (Toizumi [75]). Although the plot

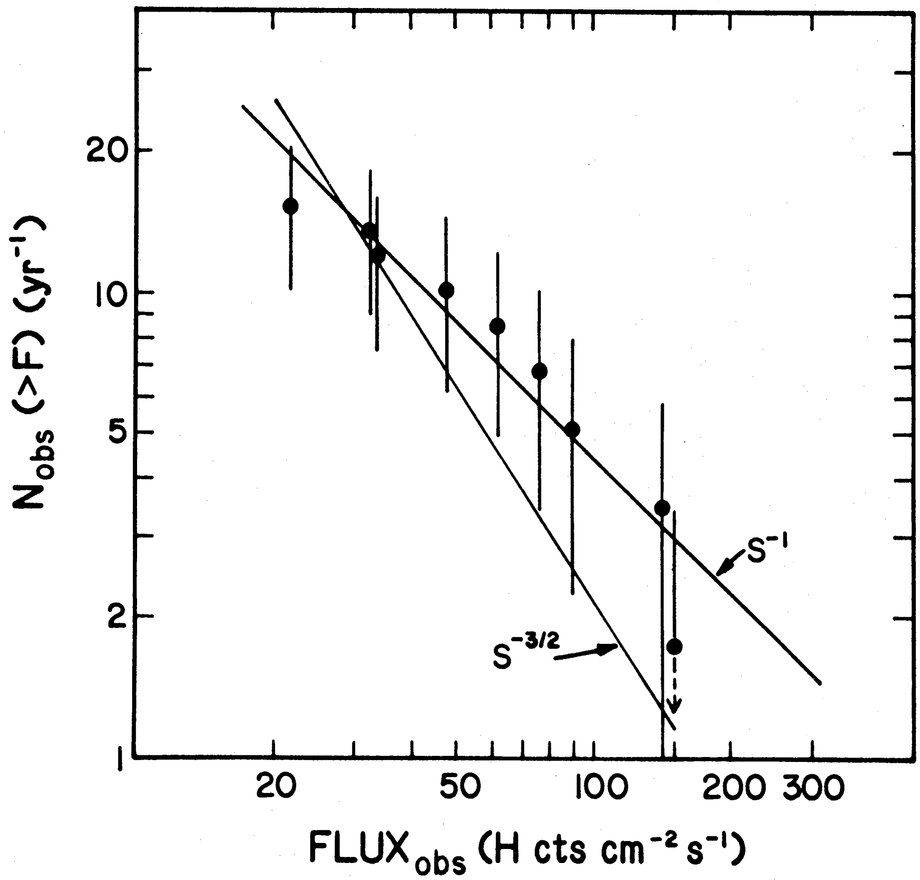

Figure 2.9: Log$N$-log$S$ plot obtained by HEAO-1. The error was estimated with Poisson distribution. The lines marked S^{-1} and $S^{-3/2}$ are best fits to the eye.

obeys the S^{-1} function in the brighter fluence band ($S > 0.8$ counts cm^{-2}), another power-law like component with the index of $-3/2$ appears in the fainter region. They discussed the possible origin of the components as flares of active stars, AGNs and both prompt emissions and afterglows of GRBs.

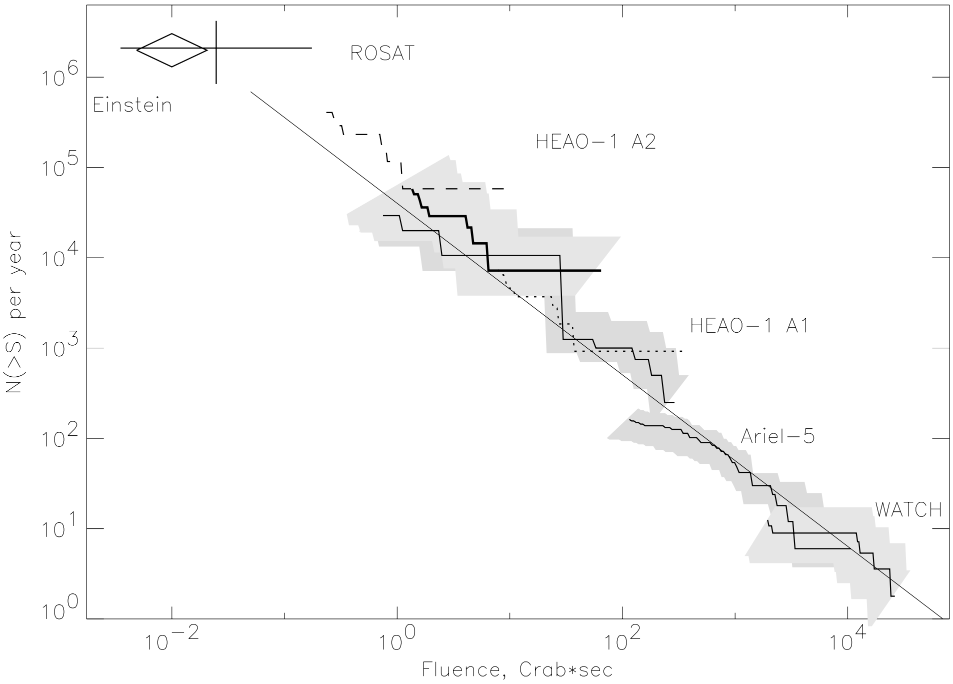

FIGURE 2.10: Log$N$-log S plot of short X-ray transients assembled with the archival data of Ariel V, HEAO-1, WATCH, *ROSAT* and *Einstein*. The thick solid line represents the best-fit power law with Ariel V, HEAO-1 and WATCH data. The index of the function is 0.95. Statistics and systematic errors of each distribution are shown as the shadowed areas. The thick curve is averaged data of HEAO-1 obtained from the dashed and dotted curves which mean difference of assumed event duration to correct HEAO-1 data.

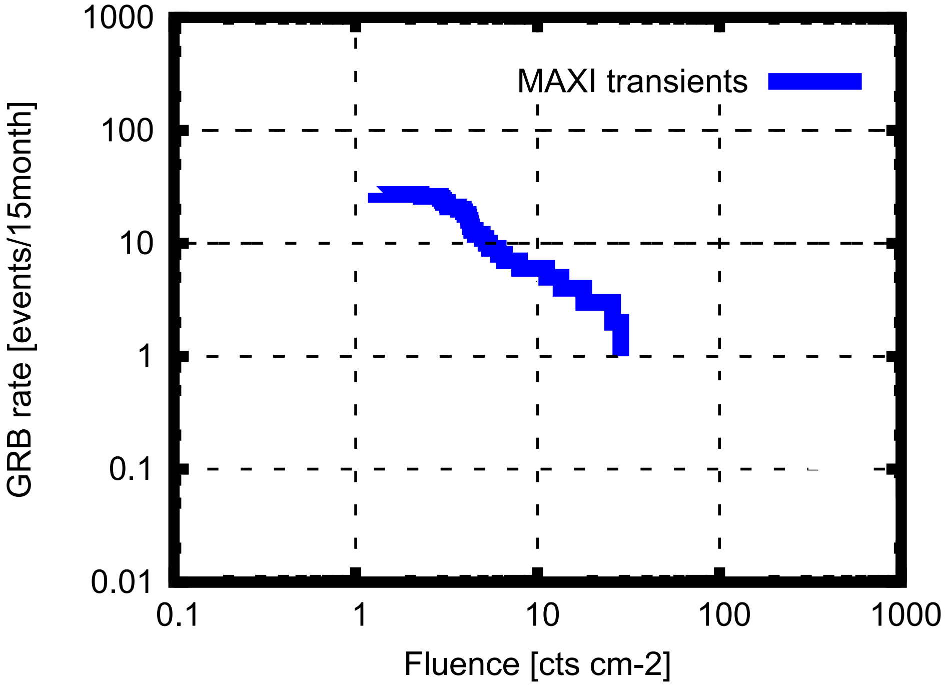

FIGURE 2.11: Log$N$-log S plot of short X-ray transients obtained with MAXI in the previous study. This plot includes 29 transients whose detection probability is more than $\sim 9\sigma$ level.

Chapter 3

Observatory – MAXI

3.1 MAXI

3.1.1 Overview of MAXI

Monitor of All-sky X-ray Image (MAXI) is the first astronomical mission operated on the International Space Station (ISS). It was delivered to the ISS by Space Shuttle Endeavor on July 16 2009 and installed on the Japanese Experiment Module Kibo Exposed Facility (JEM-EF) on July 24. Since August 15 MAXI has performed nominal operation for more than four years. The mission is reviewed in Matsuoka et al. [47]. Picture of MAXI installed on JEM-EF[1] and overview of the MAXI components[2] are shown in Figure 3.1 and 3.2 (Matsuoka et al. [47]), respectively. MAXI has two kinds of X-ray cameras, Gas Slit Camera (GSC), and Solid-state Slit Camera (SSC). The information of the GSC instruments is described in Mihara et al. [49], and the in-orbit performance is described in Sugizaki et al. [74]. Tomida et al. [76] and Tsunemi et al. [78] describe the performance of SSC on the ground and in-orbit, respectively. In addition to these observational equipments, MAXI has some controlling and operating systems, e.g., Radiation Belt Monitor, Visual Star Camera, Ring Laser Gyroscope, Loop Heat Pipe and Radiation System, and Mission Data Processor. See publications listed in the web site of MAXI[3] to obtain information about these subsystems.

---

[1] `http://iss.jaxa.jp/kibo/archive/2010/09/good_design_award_2010.html`

[2] `http://www.jaxa.jp/press/2009/08/20090818_maxi_j.html`

[3] `http://maxi.riken.jp/top/`

3.1.2 Data processing flow of MAXI

MAXI provides some kind of data; e.g., X-ray observational data and house keeping data. They are processed on data processor of MAXI and transported to ground stations of NASA (National Aeronautics and Space Administration) through data relay satellites. The telemetry data transported to Tsukuba Space Center of JAXA (Japan Aerospace Exploration Agency) is stored on a database, called as MAXI-DB, which is designed to handle MAXI data. From the MAXI-DB, the MAXI science team constructs observational data which include information of

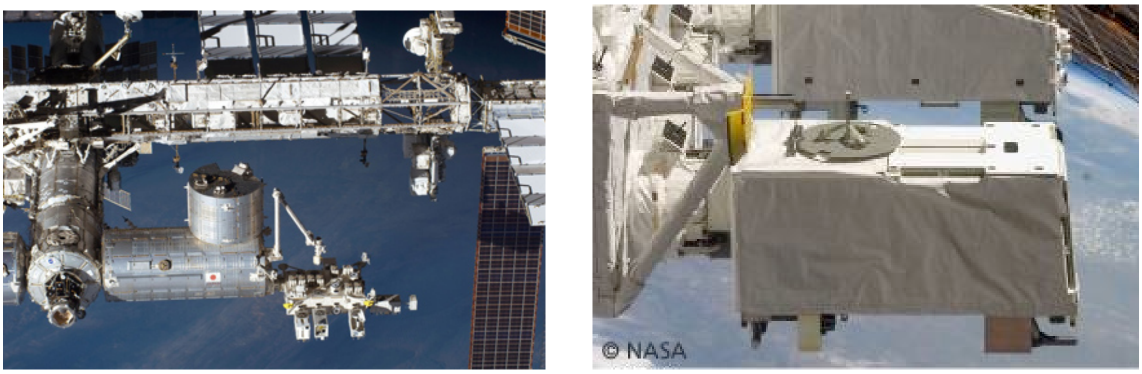

FIGURE 3.1: Left: Picture of JEM, JEM-EF and MAXI. MAXI mounted in front of the JEM-EF is located at a center lower part in the picture. Right: Overview of MAXI. The left side structure is a docking port of the JEM-EF.

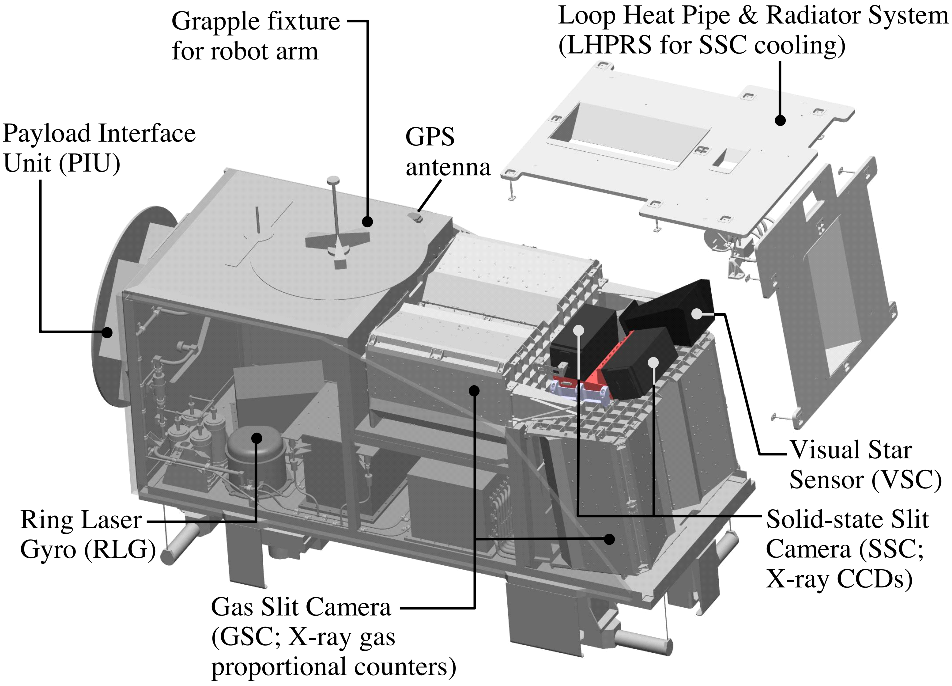

FIGURE 3.2: Layout of MAXI instruments. The GSC units are mounted on the front and upper side of MAXI. The cameras on the front corner of MAXI are SSC. Other subsystems are also shown.

detected X-ray events for each day and each camera of GSC and SSC. Using a function providing real-time data from MAXI-DB, we operate a system to discover and report activities of X-ray sources, which is called as “Nova Search” system.

To be convenient to use the data in MAXI-DB, they are converted to binary files with the format of FITS (Flexible Image Transport System[4]), which is a standard data format to analyze and archive the astronomical data of spectra, images and tables contained any information. In addition to our standard scientific analysis, the FITS formatted data are used to publish daily updated light curves for more than 400 X-ray sources in the MAXI web site. Although the only MAXI science team can access these data, the MAXI on-demand process system[5] provides an indirect analysis environment to make images, spectra and light curves in any region and time duration.

3.2 GSC

3.2.1 Overview of GSC

GSC is a set of twelve X-ray sensitive cameras consisting of one-dimensional position sensitive proportional counters and slit-slat collimators. The layout of the counters on MAXI is shown in Figure 3.3 (Mihara et al. [49]). The six GSC cameras (GSC 0, 1, 2, 6, 7 and 8), which point toward tangential direction of the ISS orbit, join a group called as GSC-H (“H” means horizontal). The others (GSC 3, 4, 5, 9, A and B) monitoring the zenith sky are GSC-Z. GSC constantly monitors approximately 85% of the whole sky for every 92-minutes ISS orbit using thin-long field of view with the systematic position accuracy of 0.2°. The capability to obtain spectral information ranges from 2 keV to 30 keV with the energy resolution of 18% at 5.9 keV.

3.2.2 Components of GSC

A camera of GSC consists of three main components; an X-ray detector, front-end electronics and a set of slid-slat collimators. This section explains configuration of these components.

The X-ray photon detector of the GSC camera is a one-dimensional proportional counter filled with xenon (Xe) gas. Electrons converted from energy of an incident photon (or a charged

---

[4] `http://fits.gsfc.nasa.gov/`

[5] `http://maxi.riken.jp/mxondem/`

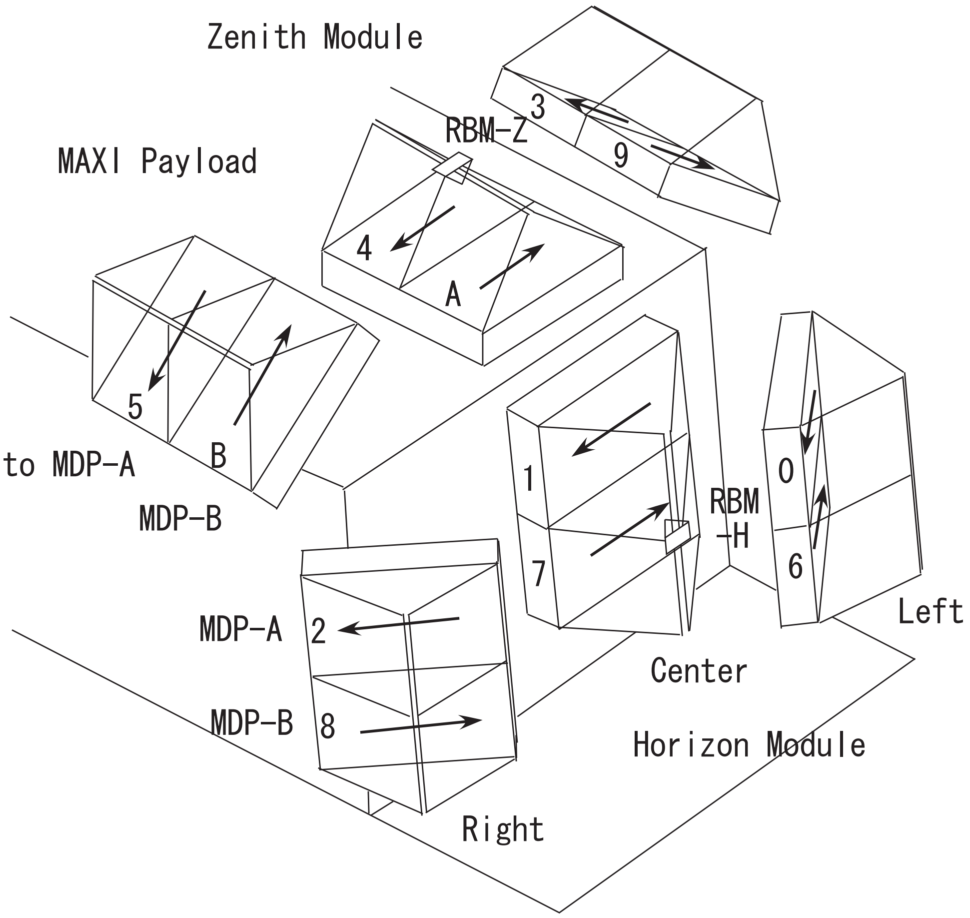

Figure 3.3: Schematic overview of GSC cameras on MAXI. A set of a triangle and a small cuboid is a GSC camera consisting of collimators and a proportional counter. The ID numbers of the cameras are marked as 0, 1, . . . , 9, A, B. Three pairs are mounted on the side plane of MAXI and the other on the top. An arrow in each counter is a direction of a carbon wire along the detector coordinate. The GSC 0–5 are connected to Mission Data Processor A (MDP-A), and the others to MDP-B. Radiation Belt Monitors (RBMs) are mounted on each center camera.

particle such as proton) by photoelectric effect are multiplied and accelerated towards the anode wire with the high voltage in the chamber of the counter. An incident position of a photon or a particle along the wire is determined with a pulse height ratio provided by readouts at both anode ends.

Figure 3.4 shows a picture and a top view of a GSC proportional counter (Mihara et al. [49]). X-ray photons enter the top window of the counter that is sealed with a beryllium foil whose thickness is 100 μm. To support tension of the beryllium foil in vacuum, the window is separated by grid structures which are placed parallel to anode wires and vertically placed at the center of the counter. The body of the counter is made of titanium, since the heat-expansion coefficient is close to that of beryllium. Gas consisting of Xe (99%) and CO_2 (1%) with a pressure of 1.4 atm at 0 °C is filled in the sealed chamber.

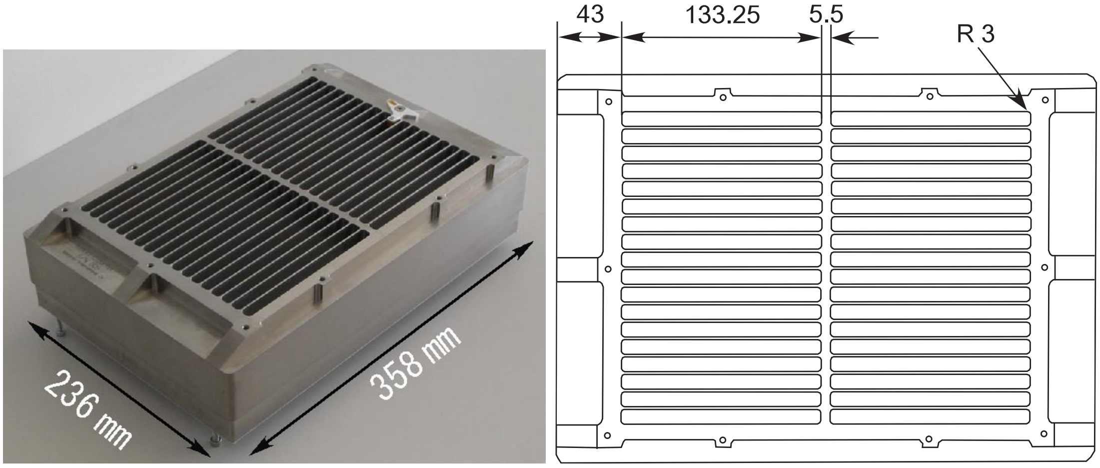

FIGURE 3.4: Picture (left) and top view (right) of a proportional counter unit. The beryllium foil is applied on the inside of the chamber. Anode wires are strained in the longitudinal direction. The thin grid structures parallel to carbon wires and a thick one perpendicular to that are support the foil. The unit of numbers is mm.

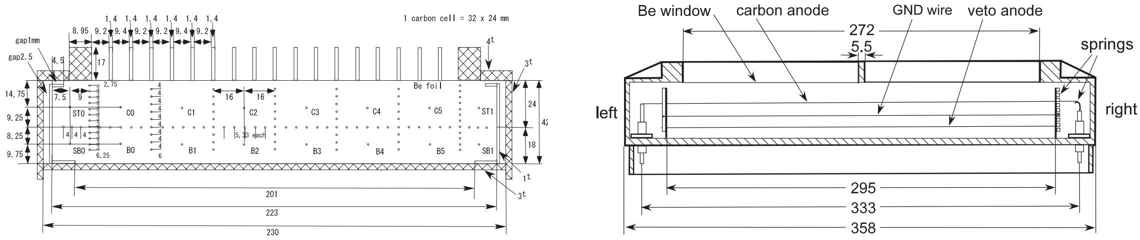

FIGURE 3.5: Cross-section views of a proportional counter unit on the perpendicular (left) and parallel (right) to anode wires. Labels C, B, ST and SB of the wires denote Carbon, Bottom, SideTop and Side Bottom. The wires aligning to separate the gas chamber are ground of the counter. The shaded region is chassis of the counter. The unit of numbers is mm.

Cross-section views of the proportional counter are shown in Figure 3.5 (Mihara et al. [49]). The carbon wires are main sensors and surrounded by the ground wires. The wires labeled with B, ST and SB in Figure 3.5 are readouts of veto signal which rejects events detected with charged particles and γ-rays with anti-coincidence protocol. The geometry of the wires has been determined to obtain adequate efficiency for X-rays in the 2–30 keV energy band. In normal operation of GSC, the high voltage of 1650 V is applied to these wires.

Number of readouts of GSC proportional counter is 14; both side of six carbon sensor anodes and two veto anodes.[6] Signals from these readouts are processed in font-end electronics boards which include a high-voltage (HV) power supply and House-Keeping (HK) electronics. Each readout is connected to a preamplifier through a coupling capacitor. On the other hand, the

---

[6] The wires of B0 to B5 in Figure 3.5 are connected in the counter and have one readout as veto signal. ST0, ST1, SB0 and SB1 are also the same.

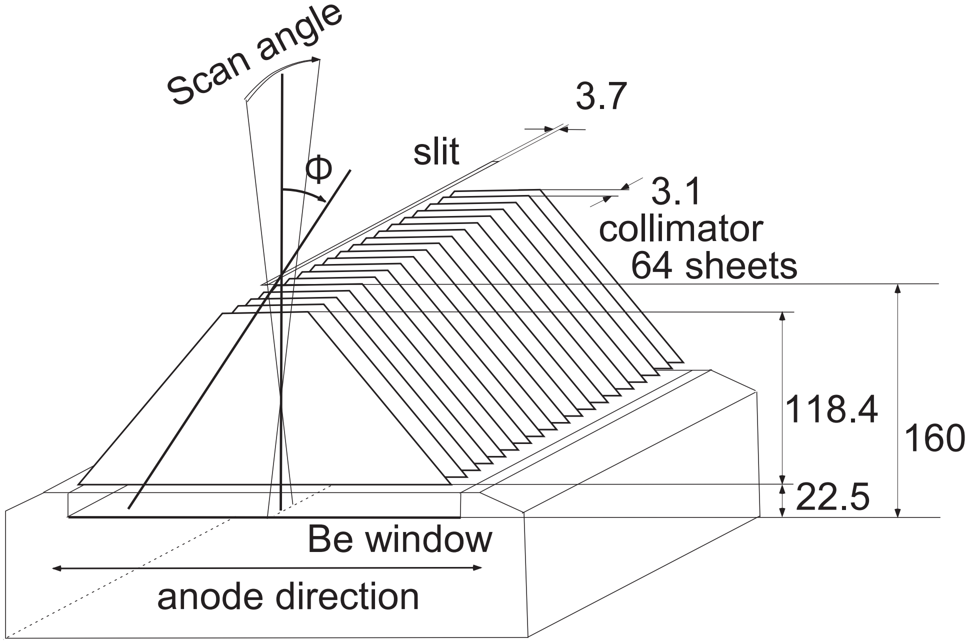

Figure 3.6: Geometry of a proportional counter (a box-like structure in the lower side), slat collimators (triangle like sheets in the middle) and a slit (a very narrow rectangle labeled as slit in the upper). The angle ϕ and "Scan angle" indicate an incident angle in the parallel and perpendicular plane to the anode direction, respectively. The unit of the numbers is mm.

HV supply is connected to all of the anode wires, thus one GSC unit has one HV supply and twelve preamplifiers. See Mihara et al. [49] to obtain more information of the circuits.

On the proportional counter, sixty-four slat collimators are align in the perpendicular direction to the anodes with the pithes of 3.1 mm. These collimators with the hight of 118.4 mm separate an opening angle of the window of the counter into many field of views (FoVs) with the width of 1.5° in full width of half maximum (FWHM). A slat is made of phosphor bronze with the thickness of 0.1 mm that stops X-rays up to 30 keV. Above the top of the slats, a slit of two parallel tungsten rods with 3.7-mm separation is located to narrow an opening angle in the plane along the anode direction as 40° in FWHM. The integrated geometry of a proportional counter, slat collimators and a slit is shown in Figure 3.6 (Mihara et al. [49]).

3.2.3 Principle of the position determination

GSC determines an X-ray incident direction in two dimensions; a coordinate parallel to the anode wires (called as detecter coordinate) is defined with photon absorbed position, and another coordinate along rotation of the ISS (scan coordinate) is encoded in the transit time within the

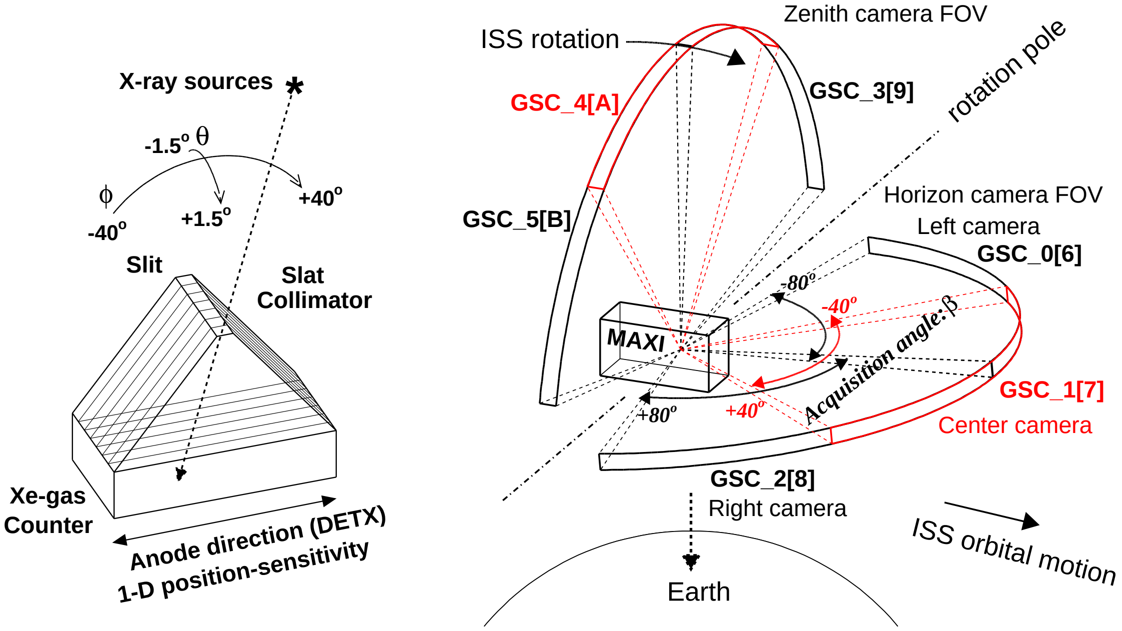

Figure 3.7: Left: A field of view (FoV) of a GSC unit. A photon from an X-ray source enters to a gap between slat collimators and is absorbed in the proportional counter. The curved arrows mean the width of FoV along the anode direction ϕ and the scan direction θ. Right: Integrated FoV of GSC is shown as solid arcs. Labels as GSC_X[Y] mean the corresponding GSC camera X and the redundancy Y.

narrowly collimated FoV. Figure 3.7 (Sugizaki et al. [74]) schematically illustrates the method to determine a photon incident position on the sky.

3.2.3.1 Detector Coordinate

A position of a photon detected on an anode wire is represented as a ratio of signal heights of both readouts. We call such position as Position Measure (PM). A PM parameter has an approximately linear relation with a position where an X-ray absorbed along the anode wire, however not exactly. Thus, ground experiments provided a conversion table of the relation between PM and photon absorbed position. The position converted from the PM value is called as DETX. Although the PM has no unit, the unit of DETX is mm. The DETX coordinate is defined with the origin of the center of the anode wire and the plus direction as the rightward side of the counter (see Figure 3.5).

Note that this DETX position does not correspond to an incident position of the photon on the beryllium window, because the DETX depends on the energy and the incident angle. In the chamber of GSC filled with Xe gas, an X-ray with higher energy runs on a longer path and ionizes electrons along the path. Photons with sharp incident angles also penetrate into the gas with longer paths. Consequently, the wider distribution of absorbed electrons along the anode wire mistakenly shifts the position represented as a DETX value from the incident position on the beryllium window with the length of an approximately mean free path of the X-ray photon. By the correction of the shift with a function of the mean free path, the measured photon energy and the gas pressure we obtain “true” positions of photons called as BEX (X coordinate on the beryllium window) position. The origin and direction of the BEX coordinate is as same as those of the DETX coordinate. The unit of BEX is also mm. We note that since a grid on the upper panel of the proportional counter shadows the center of FoV, a region with $|\mathrm{BEX}| \lesssim 10\mathrm{mm}$ is not sensitive to X-ray photons from sources but background of charged particles and gamma-rays.

The geometry of the GSC camera defines the FoV along the detector direction seeming as a sector form (see Figure 3.7). Its full width is 80° for the camera. As shown in Figure 3.3 the cameras mounted on both sides of MAXI are tilt with 40° to the opposite outward direction. Therefore, FoVs of the cameras in each group of GSC-H and GSC-Z make an obtuse (160°) FoV. The GSC-H and -Z covers the horizontal and zenith sky with the integrated FoV, respectively. Hereafter, an incident angle of X-ray photons along the detector direction is represented with θ for each GSC unit. This angle corresponds to an acquisition angle β for each obtuse FoV.

3.2.3.2 Scan Coordinate

An angle of the incident photon on the plane perpendicular to the anode direction is determined from the attitude of MAXI. A filed of view (FoV) of the GSC proportional counter is sliced lengthwise along the rotation direction of the ISS by the slat collimators. Each narrowed FoV with the width of 3° sweeps the sky by the attitude change of MAXI. Viewing from the opposite side, we can convert information of the MAXI attitude to the direction of the FoV covering an arc-like sky at a given time. The incident angle along the scan direction is called as ϕ.

The attitude information is provided by Attitude Determination System (ADS) consisting of Visual Star Camera (VSC) and Ring Laser Gyroscope (RLG) of MAXI. An accuracy of attitude determination is 0.1 arcmin with VSC when the camera observes more than three stars and 0.1° in the worst condition of ADS (Morii et al. [51]). The timing information of MAXI refers the GPS signal with the precision of 0.1 msec.

3.2.4 In orbit performance

3.2.4.1 PSF of GSC

Point spread function (PSF) describes the response of an image observation system to a point source. Generally, it reflects features of the focused optical system and statistical factors of the detector. The PSF of GSC is complex because the shape is defined with the response of the proportional counter and the FoV of the camera on the detector and scan direction, respectively.

The PSF in the detector coordinate represented as the BEX value is a complex function depending on the incident angle ϕ and the energy of the photon. In principle, the angular response of the slit-and-slat collimator and the position response of the proportional counter determine the PSF along the detector coordinate. As shown in Figure 3.8 (Sugizaki et al. [74]) the PSFs with $\phi = 5^\circ$ in the soft and hard energy bands are similar to a gaussian function and successfully reconstruct the actual observed profile of Sco X-1. By contrast, one with $\phi = 33^\circ$ in the 10–30 keV is asymmetric and cannot be approximately represented with a gaussian. Therefore, an accuracy of the position determination of sources in the hard X-ray band (> 30keV) is worser than that in the soft band, which is reasonable for a wide range of the incident angle ϕ. We note that the width of the PSF, which is approximately represented as a standard deviation σ of a gaussian function, slightly depends on the angle ϕ. The dependency is almost linear from $\phi \sim 0^\circ$ with $\sigma \sim 1.5$ mm to $\phi \sim \pm 40^\circ$ with $\sigma \sim 2.5$ mm.

Meanwhile the PSF in the scan coordinate is defines as a function of effective area of the slit-slat collimator which is determined by only the geometry of the GSC camera. The function of effective area is a triangle as shown in Figure 3.9 (Sugizaki et al. [74]). The area depends on an acquisition angle β toward an X-ray source since the scan-transit time varies with these angles. The transit time of the cameras on the left and right side of MAXI increases from ~ 40 second with $\beta \sim 0$ (and an incident angle $\theta \sim \pm 40$) to ~ 150 second with $\beta \sim \pm 80$ (and $\theta \mp 40$). On the other hand, that of the center camera has small variation as 40–50 second due to the small dependency of the scanned area on the acquisition angle β. According to the actual observation data, the duration time of one-scan transit ranges from 40–200 sec and most frequently takes about 60 sec.

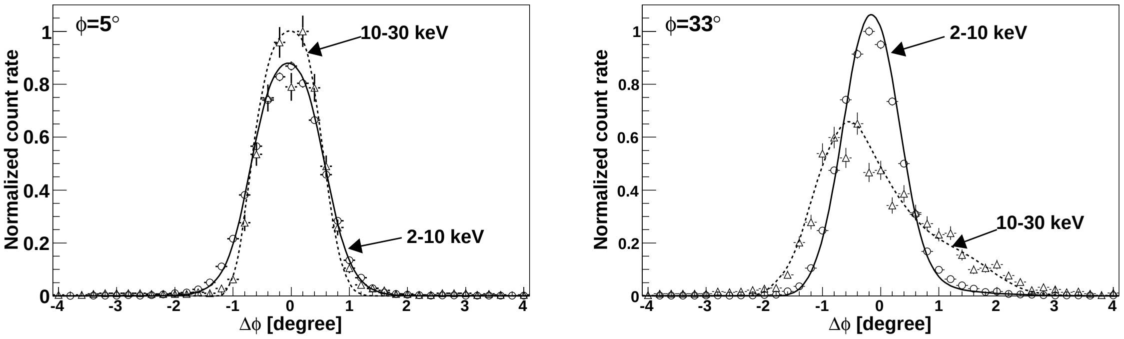

FIGURE 3.8: PSF along the detector direction at each angle $\beta = 5°$ (right) and 33° (left) in the 2–10 keV band (solid line) and 10–30 keV (dashed line). To show the PSF a power-law energy spectrum with the photon index of 2.1 is assumed. The observed count rate of Sco X-1 in 2–10 keV (circle) and 10–30 keV (triangle) are plotted with 1-σ error bars.

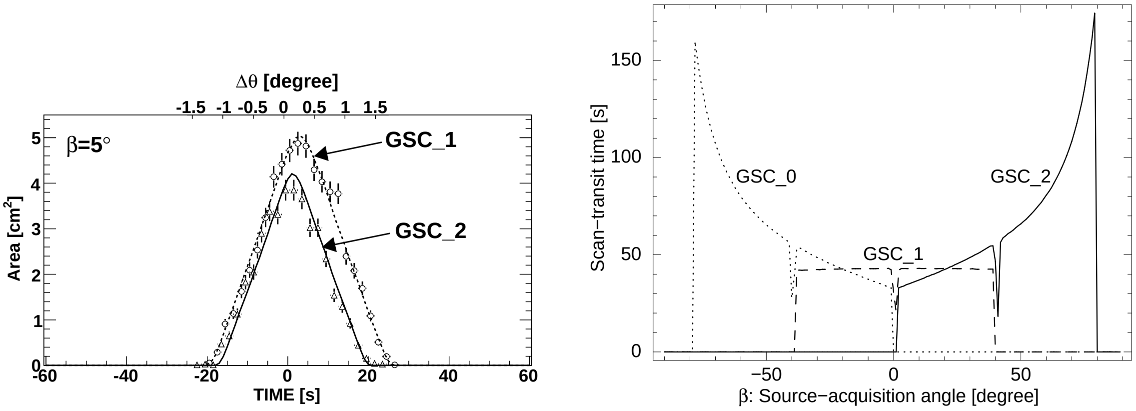

FIGURE 3.9: Left: Solid lines represent time variations of effective area during a scan transit for the two cameras at an acquisition angle $\beta = 5°$. The observed count rate of X-ray photon from Sco X-1 is plotted with 1-σ error bars. Right: Dependency of scan-transit time on the angle β for GSC 0, 1 and 2 in the ISS nominal attitude.

3.2.4.2 Alignment calibration

In early operation we found that the position of known X-ray sources are significantly deviated from the true position as large as 0.9° in 90% containment radius. Causes of this problem is predicted that the mechanical mis-alignments of the GSC cameras and the chassis of MAXI which reflect an accumulation of tolerances of the MAXI component and a vibration of the launch. Morii et al. [51] performed an alignment calibration of MAXI/GSC with reconstruction of a matrix which converts an attitude in the MAXI coordinate provided from Attitude Determination System to that in the GSC coordinated. The elements of the matrix were determined by localizations of selected bright X-ray sources, e.g., Sco X-1 and Crab nebula, for each GSC camera and each anode wire. As the result of this calibration, the systematic deviation of position accuracy was improved to $\sim 0.12°$ for Sco X-1 and $\lesssim 0.2°$ for other bright sources. Note that since this work was performed with the data in the energy band of 4–10 keV, scientific studies including position determination of X-ray sources is difficult under the present calibration.

3.2.4.3 High voltage operation

In the beginning of the mission, GSC has been operated with the high voltage (HV) of 1650 V in any time except a duration in the SAA and an exposure to the Sun. However, sudden shut downs of GSC units have been reported for the cameras 6, 9 and A (means 10) since 8 September 2009. We ascertain a large amount of discharges in the counters as the cause of the shut down. In order to avoid risk of another accident, the HV of some GSC cameras have been reduced to 1550 V or turned off. In addition, we have ceased the operation of GSC at the high latitude above 40° since 23 September 2009. The summary of operation efficiency of GSC is shown in Figure 3.10 (Serino [68]). Now, the HV of the cameras 1, 8 and B (means 11) also have been turned off to preserve redundant counters. In contrast to them, the camera 4 and 5 have been almost perfectly operated with the HV of 1650 V since the first light of GSC.

3.2.4.4 Background environment

One of contributors to background for X-ray detecter is Cosmic X-ray Background (CXB). The CXB is diffuse X-ray emission from celestial sources which was discovered by the observation with a rocket (Giacconi et al. [19]). High-resolution observations of Chandra X-ray observatory revealed a lot of extra galactic sources such as active galactic nuclei mostly contribute to the CXB (Setti & Woltjer [70]). Spectral CXB property in Moretti et al. [50], the flux in the 2–10 keV band, which is included in the GSC energy band, is 5×10^{-12} erg s^{-1} cm^{-2} deg^{-2}.

Another contributor of background is called as Non X-ray Background (NXB). The NXB is mainly caused by detections of incident charged particles such as protons and electrons. Incoming to the proportional counters of GSC, these particles ionize the Xe gas as same as X-ray photons. Although most of such "fake" events by the high energetic particles is ignored to perform anti-coincidence with veto triggers, reminded events contribute to the background of the GSC camera. Such charged particle mostly distributes in area of the SAA and in radiation belt at high latitudes. Radiation Belt Monitors (RBMs) onboard MAXI measures flux of the charged particles and ceases the operation of GSC to prevent from high count rate due to the particles.

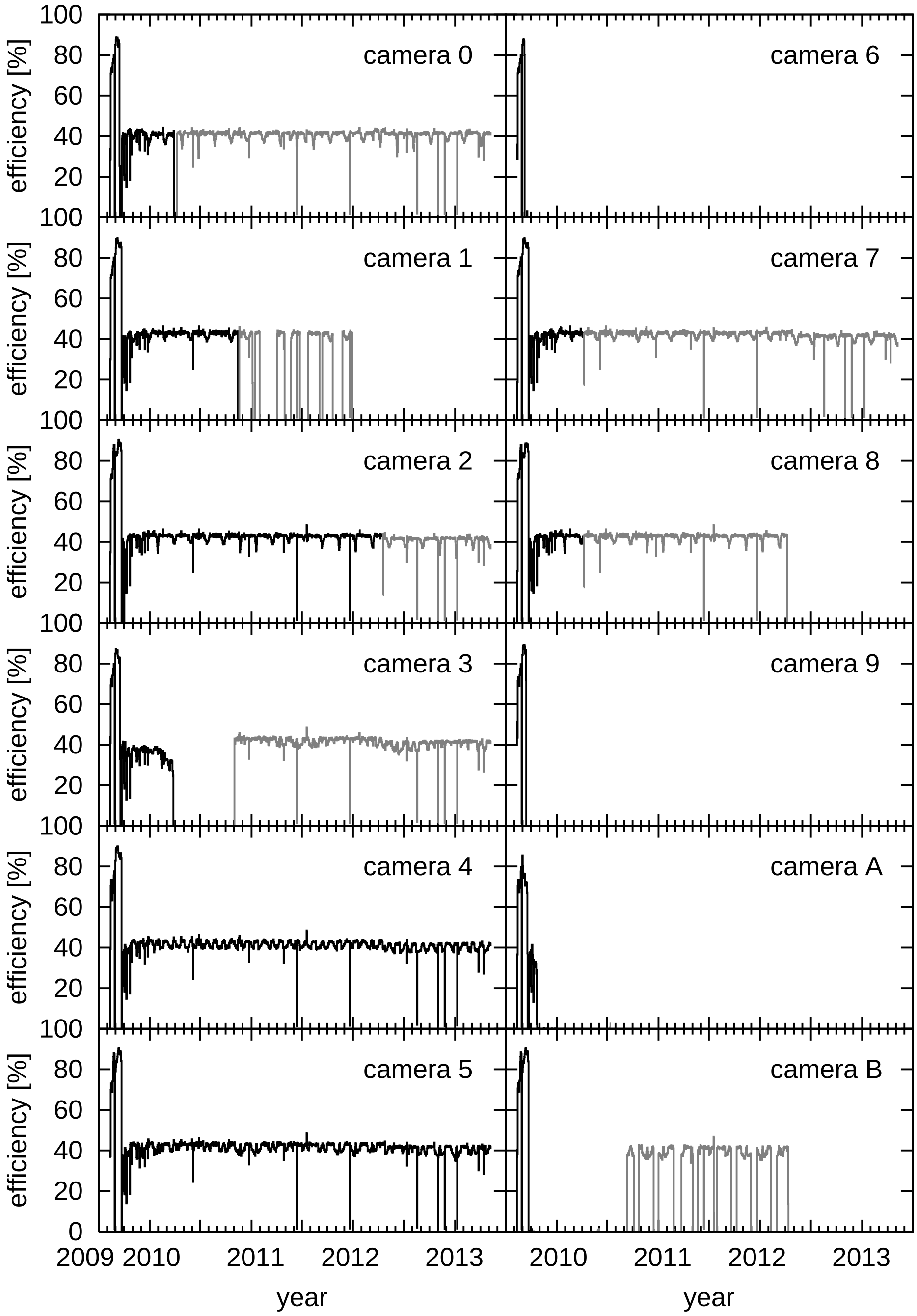

Figure 3.10: The operation history of GSC cameras. The 100% efficiency means the GSC has been operated for the whole orbit of the ISS. The black and gray lines represent the high voltage configuration of 1650 V and 1550 V, respectively.

High energetic photons, i.e., γ-ray, also contribute the NXB in the MAXI operation. The possible origins of the photons is astrophysical γ-ray emitters, such as active galactic nuclei and pulsars. As same as the case of charged particles, incoming γ-rays are rejected by the anti-coincidence. However, γ-rays scattered by components of detectors and coming from side or back of the detectors do not trigger the veto system and detected as background. In fact, the origin of these γ-ray is not only celestial sources, but also Cs^{137} source mounted on the bottom of Soyuz spacecraft. The source on Soyuz is component of a height indicator which is used during Soyuz landing on ground. When Soyuz attached on the nearest port of the ISS from MAXI, background of GSC has significantly increased. The history of the background as shown in Figure 3.11 obviously demonstrates the drastic variation of the dairy background rate.

The X-ray emissions in the solar system are also effective to background of MAXI. The Sun is the most powerful X-ray (and charged particle) source in the environment of the ISS. As mentioned in section Section 3.2.4.3, since GSC is not operated when the FoV sees the Sun, the solar X-ray is not dominant background. However, when solar flare emits a great amount of X-rays, background suddenly increases around the Sun region whose area is larger than the HV shutting down duration. In addition to the direct effect of the Sun, a reflection of the solar X-ray with the solar paddle of the ISS is also detected by GSC. The solar paddles almost always cover a part of FoV of some GSC cameras, especially those mounted on the left side of MAXI, and reflect solar X-rays. The effect of the reflection is significant after the solar flare and appears belt-like background increasing in all-sky images.

In the geometry of GSC camera, there is a gap between two units of the GSC camera as shown in Figure 3.12. This brings up an unexpected background increasing during solar flares. An X-ray photon entering to the slit of GSC unit with the particular incident angle along the scan direction travels above the slat collimators and in the gap between the units. Finally, the photon penetrates into the beryllium window of the next proportional counter without any interruption by the grid on the counter. Although this problem is not normally considered, when the flaring Sun is close to the area where photons can penetrate into the next counter, bright source-like excesses come up on the GSC observational data. We call such excesses as "sun leak events".

The excesses often trouble daily operation, health check of the counters and transient source searching system. Fake detections of the excesses can be ignored with check of the position of the Sun, since this problem only occurs when the flaring Sun aligns with the possible path of the sun leak event. In addition, such excesses are only detected with the anode wire labeled as

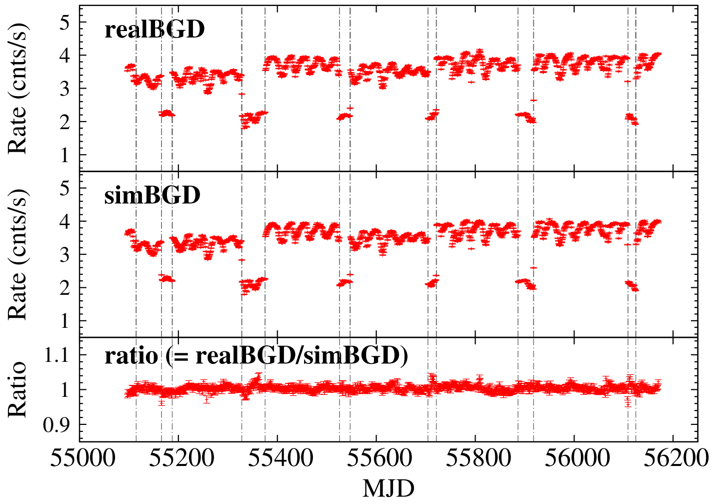

Figure 3.11: Top: History of the actual background rate of the GSC 4 counter in the 4–10 keV. The plotted data has 1-σ error bar in a one-day bin size. The dot-dashed lines indicate the dock/undock timings of the Soyuz spacecrafts. Middle: The same plot is provided by simulations to make source catalog in Hiroi et al. [28]. Bottom: The ratio of the actual data and simulation.

C5 in Figure 3.5. Thus, we plot positions of the excesses which are detected with large X-ray events in the PSF by only the C5 anode wire in the plane of the detection coordinate θ and the scan coordinated ϕ. This is approximately represented with a quadratic function as shown in Figure 3.13.

An example of an all-sky map is shown in Figure 3.14. There are some blank regions in the map. Circular regions at the upper left and lower right side are an uncovered region along the rotation axis of the ISS. Since the FoV along the detector coordinate is not 180°, GSC cannot monitor regions near the axis. Some GSC cameras have not been operated, hence the blank including the galactic center is not covered with any GSC cameras. To prevent the proportional counter from unprocessible high count rate the high voltage of GSC is shut down in the curved belt-like region traversing longitudinally. This map includes effects of solar flares; enhanced emission of solar X-rays, reflection from the solar paddle and a sun leak event. The semicircular orange-colored region at the lower side of the figure is a direct effect of the solar flares. The source-like excess at the right side of the region is a sun leak event. The two orange belts at the upper side are reflection of solar X-rays from the solar paddles of the ISS.

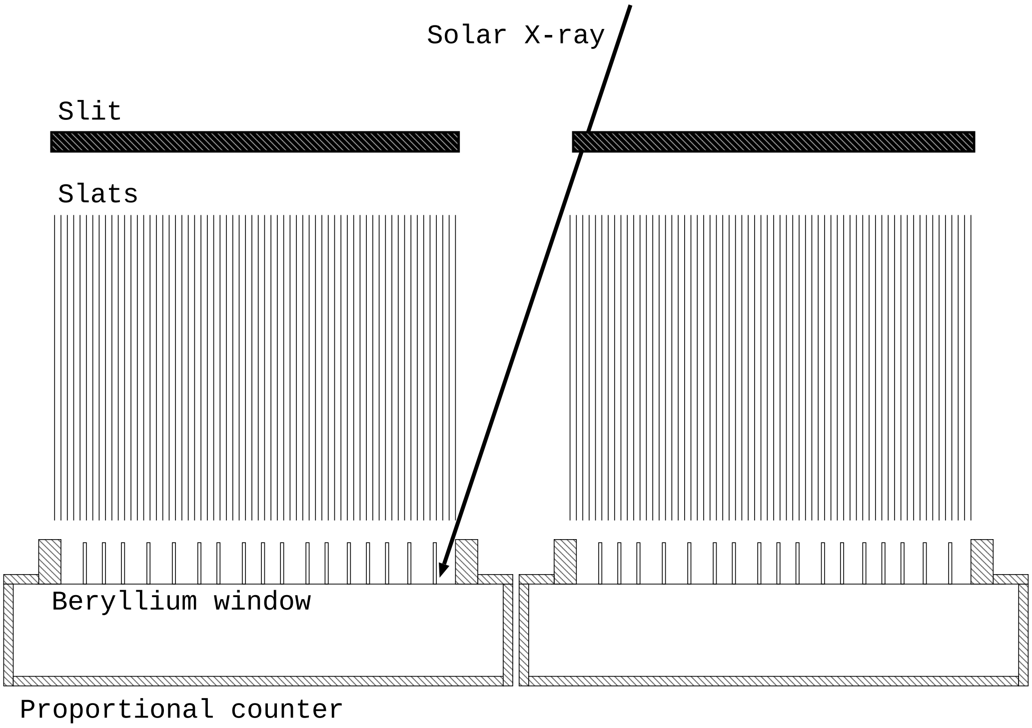

FIGURE 3.12: Geometry of a GSC camera pair and trajectory of the sun leak event photon. An incident X-ray to the slit of the right counter with an angle penetrates into the region between the cameras and enters into the beryllium window of the left proportional counter. Finally the photon is detected with the C5 anode wire of the left counter. The box at the center is a supporting structure of the slat collimators which is a triangular frame without any block of the incident photons.

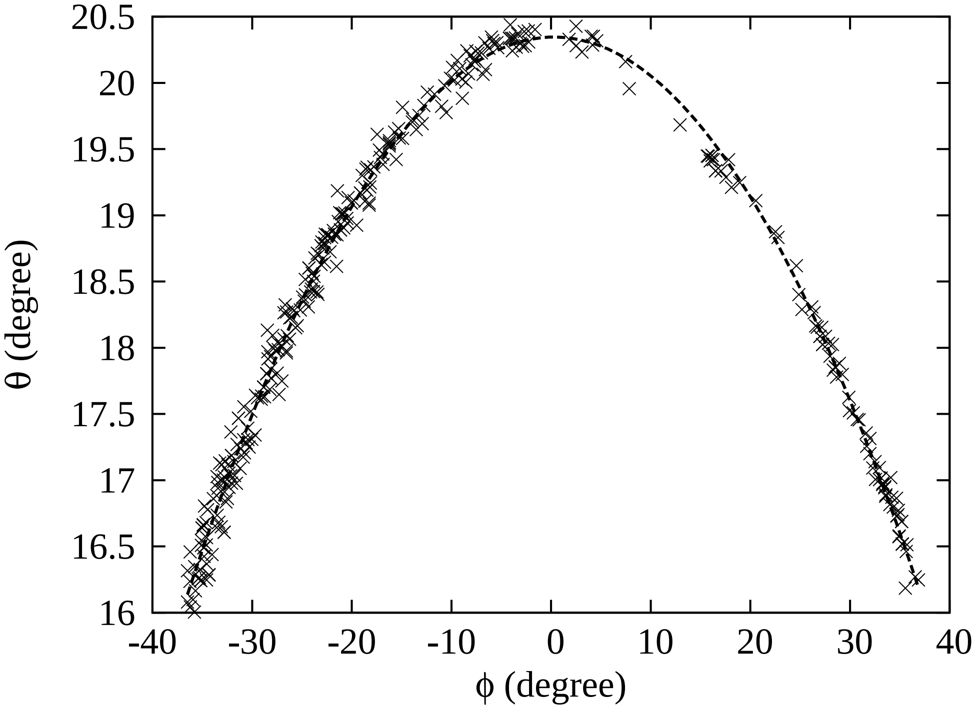

FIGURE 3.13: Angular distribution of sun leak events in the ϕ-θ coordinate is plotted as crosses. The dashed line is a fitted quadratic function.

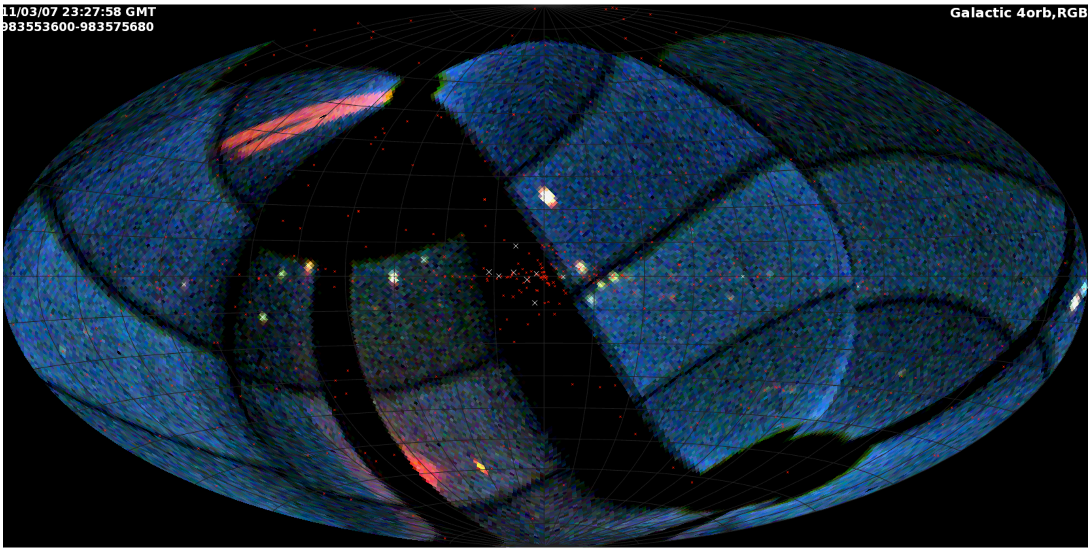

FIGURE 3.14: Example of all-sky map obtained with GSC in March 7 2011 17:30 – 23:30 UT, when M-class flares were reported. X-ray events are plotted in the galactic coordinate (the origin corresponds to the galactic center and the equator line is the galactic plane) with pseudo colored; red in 2–4 keV, green in 4–10 keV and blue in 10–20 keV. Red crosses indicate positions of known X-ray sources.

3.3 SSC

Solid-State Camera (SSC) is another X-ray detector of MAXI which is sensitive to photons in the 0.5–12 keV energy band. It has two cameras; one (called as SSC-Z) is placed to monitor the zenith sky, the other (SSC-H) sees +20° above the horizontal direction. The layout of the SSC cameras are shown in Figure 3.15 (Tomida et al. [76]). Each camera has CCD units, preamplifiers, multiplexers, a collimator and slit unit, and a calibration source. Information of systems and in-orbit performance were reported in Tomida et al. [76] and Tsunemi et al. [78]. In addition, recent scientific result with SSC were also published; e.g., Kimura et al. [35] and Morii et al. [52].

In a SSC camera, 16 CCDs which are front-illuminated p-type are aligned in 2×8 array. The design of CCD wafer and electronics of the SSC determine observable energy band as 0.5–12 keV. Although the surface of the CCD is coated with 0.2-μm aluminum, the edge of the CCD wafer is not coated. In orbit, the Sun light illuminates the CCD and imposes careful handling of scientific analysis to the MAXI science team.

Twenty-four slat collimators and a slit are located above the CCD unit as shown in Figure 3.16 (Tomida et al. [76]). They flatten the field of view as $1.5° \times 90.0°$. Principle to determine positions of X-ray sources with SSC is similar to the case of GSC, alternating the proportional

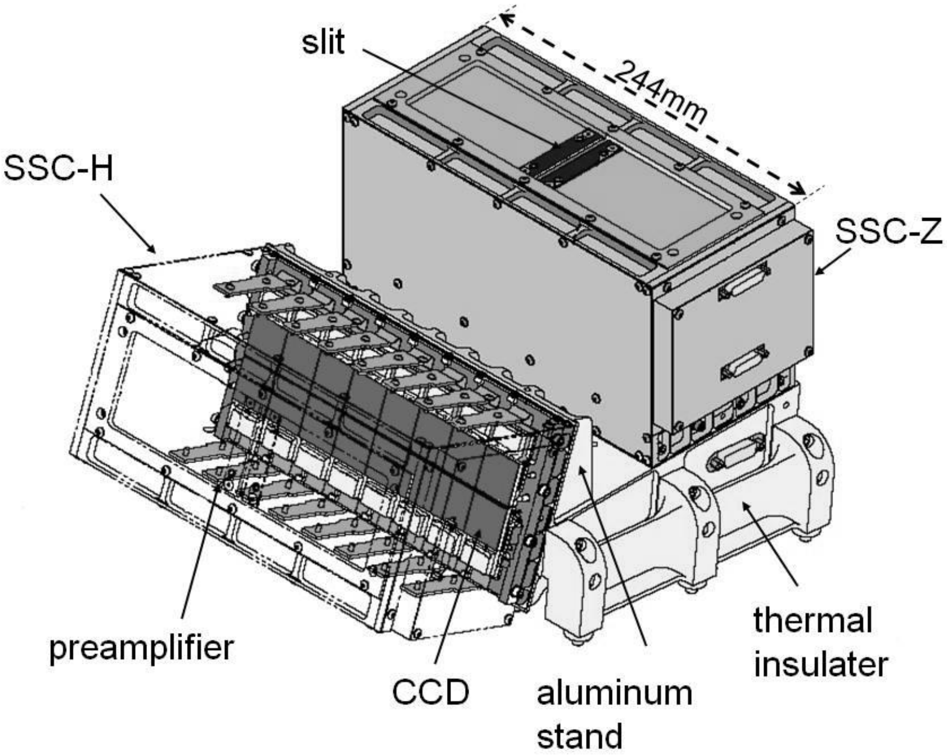

Figure 3.15: Exploded view of SSC consisting of two cameras. Each camera mounted on the aluminum stand has a CCD array, preamplifiers, slats collimators and a slit.

counter and the CCD array. With the fan-beam FoV, SSC covers 71% of entire sky in a single orbit of the ISS. Note that, however, the leak of the Sun light during provides scientifically unavailable data in the day-time.

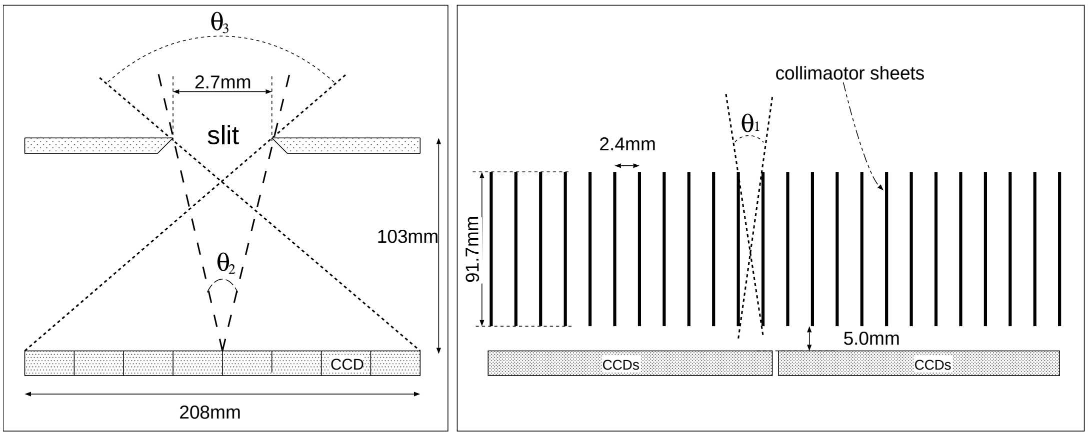

Figure 3.16: Schematic view of a SSC camera consisting of a CCD array, stats collimators and a slit. Left: the geometry perpendicular to the rotation direction of the ISS. The scale is modified easy to see. θ_3 is the width of the long FoV with 90°. $\theta_2 = 1.5°$ is the angular resolution at the acquisition angle of 0.0°. Right: side view of the camera parallel to the rotation direction. The width of narrow FoV is $\theta_1 = 3°$.

Chapter 4

Analysis

We have developed a new procedure to detect short X-ray transients from the archived MAXI-GSC data. In this chapter, we describe the analysis method to search for short transients which are detected in one-orbit transit of the ISS every 92 minute. The method is consisted of three major steps (data selection, global search and localization) and some small procedures (clustering, flux calculation and candidate selection).

4.1 Data selection and screening

We analyzed event data of the GSC which has been obtained in 1327 days from October 1 2009 to May 20 2013. We ignore data in the early operation from August to September 2009 which included difference of operation configuration and some troubles (e.g., high voltage breakdown) as mentioned in Section 3.2.4.3. Since some cameras (GSC 6, 9, A and B) had been damaged and have been turned off, we do not use the data provided by these cameras. Another camera GSC 3, which was damaged on March 26 2010 and has been operated without veto anti coincidence, is omitted from our analysis too. Thus, in our study to search for transients, we use the seven healthy GSCs (Zenith: GSC 4 and 5, Horizontal: GSC 0, 1, 2, 7, and 8).

The event data of GSC is processed with the most up-to-date software (version 1.4) and calibration data base (updated on 25 February 2013) which are provided by the MAXI science team. Each data file formatted with the FITS contains table of daily X-ray events detected with one of the GSC counters. The table in the file consists of columns of CAMERAID, MAXITIME, BEX and PI and others which are not used in our analysis. Here, CAMERAID is the ID number of each GSC camera such as $0, 1, \ldots, 9$, 10 (camera A) and 11 (camera B). MAXITIME is the photon arrival time stamped by the clock of MAXI. BEX is the incident position of X-ray photon projected back on the beryllium window of the proportional counter assuming the energy dependent mean free path in the Xe gas. The energy channel of X-ray events are stored in the PI (Pulse Invariant) column. The value of PI is proportionally converted to the energy of X-ray photon in unit of keV.

First, we make ROOT formatted files from the FITS formatted event files with the conversion program provided by the MAXI science team. ROOT[1] is a framework to handle and analyze enormous amount of scientific data collected by detectors associated with particle accelerators of CERN. It provides functions to make histograms and graphs, to fit these data with statistical processing and to store the detected event data structured like trees. Next, we extract X-ray events in the 4–10 keV energy band from the ROOT data. This energy band is chosen because the detection efficiency of the GSC proportional counter is almost 100% in the 4–10 keV band (Matsuoka et al. [47]). Finally, to perform global transient search described in the Section 4.2, we make two-dimensional histograms in the MAXITIME-BEX plane. The histogram is made for each event files with the MAXITIME bin size of 4.0 s and the BEX of 1.0 mm. An angular resolution corresponding to the bin is $\sim 0.3^\circ \times 0.3^\circ$, which is small enough to determine the position of transient events in the MAXITIME-BEX coordinate with our analysis.

In order to avoid false source detection caused by leaking photons from bright persistent sources or the sun, and fluctuations of the background, we created mask histograms for the following items.

1. Regions near both ends of the carbon anode wires of the counter ($|\mathrm{BEX}| \geq 120$ mm)
2. Regions covered by the solar paddle of the ISS
3. Galactic plane (galactic latitude $|b| < 10.0^\circ$)
4. Neighborhood of bright persistent sources (the radius of 6° around Sco X-1, and 4° around other bright sources)

Figure 4.1 is a result of the data screening with these criteria. We note some of these items in the following subsections.

---

[1] `http://root.cern.ch`

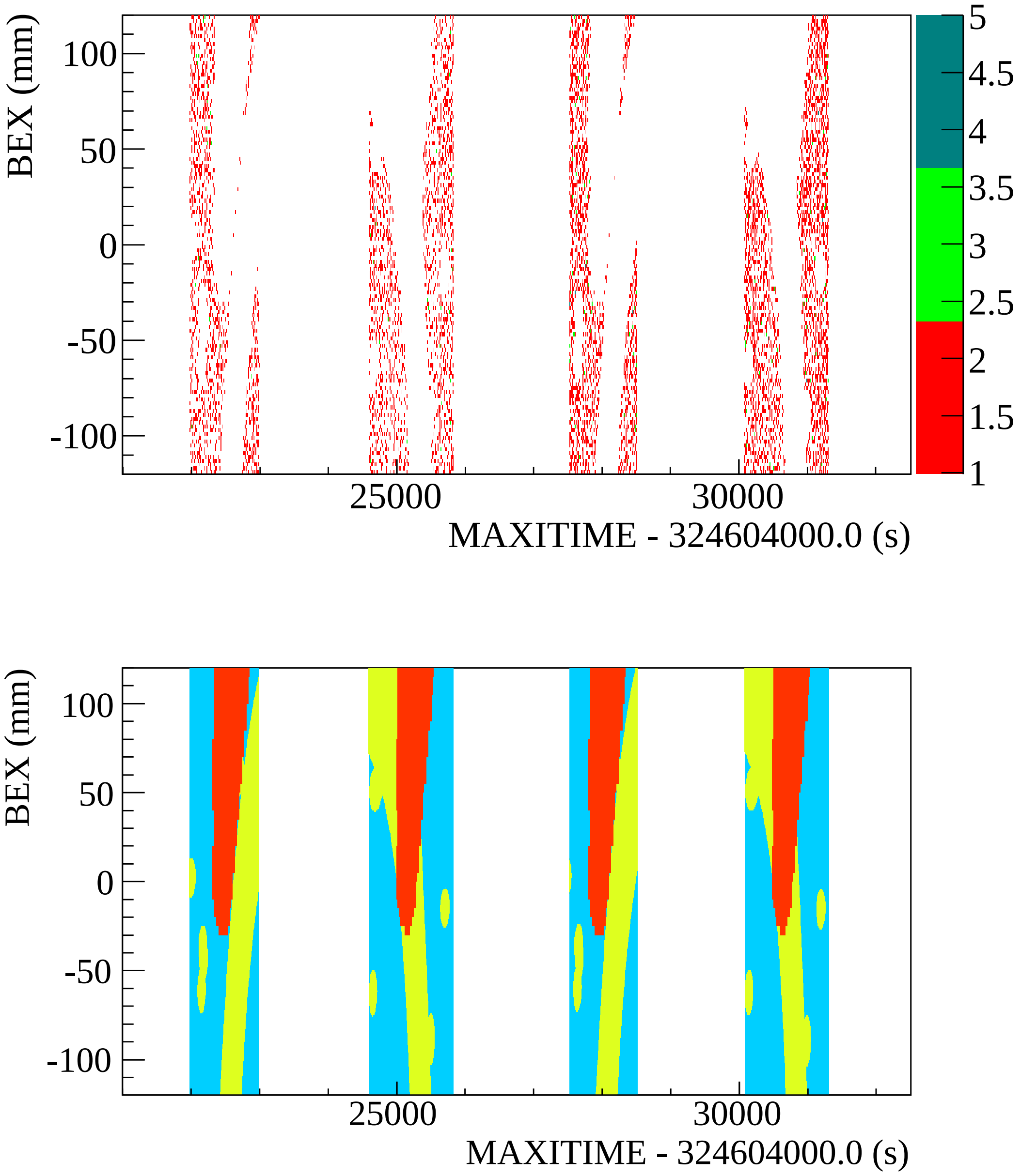

FIGURE 4.1: An example of result of data screening. The data was provided with the GSC camera 0 on April 15 2010. Up: The two-dimensional histogram shows an X-ray event map in the MAXITIME-BEX coordinate. Events in blank regions are excluded with a mask as shown in the lower panel. Low: X-ray events in the blue colored region are available to our analysis. We do not use events in the yellow and red filled region which correspond to the galactic plane and persistent sources, and solar paddle of the ISS, respectively. In the white filled duration, GSC has not been operated.

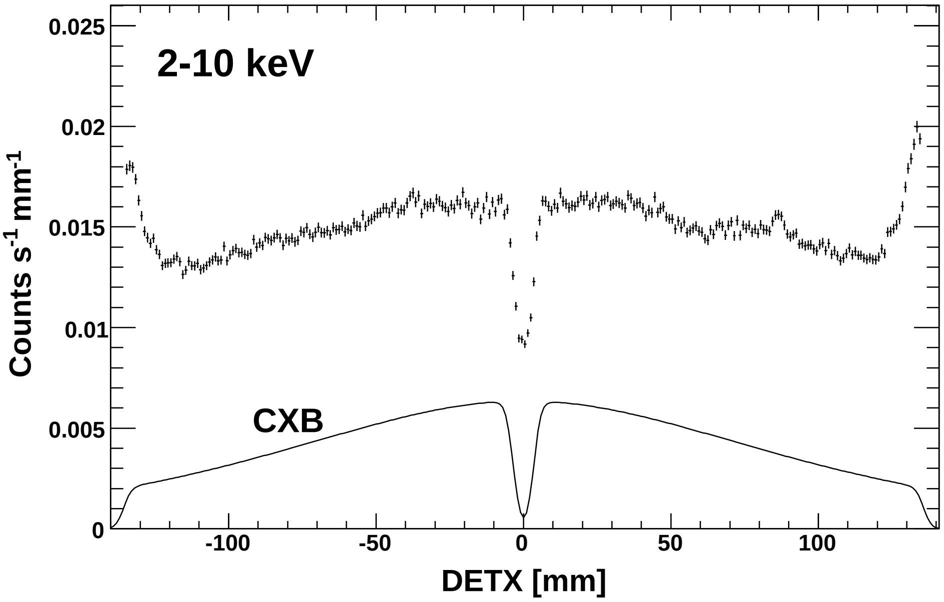

FIGURE 4.2: The actual background distribution along the anode wire direction in the 2–10 keV energy band. The solid line shows an expected contribution of CXB. The dip at DETX = 0 mm is a shadow of the grid structure on the center of the short side of the proportional counter.

4.1.1 Near the ends of carbon wire

GSC has the anti-coincidence system using the veto anodes placed in parallel to the main anode wires in the sides and bottom to reduce particle events and γ-rays which contribute to non X-ray backgrounds (NXBs). The distribution of X-ray background consisting of NXB and cosmic X-ray background (CXB) along anode wire is shown in Figure 4.2 (Sugizaki et al. [74]). In $|\mathrm{BEX}| > 120$ mm the background clearly increase. Because the both ends of the anodes are not guarded by the veto anodes (see Figure 3.5), and directly detect events due to the NXB. In consequence, events of the NXB may be accidentally detected as a transient candidate. Thus, we ignore events associated with the both ends of the anodes, $|\mathrm{BEX}| > 120$ mm.

4.1.2 Exclusion of region covered by solar paddles

Main energy source of the ISS is the photovoltaic arrays, which referred as the Solar Array Wings. The arrays attached to the truss structures of the ISS rotate around an axis along the paddle and another axis along the truss to keep an appropriate angle toward the Sun. According to the geometry, part of the GSC FoV is covered by the arrays for certain periods in the orbit. Since the covered region is not useful for scientific analysis, we ignore the regions by masking event maps in the MAXITIME-BEX coordinate. The regions covered by the paddles are calculated from the auxiliary data of the ISS. This data includes rotation angles along the paddle and the truss with every second. We assume that the paddle is face-on to a GSC camera to conservatively exclude the covered regions. The covered areas of the GSCs mounted on the left side and the center of MAXI are larger than that for the cameras mounted on the right side.

4.1.3 Exclusion of the Galactic Plane

Since the PSF of GSC is not sufficiently small to identify X-ray sources around the galactic center and the plane, we ignore these regions in our analysis. We exclude the galactic plane region with the galactic latitude b less than $+10°$ and larger than $-10°$, which includes almost all of the galactic center region. In the MAXITIME-BEX two-dimensional histogram, sometimes, the part of galactic plane occupies large area as shown in Figure 4.1. The percentage of area excluded with this criterion is about 17% of the whole sky.

4.1.4 Exclusion of region around bright sources

Bright, persistent and known X-ray sources may cause erroneous detection of transients in their neighbourhood with the method used in our analysis. To avoid such false detections, we exclude X-ray events associated with the bright X-ray sources. The list of these sources is shown in Table 4.1. They are chosen from the MAXI/GSC 37-month source catalog (Hiroi et al. [28]) with the flux of > 30 mCrab. The threshold of the flux is less than the detection limit of GSC ($\gtrsim 50$ mCrab) during one-orbit scan transit. Considering the PSF of GSC, we chose a radius of excluded region as 4° in the sky coordinate for each source. Since photons of Sco X-1, the brightest X-ray source in the MAXI-GSC energy band, leak from 4° excluding region, the radius must be larger, 6°, to reduce false detections around the source.

4.2 Global search

4.2.1 Method of global search

We search candidates of transient sources estimating probability of an assumption that number of X-rays detected in a test region is consistent with the number of the expected background counts. First, as shown in Figure 4.3, a foreground region and two background regions are placed on the MAXITIME-BEX histogram. The widths along the MAXITIEME coordinate

Table 4.1: List of bright sources

Name	R.A.	Dec.	flux*
SMC X-1	19.27	-73.44	26.3
Perseus Cluster	49.95	+41.51	52.7
X Per	58.85	+31.05	46.9
LMC X-2	80.12	-71.96	23.0
LMC X-3	84.73	-64.08	14.1
LMC X-1	84.91	-69.74	13.7
MAXI J0556-331	89.20	-33.20	11.6
Mrk 421	166.11	+38.21	15.1
NGC 4151	182.64	+39.41	10.1
Virgo Cluster	187.71	+12.39	16.2
Coma Cluster	194.95	+27.98	21.0
Cen A	201.37	-43.02	24.8
Sco X-1	244.98	-15.64	14780.1
4U 1626-67	248.07	-67.46	21.4
Her X-1	254.46	+35.34	26.3
Swift J1753.5-0127	268.37	-1.45	41.0
4U 1822-371	276.44	-37.11	33.0
HETE J1900.1-2455	285.04	-24.92	26.6
4U 2127+119	322.49	+12.17	13.8
Cyg X-2	326.17	+38.32	541.3

* unit of mCrab in 4–10 keV in Hiroi et al. [28]

of the foreground and background regions are 0.75 and 1.0 times of the scan-transit time, respectively. The gap between the regions has the width of 0.25 times of the scan-transit time. The width along the BEX for each region is fixed as 6 mm, which is ~ 80% of the width of the PSF. An example of the global search corresponding to a known GRB (GRB 100510A) is shown in Figure 4.3.

Second, we attempt null hypothesis that number of X-ray events in a test region has a Poisson distribution whose mean is the number of background events. The mean, N_b, is estimated with the following equation;

$$N_b = \frac{N_1 + N_2}{A_1 + A_2} \times A_f. \tag{4.1}$$

Here, N_1 and N_2 are numbers of events in the left-side and right-side background regions, A_1 and A_2 are areas of the regions, respectively. In addition, we define N_f as the number of events in the foreground region with the area of A_f. The areas of foreground and background regions are calculated from the mask to consider the partial lack due to data screening criteria as mentioned in Section 4.1.

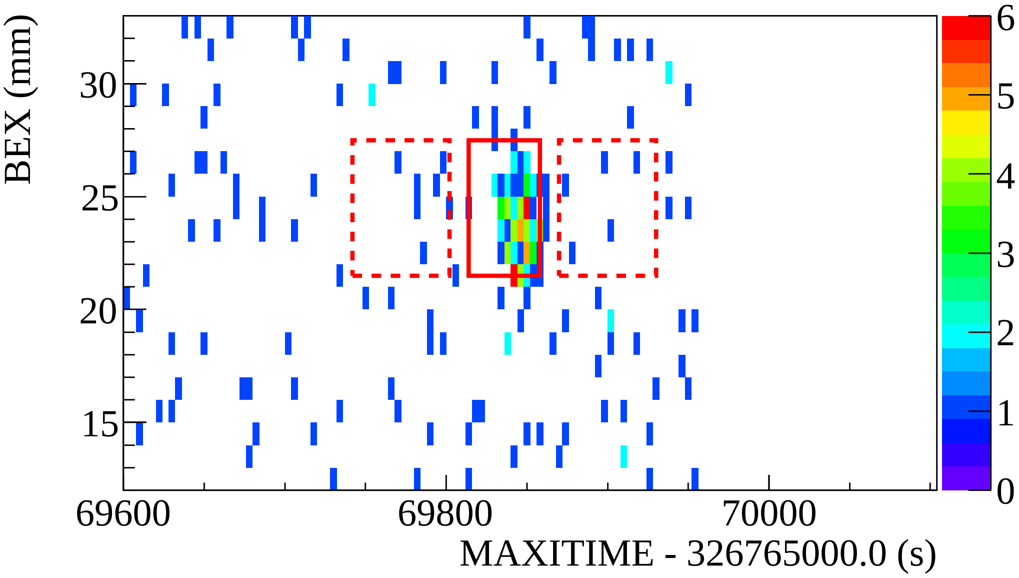

Figure 4.3: An example of global search performed data obtained on 10 May 2010. Boxes on the histogram which represent an event map are foreground (solid) and background (dashed) regions. The horizontal axis is the MAXITIME coordinate with the shift to clearly see. There is no X-ray event in the right side blank region.

Third, we calculate a probability to establish the null hypothesis: number of X-ray events has a Poisson distribution with the mean of N_b. The probability P_{null} is estimated from the upper tail of the cumulative Poisson-distribution function with the number of foreground events N_f as,

$$\begin{aligned} P_{\text{null}} &= \int_{N_f}^{+\infty} \frac{N_b^x e^{-N_b}}{x!} dx \\ &= 1 - \frac{\Gamma(N_f+1, N_b)}{N_f!}. \end{aligned} \tag{4.2}$$

Here, the value x is a dummy variable representing number of foreground events. In Equation 4.2 which is called as "survival function", the second term is the cumulative distribution function of the Poisson distribution represented with an incomplete gamma function $\Gamma(x, y)$. For example, the test case shown in Figure 4.3 has $N_b = 7.0$ and $N_f = 94$, thus the null hypothesis probability P_{null} is very small, $10^{-87.9}$. If the probability is small enough to reject the null hypothesis, we allege that the events in the foreground region is significantly detected as a transient source with this global search process.

Hereafter, we name a series of the processes as *trial*. Subsequently, we iterate the next trial with

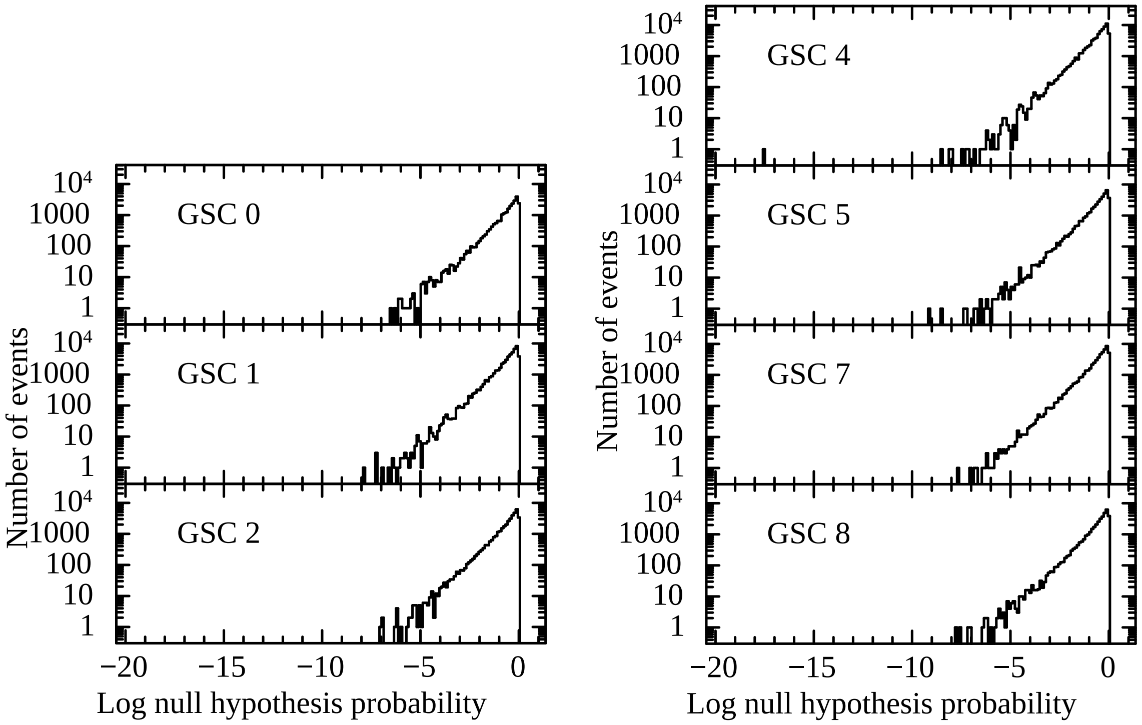

FIGURE 4.4: An example of the distribution of null hypothesis probability. These results are obtained from data on 15 April 2010. A significant detection with log $P_{\rm null} \sim -17.5$ in the "GSC 4" panle is GRB100415A.

new foreground and background regions whose positions are moved from that of the previous trial by the half width of the previous foreground region along the MAXITIME and BEX coordinates.

4.2.2 Determine threshold

In the global search we perform about 3.7×10^8 trials for 1327-days 7-cameras data. Histograms of $P_{\rm null}$ obtained from the data on 15 April 2010 are shown in Figure 4.4 as one result of the global search. The histograms have a power-law like distribution in the higher probability region and reach at zero at $P_{\rm null} \sim 10^{-6}$–$10^{-7}$. In data obtained on other days similar distributions are confirmed. A possible origin of the distribution is a fluctuation of Poisson-distributed background. According to the distribution, we decided that the threshold of null hypothesis probability of candidates is 10^{-5}, so as to tolerate trials with less significance. The trials with the probability of $P_{\rm null} < 10^{-5}$ are applied to the detailed analysis. The global search with this threshold will trigger ~ 1 false detection for each one-day and one-camera data which includes a several 10^5 trials.

4.3 Clustering of candidates

In the global search, bright transients may be redundantly detected with significant null hypothesis probabilities since a test region covers other neighboring regions. These redundancies must be ignored as much as possible to save calculation time in the following analysis steps. In the MAXITIME-BEX coordinate, we assume that a group of trials in a rectangular region associates with a possible transient. To prevent from incorrect grouping, we chose the width of the region as 70% of the scan-transit time and the width of the PSF along the MAXITIME and BEX coordinates. Then, we determine a new position associating with the possible candidate as the position of the trial which has minimum null hypothesis probability in the group. After the global search, the trials with $P_{\mathrm{null}} < 10^{-5}$ were applies grouping process and were reduced into 306081 trials.

4.4 Detailed analysis

4.4.1 Method of localization

Since positions of the trials are roughly determined in the global search process, we perform precise position determination with the following steps. We perform similar calculation of null hypothesis probability as the global search with a picture-frame-like background region around the roughly determined position. The shape of the background region and foreground region are shown in Figure 4.5. Here, the background region has the inner and outer width as 1.25 and 3.25 times of the PSF (the scan-transit time along the MAXITIME coordinate and the width of the gaussian-like PSF along the BEX coordinate), respectively. Contrary to the method of the global search, this background region considers the fluctuation of background events not only along the MAXITIME coordinate but also the BEX one. We apply the width of the foreground region as 0.75 times the PSF. With these regions the null hypothesis probability under assumption of Poisson-distributed background is re-calculated by same equation of the global search. To search the precise position associated with the trial, we iterate this re-calculation around the roughly determined position. The region of the iteration is 5.25 times larger than the PSF in each coordinate. Finally, we determine a precise position which has minimum null hypothesis probability in the region of the iteration. With the refined position, we evaluate foreground and background fluxes in Section 4.5. A relation between the estimated null hypothesis probability and the count rates of a source and background is shown in Figure 4.6. On the right lower corner, where the source count rate is brighter and the background is fainter, the probability P_{null} is smallest $< 10^{-100}$. This plot clearly supports the validity for the localization process.

4.4.2 Detection threshold

A histogram of null hypothesis probability obtained by the localization process for all trials is shown in Figure 4.7. Contrary to the global search, the histogram has two components; the power-law like distribution in the high probability range, and another component in $P_{\mathrm{null}} \lesssim 10^{-12}$. While the former is interpreted as the accidental detections due to fluctuation of the Poisson-distributed X-ray background, the latter must be contribution of real X-ray transients. Considering completeness of the contribution, we determined the threshold of significant detection by the localization as $P_{\mathrm{null}} < 10^{-9}$. Based on the threshold and assumption of the Poisson-distributed X-ray background, number of false detection should be ~ 1 in all analyzed data, which include 10^5 trials/camera/day cameras days $\sim 10^9$ trials.

4.4.3 Estimation of position error

In this section we estimate an error in position determined by the aforementioned localization process. We performed the same processes of transient search to three known brighter and persistent X-ray sources; Cyg X-2, Perseus Cluster and X Per. Since the X-ray events associated with these sources are excluded by the data selection as mentioned in Section 4.1.4, we especially make MAXITIME-BEX two-dimensional histograms which include their X-ray events. Then we apply the same processes (global search, grouping and position determination) to the special histograms and obtained plausible positions as summarized in Figure 4.8. For brighter source Cyg X-2, the error with 90% confidence level is $\sim 0.5^{\circ}$. On the other hand, the errors of the fainter sources (Perseus Cluster and X Per) are $\sim 1.0^{\circ}$. We adopt a typical error of the position determination as 1.0° conservatively through this paper.

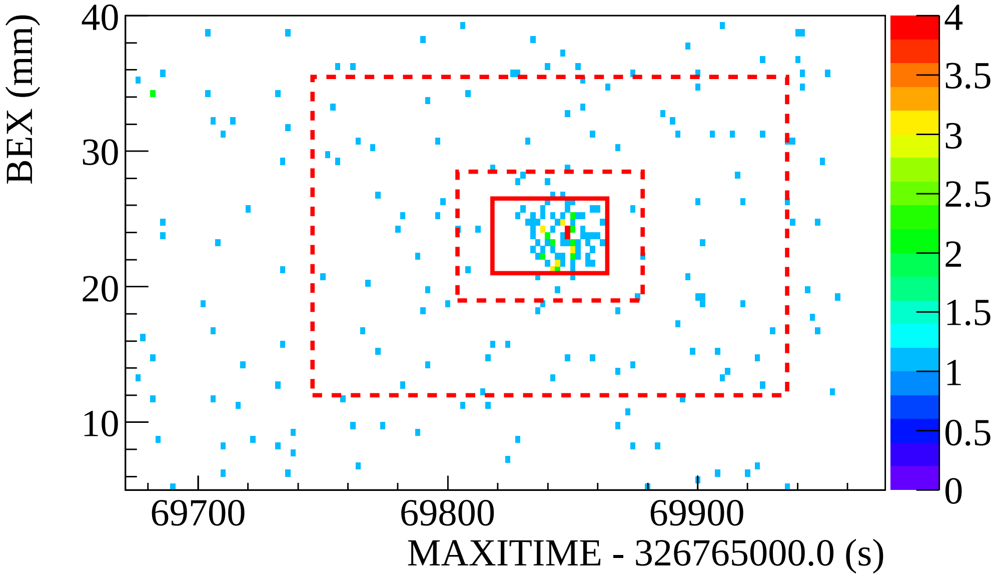

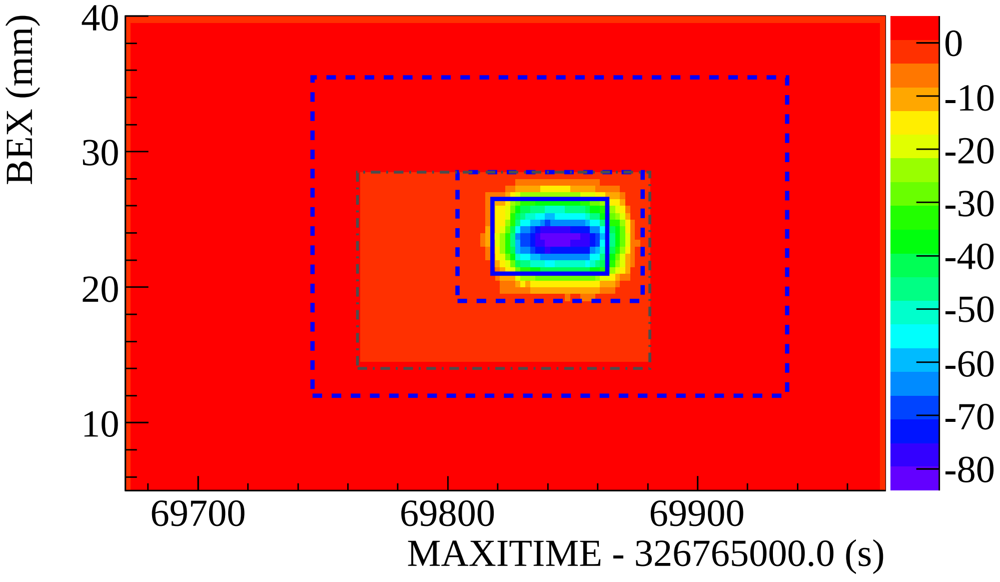

FIGURE 4.5: Upper: An event map in the MAXITIME-BEX coordinate and boxes to estimate number of foreground and background events. The events in the solid box and dashed frame are estimated as the foreground and background events, respectively. Lower: The distribution of null hypothesis probability. To facilitate visibility, the color of the box and frame in the upper panel are changed from blue to red. The black dash-dot box is a region where the program performed the iteration of position determination.

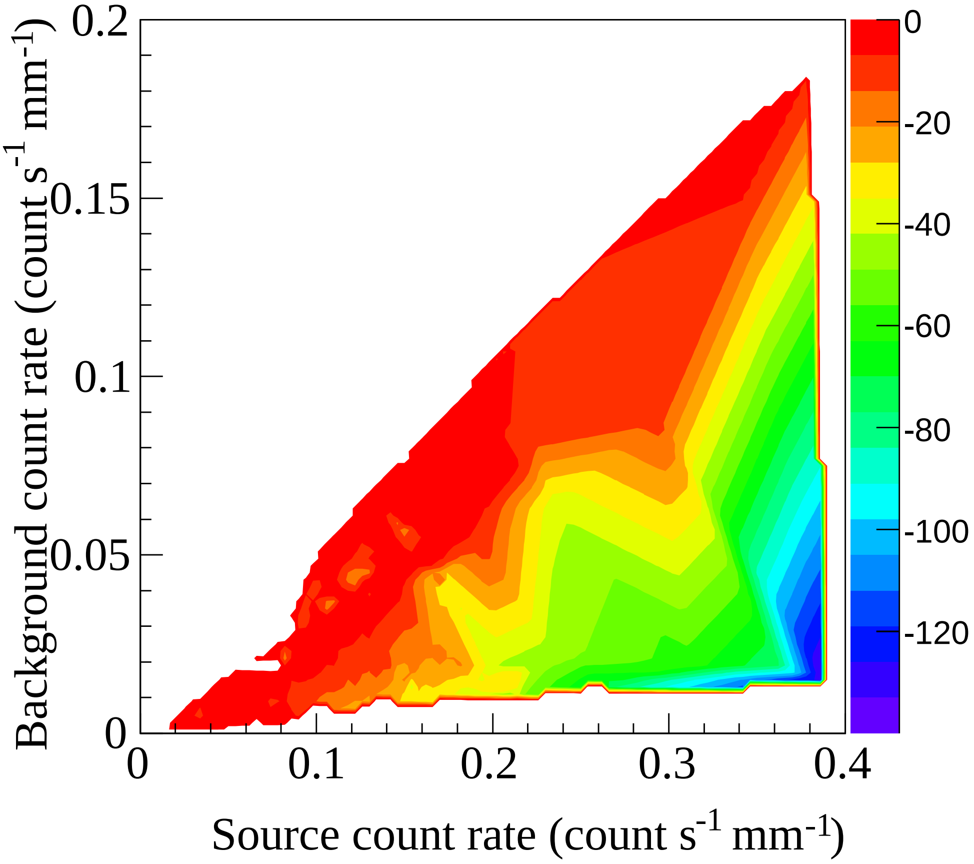

Figure 4.6: Contour plot of null hypothesis probability estimated in the localization process. The horizontal axis represents source count rate which is a difference of those in the foreground region and background region. The vertical axis is count rate in the background region.

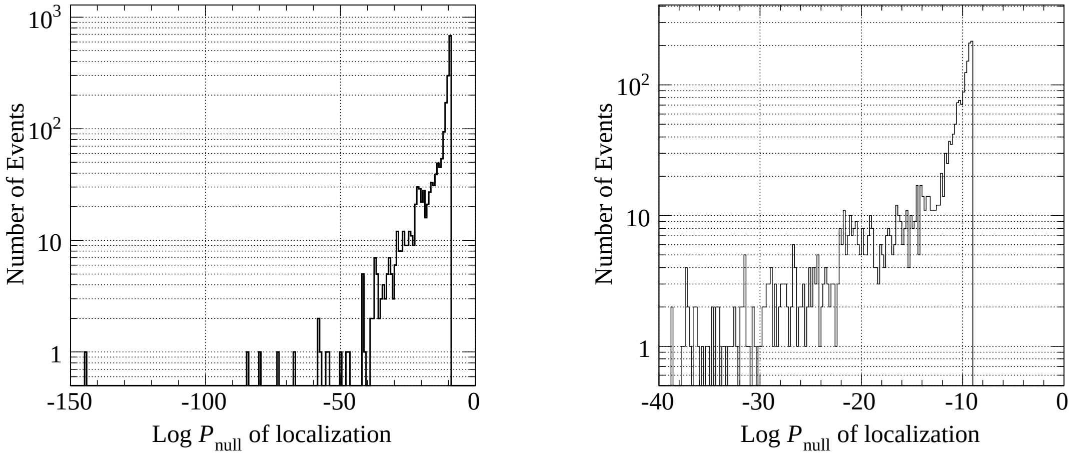

Figure 4.7: Histogram of null hypothesis probability P_{null} calculated in the localization. The right panel is an enlarged view around $-100 < \log P_{\mathrm{null}} < 0$.

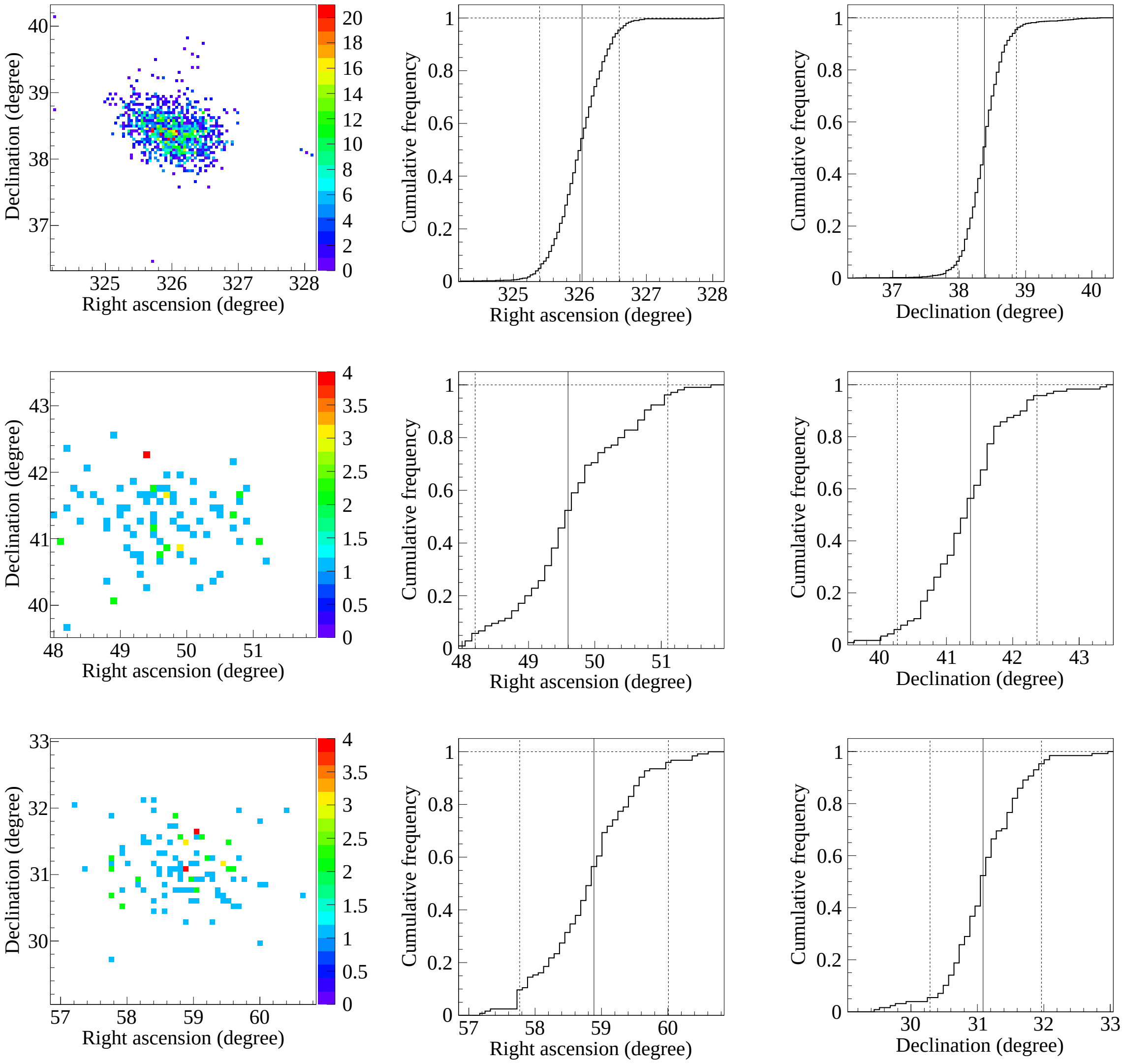

FIGURE 4.8: Result of error estimation of position determination with Cyg X-2 (upper panel), Perseus Cluster (middle) and X Per (lower). Right: A distribution of the positions determined from 46-days 7-cameras data set. Center and Left: Cumulative histograms of the distribution along R.A. and Dec. The three vertical lines from left to right define cumulative frequency of 5%, 50% and 95%, respectively.

4.5 Calculation of X-ray flux

After the position determination we calculate X-ray flux of transient candidates. The energy bands of the flux are 2–20, 2–8, 8–20 keV and 4–10 keV. The source flux $F_{\rm X}$ is represented as

$$F_{\rm X} = \frac{N_{\rm fore} - N_{\rm back}}{AT}. \tag{4.3}$$

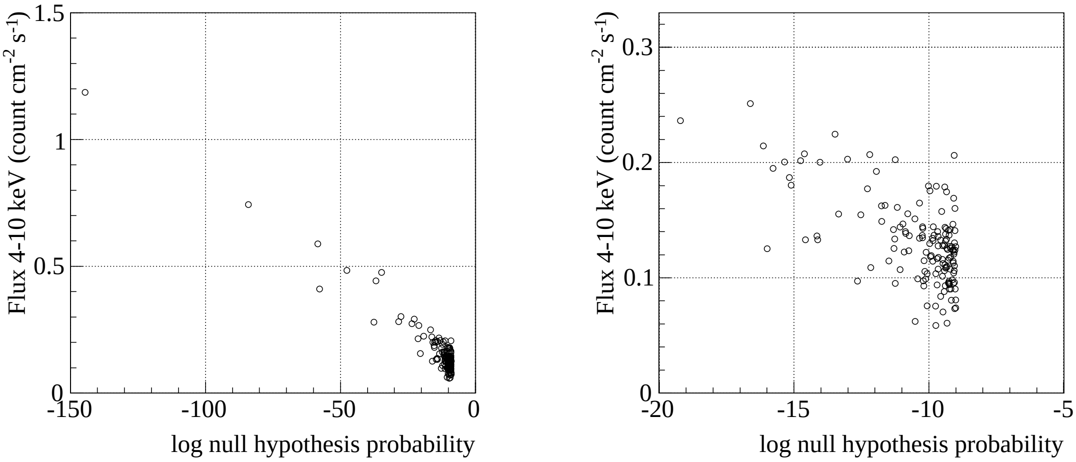

FIGURE 4.9: Scatter plot of null hypothesis probability $P_{\rm null}$ calculated in the localization and source flux calculated with Equation 4.3. The right panel is an enlarged view around $-20 < \log P_{\rm null} < 0$. The plots do not include trials which corresponds to possible sun leak event

Here, $N_{\rm fore}$ and $N_{\rm back}$ are number of X-ray events in the foreground and background regions which are located by the aforementioned method of the localization analysis in the MAXITIME-BEX coordinate. An effective area, A, associated with a position of a candidate is obtained from functions in MAXITOOL and MAXIUTIL, which are libraries to hundle MAXI's observational data probided by the MAXI science team. A scan-transit time T is calculated from a rotation angular velocity of the ISS and an angle corresponding to the width of the foreground region in the celestial coordinate. The correlation between the source flux and the null hypothesis probability which is calculated in the localization process is shown in Figure 4.9. The figure provides that the flux is proportional to the probability and the minimum detected flux is ~ 0.06 count cm^{-2} s^{-1}.

As a result of the calculation, we obtain the flux in unit of count cm^{-2} s^{-1}. A conversion from the unit of "count" to that of "photon" is generally cumbersome because the energy response of GSC has to be considered. However, the flux with the unit of "count" in the 4–10 keV band may be directly assumed to be that in the "photon" unit without much error since the detection efficiency of GSC is almost 100% in this energy band (Matsuoka et al. [47]).

4.6 Check candidates

Although we checked for clustering of extracted trials, multiple detections may remain in the localization process. In order to omit such duplicated detections, each candidate with the refined position is checked for whether it is multiply detected with the tolerance of 2° and 1000 sec. This time tolerance is chosen to extract multiple detections within a orbital period of the ISS (~ 92 min).

In order to avoid false detections we check the detected candidates for the following criteria.

1. Association with "sun leak" events
2. Background-enhanced region due to solar X-ray
3. Lack of effective area in the localization process
4. In $|\mathrm{BEX}| \leq 20$mm and ≥ 100mm
5. Association with outbursts of a known X-ray source

4.6.1 Candidate associated with the solar X-ray leak

As describe in Section 3.2.4.4, due to illegal path to penetrate solar X-rays into the GSC proportional counter, the "sun leak events" were reported at the times of large solar flares. Since the geometry of the GSC camera defines the path, we can predict the unique loci of these events in the scan and detector coordinates with the quadratic function shown in Figure 3.12. To ignore such sun leak events from the detected transient candidates, we calculate a scan angle θ and a detector angle ϕ of each candidate. Next, we check an angle of θ_{leak} which is calculated from the function with the ϕ value. If the θ of the candidate is included within a tolerance of the θ_{leak}, 1.5°, we exclude the candidate.

4.6.2 Exclusion of events in background-enhanced region due to solar X-ray

When the solar flare occurs, X-ray background of GSC temporally increases. Figure 4.10 shows the distribution of background count rate which is obtained in the global search process. The distribution has a cluster in the lower count rate and the others out of the region. These outliers will be associated with the count excesses caused by solar flares. Thus we ignore such trials with high background count rate to prevent false detections caused by temporal increase of background.

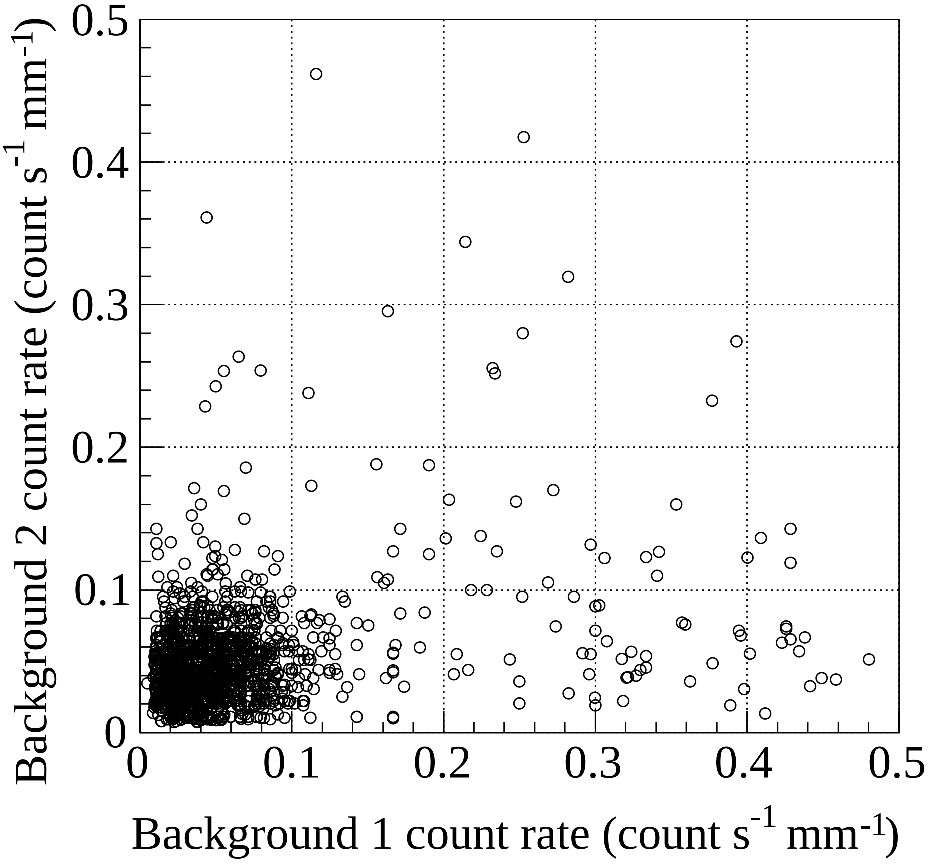

FIGURE 4.10: Scatter plot of count rate in the background regions. Background 1 and 2 correspond to before and after the foreground region. The unit of count s^{-1} mm^{-1} means number of event counts in a second and a mm in the BEX coordinate. The plot does not include trials which corresponds to possible sun leak event and have $P_{\text{null}} > 10^{-9}$.

4.6.3 Exclusion of events with lack of effective area in the localization process

In the data selection (Section 4.1) we ignore events near the galactic plane and the several persistent X-ray sources. As the result, trials of the global search and the localization often have partial lack of the effective area. Because number of background X-ray counts in a test region is several or about ten at most, the lack will affect to estimation of null hypothesis probability. Thus, we accept only trials with no or small lack of effective area of foreground and background. The threshold of acceptance is decided as 10% of the foreground and background area whose widths along the MAXITIME and BEX coordinates are determined from the PSF of GSC. In other wards, the following study ignores the trial with the < 90% area of the testing region.

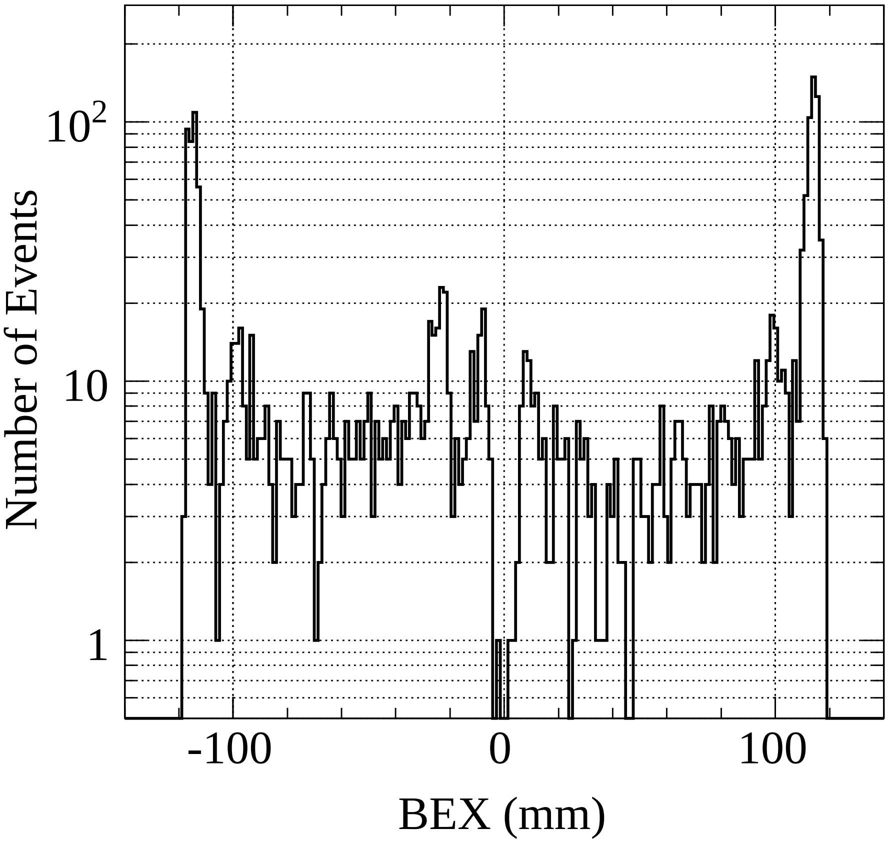

FIGURE 4.11: Distribution of detected candidates in the BEX coordinate. The plot does not include trials which corresponds to possible sun leak event and have $P_{\mathrm{null}} > 10^{-9}$.

4.6.4 Exclusion of events in the center and both sides of BEX

Geometry of the GSC proportional counter makes the X-ray sources in centain BEX coordinate ranges to be undetectable. The first one is dead region under the shadow of the grid structure which supports the window of the proportional counter perpendicular to the anode wires. In the BEX coordinate the region corresponds to $|\mathrm{BEX}| < 20$ mm (see also Figure 4.2). We ignore trials located in the region from the detected candidates. Another undetectable region is the both side of the anode wires. Although we ignored X-ray event in $|\mathrm{BEX}| > 120$ mm in the first data screening process, a large number of detections are clearly seen in Figure 4.11. This may be originated from additional background due to the charged particles and γ-ray photons mounted on the Soyuz. In order to obtain more plausible candidates we additionally neglect these trials in the region of $|\mathrm{BEX}| > 100$ mm.

4.6.5 Exclusion of candidates associated with outbursts of a known X-ray source

The detected candidates include an X-ray source which is not a short transient event, MAXI J1659−152. MAXI J1659−152 is a "transient" which has continuously emitted bright X-rays in 2010 (Kalamkar et al. [32]). Since this is located at the galactic latitude $b = +16.5°$ and has the relatively fainter averaged flux of 8.4×10^{-11} erg cm^{-2} s^{-1} $\sim$ 7mCrab (Hiroi et al. [28]), we do not screen out X-ray events near the source in the data selection process (Section 4.1). However, the peak flux of the source was very high ($\sim$ 1 Crab) during the outburst. Thus the trials associated with MAXI J1659−152 are detected by the procedure of our analysis. Since such trials are not short transients which are targets of our survey, we additionally ignore the trials which are detected near MAXI J1659−152 within 3°.

4.6.6 Manually exclusion of obviously false detection

Checking event maps and light curves of all detections, a candidate in the data obtained on February 21 2011 emerges as a suspicious detection. The event map of the candidate shows an extended distribution of X-ray events which is apparently larger than width of the PFS of GSC as shown in Figure 4.12. Since the candidate was detected on the edge of the GSC camera, incresing of charged particles is a sutable origin to this extended emissions. The candidate passes all criteria of exclusion as itemized in this section, however, we assume it as a false detection and will ignore it from the following analysis.

4.6.7 Effect of the exclusions to our analysis

We performed the data selections in the global search and exclusions to prevent from false detections as described in previous sections. Here, we evaluate the effect of these treatments to our analysis. Figure 4.13 shows a distribution of number of bins in the analyzed MAXITIME-BEX histograms. The "original" data with no screening and exclusion typically have 8×10^6 bins in the histograms. After the data selection as mentioned in Section 4.1 and the exclusions described in this section, we obtain "cleaned" and "available" event data which consists of 75% and 25% of the "original" data. Two of the most effective exclusion from the "original" to "available" are masking of the events detected at BEX of $|\mathrm{BEX}| < 100$ mm and > 20 mm, and neglecting of *trials* which have small covering area due to the lack of exposure (see Section 4.6.3

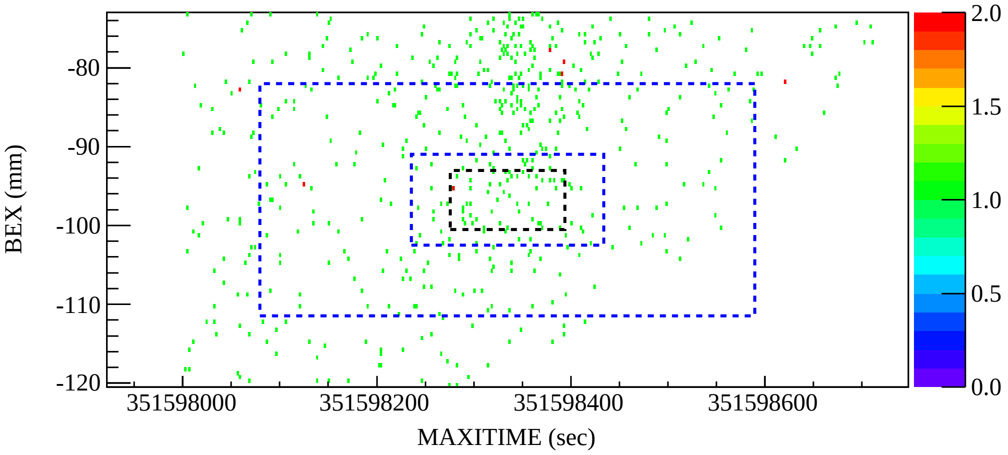

FIGURE 4.12: Event map of a candidate of short X-ray transient detected on February 21 2011. The black dashed box and blue dashed frame are foreground and background regions which are used to estimate flux and P_{null} in the localization process. The excess emission is distributed in the center of the map and extended from the black dashed region whose width along the BEX coordinate is 0.75 time of the PSF of GSC.

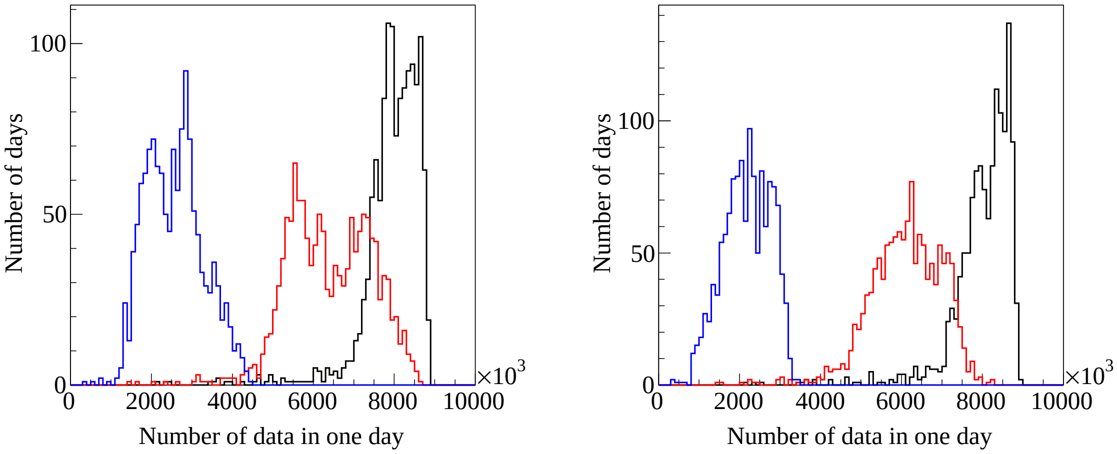

FIGURE 4.13: The black, red and blue histograms demonstrate distribution of available event in the "original", "cleaned" and "available" data, respectively. The plots in the left and right panels are obtained with the GSC 4 and 5 cameras. The horizontal axis means number of available bins of the MAXITIME-BEX histogram which includes X-ray events obtained in one day. The vertical axis is number of the event data.

and Section 4.6.4). The former criterion reduces one-third of the X-ray counts of the "original" data. The later one neglects a number of *trials* around the lack of the exposure due to the shut on/off of the HV, screening of the Galactic plane and neighbors of the bright sources. In addition, the neglecting will affect detections of GRBs, which will be described in Section 5.1.1.2.

Chapter 5

Discussion

As a result of our analysis, we obtain 146 short X-ray transients (SXTs) with the null hypothesis probability of $P_{\text{null}} < 10^{-9}$. Here, we perform cross-matching of the candidates with selected catalogs and discuss the statistical features and the origins of the X-ray sources.

5.1 Catalog Matching

We perform source identification with catalogs of GRBs and non-GRBs. The latter contains persistent X-ray and gamma-ray sources that possibly produce short X-ray transient (SXT) events. The estimated accuracy of our transient search reported in Section 4.4.3 is 2° for events near the detection threshold. Since it is much larger than the errors in the non-GRB source catalogs, which are sub-degree at a maximum, we accept the 2° tolerance in the cross matching. On the other hand, the positional error in the *Fermi*-GBM catalog is larger than that of our SXTs, hence we chose larger tolerance for it. The GRB and non-GRB catalogs used in this cross matching are summarized in Table 5.1 and Table 5.2, respectively.

All of the results are listed in Table A.1. The detected time, position (Right Ascension and Declination) and null hypothesis probability P_{null} are determined by the localization method described in the previous chapter. The flux in the 4–10 keV is estimated by the method described in Section 4.5. If a candidate is associated with a GRB, name of the GRB, time lag (the plus or minus signs mean whether the SXT was detected after or before the GRB) and angular distance between them are shown in the counterpart entry. In the following subsections we will describe the characteristics of the associated sources and possible origins of the detected SXTs.

5.1.1 SXTs associated with GRB sources

5.1.1.1 GRB source Catalogs

We check associations of the detected SXTs in this method with the known GRBs that triggered MAXI-GSC, *Swift*-BAT, and *Fermi*-GBM based on both positional and temporal coincidence. The compared catalogs are listed in Table 5.1. The MAXI-GSC GRB catalog (Serino [68]) includes 35 GRBs, of 2 GRBs were discovered in August and September 2009 when are not included in our present analysis. They reported that only one-third of them were confirmed with other satellites and the spectral characteristic is similar to that of X-ray flashes (XRFs). The GRB-SXT association is also checked with GRBs detected with other X-ray and γ-ray satellites, namely, *Swift* and *Fermi*. For *Swift* GRBs we use the second *Swift*-BAT catalog (Sakamoto et al. [66]), which contains only GRBs detected in 2004–2009. We therefore obtained a catalog of additional GRBs detected since 2010 from the *Swift* scientific team (Sakamoto 2014, private communication). The *Fermi* GBM Burst catalog (Paciesas et al. [56]) contains the GRBs detected by the Gamma-ray Burst Monitor (GBM) of the*Fermi* γ-ray Space Telescope, which has been monitoring GRBs since 2008 with in the 8 keV – 40 MeV energy band.

Since the positional accuracy of the *Swift* is an order of arcmin, significantly smaller than that of MAXI-GSC in our analysis, we adopted a position tolerance of source matching for them as 2°, our positional accuracy. On the other hand, we adopted the tolerance for *Fermi*-GBM events as 5°, their typical accuracy (Ukwatta et al. [79]). The tolerance of the temporal coincidence is chosen to be one day in order to include not only the prompt emission, but also possible precursors and afterglows.

5.1.1.2 Result of cross matching

The cross matching of the SXTs in the present analysis with the previously reported GRBs are listed in Table A.1. Here, we summarize associations of the SXTs with the previously reported GRBs with MAXI-GSC in Table A.2. Both of them are based on the same observations, but the detection algorithm is different. Our transient search analysis successfully detects 11 of the 33 GRBs which have been reported since October 2009 until April 2013. However the remaining 22 GRBs are not confirmed in our analysis.

One reason is simple; some of these occurred in the temporal or detector region filtered out in our analysis. In the global search process, we set background windows excluding time intervals near the shut down or turn on of the GSC HV (high voltage). Thus, this configuration neglects SXTs that occurred near these times. For example, GRB 091120, one of the brightest GRBs detected with MAXI-GSC, occurred 20 sec before the shut off of the HV to prevent from exposure to the Sun and is not detected in our transient search procedure. Another problem is the exclusion of the transient candidates based on several parameters as described in Section 4.6. These criteria resulted in ignoring nen GRBs due to the position near the detector end, lack of effective exposure, or a high background rate.

Other missing detections are not simple to explain. According to the result shown in Figure 4.9, we roughly obtained the effective detection limit with our analysis as 0.1 counts cm^{-2} s^{-1} $\sim$ 100 mCrab. The GRBs which are not detected by our method has the flux of a several times 10^{-9} erg cm^{-2} s^{-1}. The flux is comparable with the estimated detection limit. We note that the limit depends on fluctuation of non-X-ray backgrounds (NXBs). In the environment of MAXI, the NXB temporally varies and affects the detection limit. The uniform choice of background used in the present analysis may not be optimal in these events.

The cross matching of the SXTs with the GRB catalogs suggests one suspicious and another confirmed detections of GRB afterglows. The suspicious one is SXT 100907 detected about 1500 sec after the trigger of GRB 100907 by *Fermi*-GBM with angular distance of 14°. The temporal and positional coincidence possibly indicated the association, however the detected position is near one of YSOs, YZ CMi. From this YSO, an X-ray flare SXT 110308 has already been detected and reported as Serino et al. [69]. Thus, a flare of the YSO is more likely origin of the SXT rather than a GRB afterglow. On the other hand, SXT 121027 is temporally ($\sim$ 2400 sec after the GRB trigger) and positionally (within 0.31°) consistent with GRB 121027A. The observation of the *Swift*-XRT revealed that this GRB exhibited a special light curve including a bump of X-ray flux from 10^{-11} erg cm^{-2} s^{-1} to 10^{-8} erg cm^{-2} s^{-1} in the duration 10^{3}–10^{4} sec after the GRB trigger (Wu et al. [83]). It is the only SXT in our analysis that is clearly identified with a GRB afterglow.

Table 5.1: GRB catalogs used for source identification

Name	Objects*	N_{ass}	Reference
MAXI-GSC GRB	33	11	[68]
Swift-BAT GRB	15+298	2	[66]†
Fermi-GBM burst	819	2	[56]

* Number of GRBs detected in the term of our study.
† private communication.

5.1.2 SXTs associated with non-GRB sources

5.1.2.1 Non-GRB source Catalogs

The detected SXTs are tested for matching with some X-ray/γ-ray source catalogs; MAXI-GSC 37-month catalog, *Swift*-BAT source catalogs, *Fermi*-LAT 2nd catalog, and RXTE slew survey catalog. The MAXI-GSC source catalog (Hiroi et al. [28]) includes high Galactic-latitude ($|b| > 10^{\circ}$) 500 X-ray sources detected with GSC in the first 37 month. The dominant categories of the identified sources in the catalog are galaxy clusters and Seyfert galaxies. In addition, active stars and X-ray binaries including newly discovered ones are also listed. The *Swift*-BAT 70-month catalog (Baumgartner et al. [4]) and the *Swift*-BAT Hard X-ray Transient Monitor catalog[1] (Krimm et al. [41]) list a large number of hard X-ray sources including those that possibly show X-ray flares and outbursts (i.e., AGNs, X-ray binaries and flare stars); the former includes sources detected in the first 70 months of the data between 2004 December and 2010 September, and the later frequently updated by the Swift science team when a new active source is reported.

Fermi-LAT catalog (Nolan et al. [54]) includes γ-ray sources detected in the first 24 month period of the observation by the Large Area Telescope (LAT) in the 100 MeV to 100 GeV energy range. The most dominant contributors are blazars which occupy more than half of the cataloged sources. In addition, minor groups are pulsars, supernova remnants and other various type sources. While significant fraction of the sources in the catalogue are not identified with known sources, many of them are likely to be pulsars or blazars that are faint in other energy bands.

RXTE slew survey catalog (Revnivtsev et al. [61]) provided 294 source from six-year long observation of the RXTE satellite in the 3–20 keV band. The sources are associated with

---

[1] `http://swift.gsfc.nasa.gov/results/transients/`

Table 5.2: Source catalogs used for source identification

Name	Objects*	N_{ass}	N_{ramdom}	Reference
Swift-BAT 70 month	887 (1210)	30	33.3 ± 2.0	[4]
Swift-BAT Monitor	571 (982)	34	20.7 ± 1.5	[41]
CAB	347 (409)	19	13.0 ± 1.4	[13]
MAXI-GSC 37 month	500 (500)	35	24.4 ± 1.6	[28]
Fermi-LAT	1366 (1873)	50	48.4 ± 1.9	[54]
Globular Cluster	157 (157)	8	2.5 ± 0.6	[25]
RXTE slew	321 (321)	28	12.3 ± 1.2	[61]
VERON	1364 (1374)	49	33.9 ± 1.8	[81]
SACY	1645 (1791)	41	41.8 ± 2.4	[77]
NYMG	73 (73)	6	2.4 ± 0.6	[44]

* Number of sources outside of galactic plane region. Value in parentheses is total number of cataloged sources including galactic plane.

AGNs, galaxy clusters and known Galactic X-ray binaries. The position accuracy of the slew survey, less than 1°, is comparable to that of GSC in our analysis.

In addition to these general X-ray/γ-ray source catalogs, we should also test catalogs for classes of possible SXT sources; AGNs, active stars and globular clusters. The VERON catalog (Véron-Cetty & Véron [81]) contains numerous quasars and blazars. Since the positional errors of the SXTs in our analysis is too large for reliable cross matching with the quasars, we only used 1374 BL Lac sources in this catalog in our discussion. Active stars are potential sources of X-ray flares, for which we consulted three catalogs: Chromospherically Active Binary catalog (CAB; Eker et al. [13]), Search for associations containing young stars catalog (SACY; Torres et al. [77]), and Nearest Young Moving Groups catalog (NYMG; López-Santiago et al. [44]). The CAB catalog includes binary stars with a strong chromosphere and coronal activity. The SACY catalog is based on the optical spectroscopy survey to search for young stars among the ROSAT all-sky survey X-ray sources. The NYMG catalog lists possible members of YSOs close to the Sun. Note that the positional distribution of source in the SACY catalog is dense in the southern hemisphere, especially in regions around the Large Magellanic Cloud. We check possible associations of the SXTs with globular clusters, which often host X-ray binaries, using the 2010 edition of milky way globular clusters catalog (Harris [25] with updates on the web site[2]). This catalog contains well-known 157 globular clusters in our galaxy.

---

[2] `http://physwww.mcmaster.ca/~harris/Databases.html`

5.1.2.2 Results of the cross matching

The result of the cross matching with non-GRB source catalogs is shown in Table A.1. Before discussing each SXT and its origin, we check contribution of false associations with the sources in the catalogs. For each catalog, we estimated number of accidental associations, $N_{\rm random}$, with Monte Carlo method. In the method, 1000 test sources are randomly produced in the all sky, and then tested for positional matching with the sources in the catalogs with 2° positional tolerance. We performed one hundred trials with the test sources and obtained averages and standard deviations of accidental associations as the raw of $N_{\rm random}$ in the Table A.1. We find that the number of accidental associations is comparable to that of the detected counterparts in most catalogs owing to the large positional error. On the other hand, the matching results of the *Swift*-BAT monitor catalog, MAXI-GSC catalog and RXTE slew catalog seem to show excesses of $N_{\rm ass}$ over the accidental associations.

On the basis of these possible non-accidental associations, we discuss the nature of SXTs associated with some categories of possible SXT progenitors. As mentioned in Section 2.1.3, SXTs associated with the globular clusters are likely be X-ray bursts from neutron stars in LMXBs. Four SXTs (SXT 091105, 100813, 110110 and 120805) are associated with LMXB 4U 0513−40 located in the globular cluster NGC 1851. They have the flux of 0.1–0.5 counts $\rm s^{-1}$ $\sim$ a few times 10^{-9} erg $\rm cm^{-2}$ $\rm s^{-1}$ and the hardness ratio of 0.2–0.4. Such detections are consistent with the large amplitude variability of the source in $\sim 10^{-11}$–10^{-10} erg $\rm cm^{-2}$ $\rm s^{-1}$ and the maximum of 10^{-9} erg $\rm cm^{-2}$ $\rm s^{-1}$ (Fiocchi et al. [15], Maccarone et al. [45]). The SXT 120804 is associated with MAXI J1647−227 which is discovered with MAXI-GSC (Negoro et al. [53]) in June 2012 and identified as a binary with a neutron star because of the detection of the type I X-ray burst Kennea et al. [34]. The detected SXT is most likely another X-ray burst from MAXI J1647−227.

X-ray flares of RS CVn and dMe stars are also major constituents of the detected SXTs. SXT 100123, 111229s, 120310s and 130226 can be identified as such flares from a RS CVn, HR 1099. Some of them are successively triggered in more than two consecutive scan transits of GSC. The dMe star, AT Mic, is the probable progenitor of SXTs 110221, 110902 and 120419. The hardness ratios of the flares, 0.03–0.2, are relatively smaller than that of X-ray bursts of neutron star binaries since spectrum of stellar flare is thermal emission of optically thin plasma with relatively low temperature. Although young stellar objects are also possible SXT sources, accidental association is not negligible as mentioned above. We only suggest a likely association of SXT 100907 as YZ CMi.

Third promising origin of SXT is X-ray flares from blazars, especially BL Lac objects. STXs associated with some BL Lacs, Mrk 205 and PKS 2149−306, and a few Seyfert galaxies are detected, however relatively large null hypothesis probabilities, 10^{-10}–10^{-9}, call for careful confirmation. Moreover, similar to the case of active stars, the large number of catalogued sources make accidental association more likely.

5.2 Hardness of the detected SXTs

Hardness ratio, which is a fraction between fluxes in two different energy bands, is an useful indicator of spectral features of X-ray sources. In the case of stellar flares, since the emission is thermal radiation form optically thin plasma on the photosphere, the hardness ratio is smaller, i.e., its spectrum is softer. In other classes of X-ray sources whose spectra are represented with power-law function, such as GRBs, flares of AGNs have various hardness values depending of the spectral indices. X-ray bursts of LMXBs have harder spectra than stellar flares. They are described with blackbody radiation with temperatures of a few keV.

In our analysis the hardness ratios of the detected SXTs are calculated in the 2–8 keV and 8–20 keV energy bands and listed in Table A.1. Their distribution and relation with the X-ray flux are shown in Figure 5.1. A dominant population is located around the hardness of 0.3–0.7 regardless of the significance (null hypothesis probability) of events. In contrast, the hardness ratios of the detected GRBs are widely distributed in 0.1–0.7. Comparing the hardness distribution shown in Figure 5.2 (Serino [68]), the difference between the populations are more obvious. The distribution of the sources that do not include the GSC-triggered GRBs is similar to that of X-ray bursts rather than that of GRBs and stellar flares. This implies that the SXTs detected with our analysis are not stellar flares but more likely X-ray bursts of neutron star binaries or other class of events whose spectra have a hard component in the 8–20 keV band.

Assuming the spectra of the SXTs as power-law like non-thermal emission or thermal blackbody radiation, the expected relation between the hardness and the parameters of these spectral functions are shown in Figure 5.3. The power-law function is defined as photon flux density $dN/dE = E^{-\Gamma}$, with the photon index of Γ. The spectral parameter of the blackbody function is its temperature kT in unit of keV. Note that we ignore interstellar absorption component

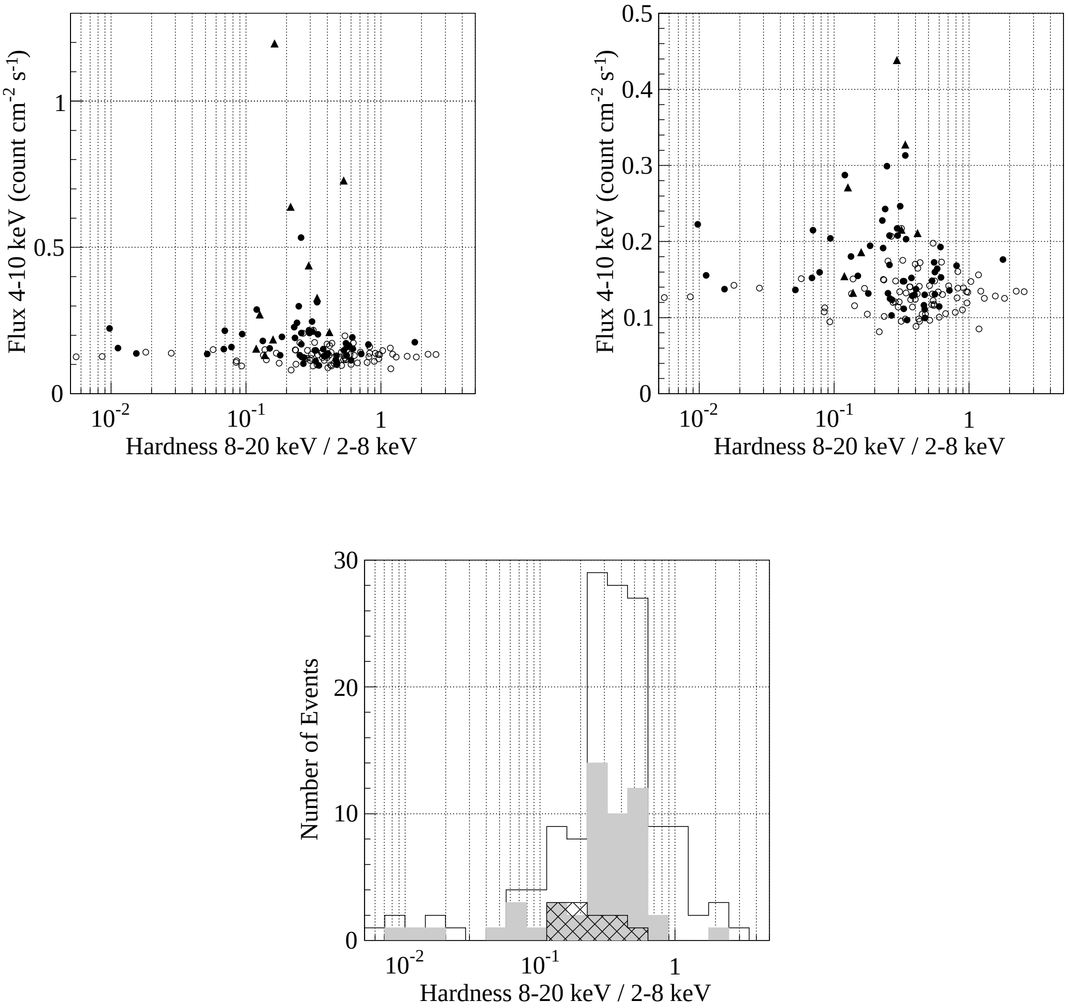

FIGURE 5.1: Hardness-flux diagram (upper) and histogram of hardness (lower). The right upper panel shows an enlarged view of the left one. The candidates which do not include the GSC-known GRBs and has the $P_{\mathrm{null}} < 10^{-9}$. are represented as the open circles and blank histogram. The black-filled circles and gray-filled histogram are that with the $P_{\mathrm{null}} < 10^{-10}$. The GSC-known GRBs are shown as the triangle marks and hatched histogram.

from the estimation since the effect is very small in our sample taken off the galactic plane and measured above 2 keV. From Figure 5.3, spectra of the SXTs with the hardness ratio of ~ 0.5 have the flat power-law index $\Gamma \sim 1.0$ or the relatively high blackbody temperature $kT \gtrsim 2.0$ keV. The photon indices are consistent with that of GRB spectra in the soft X-ray/γ-ray band (Sakamoto et al. [64]). Moreover, the temperatures are also comparable to those of X-ray bursts from LMXBs (Galloway et al. [18]). From the aspect of distribution of hardness ratio, the dominant origins of the detected SXTs are GRBs with hard X-ray spectra and/or XRBs from LMXBs.

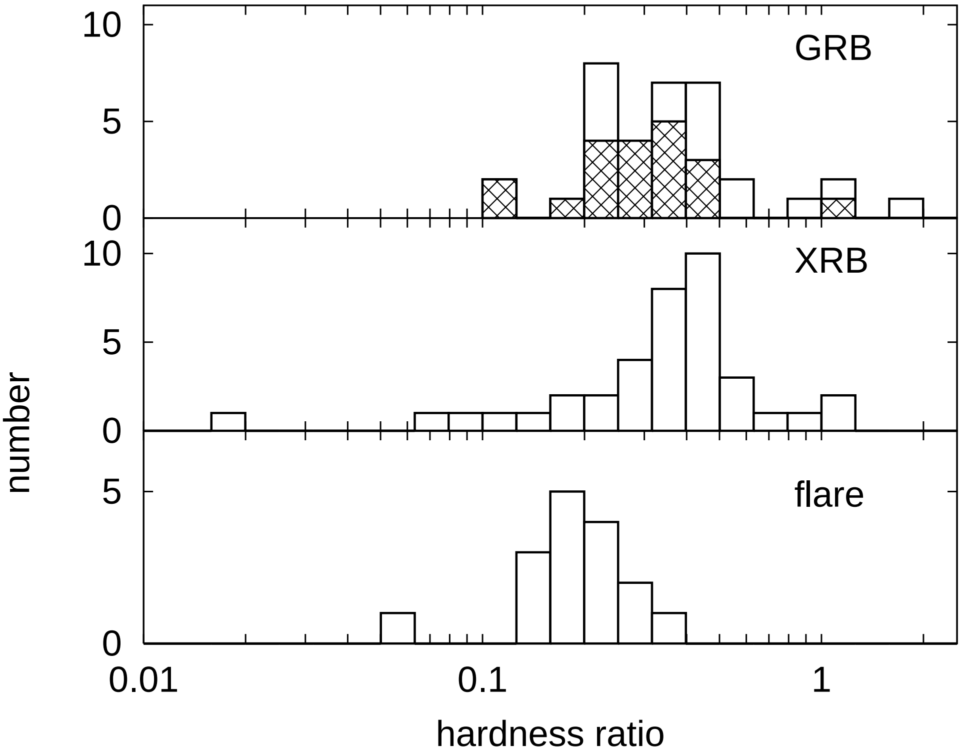

FIGURE 5.2: Histogram of the hardness ratio of the GRBs, X-ray bursts (XRBs), and stellar flares discovered with GSC (Serino [68]). In the upper panel the hatched histogram means the GRB detected with only MAXI (without any other observatory).

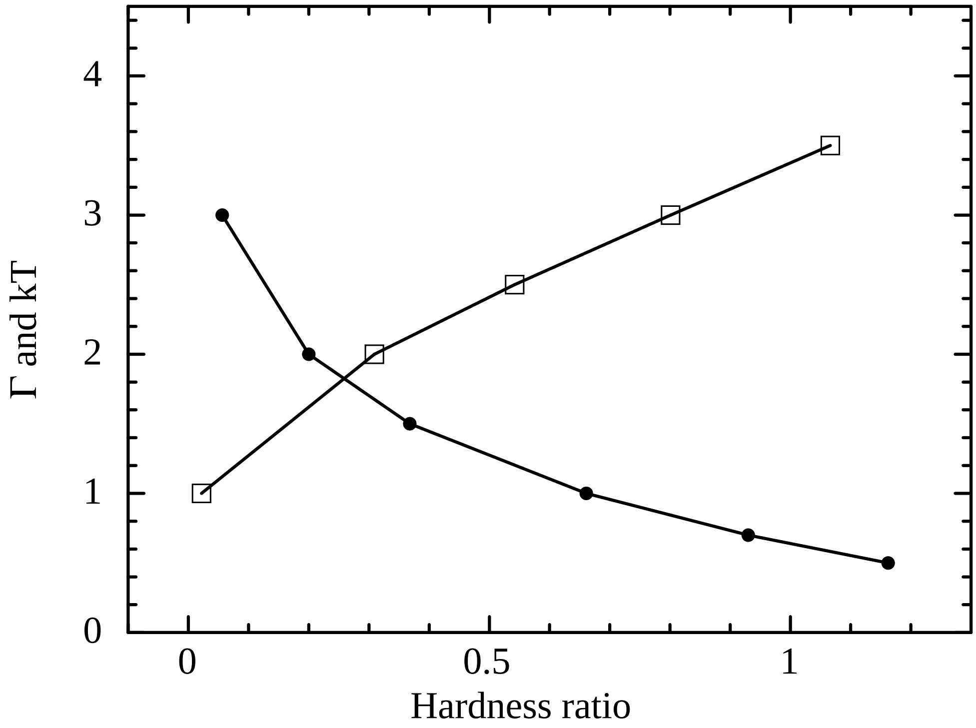

FIGURE 5.3: Correspondence of hardness ratio to photon index Γ (filled circle) and temperature of blackbody kT (box). The definition of Γ and kT is shown in the text.

Table 5.3: Statistical test of isotropy

Test	$P_{\mathrm{null}} < 10^{-9}$	$P_{\mathrm{null}} < 10^{-10}$	Expected
$\langle \cos\theta \rangle$	-0.01 ± 0.14	0.04 ± 0.16	0.020
$\langle \sin^2 b - 1/3 \rangle$	0.11 ± 0.06	0.11 ± 0.06	0.066

5.3 Spatial distribution

The spatial distribution of the detected transients is shown in Figure 5.4 in the Galactic coordinates and the equatorial coordinates. The distribution looks roughly uniform over the sky. We verify the impression by calculating dipole and quadruple statistics which are described in Section 2.3.1. If the exposure and effective area of the observation are even, an uniform distribution over the sky implies a isotropy of the source distribution. However, the exposure of GSC strongly depends on an angle toward the rotation axis of the ISS orbit. In the verification of spatial distribution of SXTs detected with GSC we have to consider not only the distribution of the SXTs but also the anisotropy of the exposure map.

Figure 5.5 is the spatial distribution of the GSC exposure in the 43 month. The unit of the exposure is product of time in second and effective area in cm^2. The belt-like blank region and the blank circles correspond to the Galactic plane and the bright sources excluded from our analysis, respectively. The effective exposure is slightly larger at the high declination. Note that the lighter regions at the equatorial poles results from the blind areas in the GSC whose field of view across the direction of motion is not 180° but 160°.

In order to investigate an isotropic distribution of the detected sources, we make histograms of the dipole and quadruple statistics for the SXT candidates and the distribution of the effective exposure, as shown in Figure 5.6. The resulting statistics are calculated from these histograms and summarized in Table 5.3. The errors are standard deviations. We conclude that those quantities obtained from the data and the exposure map are consistent with the isotropic distribution of the detected SXTs.

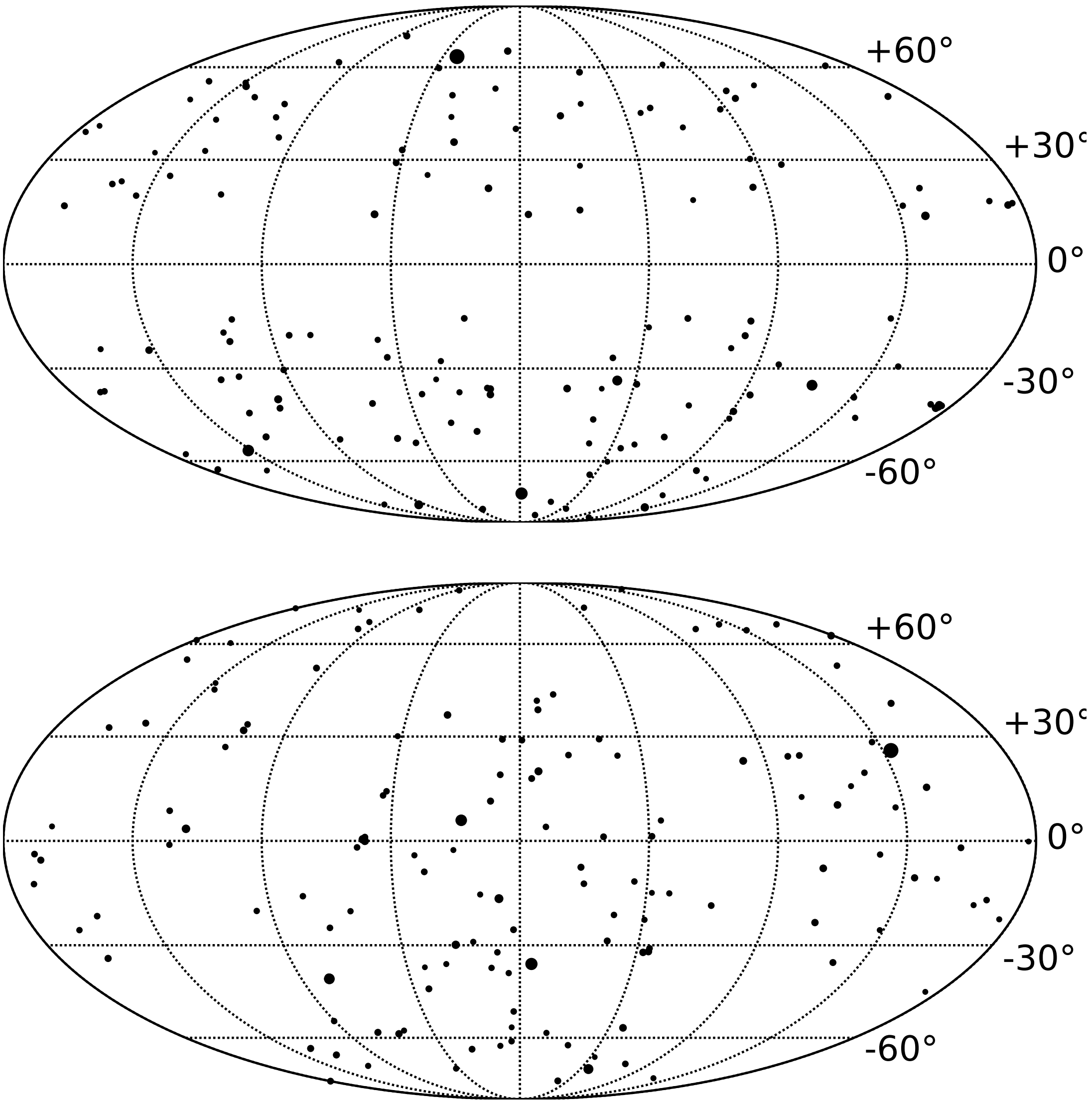

FIGURE 5.4: Map of detected X-ray transients in the Galactic coordinate (upper) and the equatorial coordinate (lower). The radii of the circles are proportional to the logarithm of the X-ray fluxes in the 4–10 keV band.

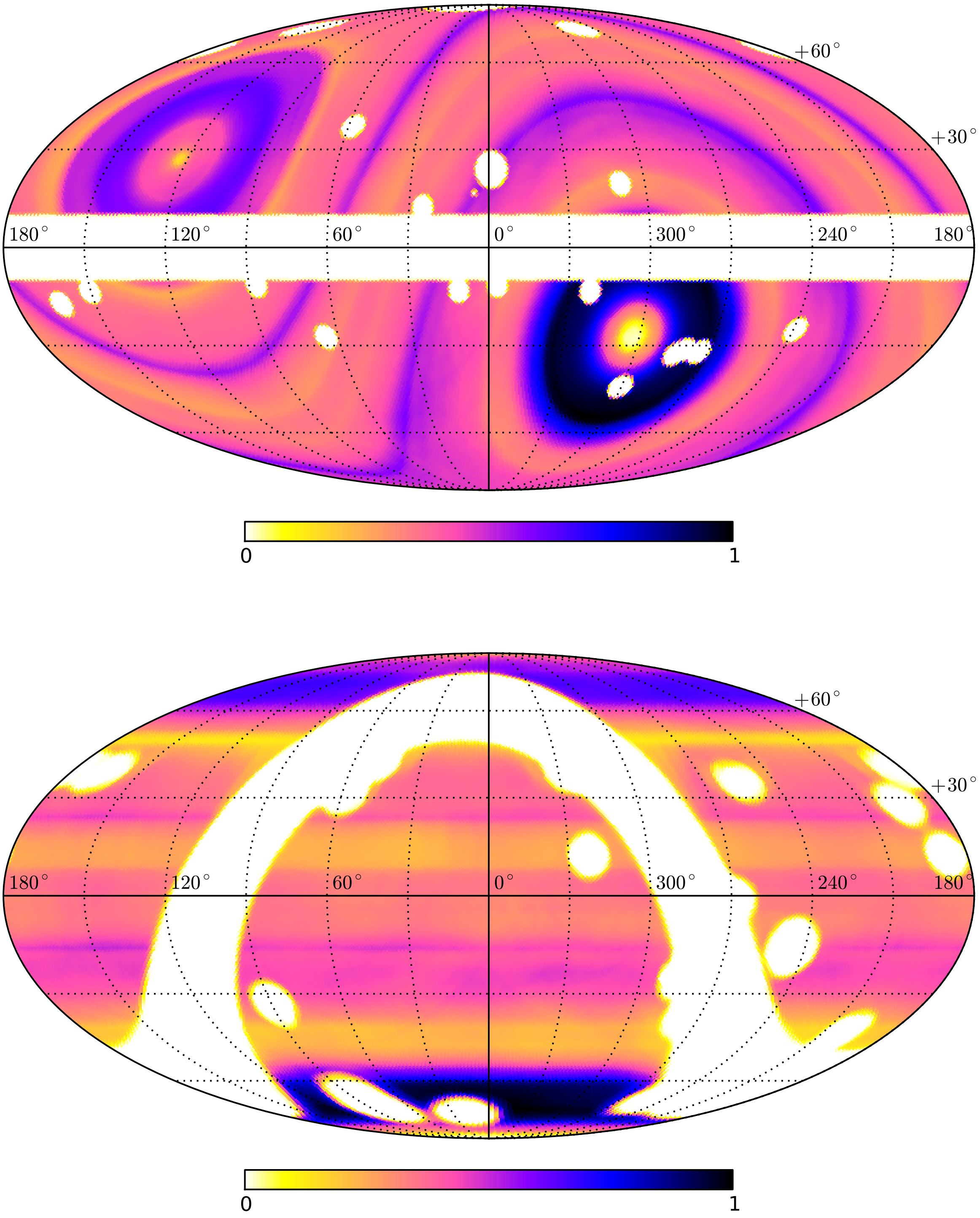

FIGURE 5.5: Normalized exposure map of our analysis in the Galactic coordinate (upper) and the equatorial coordinate (lower). The normalization factor is 5993982 cm^2 s.

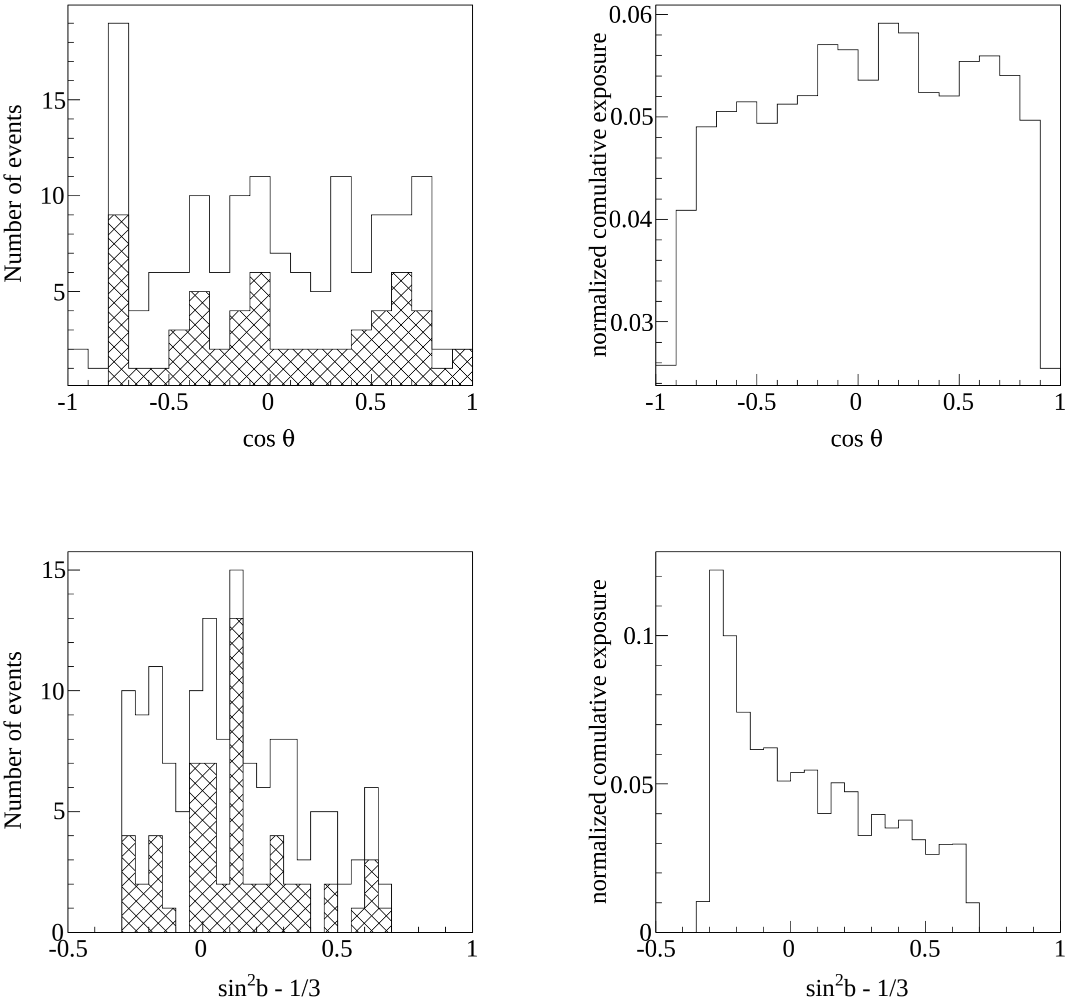

FIGURE 5.6: Distribution of $\cos\theta$ and $\sin^2 b - 1/3$ obtained from the detected SXTs (left panels) and the exposure map (right panels). The hatched histograms in the left panels are provided from the SXTs with $P_{\rm null} < 10^{-10}$.

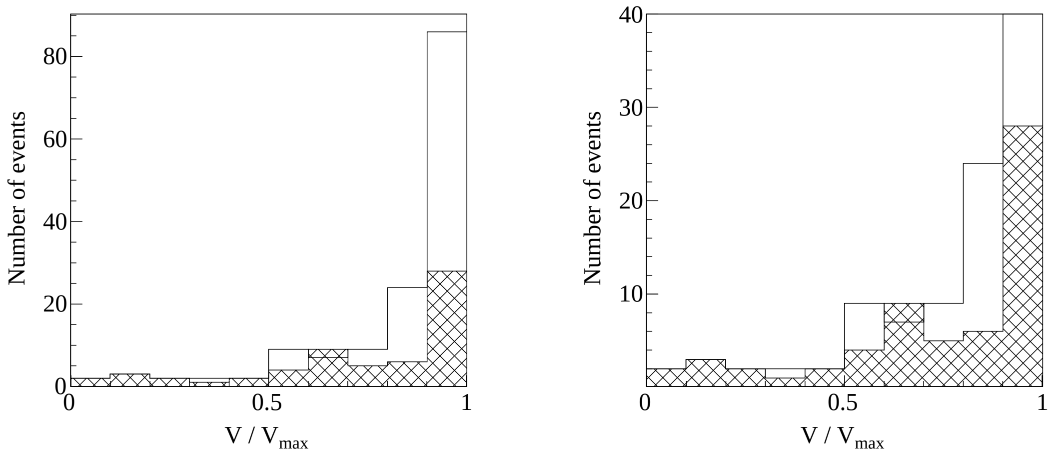

FIGURE 5.7: Histogram of $V/V_{\rm max}$ of the SXTs with $P_{\rm null} < 10^{-9}$ (blank) and $< 10^{-10}$ (hatched). The right panel is an enlarged view of the left histogram.

5.4 Study of spatial distribution

5.4.1 $V/V_{\rm max}$ test

Supposing the specially uniform distribution of SXTs in the Euclidean space, the $V/V_{\rm max}$ test will provide the average of 0.5. In the test we calculate each $V/V_{\rm max}$ value from the foreground and background X-ray counts which are evaluated in the localization process for each SXT. The minimum detection limit $C_{\rm lim}$ is obtained as a solution of the inverse function of the Poisson-distribution survival function with the mean of $N_{\rm b}$ (Equation 4.2), number of the background counts which is normalized with the area ratio of the fore and background regions, and the threshold upper tail probability of 10^{-9}.

The histogram of the $V/V_{\rm max}$ is shown in Figure 5.7. From the distribution of the SXTs with the null hypothesis probability of 10^{-9} and 10^{-10}, we obtained the average of $V/V_{\rm max}$, $\langle V/V_{\rm max}\rangle = 0.829\pm0.024$ and 0.739 ± 0.037, respectively[3]. These values are significantly different from the expected value 0.5 for the uniform spatial distribution. Moreover, the distribution as shown in Figure 5.7 is dominant in the $V/V_{\rm max} = 0.9$–1.0. This strongly suggests that the SXTs with the lower flux contain false detections whose foreground counts accidentally (or more likely systematically) include a few additional counts thereby exceeding the detection threshold.

---

[3] The errors are estimated from $(12n)^{-1/2}$, where n is the number of the SXTs

5.4.2 Log$N$-log S plot

We made log N-log S plot to investigate the spatial distribution of the detected SXTs and compare it with the results from other satellites. Figure 5.8 shows the plot with each threshold of null hypothesis probabilities; $P_{\rm null} < 10^{-9}, 10^{-10}, 10^{-15}$ and 10^{-50}. Supposing no temporal variability of an X-ray flux during the scan transit of GSC, we obtain the fluence integrated the count flux reported in Table A.1 over 30.0 sec which is the half width of the typical scan transit time as described in Section 3.2.4.1.

In the bright fluence region ($S \gtrsim 8$ photon cm^{-2}) of the plot with $P_{\rm null} < 10^{-9}$, the plot will represented with the $S^{-3/2}$ distribution, however it may not be consistent with results of other surveys which has the S^{-1} function. The abnormal feature will be acceptable with considering the fluctuation of the small number of SXTs. In fact, our study unfortunately does not detect some of the brightest GRBs as listed in Table A.2. If they contributed to the log N-log S plot, it would provide more reasonable result in our analysis.

In contrast, the histogram in the fainter region is complex, because that with $P_{\rm null} < 10^{-9}$ shows much steeper power-law function with the index of $\gtrsim 3$. That is inconsistent to the traditional short X-ray transient surveys. To explain such unreasonable distribution, we will have to accept that the SXTs with $P_{\rm null} < 10^{-9}$–10^{-10} include false detections, as mentioned in Section 5.4.1. The histogram with the $P_{\rm null} < 10^{-10}$ in the fainter fluence region ($S \lesssim 8$ photon cm^{-2}) has the $N \propto S^{-3/2}$ distribution and is consistent with the expectation of uniformly distributed transient phenomena. According to the past studies of GRBs, however, the slope of the plot in the low fluence region should be typically flatten owing to a cosmological effect. The different feature of the log N-log S plots in our analysis and traditional surveys implies that our result includes close (low-redshift) and intrinsically dim SXTs. The possible origins are X-ray activities of active stars and X-ray binaries in our galaxy, and XRFs (X-ray flashes), which are probably occur in closer regions than hard (classical) GRBs (Sakamoto et al. [62]). They are expected to show a log N-log S curve with slopes steeper than that of GRBs. Note that even though we carefully searched SXTs in the MAXI-GSC data, the detections with $P_{\rm null} < 10^{-10}$ may still include additional false detections.

Figure 5.9 shows a log N-log S plot that is corrected to be consistent with the uniform distribution in space for the detected SXTs, so that an average of $V/V_{\rm max}$ becomes close to 0.5. First we calculate average number of SXTs in the $V/V_{\rm max}$ histogram using the bins below 0.5 in Figure 5.7. Next we discounted weight for the SXTs with $V/V_{\rm max} > 0.5$ per bin width of 0.1, so that the $V/V_{\rm max}$ bins above 0.5 have counts equal to those below 0.5. With this discount weight we plot the $\log N$-$\log S$ histogram as shown in Figure 5.9. As a result the contribution of the $V/V_{\rm max} > 0.5$ SXTs to the $\log N$-$\log S$ plot decreases. The distribution in Figure 5.9 shows no excess over the $-3/2$ slope and becomes shallower in the region of the faint fluence.

When we choose the detection threshold of $P_{\rm null} = 10^{-9}$ in Section 4.4.2, number of false (accidental) detection is estimated as ~ 1 for the analyzed data set consisting of $\sim 10^9$ trials. Conversely, the 84 SXTs with the $P_{\rm null} = 10^{-9}$–10^{-10} seem to include much more false detections than the expectation. This inconsistency casts doubt on the basic assumption that the fluctuation of the GSC background is the Poisson noise. The environment of MAXI possesses various origins of background for the X-ray detectors; not just NXB and CXB, but solar X-ray emission, its scattering and reflection to structures of the ISS and the Cs^{137} source mounted on the Soyuz spacecraft. Such background sources may generate unexpected (and maybe systematic) false detections which are difficult to discard in our analysis.

Our transient search provide a few bright SXTs which has the fluence of > 10 counts cm^{-2} in the $\log N$-$\log S$ plot. From this result we estimate the number of SXTs per year for the entire sky. Here, we should consider the following correction factors: effective time duration of the GSC operation $f_{\rm ope}$, field of view in the one-scan transit $f_{\rm FoV}$ and data rejection factor applied in our transient search process $f_{\rm ts}$. Since the GSC is turned off in the South Atlantic Anomaly (SAA) and high-latitude regions of the orbit, the operating efficiency (ratio of the observing time to the total real time in orbit) , the $f_{\rm ope}$ is estimated as $\sim 40\%$ in a day. The fraction of the field of view with respect to the entire sikh, $f_{\rm FoV}$, is 1.48%, as derived from two $160^\circ \times 3^\circ$ field of view of the GSC-H and GSC-Z. The efficiency of the analyzed data has been already mentioned in Section 4.6.7 and estimated to be $\sim 25\%$ of the original data observed with GSC. As a result, we obtained the number of the SXTs per a year for the whole sky as the order of 10^3 with the correction factor of $0.4 \times 0.015 \times 0.25 = 1.5 \times 10^{-3}$. According to the $\log N$-$\log S$ distribution of Arefiev et al. [2] as shown in Figure 2.10, an expected number of brighter SXTs which last X-ray events with the flux of 1 Crab with a duration of 60 sec (comparable to the GSC one-scan transit) is estimated to be $\approx 10^3$. This is roughly comparable to the expected number of SXTs in our analysis.

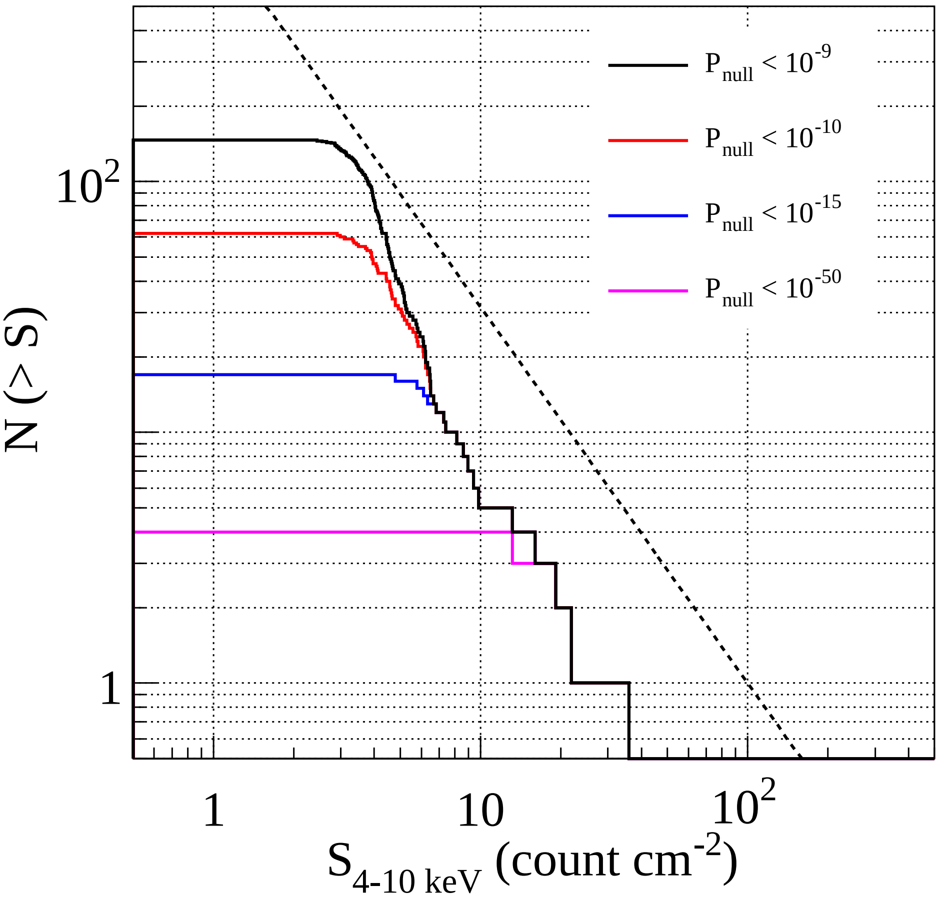

FIGURE 5.8: The log N-log S plot of the 146 SXTs. The colors mean difference of detection thresholds. The dotted line is power-law function with the index of $-3/2$.

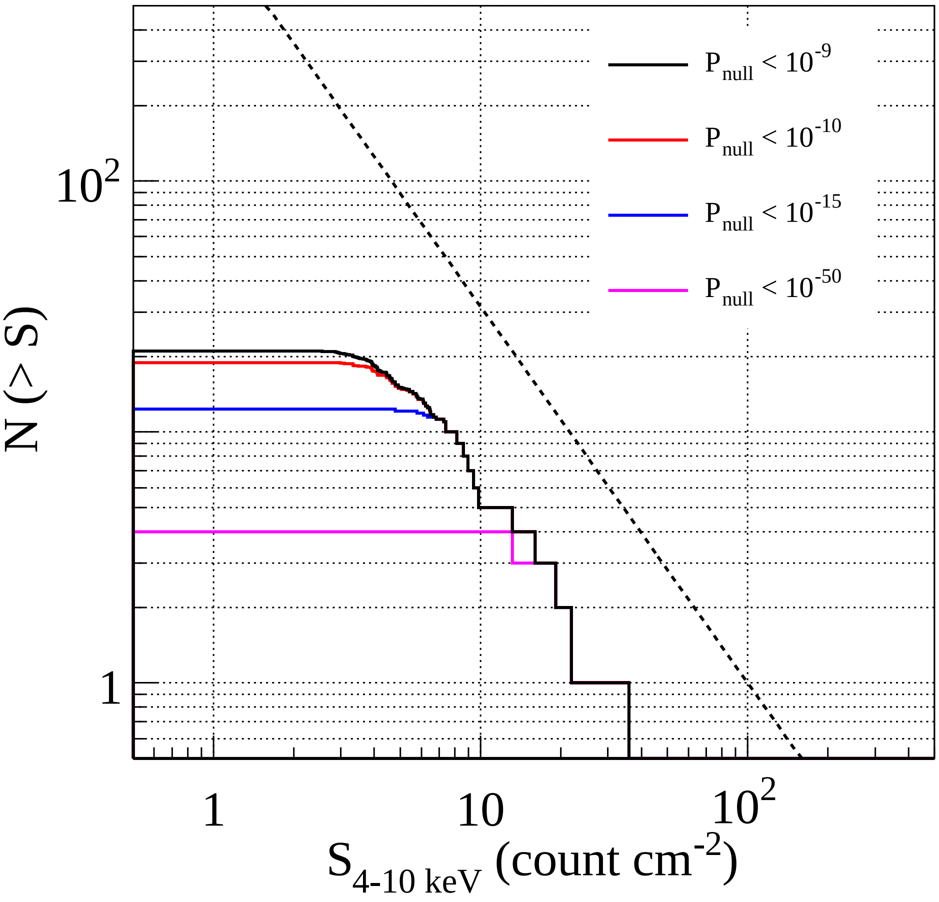

FIGURE 5.9: The log N-log S plot corrected to consider uniform spatial distribution.

5.5 Origin of the low-flux SXTs

In Section 5.4.1 and Section 5.4.2, we found that the detected SXTs with the lower flux provide V/V_{max} and $\log N$-$\log S$ plots that are astrophysically unreasonable. Here, we examine distributions of the SXTs with respect to their detected time, detector and position on earth in order to investigate the origin of such results.

First, we focus on temporal and/or detector-based bias in detection of the SXTs. If false detections originate from solar flares, the SXTs may have temporally-biased with the solar activity. On the other hand, NXB (charged particles and γ-ray photons) may induce false faint (large V/V_{max}) SXTs localized in particular locations in detectors. Figure 5.10 shows histograms of the 146 SXTs to the detected time, GSC camera and position on the detector coordinate. These histograms indicate the detections of the SXTs are uniformly distributed to time and detector coordinate without considering the V/V_{max} values. Thus, solar X-rays, external charged particles and/or high-energy photons are probably not suitable to the origin of excess detections with larger V/V_{max}.

In Figure 5.10, the numbers of SXTs are not even across the GSC cameras. It is generally possible since the rejection of X-ray events in the galactic plane may affect this inhomogeneous distribution, However, cameras 1 and 7 should have approximately equal number of SXTs since they share the same monitoring field in the sky (see Figure 3.3). Nevertheless the number of the SXTs detected with the GSC 7 is about three times larger than that detected with GSC 1. It is noteworthy that this unevenness is particularly noticeable in SXTs with large V/V_{max} values. The number of the $V/V_{\mathrm{max}} > 0.9$ SXTs detected with the GSC 7 is twice as large as that with the GSC 1. This fact suggests that noise of the detectors and/or their processing circuits may produce such “suspicious” SXTs.

Second, in order to distinguish false detections originated by NXB, here mainly considering charged particles, we make map of detected positions of the SXTs on earth as shown in Figure 5.11. If charged particles will accidentally trigger SXT-like events, the positional distribution of the SXTs should be localized in the high latitude region and around the SAA, where the particles are more dense. In contrary to this anticipation, the map has uniform distribution to the SXTs. Thus, we imply that the SXTs with the large V/V_{max} are not originated with the excess of the charged particles.

Third, another benchmark to investigate contribution of the NXB to the “false” detections using the VETO signal counts. The VETO anode wires are located under photon signal anodes wires and both sides of a GSC camera (see Section 3.2.2), and they are sensitive mostly to charged particles penetrating the detector walls or electrons produced in the detector material. A sudden increase of NXB may cause a false SXT, but that should be also noticeable in the increase of VETO counts. In Appendix B, we show maps of X-ray events in GSC, light curves (count rate time history), and plots of the VETO temporal variation for the detected 146 SXTs. One of the SXTs, SXT 120416 may be associated with a short term variation of the VETO counts as shown in Figure B.115. However, looking at the VETO plots, almost all SXTs are detected with the stable and relatively law (100–300 counts) and stable VETO counts. This result also supports that the SXTs are not accidentally triggered by temporal variation of the density of the charged particles.

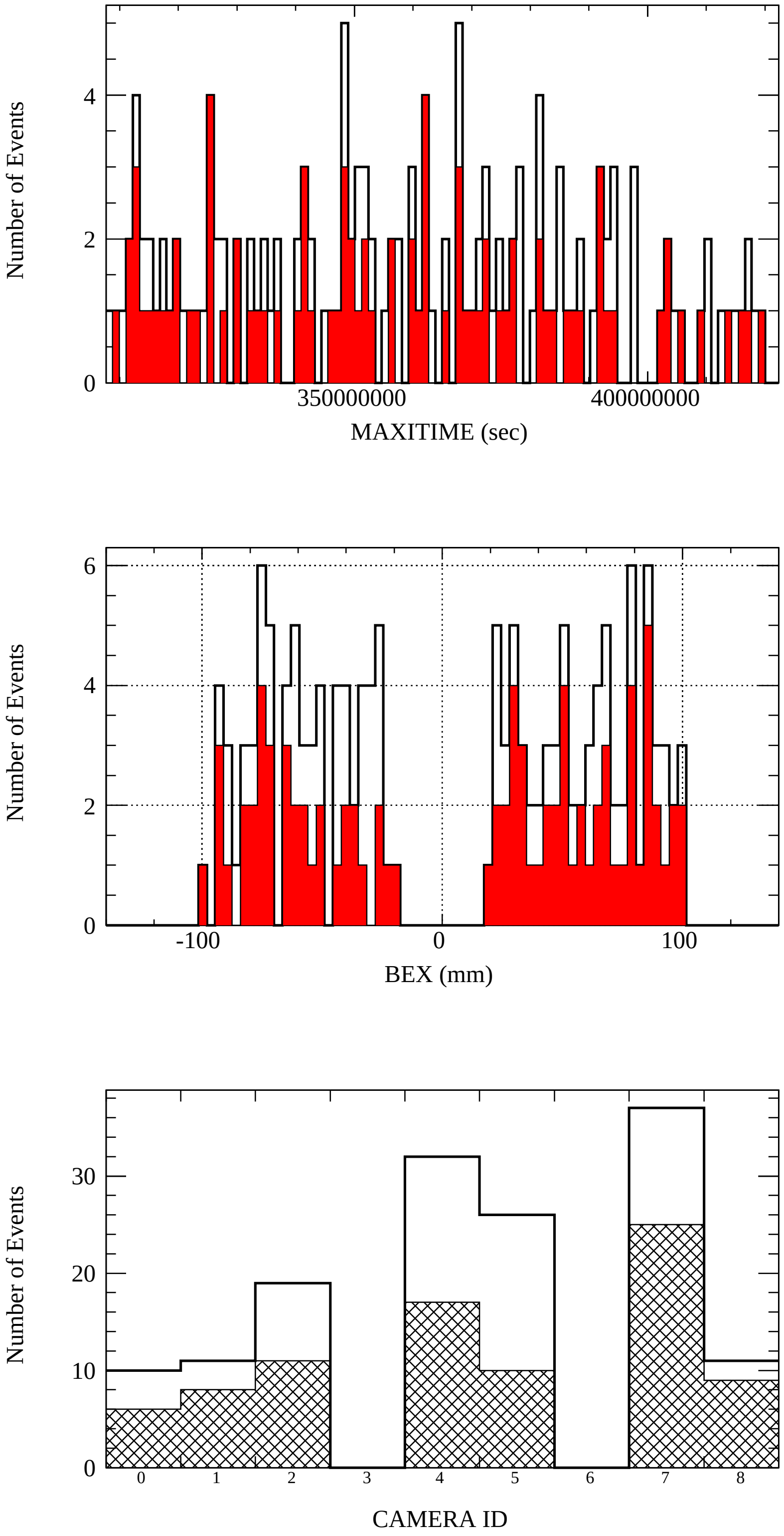

FIGURE 5.10: Histogram of the SXTs to detected time, detector coordinate and GSC camera. The SXTs with $V/V_{\mathrm{max}} > 0.9$ represented with the red ones in the upper and middle panels and the hatched one in the lower panel.

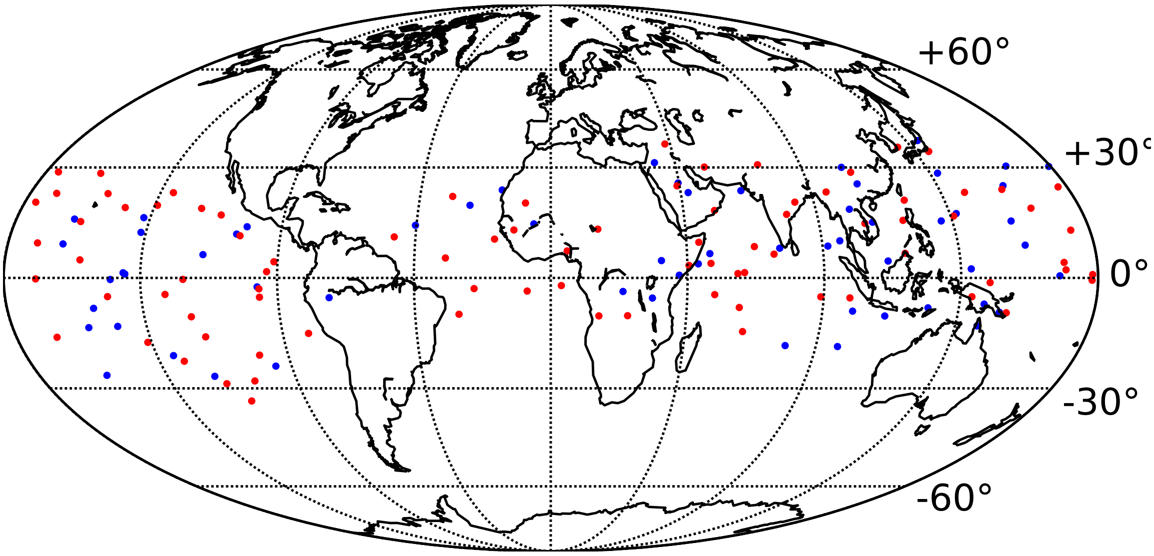

FIGURE 5.11: Positional distribution of the detected SXTs on earth. The red and blue colored points correspond to the SXTs with the $V/V_{\max} > 0.9$ and < 0.9, respectively.

Chapter 6

Conclusion

We developed a new method to systematically search short X-ray transients (SXTs) from the MAXI-GSC data obtained from October 2009 to May 2013. This method employs a simple detection algorithm in which the null hypothesis probability for the observed X-ray counts in a test region is evaluated assuming the Poisson fluctuation of the background. First, we screened out specific events on the Galactic plane, in the regions near known bright X-ray sources, and those detected in area with particularly high background. Next, we extracted candidates of short X-ray transients with the low detection threshold assuming a Poisson-distributed background. Third, these candidates were examined for their accurate positions, detection significances and X-ray fluxes. In the analysis, we only considered number of counts in a test region and did not perform any fitting to background models and the point spread function of the GSC counter. Finally, we obtained 147 SXTs with the low null hypothesis probability 10^{-9} based on the Poisson-fluctuated background.

These SXTs were checked for positional and temporal coincidence with known GRB catalogs and optical/X-ray/γ-ray source catalogs which include possible sources of short X-ray activity. We confirmed 11 SXTs as the prompt emissions of known GRBs and one as the afterglow of the untypical GRB. The cross matching with the non-GRB catalogs revealed some SXTs are positionally associated with X-ray binaries consisting of neutron stars or active stars such as RS CVn. However, the large position error provided by our analysis prevent from association of other SXTs with GRBs or other classes of sources such as blazars. As regard to hardness ratio, the detected SXTs mostly have hard X-ray spectra which are consistent with X-ray bursts of neutron-star binaries or prompt emission of hard GRBs rather than stellar flares.

The positionally isotropic distribution of the detected SXTs was confirmed with the $\langle\cos\theta\rangle$ and $\langle\sin^2 b - 1/3\rangle$ statistics, since these quantities were consistent with the expectations from the exposure map of GSC. However the $V/V_{\rm max}$ tests indicate that the spatial distribution of the SXTs is not uniform. This is probably caused by the false detections triggered by fluctuation of the background of GSC or some other unknown reasons. The $\log N$-$\log S$ plot showed similar results. The $P_{\rm null} < 10^{-10}$ SXTs provided the power-law like distribution with the slope of $\sim -3/2$. On the other hand, the SXTs with $P_{\rm null} = 10^{-9}$–10^{-10} showed steeper distributions with indices larger than $-3/2$ in the < 0.5 counts cm^{-2} lower fluence region.

The exceeding population in the $\log N$-$\log S$ plot formally indicates that the dim and distant phenomena are abundantly detected by our analysis; however, such phenomena are not astrophysically plausible. We conclude that our analysis suffers from false detections that have X-ray count slightly larger than the threshold. To investigate the origin of the detections, we examined correlations with the detected time, position on earth and increasing of background. Finally we found that the false detections are related to the noise of a detector or readout electronics. To perform advance study, we need to consider such noise in addition to the Poisson-fluctuation of the background.

Appendix A

List of Detected Transients

In our transient search analysis, we obtain 146 short X-ray transient candidates. Information of these candidates, detected time in the Universal Time, position, null hypothesis probability and fluxes, are summarized in Table A.1. Possible counterparts of the detected SXT candidates with the source catalogs listed in Table 5.1 and Table 5.2 are also shown. The counterparts of the GSC-known GRBs are shown other than the GRB itself in the table. Table A.2 summarizes information of the GRBs reported in Serino [68]. In addition, the table notes that whether our analysis detected these GRBs or not.

TABLE A.1: List of detected short X-ray transients and their possible counterparts.

Name	Time (UT)	R.A. (°)	Dec. (°)	P^*_{null}	$f^\dagger_{4-10}$	$f^\dagger_{2-8}$	$f^\dagger_{8-20}$	HR[‡]	Counterpart[§]
091012	2009-10-12 10:26:08	181.38	+63.08	-15.78	0.211	0.262	0.109	0.415	SDSS J11558+6135(8), 091012 (C:+0.00204, 0.71)
091014	2009-10-14 14:08:14	134.00	+46.60	-9.10	0.092	0.093	-0.001	-0.007	NGC 2712(1), S4 0859+47(5)
091105	2009-11-05 19:46:46	78.13	-40.56	-11.06	0.123	0.200	0.054	0.268	CXO J051406.4-400238(1), 4U 0513-40(2, 7), NGC1851(4), J052038.3-394517(9)
091115	2009-11-15 01:51:19	107.68	-71.00	-9.10	0.115	0.150	-0.005	-0.031	
091119	2009-11-19 00:15:30	98.82	+68.45	-9.25	0.114	0.126	0.048	0.381	
091202	2009-12-02 05:41:18	162.85	+54.45	-9.01	0.139	0.088	0.073	0.827	1ES 1044+549(8)
091202	2009-12-02 13:50:24	59.48	-57.39	-9.05	0.108	0.111	0.009	0.084	J041155.1-580154(9)
091204	2009-12-04 23:41:35	314.40	-22.50	-9.38	0.114	0.111	0.033	0.298	J210417.6-221011(9)
091205	2009-12-05 10:16:12	313.96	+1.29	-11.29	0.149	0.119	0.063	0.532	1RXS J205528.2-002123(5), SDSS J20549+0015(8)
091212	2009-12-12 12:46:17	47.01	-72.12	-9.33	0.120	0.143	0.039	0.274	ESO 031- G 008(1, 4), J032736.1-725044(9)
091218	2009-12-18 17:44:08	234.29	-3.86	-10.35	0.125	0.171	0.044	0.260	RXC J1540.1-0318(4)
091227	2009-12-27 12:39:05	209.61	+52.37	-9.80	0.139	0.132	0.004	0.028	SDSS J14067+5308(8)
091229	2009-12-29 13:13:23	47.36	+14.06	-10.41	0.136	0.110	0.079	0.717	
100108	2010-01-08 20:59:02	338.61	-7.45	-9.11	0.170	0.179	0.072	0.399	PKS 2227-088(1, 5), QSO B2227-0848(2)
100120	2010-01-20 16:23:29	48.44	+12.87	-9.09	0.133	0.134	0.131	0.977	
100123	2010-01-23 05:18:35	54.20	+0.35	-16.13	0.243	0.395	0.094	0.239	HR 1099(2, 3, 4, 7), SDSS J03440-0000(8)
100207	2010-02-07 09:48:24	235.52	+19.39	-9.12	0.134	0.057	0.145	2.559	3C 323.1(1)
100217	2010-02-17 19:32:04	110.19	+26.90	-9.57	0.127	0.150	0.001	0.009	V340 Gem(3), FIRST J07247+2621(8)
100220	2010-02-20 06:51:17	179.08	+61.43	-9.24	0.122	0.115	0.062	0.540	SBS 1200+608(5), SDSS J11558+6135(8)
100302	2010-03-02 06:10:59	146.49	+34.03	-11.27	0.168	0.112	0.091	0.809	SDSS J09476+3453(8)
100315	2010-03-15 19:24:43	159.32	+32.70	-9.96	0.148	0.111	0.115	1.031	SDSS J10421+3254(8)
100327	2010-03-27 17:08:43	345.93	+42.93	-9.25	0.133	0.285	0.039	0.138	PSR J2302+4442(5), 100327 (C:+0.00032, 0.08)
100415	2010-04-15 03:45:16	7.50	-16.40	-28.40	0.328	0.577	0.194	0.337	J002606.8-154217(9), 100415A (C:+0.00022, 0.83)
100418	2010-04-18 06:21:02	70.30	-24.86	-9.33	0.141	0.155	0.056	0.362	PMN J0434-2342(5), RXS J04402-2459(8)
100419	2010-04-19 18:12:35	261.20	+24.15	-9.31	0.151	0.169	0.010	0.057	
100420	2010-04-20 19:11:19	310.70	+5.76	-9.42	0.117	0.106	0.056	0.530	
100425	2010-04-25 05:18:17	256.83	+24.41	-9.14	0.149	0.194	0.045	0.234	4U 1700+24(1, 2, 4, 7)
100509	2010-05-09 15:58:48	185.88	-44.37	-10.51	0.097	0.099	0.034	0.348	2FGL J1214.1-4410(5), PKS 1224-443(8)

TABLE A.1: (Continued)

Name	Time (UT)	R.A. (°)	Dec. (°)	$P^{*}_{\rm null}$	$f^{\dagger}_{4-10}$	$f^{\dagger}_{2-8}$	$f^{\dagger}_{8-20}$	HR[‡]	Counterpart[§]
100510	2010-05-10 19:27:42	355.43	-35.65	-84.07	0.729	1.271	0.674	0.530	J234154.4-355838(9), 100510810 (B:+0.00042, 1.29), 100510A (C:+0.00038, 0.30)
100516	2010-05-16 08:05:33	2.88	-50.80	-9.86	0.135	0.077	0.094	1.220	1RXS J002159.2-514028(5), AM 1(6), RXS J00141-5022(8)
100524	2010-05-24 10:18:05	106.34	+33.66	-12.16	0.137	0.117	0.047	0.403	
100611	2010-06-11 06:24:27	352.98	+40.95	-9.84	0.124	0.109	0.040	0.369	B3 2322+396(2, 8), 1ES 2321+419(5)
100611	2010-06-11 08:41:50	37.97	-36.66	-9.74	0.089	0.105	0.043	0.404	IC 1816(1), PKS 0227-369(2, 5), RXS J02375-3603(8), J023126.4-375831(9)
100708	2010-07-08 02:17:45	227.19	+28.34	-9.07	0.133	0.157	0.053	0.341	RBS 1467(5), RXS J15087+2709(8)
100712	2010-07-12 20:38:10	179.63	+74.33	-10.05	0.112	0.106	0.035	0.329	Mrk 205(1, 4, 7), AS Dra(3)
100720	2010-07-20 16:17:56	77.43	-15.70	-9.39	0.131	0.116	0.016	0.135	
100808	2010-08-08 19:50:49	329.96	+29.24	-9.41	0.148	0.134	0.074	0.555	
100813	2010-08-13 04:18:46	78.50	-39.92	-37.62	0.313	0.492	0.166	0.337	CXO J051406.4-400238(1), 4U 0513-40(2, 7), NGC1851(4), J052038.3-394517(9)
100823	2010-08-23 17:26:15	20.51	+5.82	-58.37	0.639	1.399	0.300	0.215	HD 8357(2), UV Psc(3), NGC 6934(6), 100823A (A:+0.00046, 0.19), 100823A (C:+0.00046, 0.19)
100829	2010-08-29 18:30:01	10.36	+11.26	-9.04	0.172	0.205	0.089	0.433	BK Psc(3), GB6 J0045+1217(5), Ko 1(6), J004401.5+093302(9)
100907	2010-09-07 18:25:49	161.17	-33.97	-11.17	0.180	0.306	0.041	0.134	J104230.3-334014(9)
101019	2010-10-19 16:16:12	337.38	-12.13	-9.92	0.140	0.144	0.053	0.365	Mrk 915(1, 7), PKS 2223-114(8)
101020	2010-10-20 16:06:02	346.18	-58.22	-10.12	0.115	0.119	0.072	0.602	2MASX J23013626-5913210(1), 2MASX J23013626-5913210(4), CP Tuc(7), J225725.9-564544(9)
101025	2010-10-25 05:09:27	36.82	-4.07	-9.19	0.113	0.155	0.013	0.085	
101030	2010-10-30 13:55:11	29.19	-35.68	-9.64	0.105	0.087	0.041	0.474	ESO 354- G 004(1), J020118.8-370457(9)
101102	2010-11-02 16:30:41	4.14	-56.24	-9.02	0.097	0.111	0.057	0.511	PMN J0019-5641(5), NGC 1261(6)
101108	2010-11-08 21:25:07	308.06	+74.62	-9.24	0.125	0.058	0.107	1.834	4C +74.26(1, 4, 7), VW Cep(2), S5 2023+760(5), S5 2023+76(8)
101111	2010-11-11 07:19:06	278.15	+22.83	-15.17	0.228	0.404	0.092	0.227	
101208	2010-12-08 15:50:38	332.63	-62.74	-10.87	0.131	0.124	0.069	0.559	J222312.0-623555(9)
101220	2010-12-20 13:39:46	78.38	+73.65	-9.37	0.131	0.113	0.047	0.413	GB6 J0516+7350(5)
110106	2011-01-06 18:08:11	56.77	-1.84	-9.67	0.139	0.096	0.087	0.907	QSO B0336-0156(2), PKS 0336-01(5), SDSS J03440-0000(8), HIP17695(10)
110110	2011-01-10 09:18:45	79.11	-40.22	-14.03	0.217	0.362	0.106	0.294	CXO J051406.4-400238(1), 4U 0513-40(2, 7), NGC1851(4), J052038.3-394517(9), HD35650(10)

TABLE A.1: (Continued)

Name	Time (UT)	R.A. (°)	Dec. (°)	P^*_{null}	$f^\dagger_{4-10}$	$f^\dagger_{2-8}$	$f^\dagger_{8-20}$	HR‡	Counterpart§
110113	2011-01-13 06:41:51	353.27	+19.81	-19.20	0.247	0.378	0.116	0.308	EQ Peg(2, 3)
110115	2011-01-15 01:56:43	90.36	-54.07	-9.00	0.128	0.085	0.133	1.568	TY Pic(3)
110116	2011-01-16 20:09:21	342.06	+24.53	-9.20	0.141	0.135	0.058	0.427	BZB J2255+2410(5)
110117	2011-01-17 22:03:34	313.04	-14.73	-9.74	0.095	0.104	0.010	0.093	
110122	2011-01-22 23:07:10	6.64	+29.18	-9.72	0.156	0.085	0.100	1.172	RXC J0020.6+2840(4), RBS 0042(5), RXS J00184+2947(8)
110123	2011-01-23 09:48:28	312.31	-67.36	-9.06	0.085	0.063	0.075	1.184	
110209	2011-02-09 19:48:48	226.36	-25.52	-9.27	0.101	0.099	0.023	0.234	2FGL J1513.5-2546(5)
110215	2011-02-15 02:20:33	192.91	-16.81	-12.65	0.136	0.505	0.026	0.052	RXC J1257.1-1724(4), A1644(7)
110216	2011-02-16 11:28:47	106.52	+31.85	-10.78	0.208	0.183	0.054	0.296	
110219	2011-02-19 23:09:31	131.32	+44.48	-9.22	0.118	0.089	0.049	0.550	US 1889(8)
110221	2011-02-21 20:10:58	310.43	-31.90	-15.35	0.204	0.410	0.038	0.094	AT Mic(2, 7), 2MAXI J2037-306(4), J204151.2-322604(9)
110225	2011-02-25 04:20:19	195.97	+67.50	-9.06	0.134	0.095	0.090	0.956	
110308	2011-03-08 21:32:15	116.50	+3.41	-16.63	0.287	1.055	0.127	0.120	YZ CMi(2)
110313	2011-03-13 10:41:25	23.20	-2.58	-9.16	0.100	0.107	0.064	0.600	2MASX J01344565-0430134(1), FIRST J01271-0151(8)
110406	2011-04-06 20:22:43	241.91	+15.54	-10.15	0.103	0.116	0.031	0.266	2MAXI J1602+161(4), 2FGL J1612.0+1403(5), A2147(7), PKS 1604+159(8)
110415	2011-04-15 23:46:39	182.73	-0.18	-9.01	0.095	0.142	0.061	0.430	PKS 1215-002(8)
110423	2011-04-23 07:17:25	122.17	-1.09	-9.13	0.127	0.149	0.001	0.006	2MASX J08045299-0108476(1), PKS B0802-010(5)
110426	2011-04-26 15:08:55	221.02	-10.46	-12.19	0.186	0.384	0.061	0.158	110426629 (B:+0.00172, 3.35), 110426A (C:+0.00022, 0.36)
110505	2011-05-05 12:22:07	169.39	-3.73	-10.53	0.148	0.235	0.076	0.324	
110525	2011-05-25 14:25:31	306.83	-14.89	-9.09	0.116	0.140	0.020	0.142	J202817.1-134829(9)
110525	2011-05-25 16:06:43	227.97	+9.47	-10.07	0.116	0.118	0.055	0.464	2FGL J1506.9+1052(5)
110528	2011-05-28 13:59:14	196.76	-18.26	-9.57	0.107	0.092	0.073	0.791	
110607	2011-06-07 17:47:13	260.37	+12.43	-9.38	0.098	0.114	0.038	0.336	QSO B1722+119(2), PKS 1725+123(5), H 1722+119(8)
110618	2011-06-18 06:26:57	242.17	-76.54	-9.65	0.104	0.135	0.024	0.176	RXC J1601.7-7544(4), PKS 1610-77(5), CIZA J1601.7-7544(7), J163635.0-753603(9)
110620	2011-06-20 12:13:49	73.74	-58.04	-9.04	0.175	0.189	0.061	0.322	RBS 594(1), 2MAXI J0451-585(4), J050046.6-571511(9)
110624	2011-06-24 00:32:52	11.35	-36.85	-9.25	0.124	0.152	0.061	0.398	PKS 0042-373(5), Pyxis(6)
110625	2011-06-25 01:08:42	17.66	-29.00	-9.05	0.116	0.100	0.055	0.549	NGC 6715(6), 2QZ J011332-2956(8), J011240.6-291041(9)
110704	2011-07-04 17:58:34	200.71	+84.41	-11.24	0.111	0.094	0.044	0.469	S5 1322+83(5)
110726	2011-07-26 21:56:59	87.21	+83.64	-10.24	0.130	0.100	0.047	0.468	S5 0454+84(8)
110805	2011-08-05 17:46:09	154.00	-21.45	-9.25	0.141	0.231	-0.020	-0.085	

TABLE A.1: (Continued)

Name	Time (UT)	R.A. (°)	Dec. (°)	$P^*_{\rm null}$	$f^\dagger_{4-10}$	$f^\dagger_{2-8}$	$f^\dagger_{8-20}$	HR‡	Counterpart§
110826	2011-08-26 07:12:20	61.35	-20.02	-9.39	0.121	0.150	0.046	0.303	
110826	2011-08-26 21:10:41	114.25	-66.51	-10.34	0.173	0.173	0.096	0.552	EXO 0748-676(1, 2, 7), PMN J0730-6602(5), J075407.7-654137(9)
110828	2011-08-28 21:30:37	167.43	-5.44	-10.92	0.176	0.089	0.159	1.782	2MAXI J1108-056(4), HD96064(10)
110831	2011-08-31 08:35:42	4.59	-61.26	-9.22	0.131	0.140	0.089	0.635	J002406.7-621100(9)
110902	2011-09-02 17:38:14	312.43	-32.14	-14.15	0.203	0.281	0.096	0.341	AT Mic(2, 7), 2MAXI J2043-324(4), J204151.2-322604(9)
110907	2011-09-07 12:04:43	122.89	+8.53	-9.85	0.142	0.116	0.059	0.508	1WGA J0814.3+0858(8), BD+07_1919B(10)
110924	2011-09-24 21:07:42	287.18	-70.15	-9.34	0.142	0.120	0.085	0.707	2FGL J1902.7-7053(5)
111005	2011-10-05 15:17:34	236.35	-35.21	-13.34	0.164	0.168	0.098	0.580	J154513.6-341733(9)
111010	2011-10-10 00:27:13	7.09	+18.81	-9.43	0.150	0.205	0.048	0.232	
111015	2011-10-15 09:44:53	14.16	-15.21	-9.18	0.109	0.156	-0.003	-0.020	
111021	2011-10-21 03:55:46	323.98	+24.36	-9.47	0.121	0.098	0.028	0.283	2FGL J2132.5+2605(5), HIP106231(10)
111024	2011-10-24 07:22:09	221.97	+25.87	-144.57	1.197	2.713	0.441	0.163	2MASX J14530794+2554327(1), PKS 1441+25(5), TEX 1451+270(8), 111024A (C:+0.00049, 0.04)
111106	2011-11-06 22:02:15	28.19	-64.26	-11.08	0.153	0.132	0.082	0.619	J020212.0-623532(9)
111113	2011-11-13 14:44:43	213.05	-10.71	-10.21	0.100	0.092	0.043	0.472	2MASX J14165001-1158577(1), 1RXS J141650.6-115845(7)
111121	2011-11-21 05:03:45	4.54	-38.46	-9.50	0.120	0.089	0.086	0.967	PKS 0010-401(5), NGC 1851(6), PKS 0010-401(8)
111204	2011-12-04 10:54:07	156.90	+60.35	-9.43	0.095	0.116	0.036	0.314	S4 1030+61(2, 5), FG Uma(3), TEX 1015+594(8)
111212	2011-12-12 01:50:04	46.59	+30.11	-9.47	0.105	0.090	0.040	0.450	
111212	2011-12-12 05:08:08	359.22	+28.91	-10.23	0.138	0.343	0.005	0.015	2MASX J00032742+2739173(1), II Peg(2, 3, 7), 2MAXI J2354+286(4)
111229	2011-12-29 07:04:08	54.71	+0.44	-22.67	0.299	0.516	0.127	0.246	HR 1099(2, 3, 4, 7), SDSS J03440-0000(8)
111229	2011-12-29 08:36:34	54.10	-0.21	-10.75	0.155	0.230	0.035	0.150	HR 1099(2, 3, 4, 7), PKS 0336-01(5), SDSS J03440-0000(8)
111230	2011-12-30 09:23:16	38.68	-43.41	-16.00	0.160	0.329	0.026	0.078	CC Eri(2, 3), RXC J0232.2-4420(4), RBS 0318(5), J023423.0-434739(9)
120122	2012-01-22 22:45:02	232.79	+67.47	-10.23	0.129	0.131	0.050	0.379	
120131	2012-01-31 05:04:41	163.32	+4.09	-9.94	0.098	0.116	0.049	0.424	RXS J10561+0252(8)
120202	2012-02-02 14:20:05	95.39	+51.56	-9.23	0.161	0.117	0.097	0.827	
120207	2012-02-07 09:40:02	223.57	+65.16	-9.07	0.134	0.133	0.041	0.305	EK Dra(2), RXS J14514+6354(8), HD129333(10)
120208	2012-02-08 06:10:24	291.13	-18.39	-10.87	0.148	0.182	0.060	0.330	SWIFT J1922.7-1716(1, 2, 4), 1H 1914-194(5), TEX 1914-193(8)
120213	2012-02-13 10:08:17	33.57	-8.75	-9.66	0.148	0.178	0.051	0.286	ARP 318(1), PKS 0214-085(5), SDSS J02195-0750(8)

TABLE A.1: (Continued)

Name	Time (UT)	R.A. (°)	Dec. (°)	P^{*}_{null}	$f^{\dagger}_{4-10}$	$f^{\dagger}_{2-8}$	$f^{\dagger}_{8-20}$	HR‡	Counterpart§
120307	2012-03-07 12:47:31	184.68	-22.37	-9.29	0.105	0.082	0.055	0.669	UV Crv(3), J121814.7-205028(9)
120310	2012-03-10 06:50:06	53.95	-0.09	-14.61	0.208	0.248	0.064	0.257	HR 1099(2, 3, 4, 7), PKS 0336-01(5), SDSS J03359-0024(8)
120310	2012-03-10 08:22:24	54.19	+0.21	-11.95	0.194	0.429	0.079	0.185	HR 1099(2, 3, 4, 7), SDSS J03440-0000(8)
120310	2012-03-10 09:54:49	54.61	+0.49	-13.48	0.223	0.408	0.004	0.010	HR 1099(2, 3, 4, 7), SDSS J03440-0000(8)
120325	2012-03-25 11:20:52	330.84	+1.16	-9.35	0.151	0.181	0.025	0.138	PMN J2206-0031(5), J220028.6+011259(9)
120416	2012-04-16 19:33:52	98.65	+65.67	-9.69	0.138	0.162	0.027	0.168	VII Zw 073(1)
120419	2012-04-19 17:38:06	310.33	-30.93	-9.87	0.142	0.214	0.004	0.018	AT Mic(2, 7), 2MAXI J2037-306(4), J204151.2-322604(9)
120424	2012-04-24 16:47:57	24.42	-29.86	-20.93	0.271	0.523	0.066	0.127	BB Scl(3), 2QZ J014542-3031(8), J013500.7-295430(9), 120424A (C:+0.00050, 0.38)
120517	2012-05-17 16:25:54	253.68	-7.76	-11.24	0.215	0.308	0.021	0.070	2FGL J1656.4-0738(5)
120529	2012-05-29 00:31:35	122.53	-63.98	-9.02	0.173	0.165	0.103	0.625	2MAXI J0827-642(4), 2FGL J0807.0-6511(5), J082141.7-634045(9)
120604	2012-06-04 08:27:22	215.12	+15.20	-9.95	0.198	0.167	0.091	0.542	
120608	2012-06-08 07:00:19	352.71	+38.13	-10.02	0.169	0.137	0.035	0.257	V455 And(2), NVSS J232914+375414(5)
120619	2012-06-19 08:59:40	207.17	+40.13	-9.69	0.174	0.213	0.053	0.250	NGC 5290(1), RGB J1341+399(2), RXS J13410+3959(8)
120622	2012-06-22 03:22:34	206.24	-1.95	-11.31	0.154	0.361	0.043	0.119	SDSS J13406-0148(8), 120622A (C:+0.00056, 0.84)
120701	2012-07-01 03:12:07	2.37	-25.41	-10.18	0.152	0.174	0.065	0.374	RBS 0016(5), NGC 288(6), RXS J00085-2339(8)
120702	2012-07-02 00:35:09	355.77	+17.72	-14.12	0.156	0.500	0.006	0.011	
120702	2012-07-02 02:15:48	11.20	-62.98	-9.69	0.110	0.068	0.061	0.894	2FGL J0048.8-6347(5), J003452.2-615506(9)
120804	2012-08-04 04:15:03	251.61	-23.31	-13.02	0.191	0.275	0.064	0.231	MAXI J1647-227(2), 2MAXI J1647-229(4), 2FGL J1645.7-2148c(5), J164527.9-250319(9)
120805	2012-08-05 02:30:31	78.55	-40.25	-47.65	0.533	0.859	0.220	0.256	CXO J051406.4-400238(1), 4U 0513-40(2, 7), NGC1851(4), J052038.3-394517(9)
120810	2012-08-10 11:38:46	319.60	-11.50	-10.25	0.132	0.126	0.023	0.179	NVSS J212035-125443(5), RXS J21231-1036(8), J211909.5-124642(9)
120927	2012-09-27 17:36:52	350.92	+3.96	-9.51	0.134	0.086	0.051	0.590	NGC 7679(1)
121011	2012-10-11 11:11:04	28.89	+36.53	-9.07	0.207	0.211	0.056	0.265	XX Tri(3), RXC J0152.7+3609(4)
121014	2012-10-14 16:27:29	124.91	+73.55	-9.32	0.081	0.112	0.024	0.216	2MAXI J0825+733(4), Z Cam(7)
121027	2012-10-27 08:13:07	63.38	-58.54	-15.11	0.193	0.364	0.224	0.614	1H 0419-577(7), J041155.1-580154(9), 121027A (A:+0.02822, 0.31)
121104	2012-11-04 03:26:42	326.99	-28.72	-9.41	0.165	0.159	0.066	0.416	PKS 2149-306(1, 4, 5), QSO B2149-306(2), A3814(7), 2QZ J215200-2823(8), J214023.7-280433(9)
121218	2012-12-18 09:08:15	171.77	-12.25	-9.74	0.135	0.039	0.087	2.235	2MASX J11315154-1231587(1)

TABLE A.1: (Continued)

Name	Time (UT)	R.A. (°)	Dec. (°)	P^{*}_{null}	$f^{\dagger}_{4-10}$	$f^{\dagger}_{2-8}$	$f^{\dagger}_{8-20}$	HR[‡]	Counterpart[§]
130102	2013-01-02 04:42:29	309.07	-72.36	-57.77	0.439	0.780	0.228	0.292	2MAXI J2043-714(4), 2FGL J2042.8-7317(5), 130102B (C:+0.00054, 0.16)
130106	2013-01-06 12:13:12	324.29	-77.84	-14.57	0.160	0.195	0.109	0.557	J205919.2-781048(9)
130123	2013-01-23 07:34:58	8.70	-32.12	-10.10	0.132	0.111	0.028	0.251	J003308.1-320117(9)
130206	2013-02-06 05:22:27	307.94	-56.42	-9.52	0.217	0.218	0.069	0.315	2FGL J2039.8-5620(5), J203313.7-580625(9)
130226	2013-02-26 02:07:12	54.03	+1.06	-12.53	0.152	0.279	0.019	0.068	HR 1099(2, 3, 4, 7), SDSS J03359-0024(8)
130310	2013-03-10 12:55:36	179.80	-77.99	-9.40	0.157	0.203	-0.020	-0.098	J115941.8-760130(9)
130320	2013-03-20 01:27:56	95.29	-19.94	-9.25	0.126	0.091	0.074	0.815	PKS 0627-199(5, 8),
130325	2013-03-25 13:35:51	252.94	+65.63	-10.18	0.130	0.104	0.041	0.394	
130407	2013-04-07 23:37:24	248.23	+10.18	-14.75	0.216	0.311	0.098	0.315	130407A (C:+0.00027, 0.35)
130418	2013-04-18 00:51:11	325.78	-21.09	-9.06	0.131	0.103	0.055	0.535	RBS 1769(5), RXS J21388-2053(8)
130520	2013-05-20 14:59:38	163.57	-25.53	-9.08	0.126	0.087	0.113	1.295	NGC 3393(1), SHBL J10468-2535(8), J105604.3-265309(9)

[*] Logarithim of null hypothesis probability

[†] Unit of count $\mathrm{cm}^{-2}\ \mathrm{s}^{-1}$ in 4–10 keV, 2–8 keV and 8–20 keV

[‡] Hardness ratio between the fluxes in the 8–20 keV and 2–8 keV energy bands.

[§] Possible counterparts. Value in parentheses means catalog name including the source; (1) Swift-BAT 70-month, (2) Swift-BAT transient monitor list, (3) CAB, (4) GSC 37-month, (5) Fermi-LAT 2nd, (6) Globular Cluster, (7) RXTE, (8) VERON (blazar only), (9) SACY , (10) NYMG, (A) *Swift*-BAT GRB, (B) *Fermi*-GBM GRB, (C) GSC GRB. Two values following the alphabetical index of the GRB catalog are temporally and positionally difference between the transient and the GRB with the unit of day and degree, respectively.

Table A.2: List of GRBs detected by MAXI

Name	Time (UT)	R.A. (°)	Dec. (°)	Flux[*]	Detected ?
091012	2009-10-12 10:23:12	182.82	+63.37	0.38 ± 0.04	Y
091120	2009-11-20 04:34:40	226.81	−21.79	7.69 ± 0.23	N[†]
091201	2009-12-01 21:48:36	118.6	+16.6	0.47 ± 0.06	N[‡]
091230	2009-12-30 06:27:30	132.91	−53.88	0.27 ± 0.04	N[‖]
100315A	2010-03-15 17:13:40	74.95	−6.63	0.17 ± 0.03	N(−6.05)
100327	2010-03-27 17:08:15	346.03	+42.90	0.26 ± 0.03	Y
100415A	2010-04-15 03:44:57	7.48	−15.57	0.96 ± 0.11	Y
100510A	2010-05-10 19:27:09	355.8	−35.6	2.57 ± 0.19	Y
100616A	2010-06-16 01:42:13	50.95	−40.62	0.37 ± 0.05	N[†]
100701A	2010-07-01 06:54:28	188.86	−34.26	0.88 ± 0.09	N[†§]
100823A	2010-08-23 17:25:35	20.70	+5.84	1.85 ± 0.10	Y
100911	2010-09-11 14:58:20	103.41	−70.43	0.30 ± 0.03	N[#]
101117A	2010-11-17 07:32:59	89.63	−2.30	0.84 ± 0.09	N[‖]
101210	2010-12-10 03:38:27	61.66	−5.36	0.22 ± 0.03	N(−4.88)
110213B	2011-02-13 14:31:48	41.76	+1.15	7.53 ± 0.32	N[†]
110402	2010-04-02 02:34:07	62.52	−3.00	0.44 ± 0.05	N[†]
110426A	2011-04-26 15:08:36	221.18	−10.78	0.51 ± 0.06	Y
110916	2011-09-16 20:33:01	171.68	−17.77	0.27 ± 0.03	N[†]
111024A	2011-10-24 07:21:27	221.93	+25.87	2.76 ± 0.17	Y
120424A	2012-04-24 16:47:14	23.985	−29.87	0.47 ± 0.05	Y
120510A	2012-05-10 08:47:44	44.285	+72.850	1.52 ± 0.12	N[†]
120528B	2012-05-28 18:12:08	77.59	−37.80	1.28 ± 0.10	N[§]
120528C	2012-05-28 21:21:58	12.93	−0.95	0.32 ± 0.05	N(−3.53)

Table A.2: (Continued)

Name	Time (UT)	R.A. (°)	Dec. (°)	Flux*	Detected ?
120614A	2012-06-14 05:49:10	312.73	+65.16	0.96 ± 0.07	N#
120622A	2012-06-22 03:21:46	205.43	−1.71	0.45 ± 0.06	Y
120626B	2012-06-26 13:38:14	175.77	+68.50	0.31 ± 0.04	N(−5.83)
120711A	2012-07-11 02:45:12	94.703	−71.001	0.89 ± 0.09	N‖
120908A	2012-09-08 22:35:13	230.64	−25.79	0.18 ± 0.03	N(−8.91)
121025A	2012-10-25 07:46:30	248.75	+27.73	0.24 ± 0.04	N†
121209A	2012-12-09 21:59:11	327.02	−7.69	0.52 ± 0.06	N§
121229A	2012-12-29 05:00:21	190.10	−50.59	0.39 ± 0.05	N#
130102B	2013-01-02 04:41:42	309.58	−72.38	1.36 ± 0.11	Y
130407A	2013-04-07 23:37:01	248.10	+10.51	0.41 ± 0.05	Y

[*] X-ray flux cited from Serino [68] in the unit of 10^{-8} erg s^{-1} cm^{-2} in 2–20 keV.

[†] Occurred immediately after/before the HV on/off.

[‡] Detected by GSC 3.

[§] Detected at |BEX| < 20 or > 100 mm.

[‖] Detected near galactic plane or bright sources.

[#] Ignored because of lack of effective background area.

Appendix B

Event map, light curve and VETO curve

This appendix shows event maps, light curves and VETO count curves of all detected SXTs. The event map includes X-ray events around the SXT and regions to estimate the flux and P_{null} in our analysis. The black dashed box and blued frame are conrrespond to the region of foreground and background. The light curve is made from a projection of the event map whose width along the BEX coordinate is limited within the width of the foreground region. The time variability of the VETO counts is also shown. This count increases near the high background regions, i.e., at the high latitude and the South Atlantic Anomaly. If a SXT is accidentally triggered by the temporal fluctuaion of the background (charged paticles), the VETO count will consistently increase.

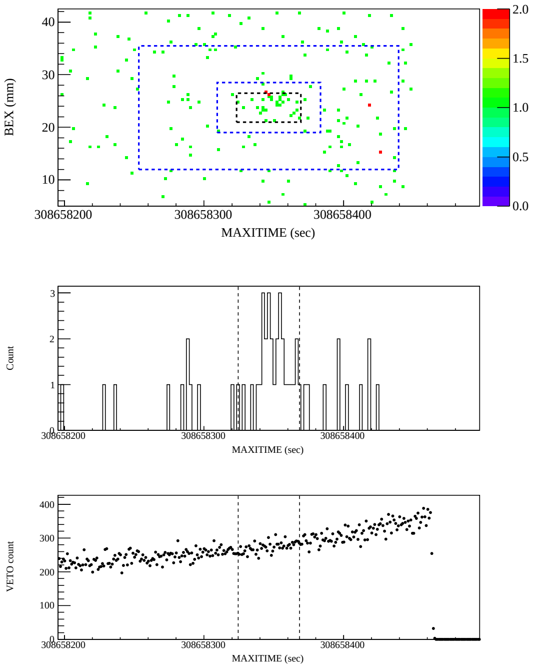

FIGURE B.1: Event map, light curve and VETO count time variability of SXT 091012 with $\log P_{\rm null} = -15.8$.

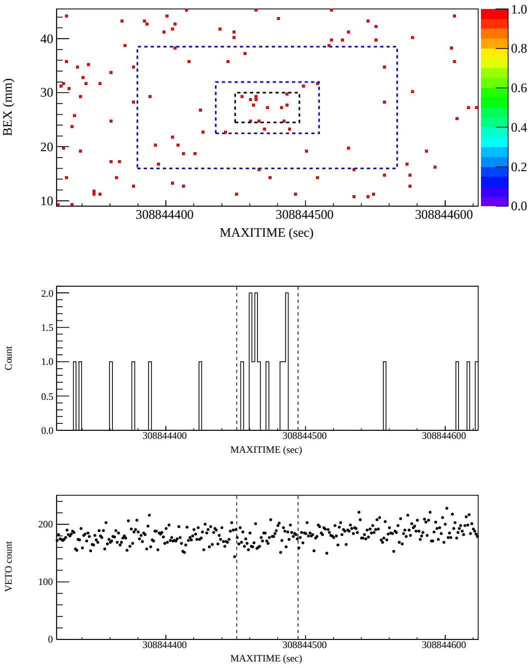

FIGURE B.2: Event map, light curve and VETO count time variability of SXT 091014 with $\log P_{\rm null} = -9.1$.

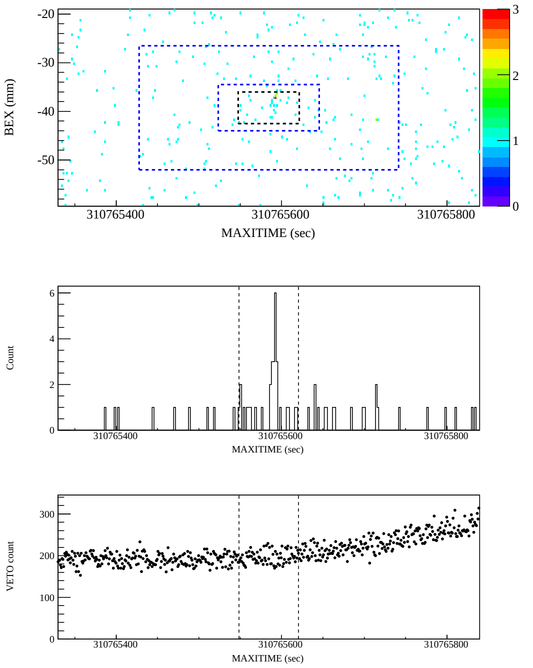

FIGURE B.3: Event map, light curve and VETO count time variability of SXT 091105 with $\log P_{\rm null} = -11.1$.

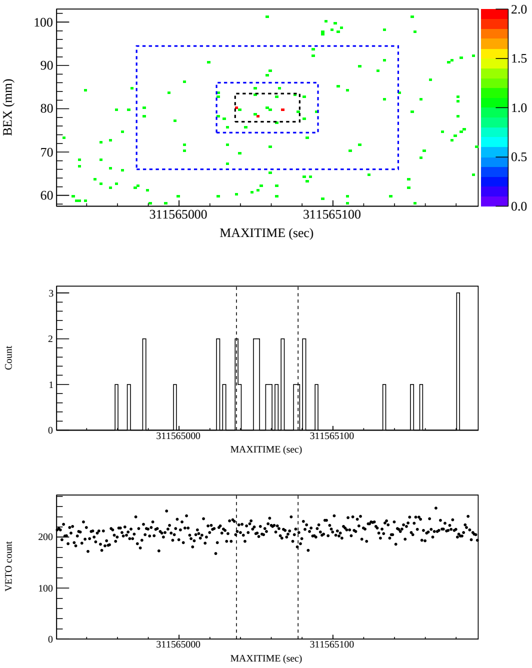

FIGURE B.4: Event map, light curve and VETO count time variability of SXT 091115 with $\log P_{\rm null} = -9.1$.

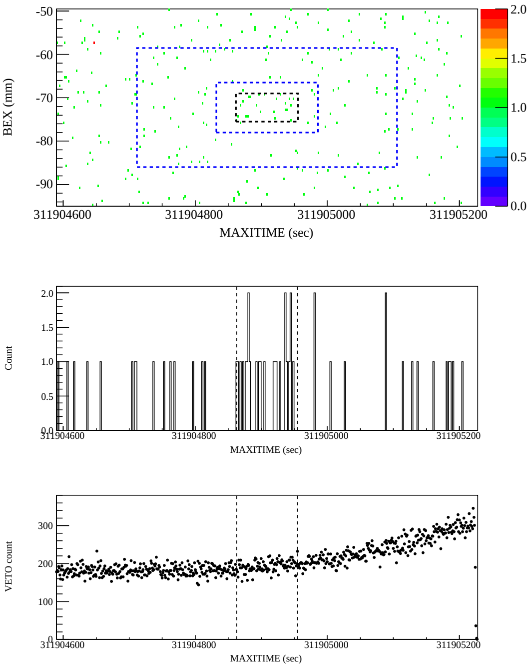

FIGURE B.5: Event map, light curve and VETO count time variability of SXT 091119 with $\log P_{\text{null}} = -9.2$.

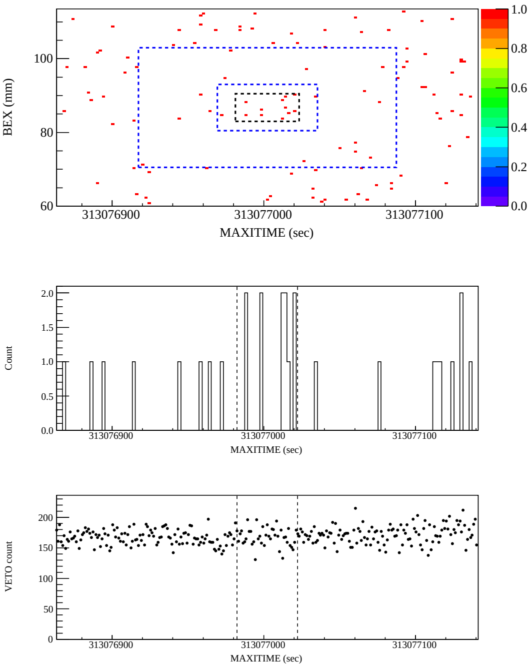

FIGURE B.6: Event map, light curve and VETO count time variability of SXT 091202 with $\log P_{\text{null}} = -9.1$.

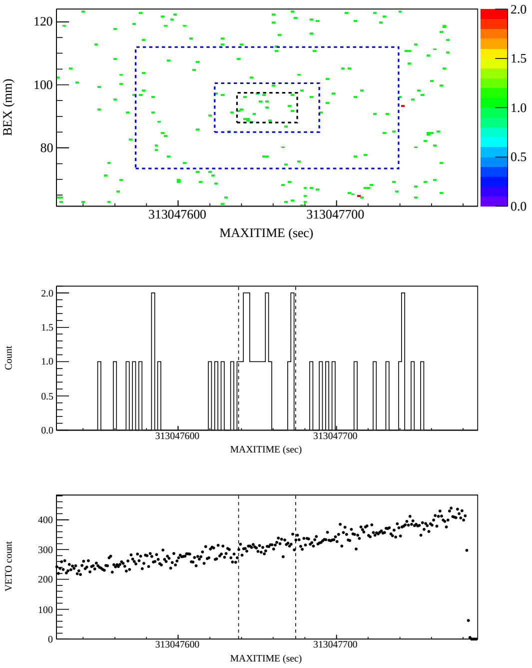

FIGURE B.7: Event map, light curve and VETO count time variability of SXT 091202 with $\log P_{\text{null}} = -9.0$.

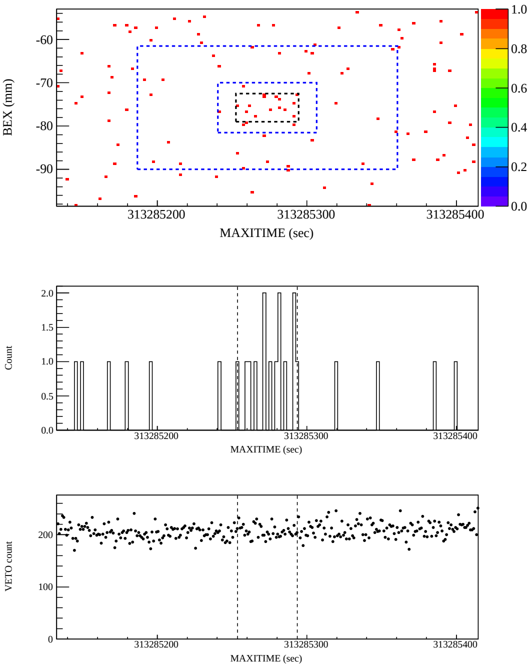

FIGURE B.8: Event map, light curve and VETO count time variability of SXT 091204 with $\log P_{\text{null}} = -9.4$.

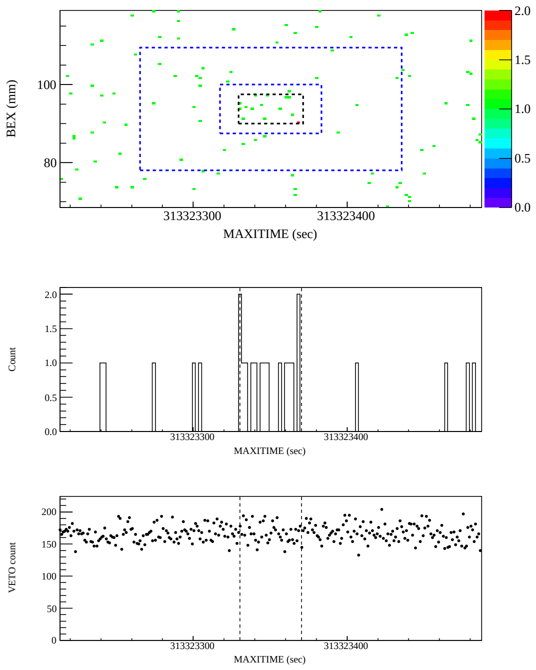

FIGURE B.9: Event map, light curve and VETO count time variability of SXT 091205 with log $P_{\rm null} = -11.3$.

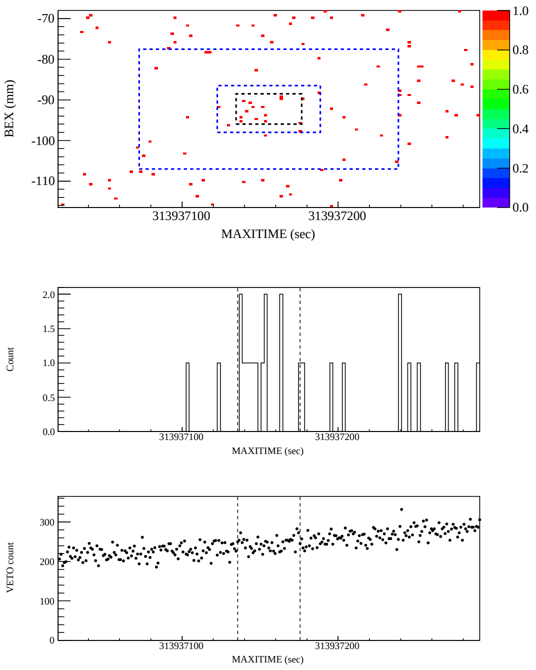

FIGURE B.10: Event map, light curve and VETO count time variability of SXT 091212 with log $P_{\rm null} = -9.3$.

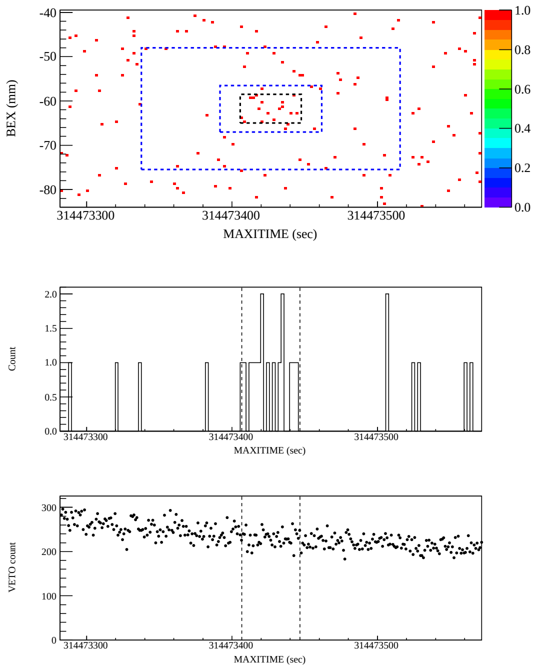

FIGURE B.11: Event map, light curve and VETO count time variability of SXT 091218 with log $P_{\rm null} = -10.4$.

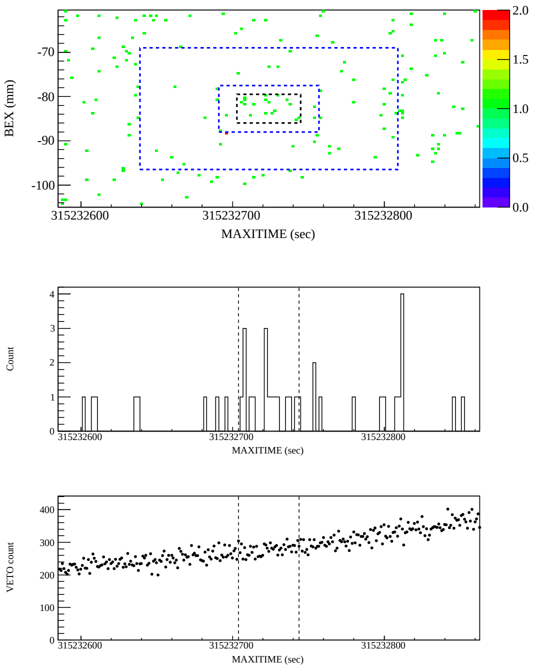

FIGURE B.12: Event map, light curve and VETO count time variability of SXT 091227 with log $P_{\rm null} = -9.8$.

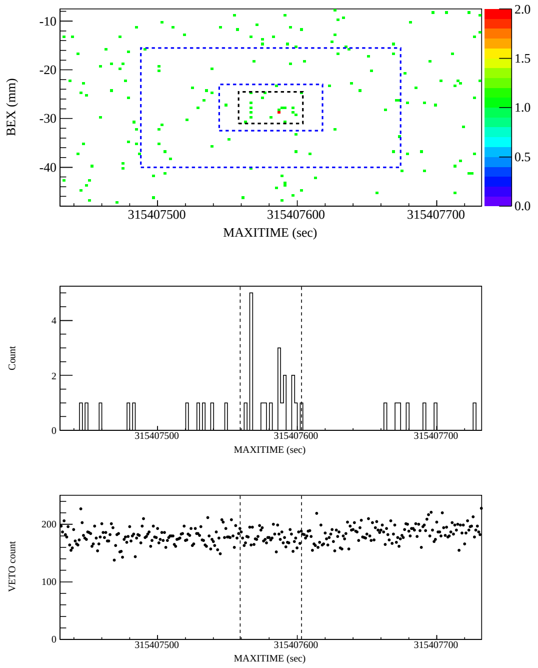

FIGURE B.13: Event map, light curve and VETO count time variability of SXT 091229 with log $P_{\mathrm{null}} = -10.4$.

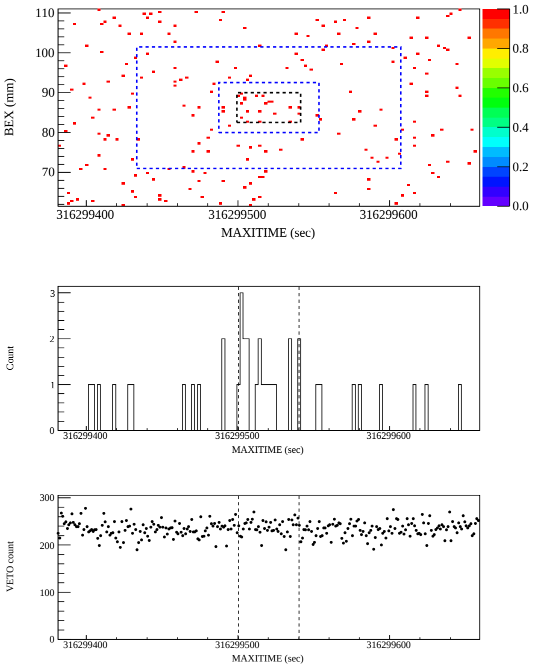

FIGURE B.14: Event map, light curve and VETO count time variability of SXT 100108 with log $P_{\mathrm{null}} = -9.1$.

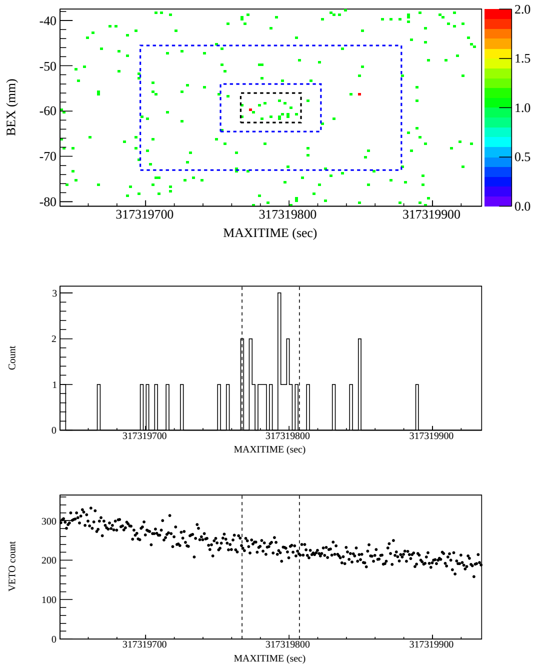

FIGURE B.15: Event map, light curve and VETO count time variability of SXT 100120 with log $P_{\mathrm{null}} = -9.1$.

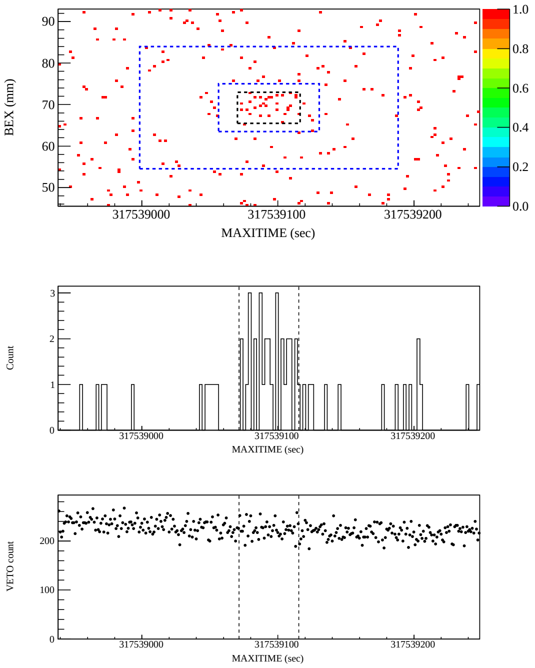

FIGURE B.16: Event map, light curve and VETO count time variability of SXT 100123 with log $P_{\mathrm{null}} = -16.1$.

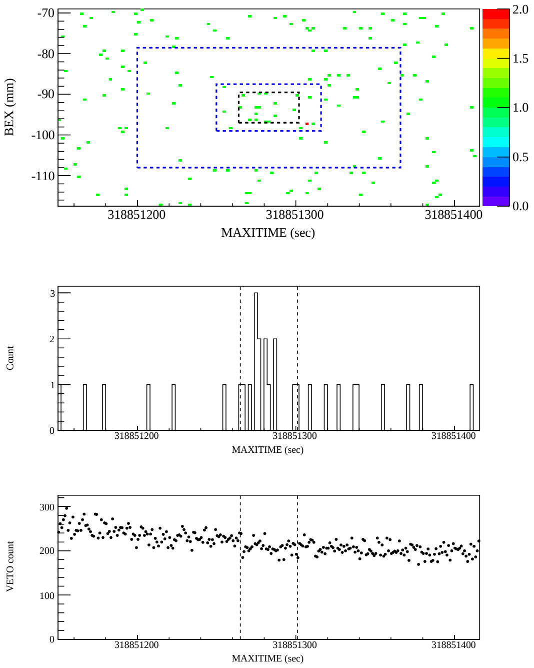

FIGURE B.17: Event map, light curve and VETO count time variability of SXT 100207 with $\log P_{\text{null}} = -9.1$.

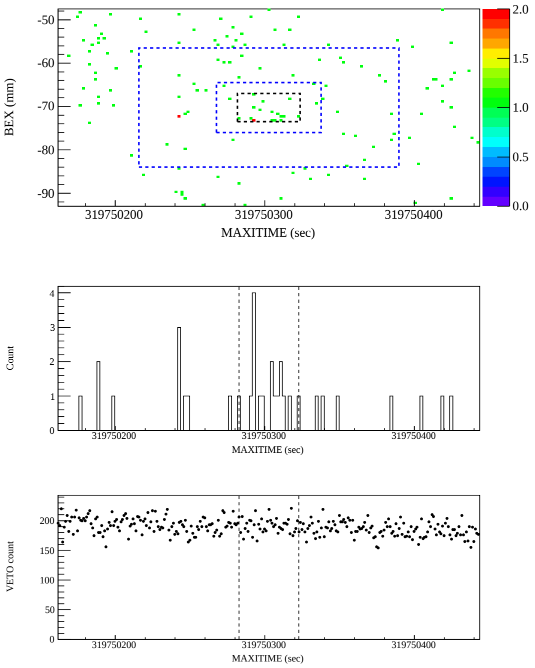

FIGURE B.18: Event map, light curve and VETO count time variability of SXT 100217 with $\log P_{\text{null}} = -9.6$.

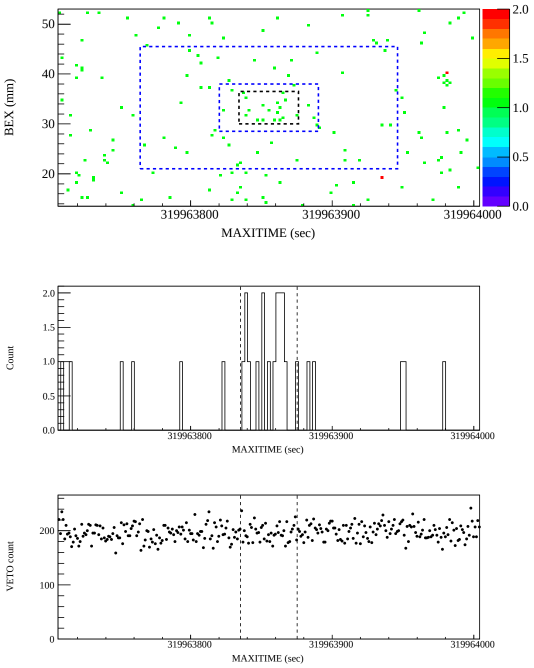

FIGURE B.19: Event map, light curve and VETO count time variability of SXT 100220 with $\log P_{\text{null}} = -9.2$.

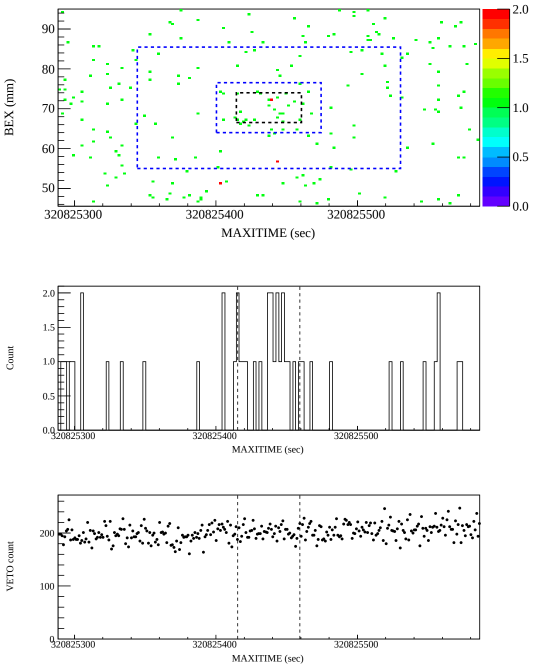

FIGURE B.20: Event map, light curve and VETO count time variability of SXT 100302 with $\log P_{\text{null}} = -11.3$.

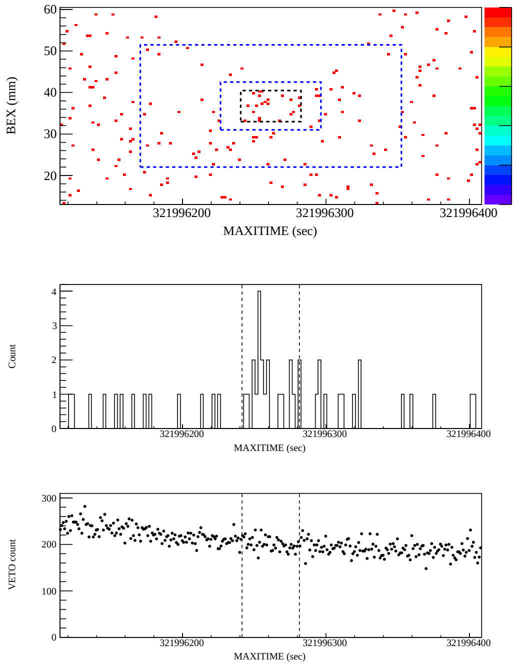

FIGURE B.21: Event map, light curve and VETO count time variability of SXT 100315 with $\log P_{\mathrm{null}} = -10.0$.

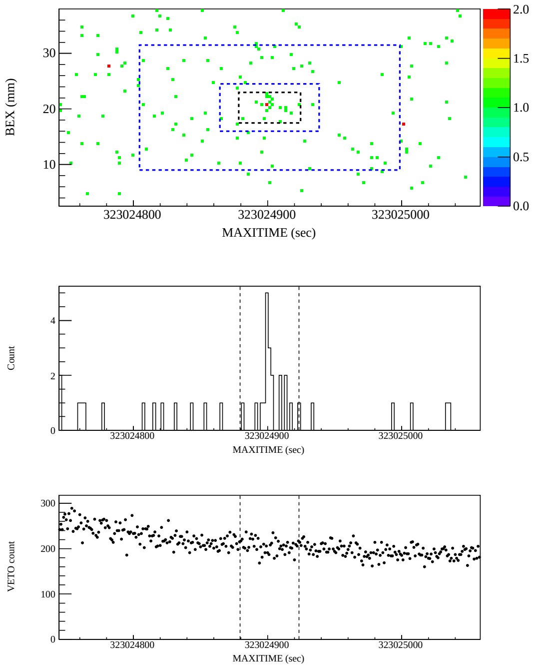

FIGURE B.22: Event map, light curve and VETO count time variability of SXT 100327 with $\log P_{\mathrm{null}} = -9.3$.

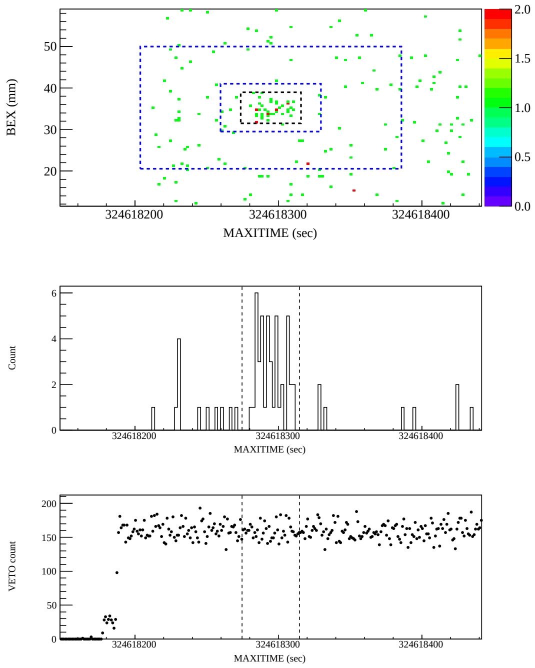

FIGURE B.23: Event map, light curve and VETO count time variability of SXT 100415 with $\log P_{\mathrm{null}} = -28.4$.

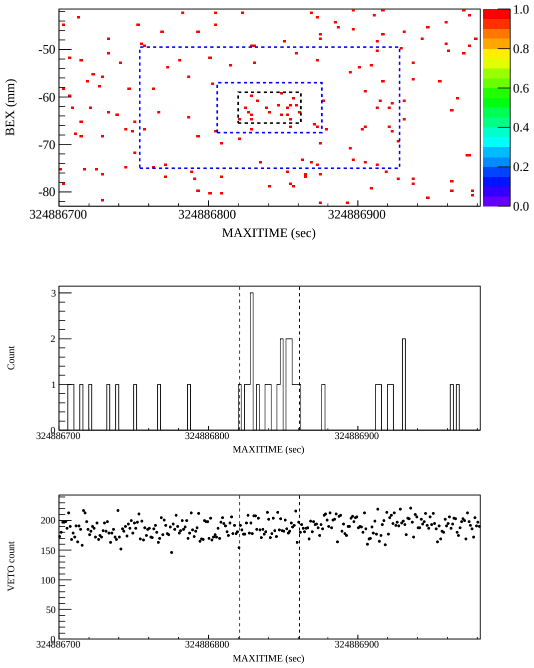

FIGURE B.24: Event map, light curve and VETO count time variability of SXT 100418 with $\log P_{\mathrm{null}} = -9.3$.

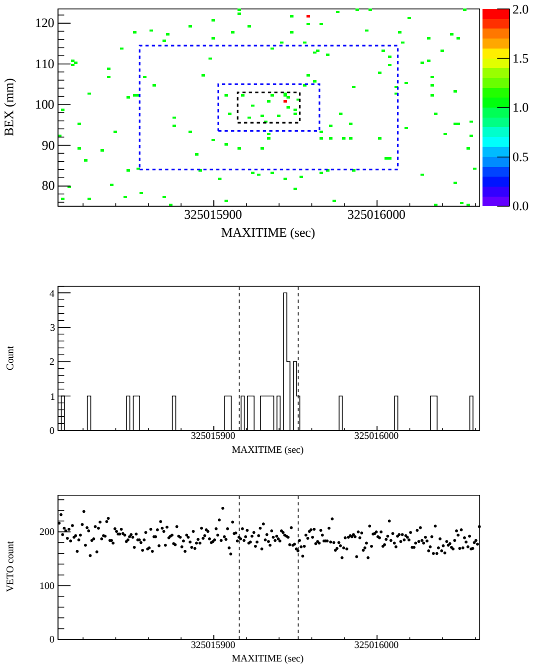

FIGURE B.25: Event map, light curve and VETO count time variability of SXT 100419 with $\log P_{\mathrm{null}} = -9.3$.

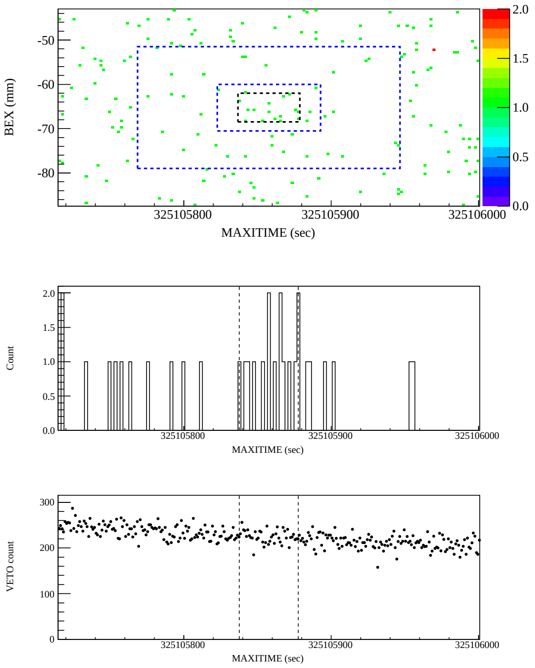

FIGURE B.26: Event map, light curve and VETO count time variability of SXT 100420 with $\log P_{\mathrm{null}} = -9.4$.

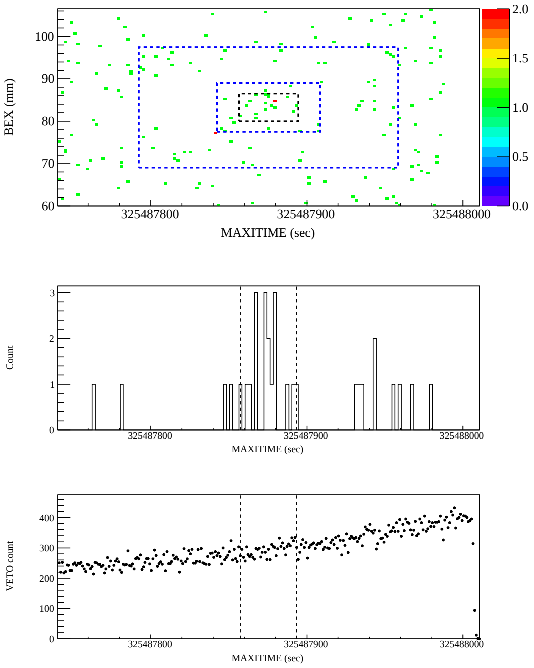

FIGURE B.27: Event map, light curve and VETO count time variability of SXT 100425 with $\log P_{\mathrm{null}} = -9.1$.

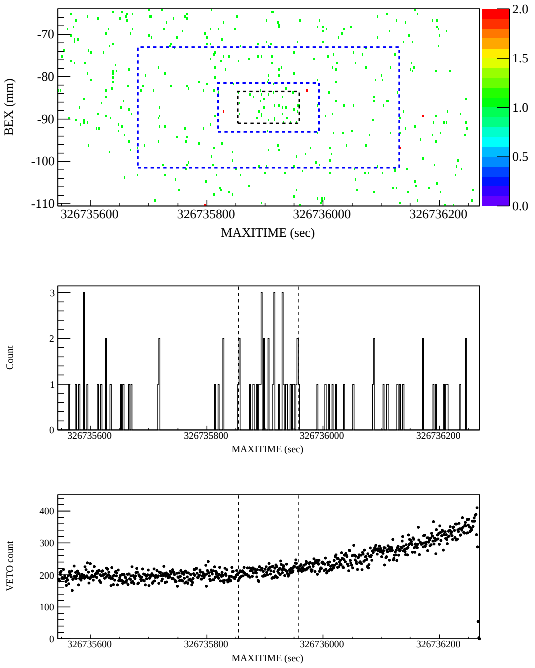

FIGURE B.28: Event map, light curve and VETO count time variability of SXT 100509 with $\log P_{\mathrm{null}} = -10.5$.

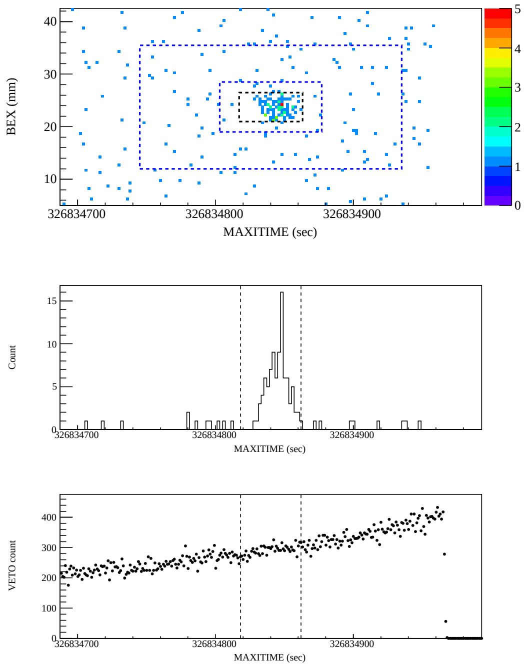

FIGURE B.29: Event map, light curve and VETO count time variability of SXT 100510 with $\log P_{\mathrm{null}} = -84.1$.

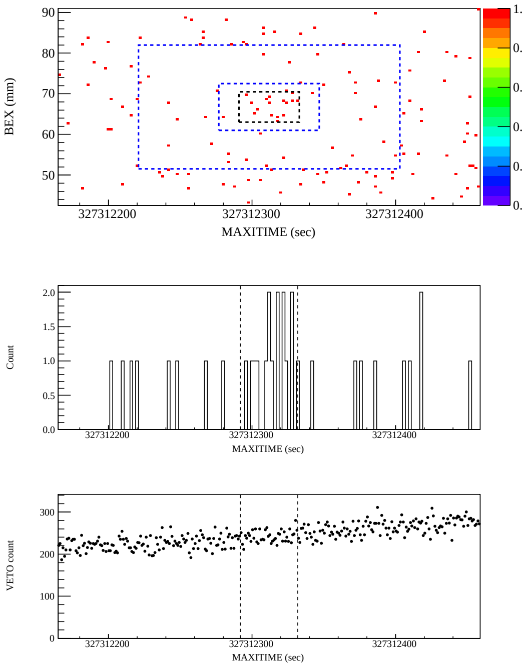

FIGURE B.30: Event map, light curve and VETO count time variability of SXT 100516 with $\log P_{\mathrm{null}} = -9.9$.

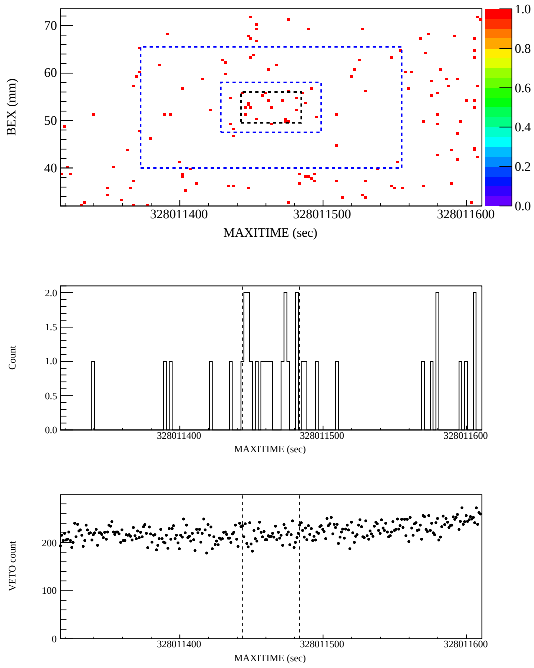

FIGURE B.31: Event map, light curve and VETO count time variability of SXT 100524 with $\log P_{\mathrm{null}} = -12.2$.

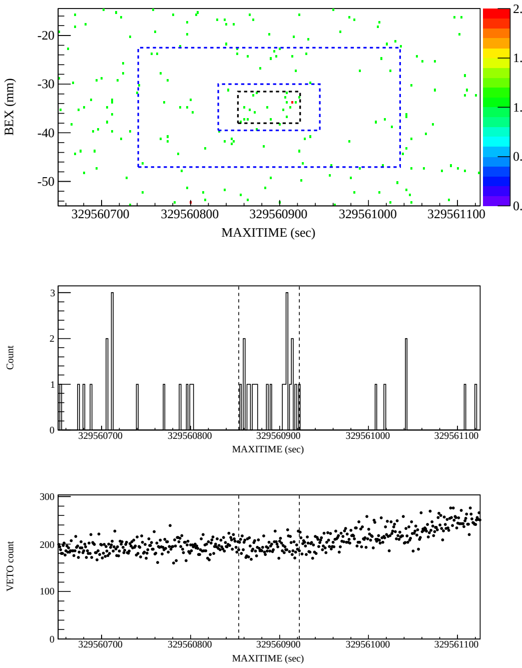

FIGURE B.32: Event map, light curve and VETO count time variability of SXT 100611 with $\log P_{\mathrm{null}} = -9.7$.

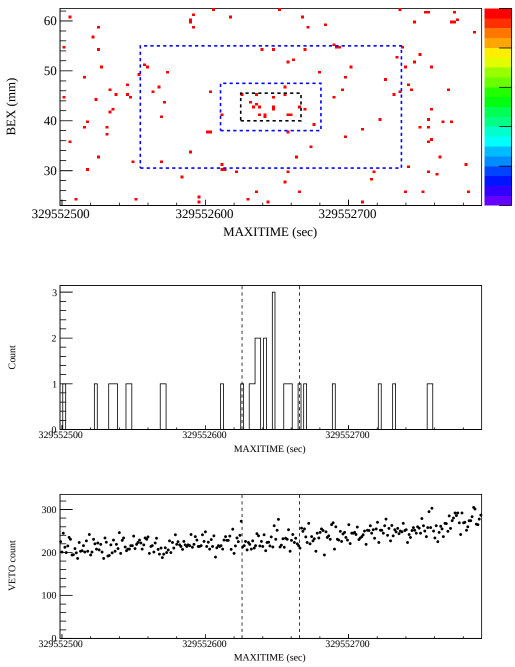

FIGURE B.33: Event map, light curve and VETO count time variability of SXT 100611 with log $P_{\mathrm{null}} = -9.8$.

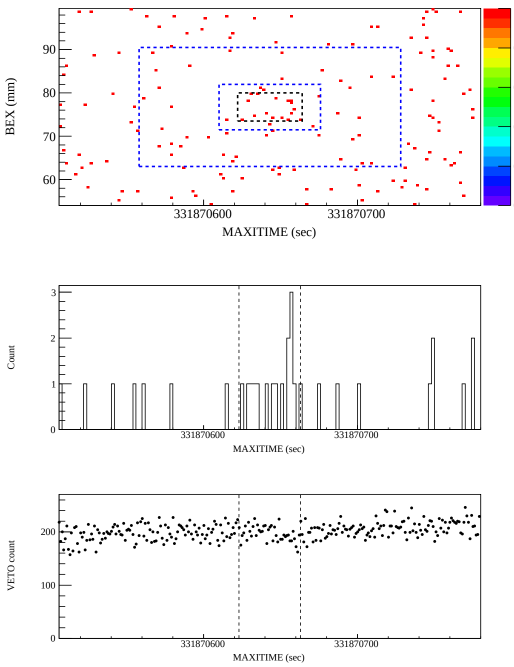

FIGURE B.34: Event map, light curve and VETO count time variability of SXT 100708 with log $P_{\mathrm{null}} = -9.1$.

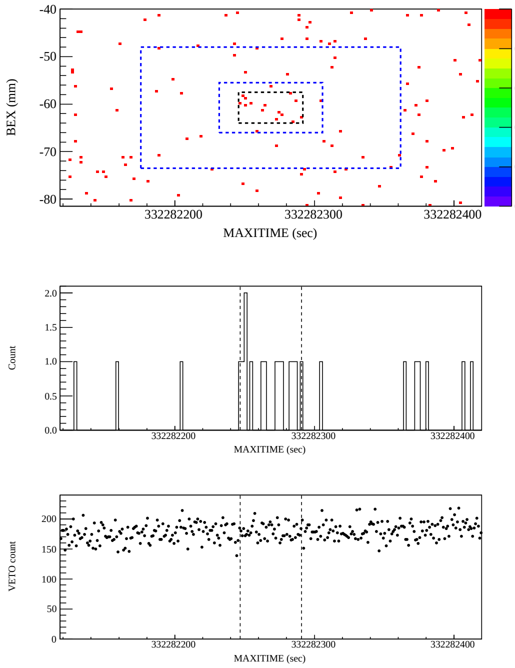

FIGURE B.35: Event map, light curve and VETO count time variability of SXT 100712 with log $P_{\mathrm{null}} = -10.1$.

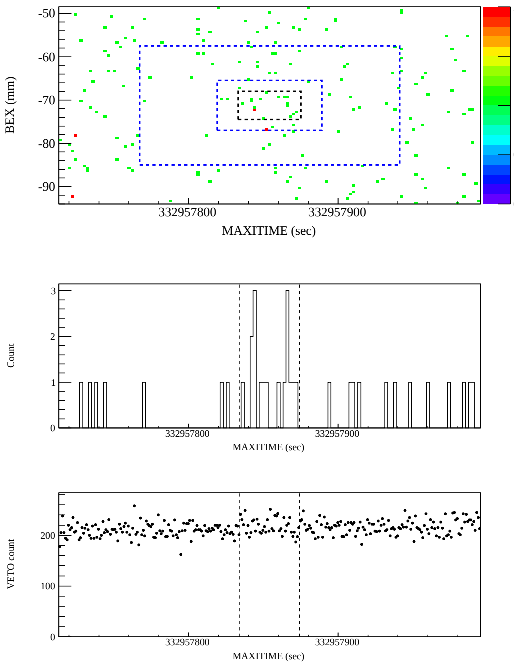

FIGURE B.36: Event map, light curve and VETO count time variability of SXT 100720 with log $P_{\mathrm{null}} = -9.4$.

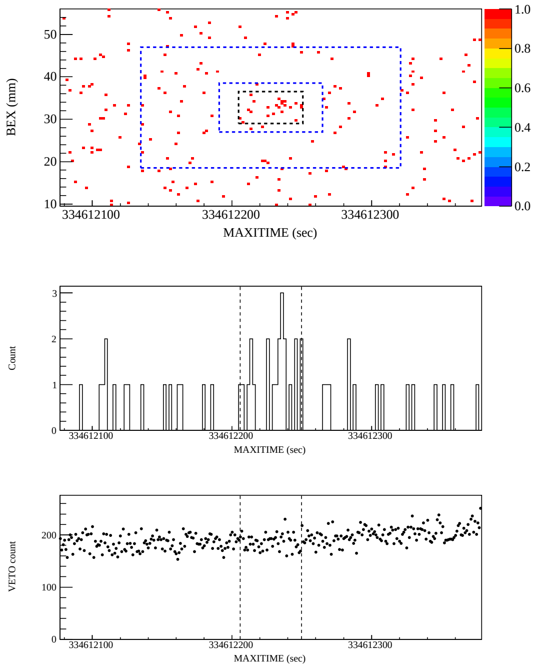

FIGURE B.37: Event map, light curve and VETO count time variability of SXT 100808 with $\log P_{\text{null}} = -9.4$.

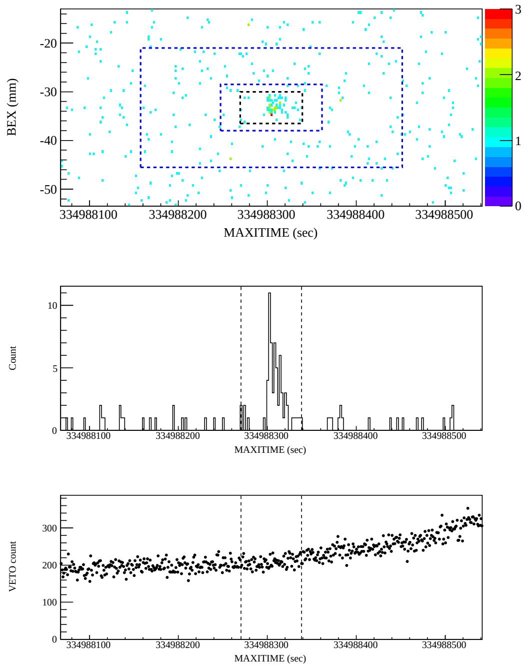

FIGURE B.38: Event map, light curve and VETO count time variability of SXT 100813 with $\log P_{\text{null}} = -37.6$.

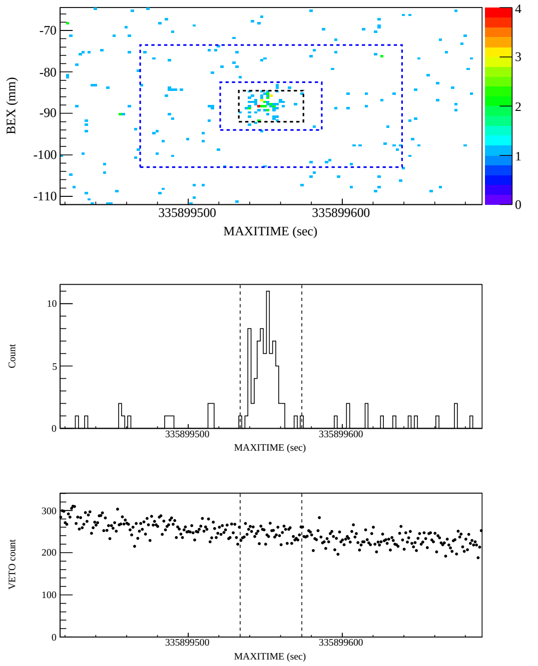

FIGURE B.39: Event map, light curve and VETO count time variability of SXT 100823 with $\log P_{\text{null}} = -58.4$.

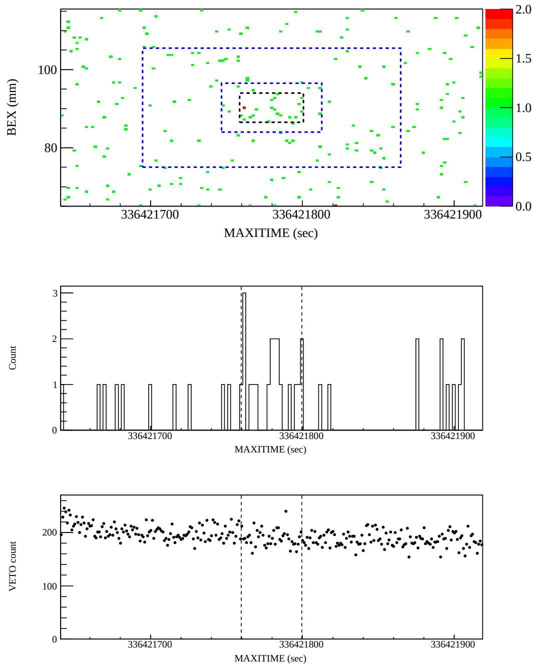

FIGURE B.40: Event map, light curve and VETO count time variability of SXT 100829 with $\log P_{\text{null}} = -9.0$.

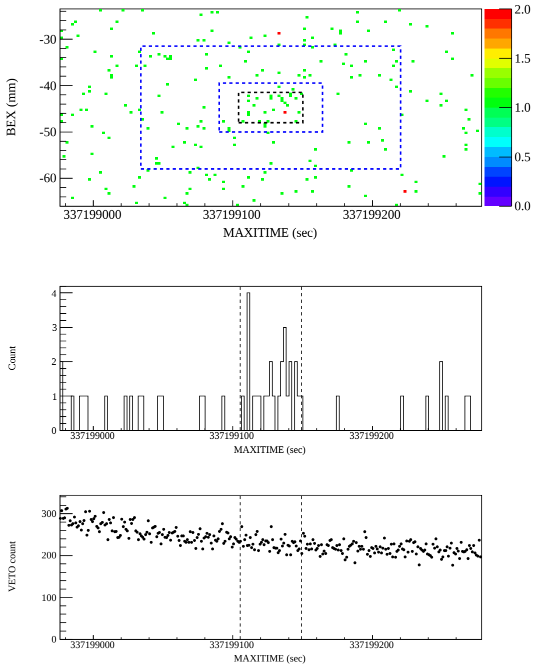

FIGURE B.41: Event map, light curve and VETO count time variability of SXT 100907 with $\log P_{\mathrm{null}} = -11.2$.

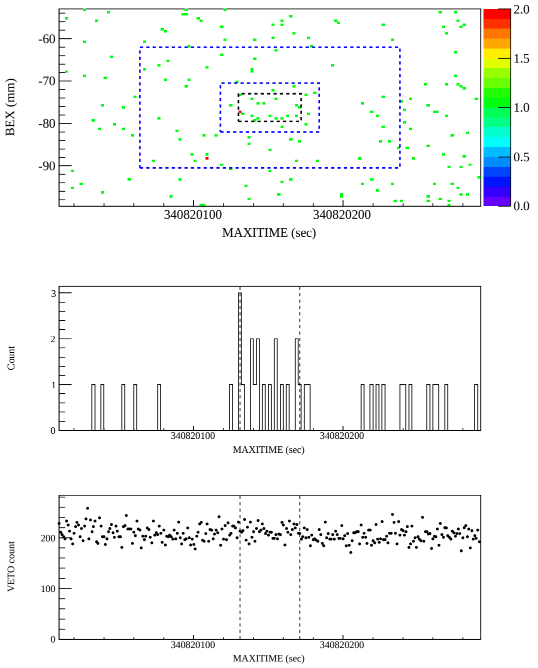

FIGURE B.42: Event map, light curve and VETO count time variability of SXT 101019 with $\log P_{\mathrm{null}} = -9.9$.

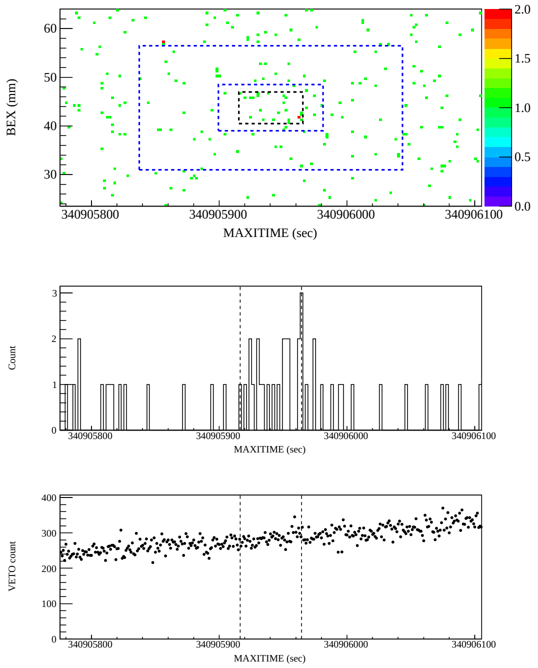

FIGURE B.43: Event map, light curve and VETO count time variability of SXT 101020 with $\log P_{\mathrm{null}} = -10.1$.

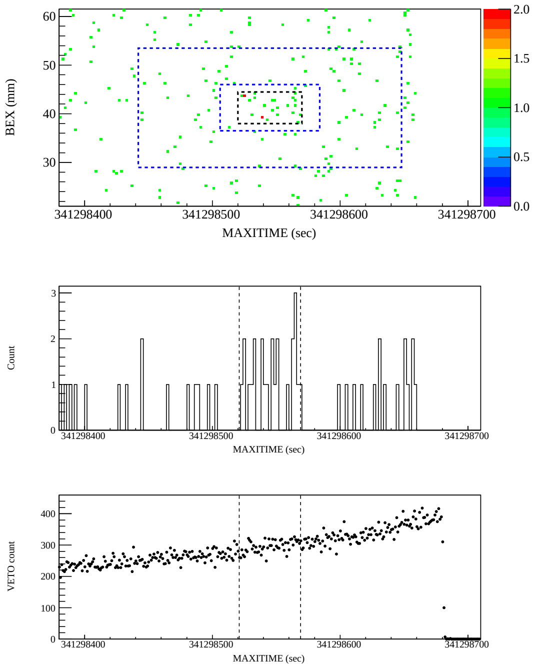

FIGURE B.44: Event map, light curve and VETO count time variability of SXT 101025 with $\log P_{\mathrm{null}} = -9.2$.

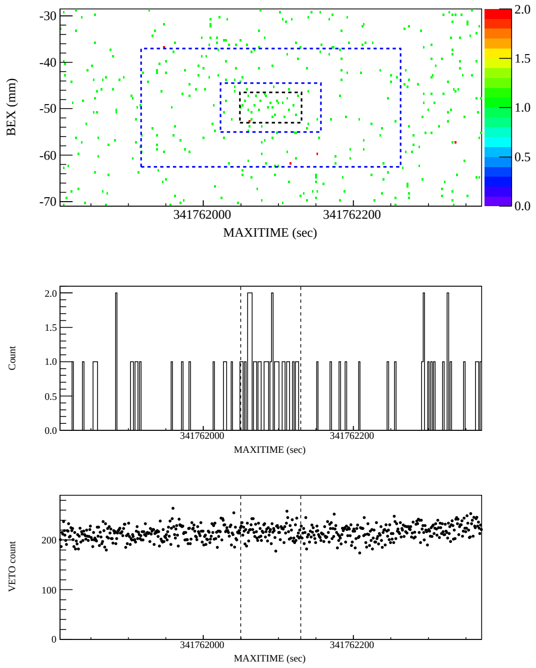

FIGURE B.45: Event map, light curve and VETO count time variability of SXT 101030 with $\log P_{\mathrm{null}} = -9.6$.

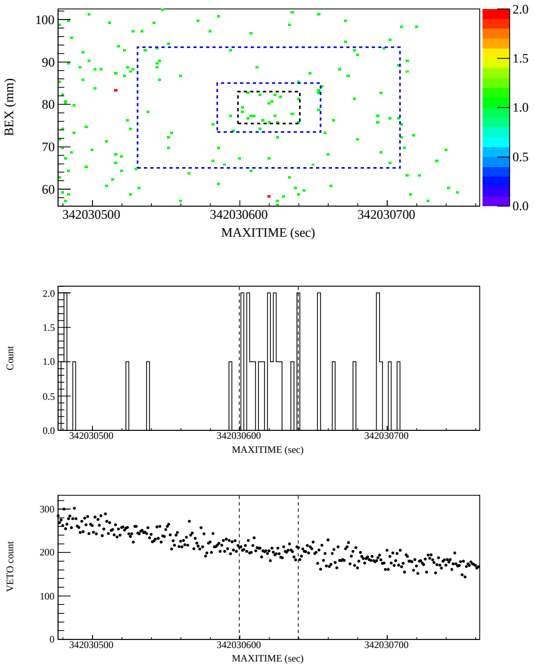

FIGURE B.46: Event map, light curve and VETO count time variability of SXT 101102 with $\log P_{\mathrm{null}} = -9.0$.

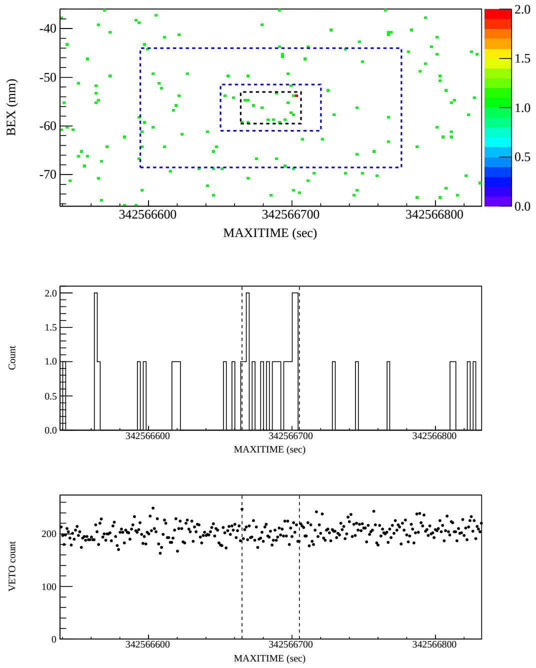

FIGURE B.47: Event map, light curve and VETO count time variability of SXT 101108 with $\log P_{\mathrm{null}} = -9.2$.

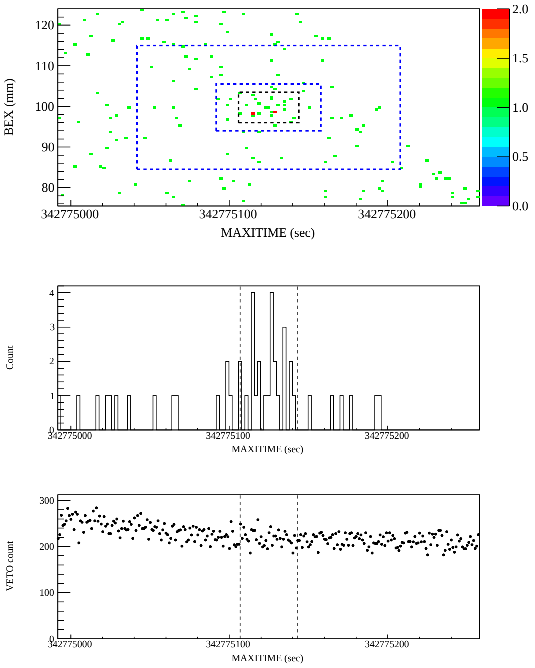

FIGURE B.48: Event map, light curve and VETO count time variability of SXT 101111 with $\log P_{\mathrm{null}} = -15.2$.

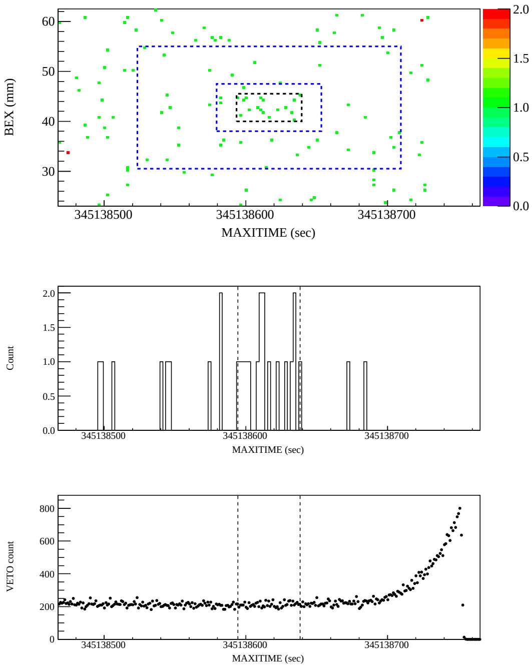

FIGURE B.49: Event map, light curve and VETO count time variability of SXT 101208 with $\log P_{\rm null} = -10.9$.

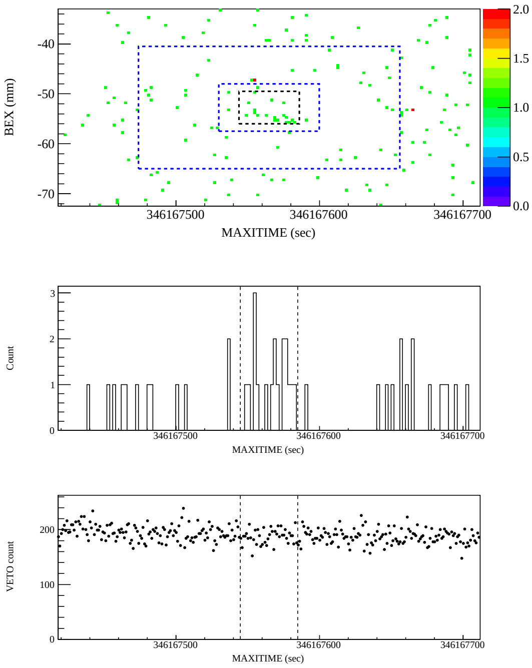

FIGURE B.50: Event map, light curve and VETO count time variability of SXT 101220 with $\log P_{\rm null} = -9.4$.

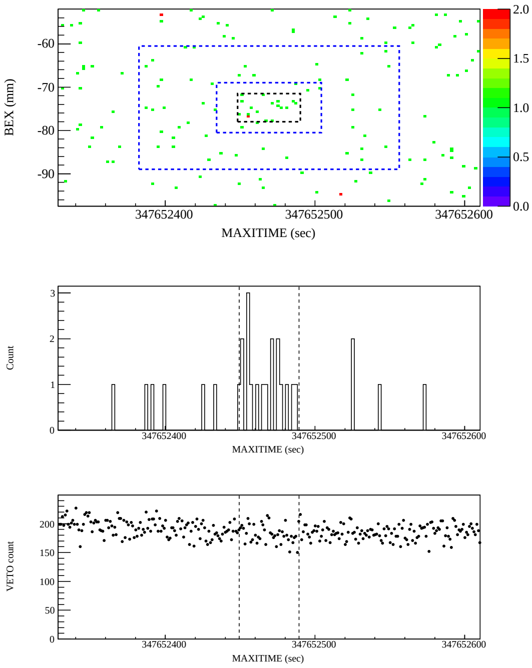

FIGURE B.51: Event map, light curve and VETO count time variability of SXT 110106 with $\log P_{\rm null} = -9.7$.

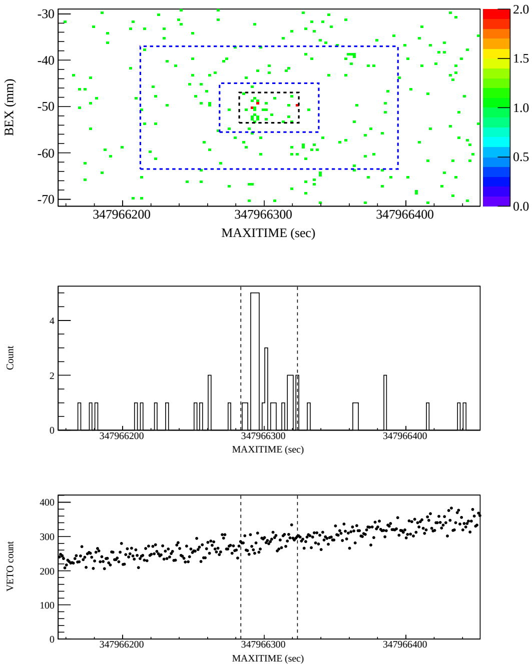

FIGURE B.52: Event map, light curve and VETO count time variability of SXT 110110 with $\log P_{\rm null} = -14.0$.

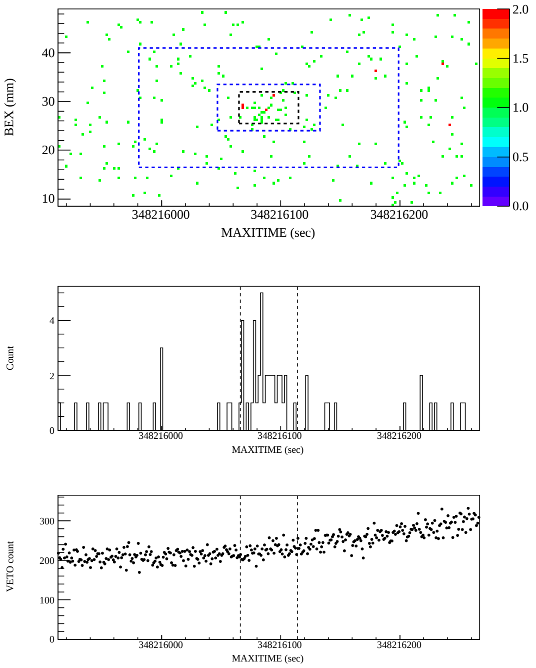

FIGURE B.53: Event map, light curve and VETO count time variability of SXT 110113 with $\log P_{\text{null}} = -19.2$.

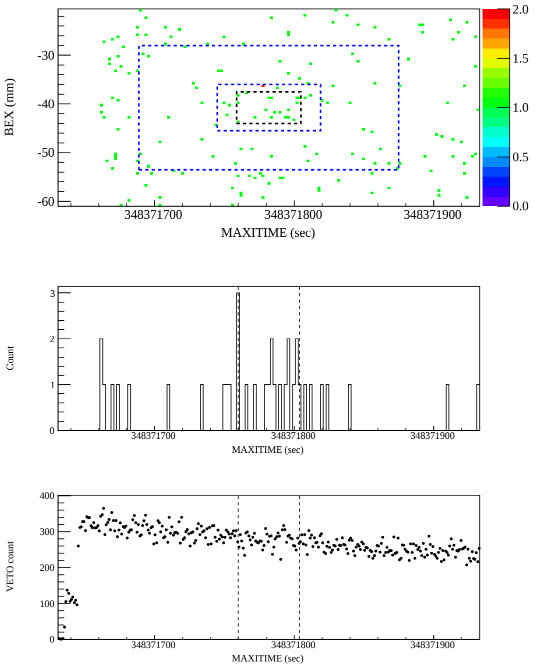

FIGURE B.54: Event map, light curve and VETO count time variability of SXT 110115 with $\log P_{\text{null}} = -9.0$.

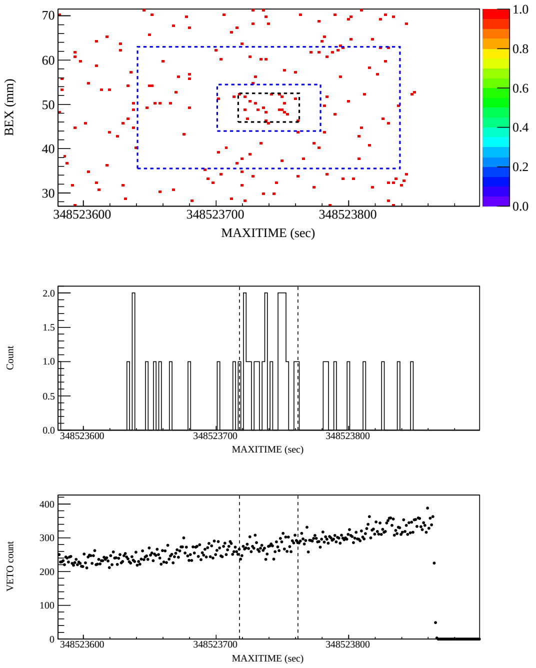

FIGURE B.55: Event map, light curve and VETO count time variability of SXT 110116 with $\log P_{\text{null}} = -9.2$.

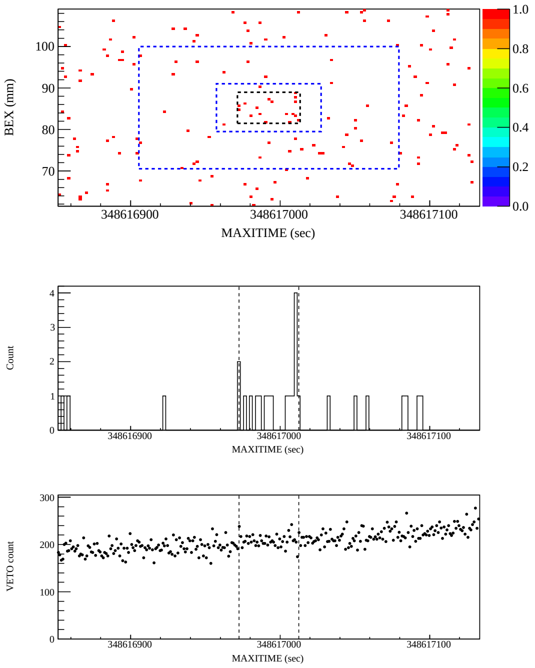

FIGURE B.56: Event map, light curve and VETO count time variability of SXT 110117 with $\log P_{\text{null}} = -9.7$.

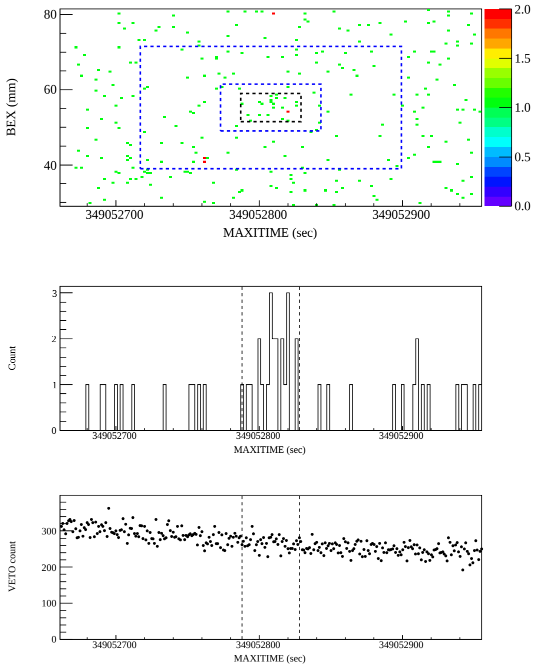

FIGURE B.57: Event map, light curve and VETO count time variability of SXT 110122 with $\log P_{\rm null} = -9.7$.

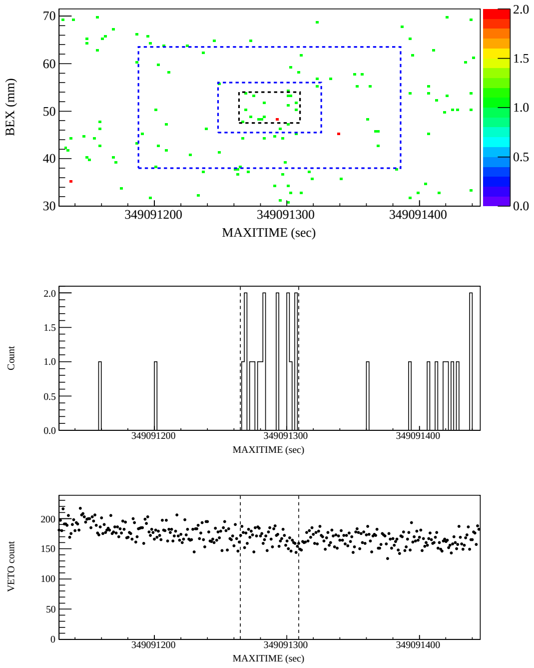

FIGURE B.58: Event map, light curve and VETO count time variability of SXT 110123 with $\log P_{\rm null} = -9.1$.

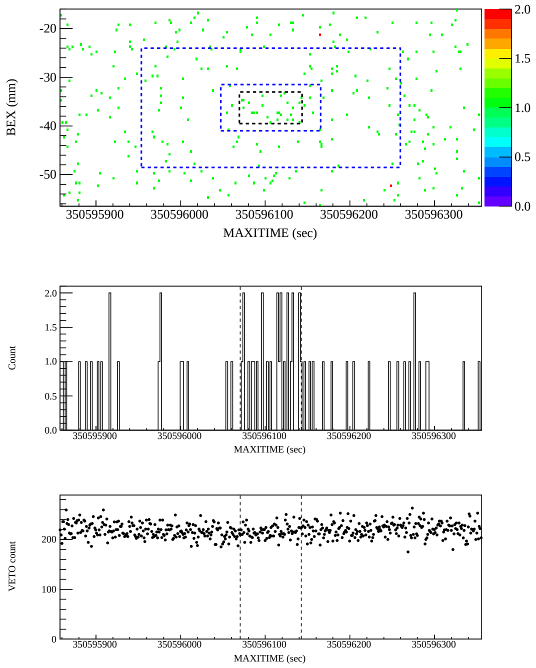

FIGURE B.59: Event map, light curve and VETO count time variability of SXT 110209 with $\log P_{\rm null} = -9.3$.

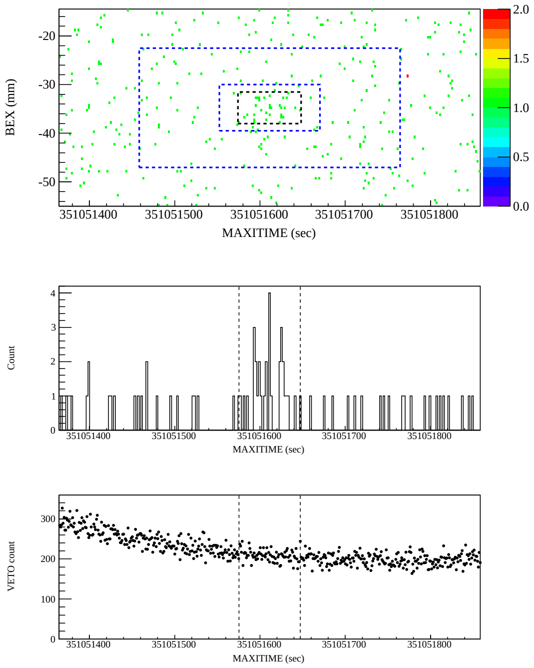

FIGURE B.60: Event map, light curve and VETO count time variability of SXT 110215 with $\log P_{\rm null} = -12.7$.

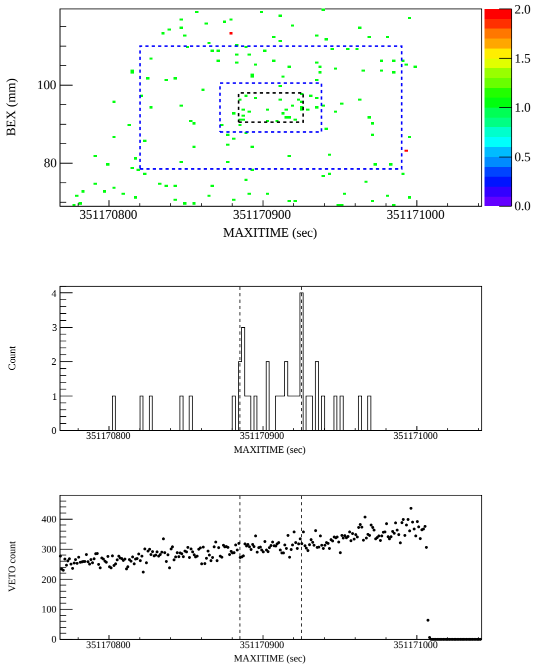

FIGURE B.61: Event map, light curve and VETO count time variability of SXT 110216 with $\log P_{\mathrm{null}} = -10.8$.

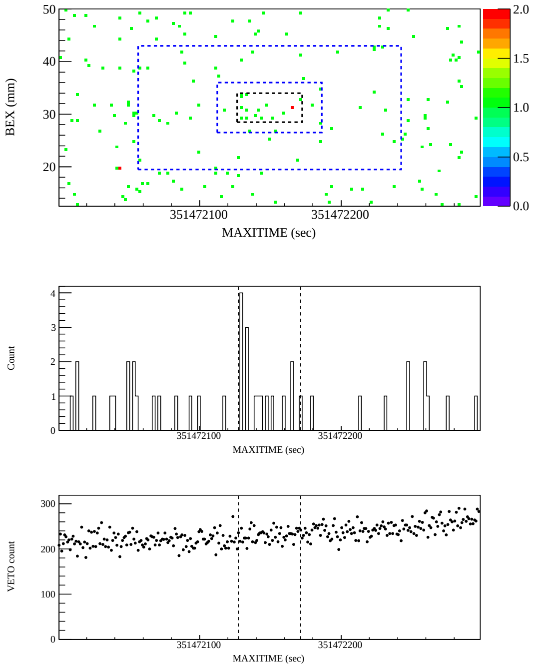

FIGURE B.62: Event map, light curve and VETO count time variability of SXT 110219 with $\log P_{\mathrm{null}} = -9.2$.

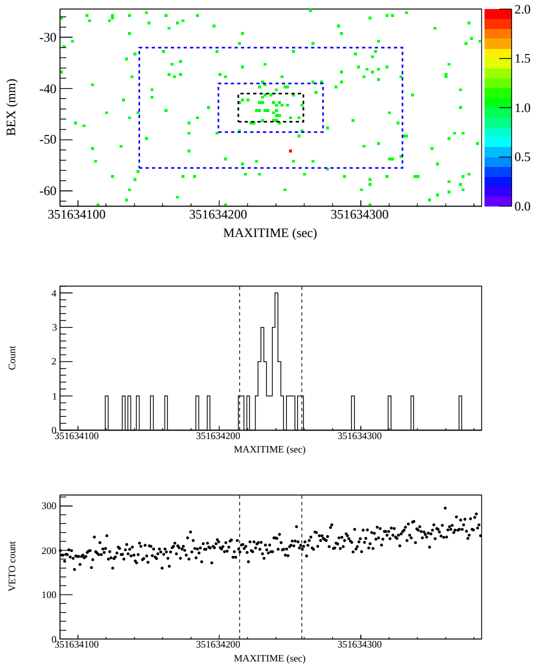

FIGURE B.63: Event map, light curve and VETO count time variability of SXT 110221 with $\log P_{\mathrm{null}} = -15.4$.

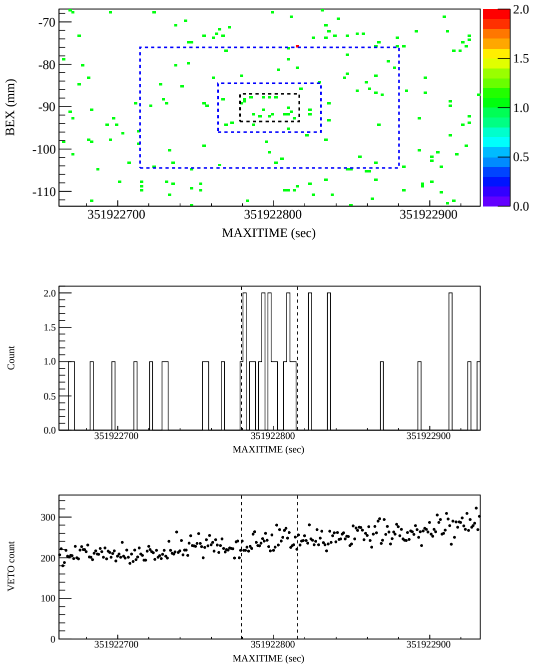

FIGURE B.64: Event map, light curve and VETO count time variability of SXT 110225 with $\log P_{\mathrm{null}} = -9.1$.

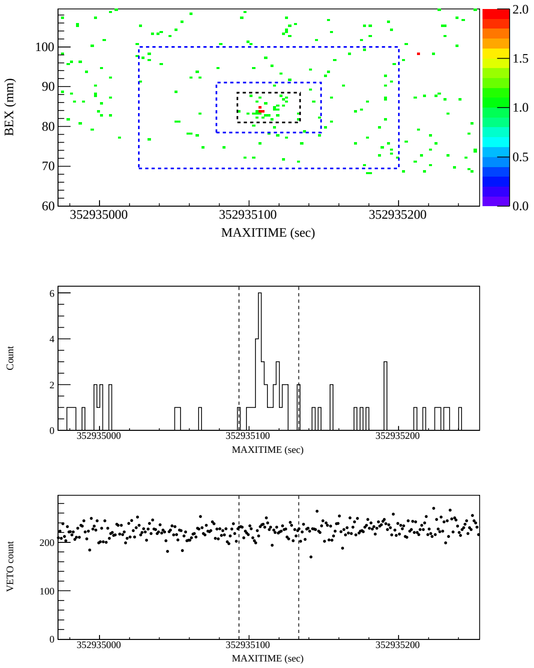

FIGURE B.65: Event map, light curve and VETO count time variability of SXT 110308 with $\log P_{\mathrm{null}} = -16.6$.

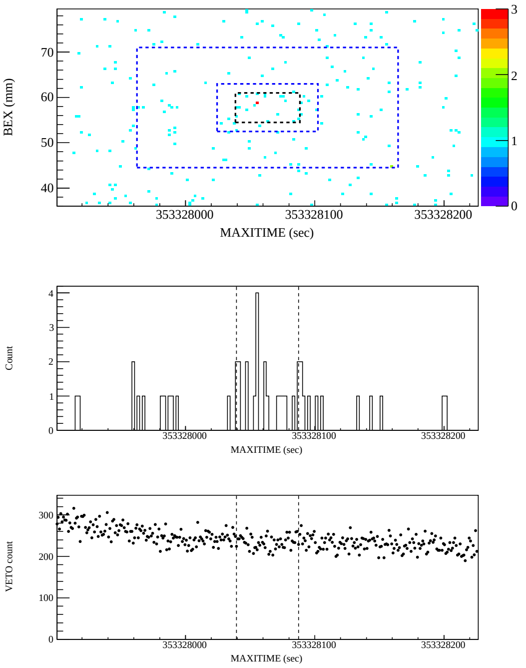

FIGURE B.66: Event map, light curve and VETO count time variability of SXT 110313 with $\log P_{\mathrm{null}} = -9.2$.

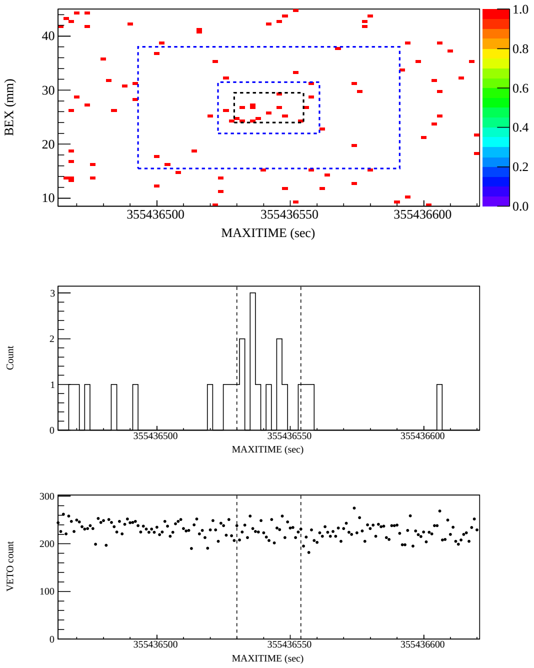

FIGURE B.67: Event map, light curve and VETO count time variability of SXT 110406 with $\log P_{\mathrm{null}} = -10.2$.

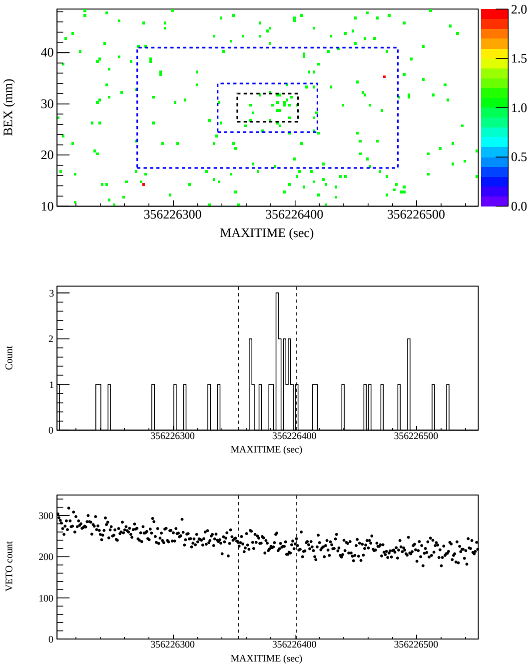

FIGURE B.68: Event map, light curve and VETO count time variability of SXT 110415 with $\log P_{\mathrm{null}} = -9.0$.

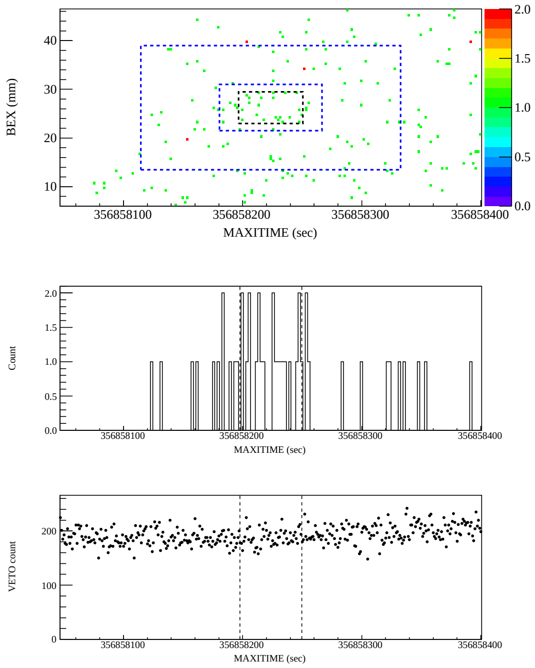

FIGURE B.69: Event map, light curve and VETO count time variability of SXT 110423 with $\log P_{\rm null} = -9.1$.

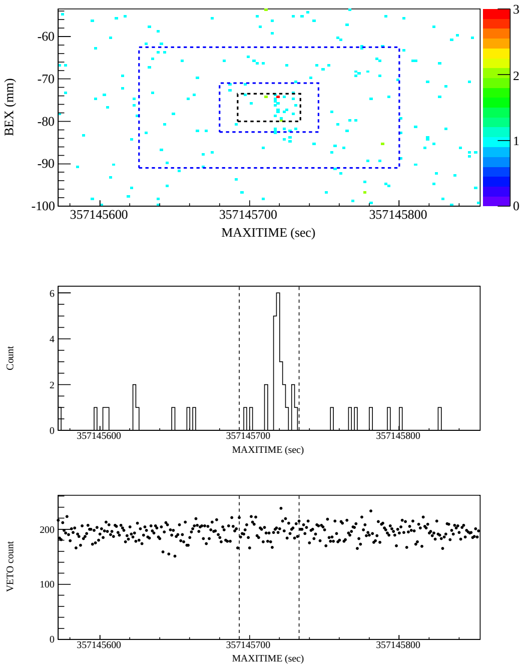

FIGURE B.70: Event map, light curve and VETO count time variability of SXT 110426 with $\log P_{\rm null} = -12.2$.

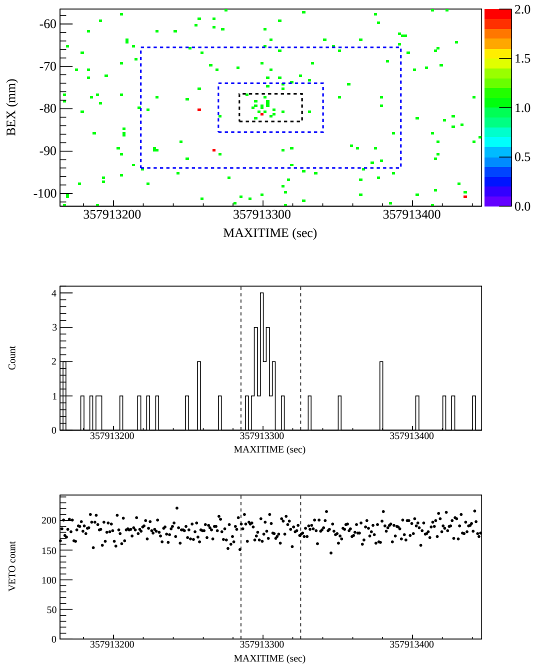

FIGURE B.71: Event map, light curve and VETO count time variability of SXT 110505 with $\log P_{\rm null} = -10.5$.

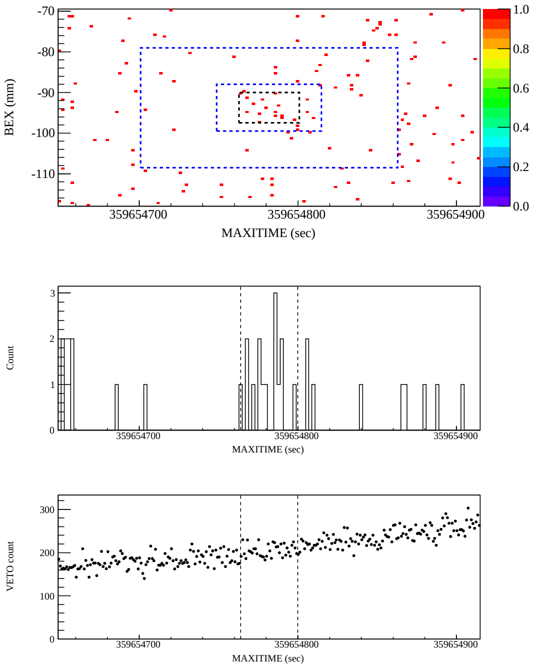

FIGURE B.72: Event map, light curve and VETO count time variability of SXT 110525 with $\log P_{\rm null} = -10.1$.

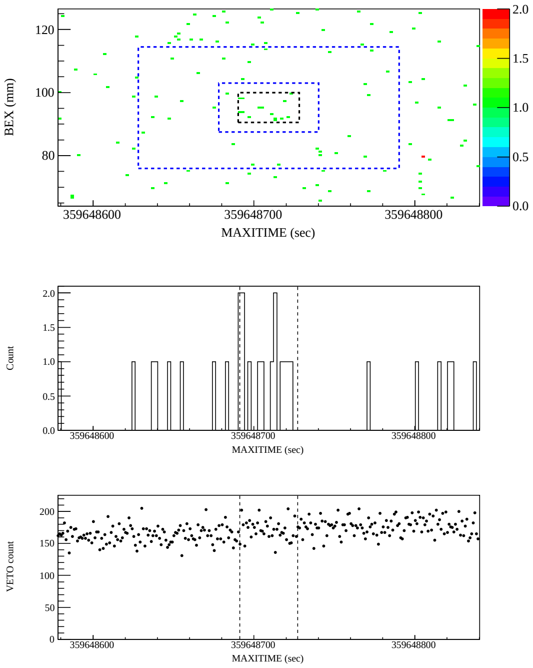

Figure B.73: Event map, light curve and VETO count time variability of SXT 110525 with $\log P_{\text{null}} = -9.1$.

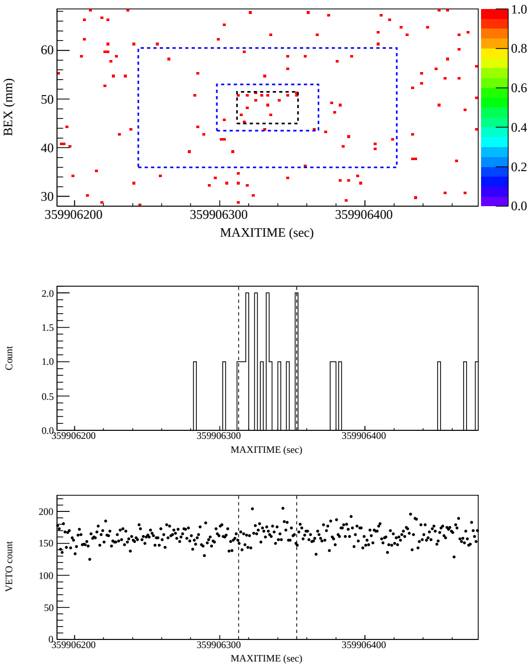

Figure B.74: Event map, light curve and VETO count time variability of SXT 110528 with $\log P_{\text{null}} = -9.6$.

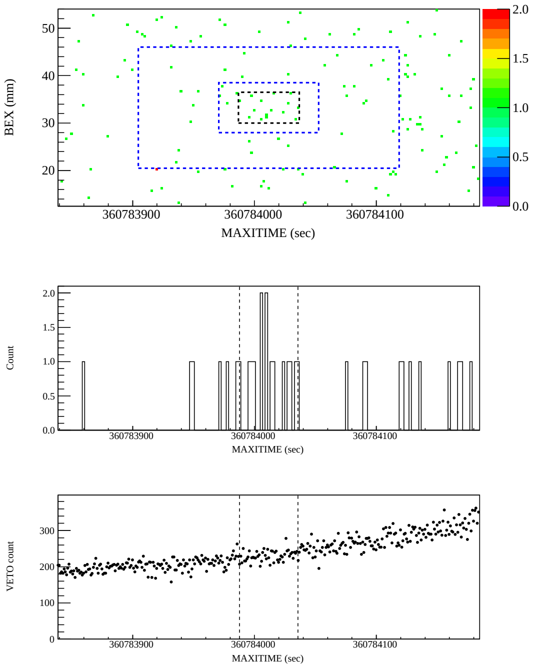

Figure B.75: Event map, light curve and VETO count time variability of SXT 110607 with $\log P_{\text{null}} = -9.4$.

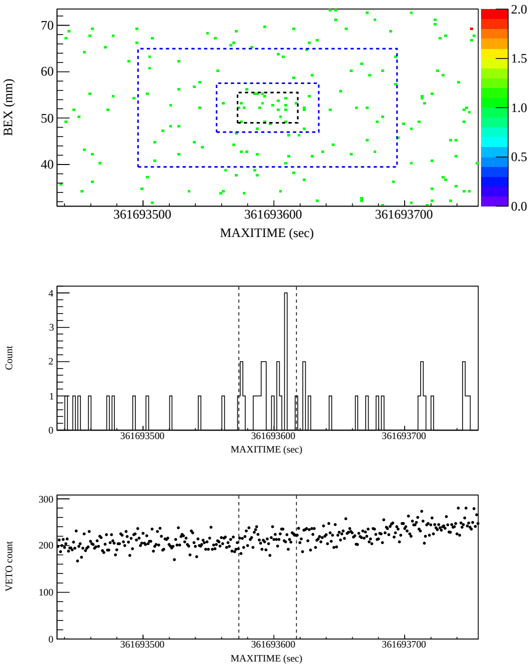

Figure B.76: Event map, light curve and VETO count time variability of SXT 110618 with $\log P_{\text{null}} = -9.7$.

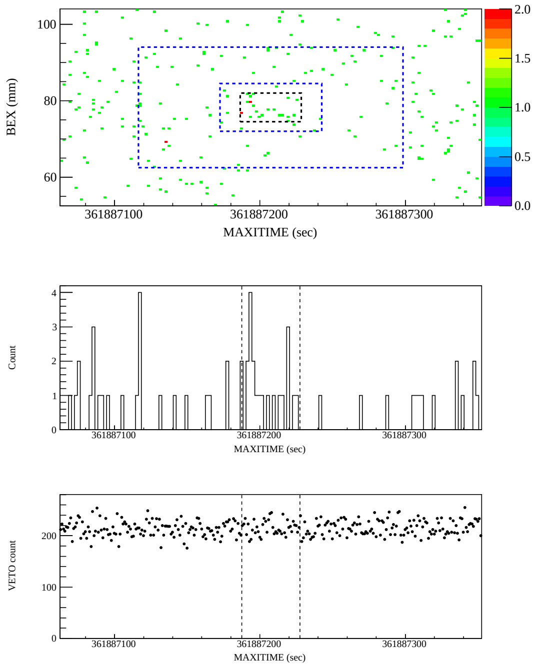

FIGURE B.77: Event map, light curve and VETO count time variability of SXT 110620 with $\log P_{\mathrm{null}} = -9.0$.

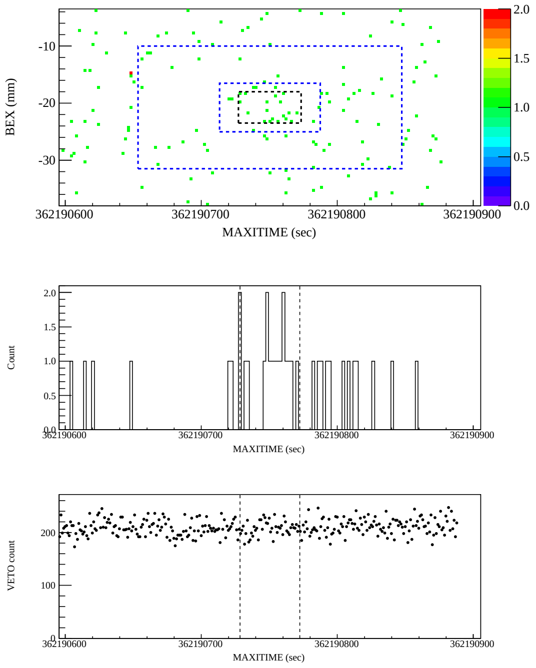

FIGURE B.78: Event map, light curve and VETO count time variability of SXT 110624 with $\log P_{\mathrm{null}} = -9.3$.

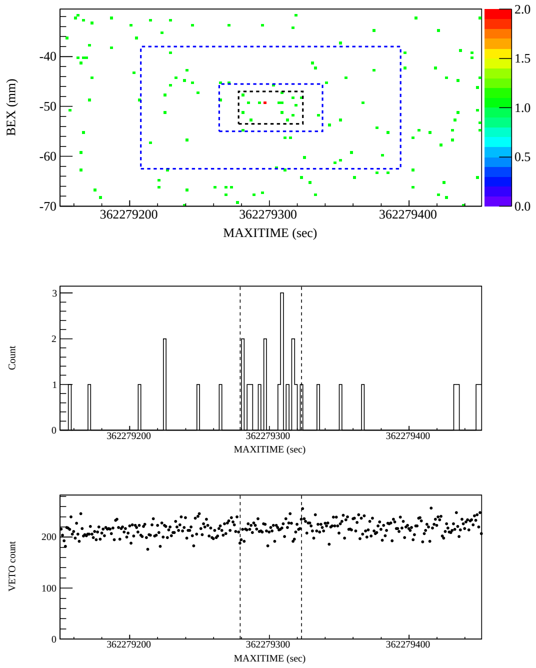

FIGURE B.79: Event map, light curve and VETO count time variability of SXT 110625 with $\log P_{\mathrm{null}} = -9.1$.

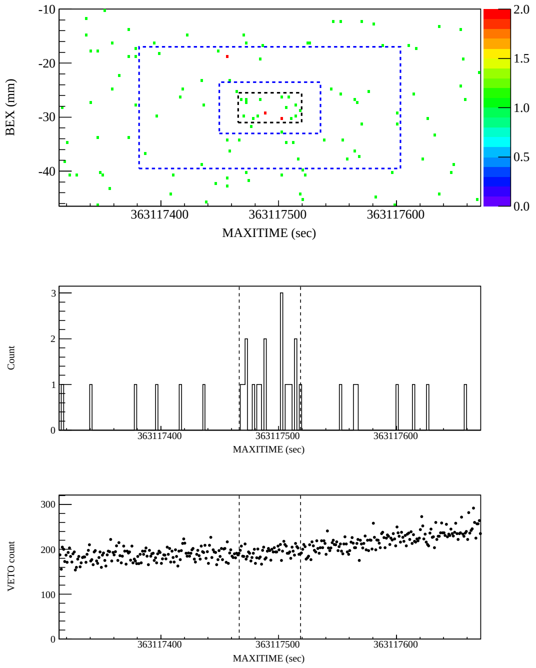

FIGURE B.80: Event map, light curve and VETO count time variability of SXT 110704 with $\log P_{\mathrm{null}} = -11.2$.

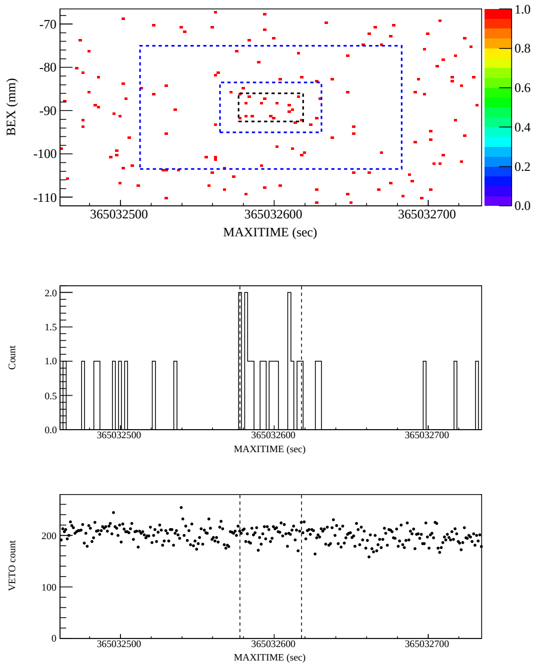

FIGURE B.81: Event map, light curve and VETO count time variability of SXT 110726 with $\log P_{\mathrm{null}} = -10.2$.

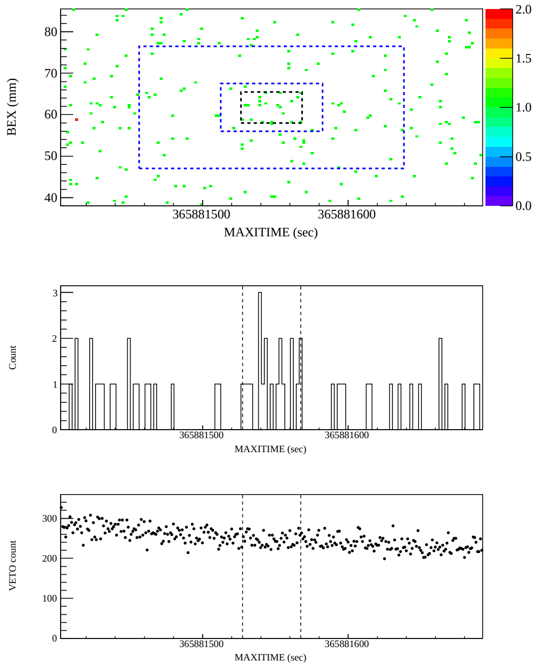

FIGURE B.82: Event map, light curve and VETO count time variability of SXT 110805 with $\log P_{\mathrm{null}} = -9.2$.

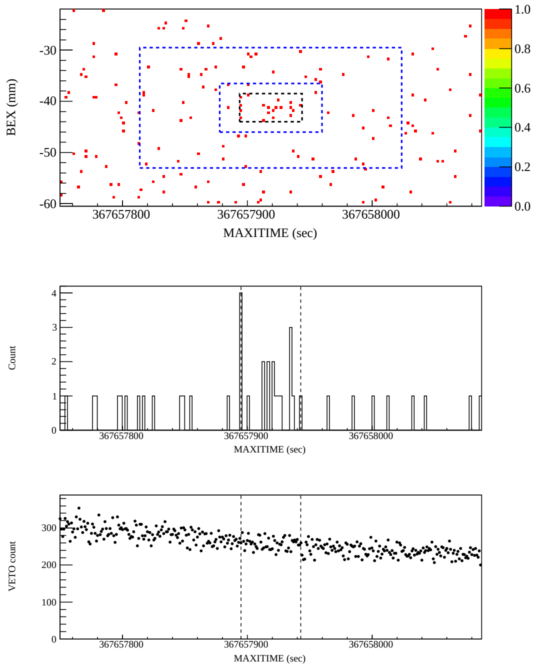

FIGURE B.83: Event map, light curve and VETO count time variability of SXT 110826 with $\log P_{\mathrm{null}} = -9.4$.

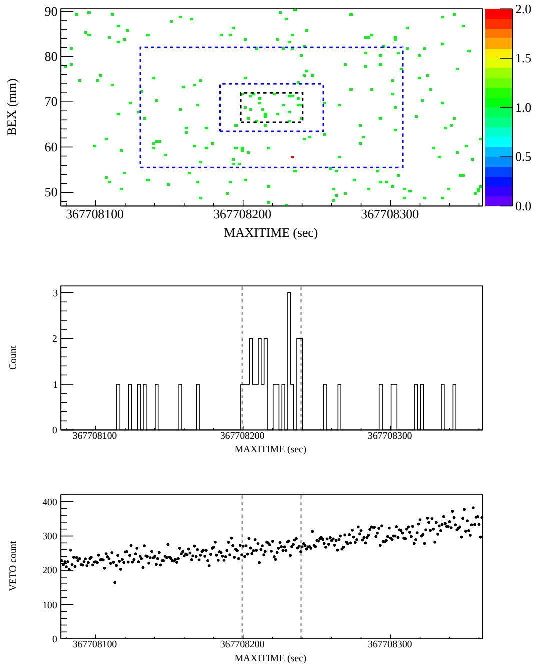

FIGURE B.84: Event map, light curve and VETO count time variability of SXT 110826 with $\log P_{\mathrm{null}} = -10.3$.

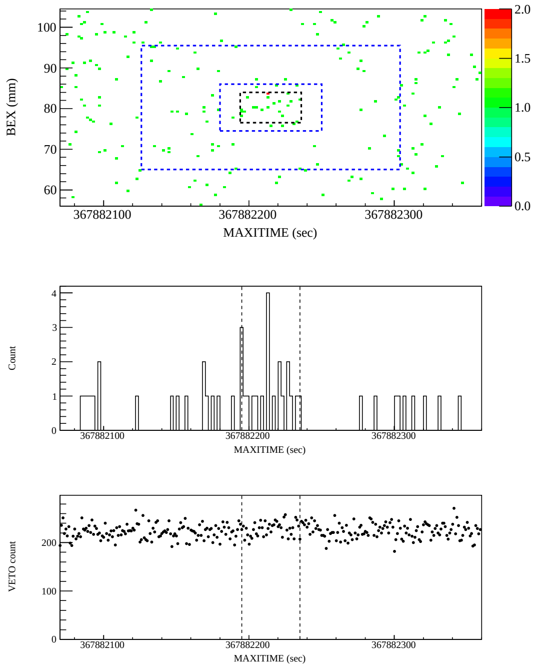

FIGURE B.85: Event map, light curve and VETO count time variability of SXT 110828 with $\log P_{\text{null}} = -10.9$.

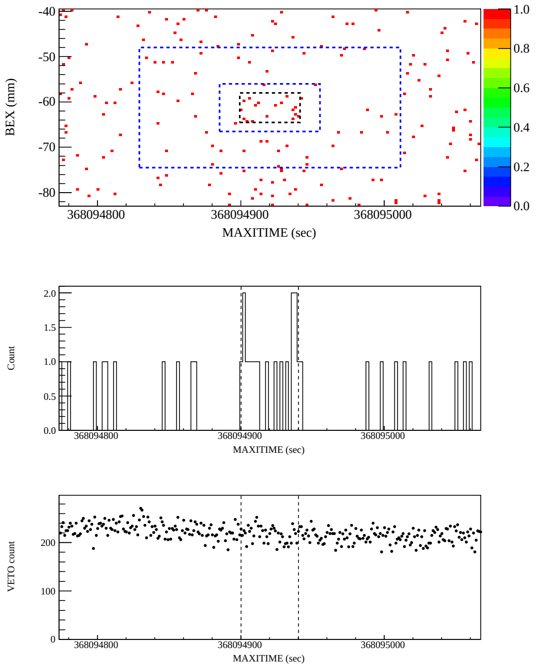

FIGURE B.86: Event map, light curve and VETO count time variability of SXT 110831 with $\log P_{\text{null}} = -9.2$.

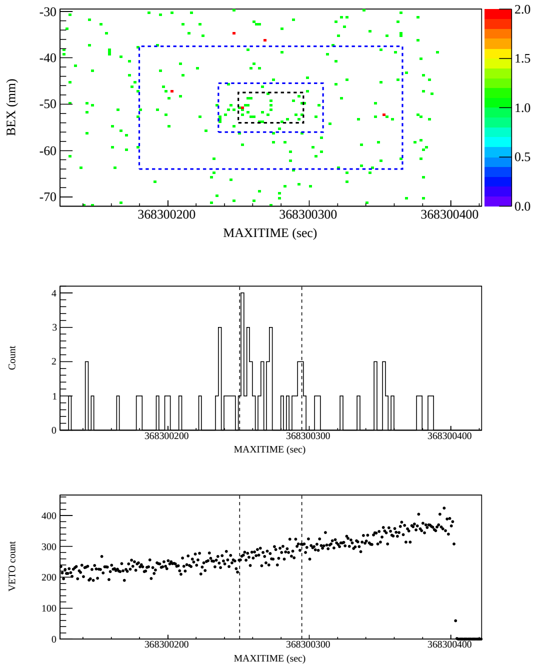

FIGURE B.87: Event map, light curve and VETO count time variability of SXT 110902 with $\log P_{\text{null}} = -14.1$.

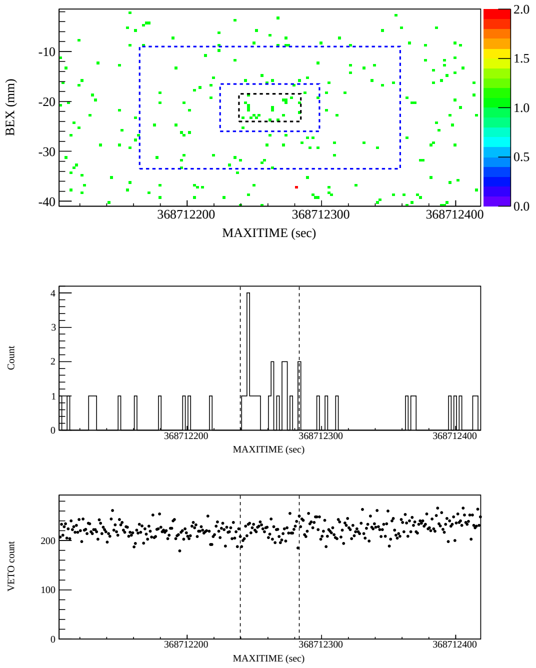

FIGURE B.88: Event map, light curve and VETO count time variability of SXT 110907 with $\log P_{\text{null}} = -9.8$.

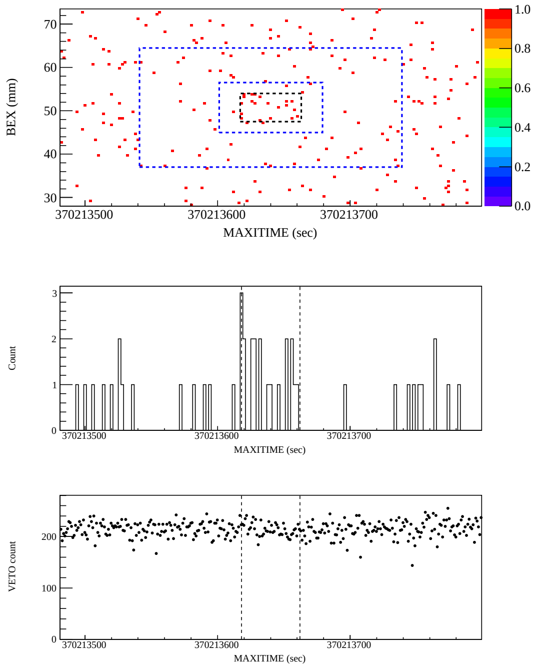

FIGURE B.89: Event map, light curve and VETO count time variability of SXT 110924 with $\log P_{\rm null} = -9.3$.

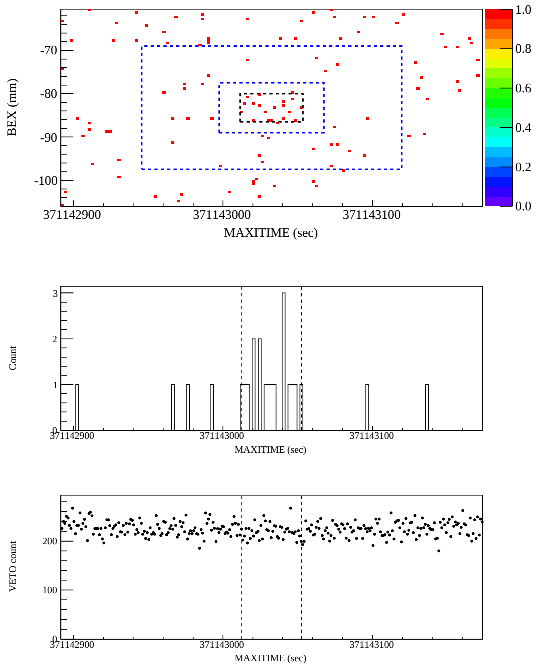

FIGURE B.90: Event map, light curve and VETO count time variability of SXT 111005 with $\log P_{\rm null} = -13.3$.

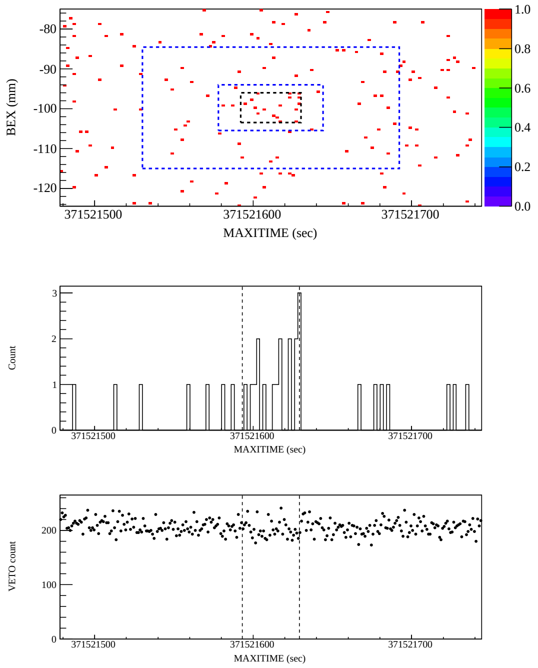

FIGURE B.91: Event map, light curve and VETO count time variability of SXT 111010 with $\log P_{\rm null} = -9.4$.

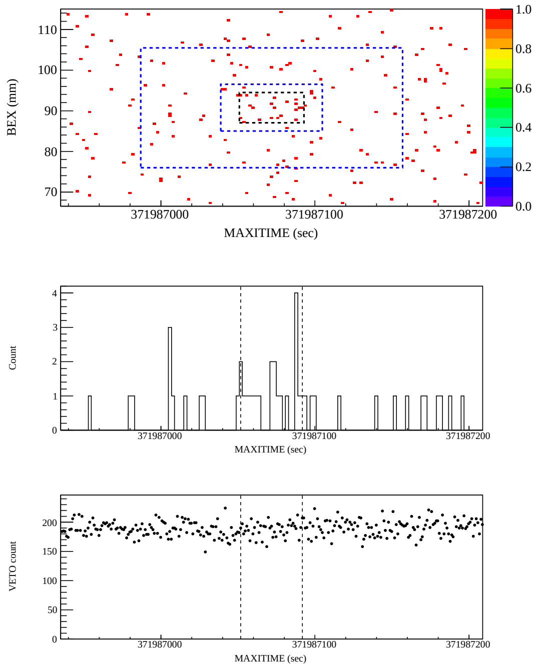

FIGURE B.92: Event map, light curve and VETO count time variability of SXT 111015 with $\log P_{\rm null} = -9.2$.

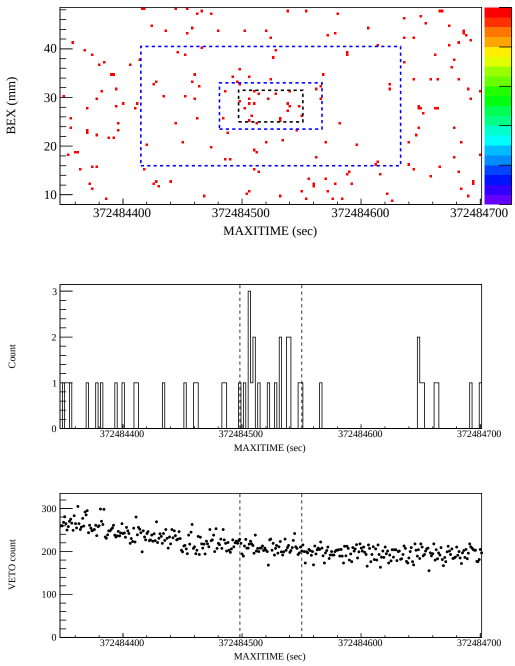

FIGURE B.93: Event map, light curve and VETO count time variability of SXT 111021 with log $P_{\text{null}} = -9.5$.

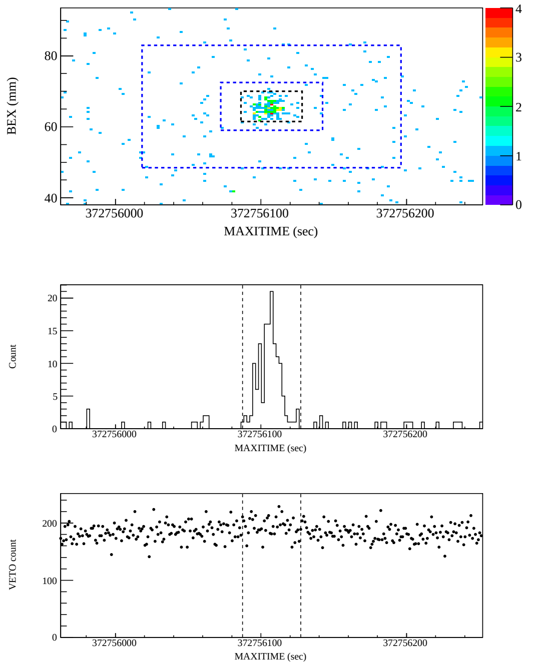

FIGURE B.94: Event map, light curve and VETO count time variability of SXT 111024 with log $P_{\text{null}} = -144.6$.

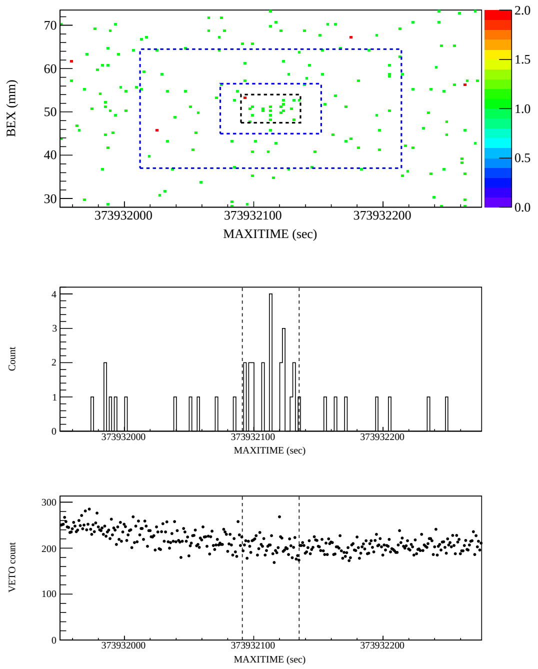

FIGURE B.95: Event map, light curve and VETO count time variability of SXT 111106 with log $P_{\text{null}} = -11.1$.

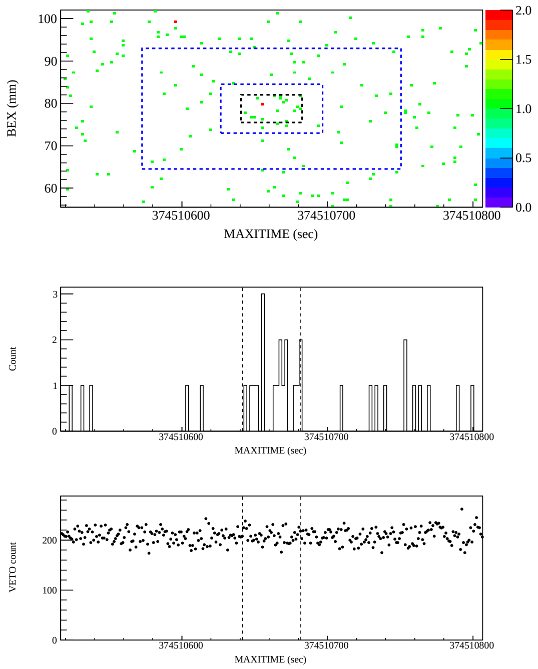

FIGURE B.96: Event map, light curve and VETO count time variability of SXT 111113 with log $P_{\text{null}} = -10.2$.

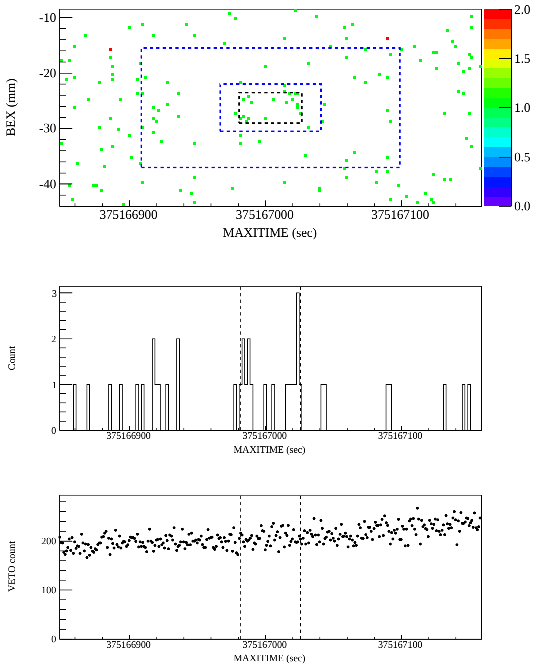

FIGURE B.97: Event map, light curve and VETO count time variability of SXT 111121 with $\log P_{\mathrm{null}} = -9.5$.

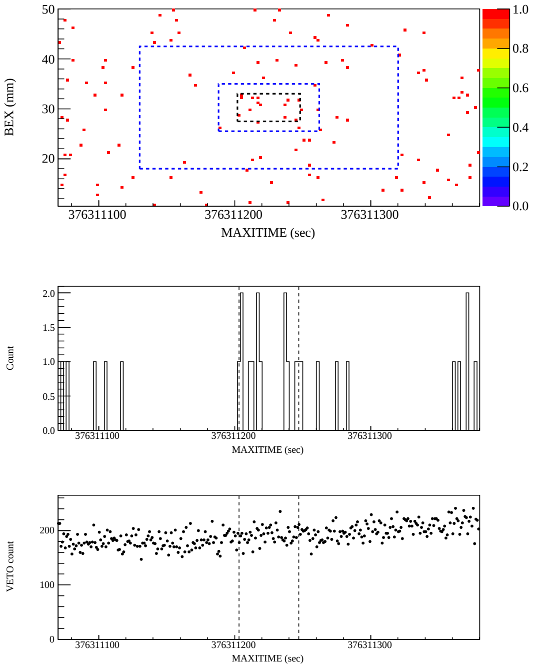

FIGURE B.98: Event map, light curve and VETO count time variability of SXT 111204 with $\log P_{\mathrm{null}} = -9.4$.

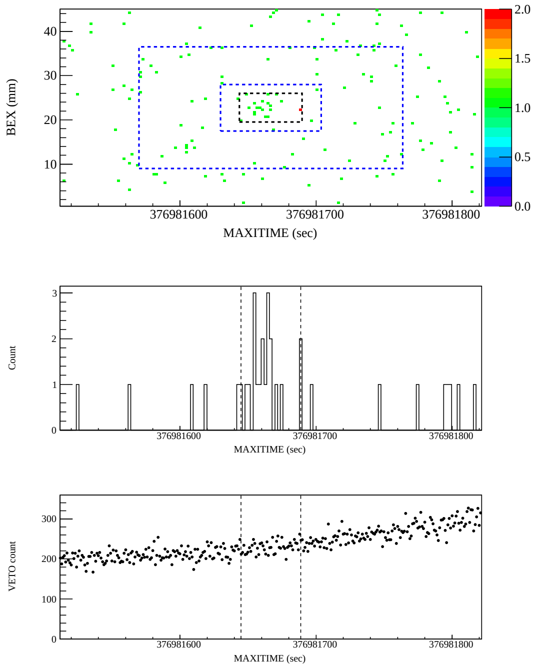

FIGURE B.99: Event map, light curve and VETO count time variability of SXT 111212 with $\log P_{\mathrm{null}} = -10.2$.

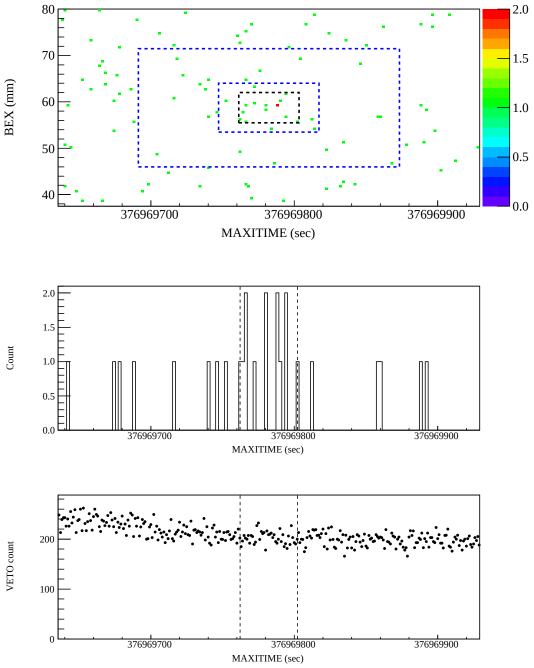

FIGURE B.100: Event map, light curve and VETO count time variability of SXT 111212 with $\log P_{\mathrm{null}} = -9.5$.

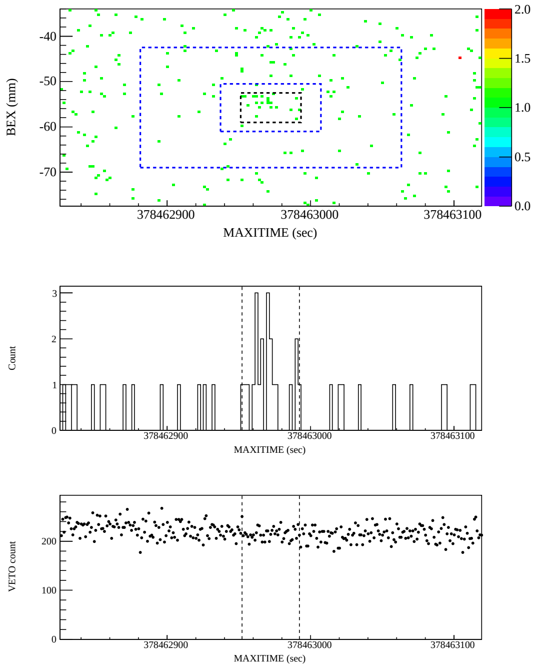

FIGURE B.101: Event map, light curve and VETO count time variability of SXT 111229 with $\log P_{\rm null} = -10.8$.

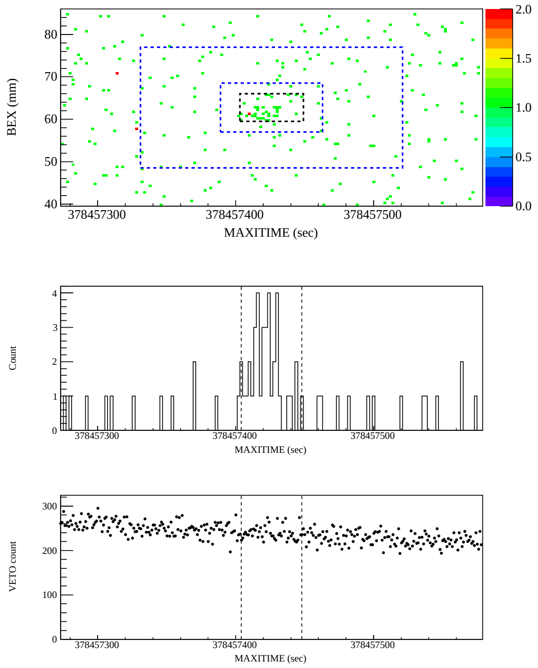

FIGURE B.102: Event map, light curve and VETO count time variability of SXT 111229 with $\log P_{\rm null} = -22.7$.

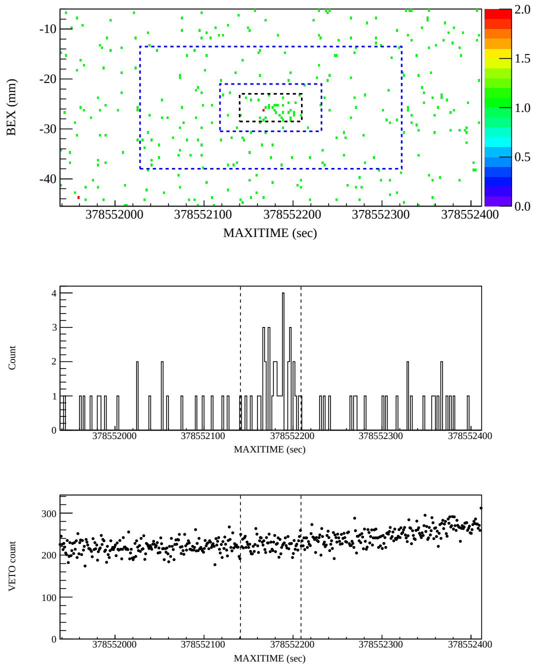

FIGURE B.103: Event map, light curve and VETO count time variability of SXT 111230 with $\log P_{\rm null} = -16.0$.

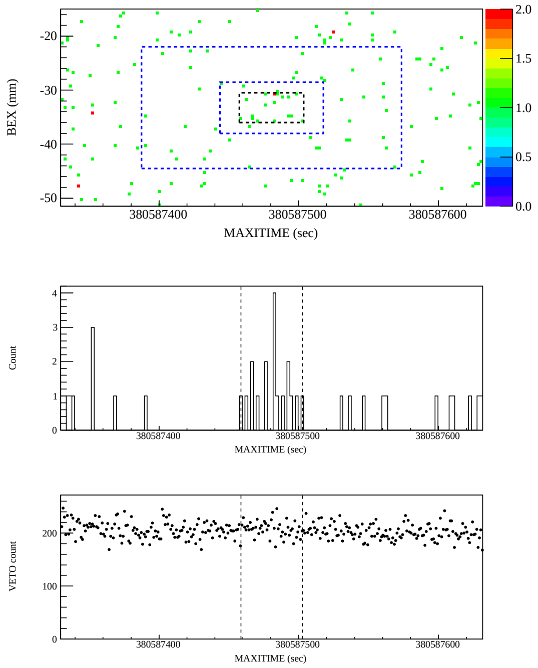

FIGURE B.104: Event map, light curve and VETO count time variability of SXT 120122 with $\log P_{\rm null} = -10.2$.

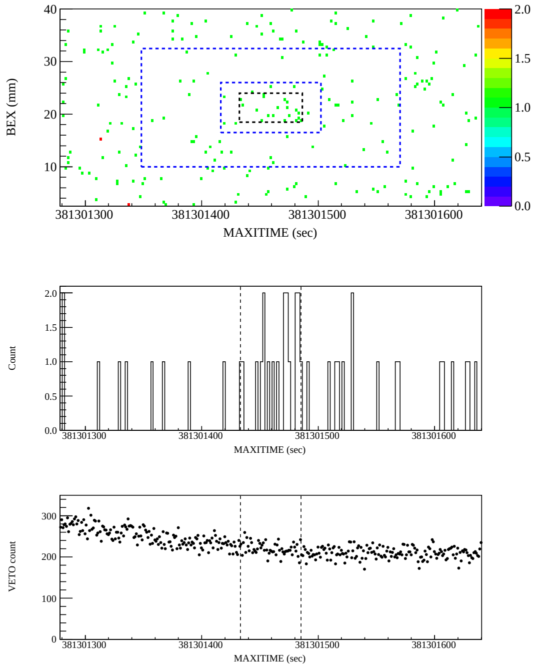

FIGURE B.105: Event map, light curve and VETO count time variability of SXT 120131 with $\log P_{\mathrm{null}} = -9.9$.

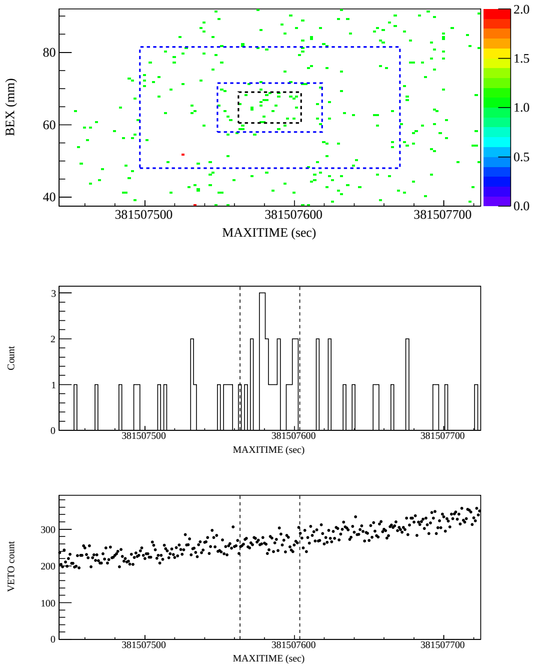

FIGURE B.106: Event map, light curve and VETO count time variability of SXT 120202 with $\log P_{\mathrm{null}} = -9.2$.

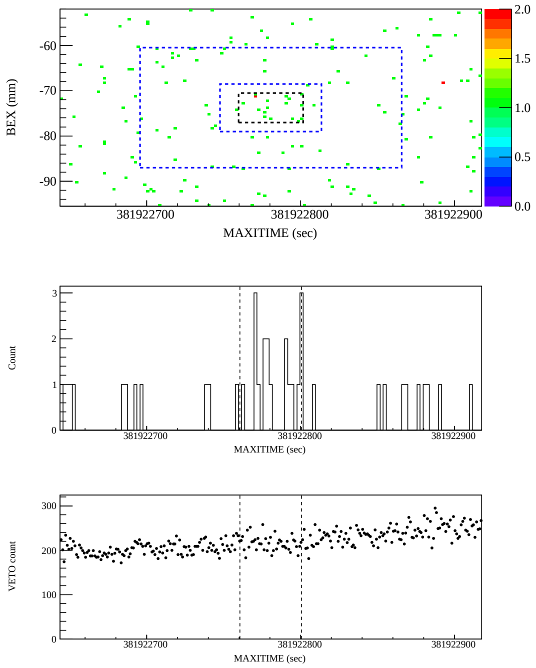

FIGURE B.107: Event map, light curve and VETO count time variability of SXT 120207 with $\log P_{\mathrm{null}} = -9.1$.

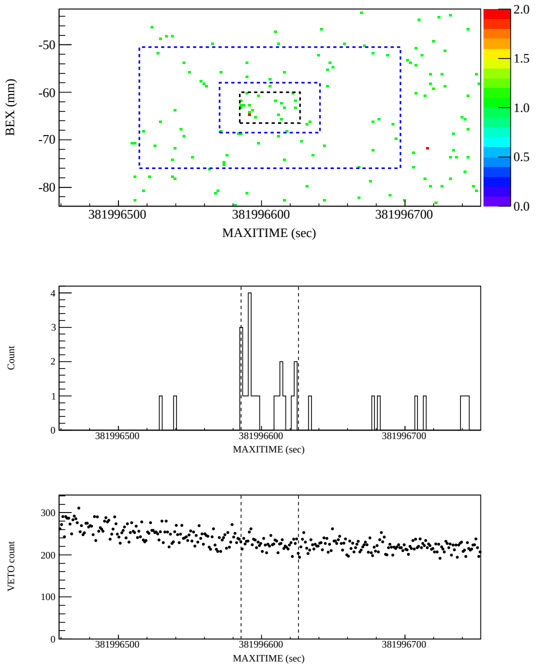

FIGURE B.108: Event map, light curve and VETO count time variability of SXT 120208 with $\log P_{\mathrm{null}} = -10.9$.

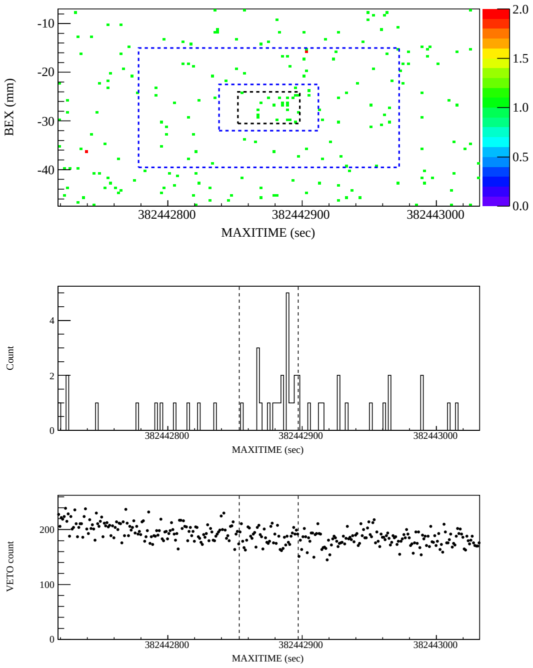

FIGURE B.109: Event map, light curve and VETO count time variability of SXT 120213 with log $P_{\text{null}} = -9.7$.

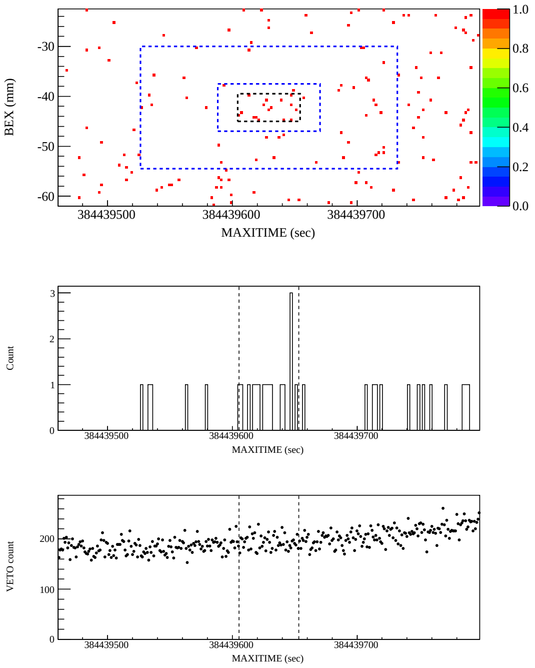

FIGURE B.110: Event map, light curve and VETO count time variability of SXT 120307 with log $P_{\text{null}} = -9.3$.

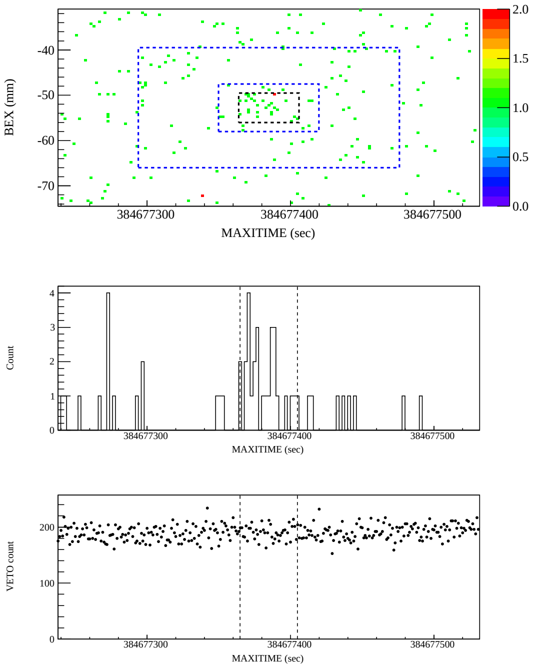

FIGURE B.111: Event map, light curve and VETO count time variability of SXT 120310 with log $P_{\text{null}} = -14.6$.

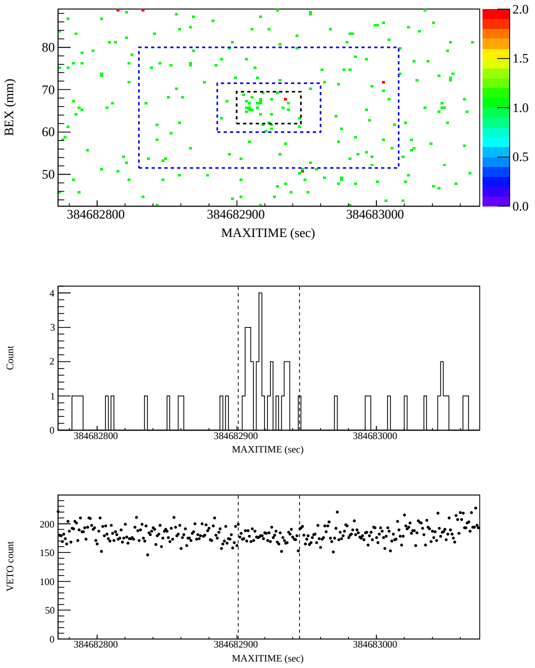

FIGURE B.112: Event map, light curve and VETO count time variability of SXT 120310 with log $P_{\text{null}} = -12.0$.

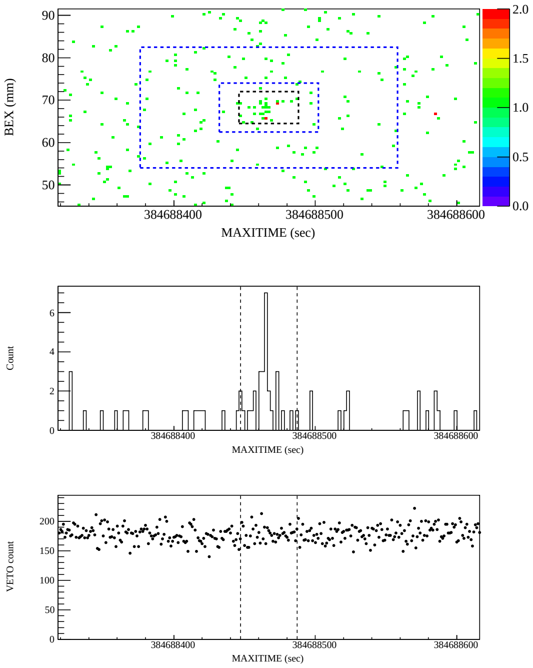

FIGURE B.113: Event map, light curve and VETO count time variability of SXT 120310 with $\log P_{\mathrm{null}} = -13.5$.

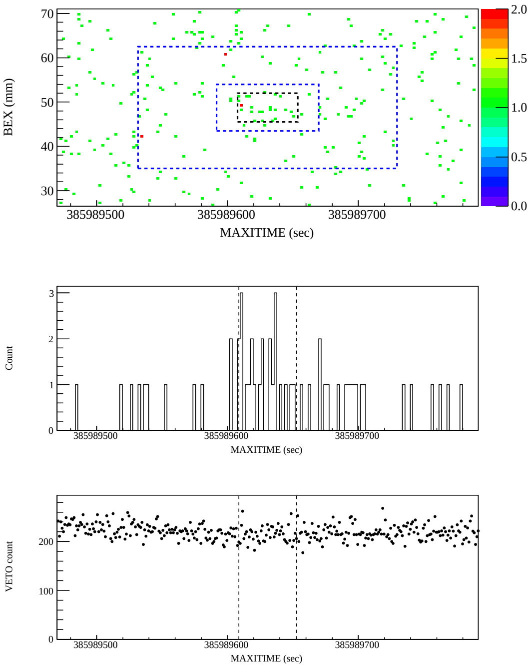

FIGURE B.114: Event map, light curve and VETO count time variability of SXT 120325 with $\log P_{\mathrm{null}} = -9.4$.

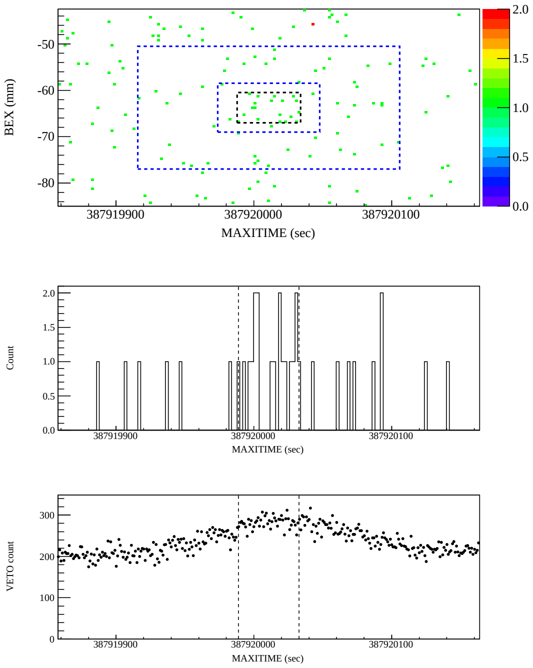

FIGURE B.115: Event map, light curve and VETO count time variability of SXT 120416 with $\log P_{\mathrm{null}} = -9.7$.

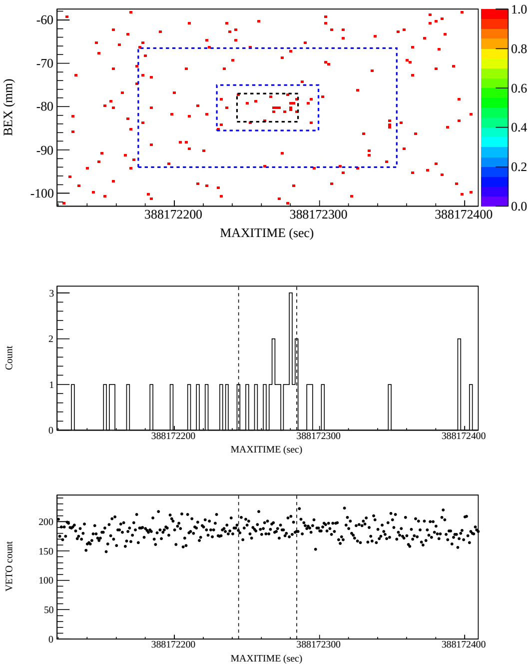

FIGURE B.116: Event map, light curve and VETO count time variability of SXT 120419 with $\log P_{\mathrm{null}} = -9.9$.

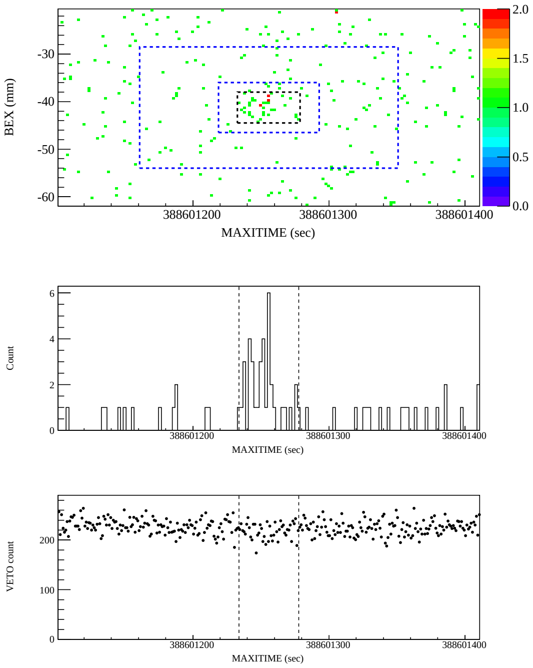

Figure B.117: Event map, light curve and VETO count time variability of SXT 120424 with $\log P_{\text{null}} = -20.9$.

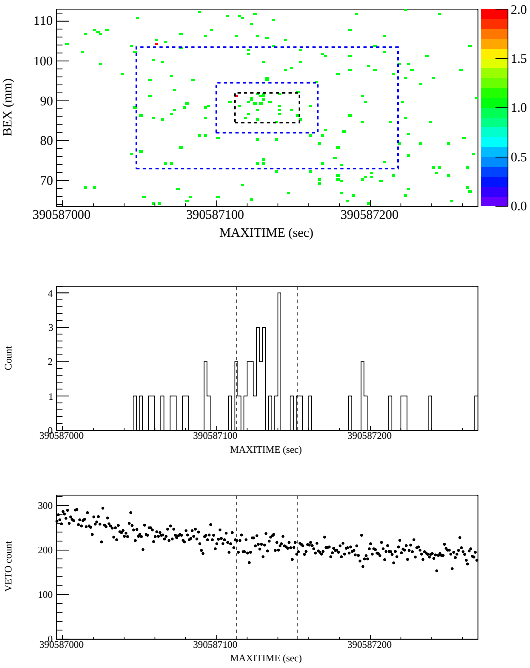

Figure B.118: Event map, light curve and VETO count time variability of SXT 120517 with $\log P_{\text{null}} = -11.2$.

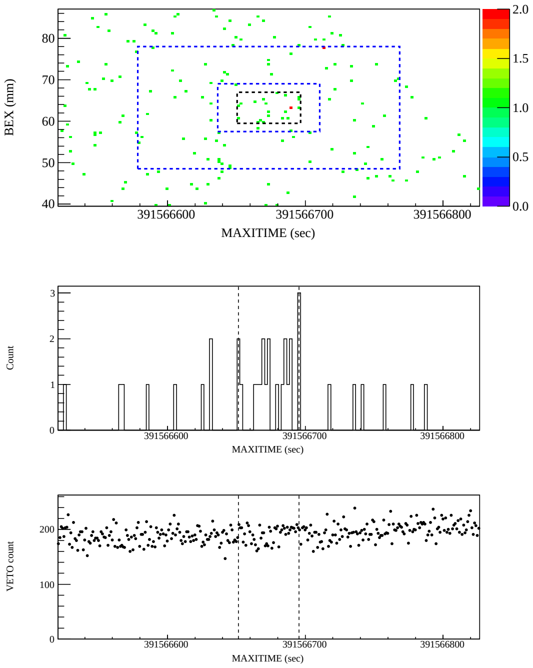

Figure B.119: Event map, light curve and VETO count time variability of SXT 120529 with $\log P_{\text{null}} = -9.0$.

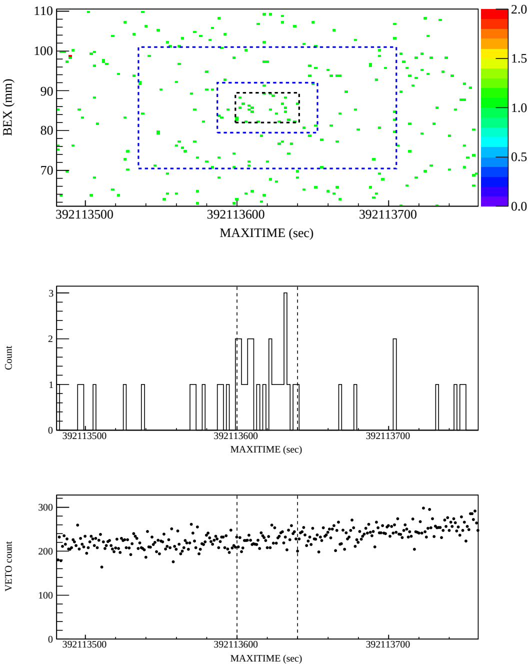

Figure B.120: Event map, light curve and VETO count time variability of SXT 120604 with $\log P_{\text{null}} = -10.0$.

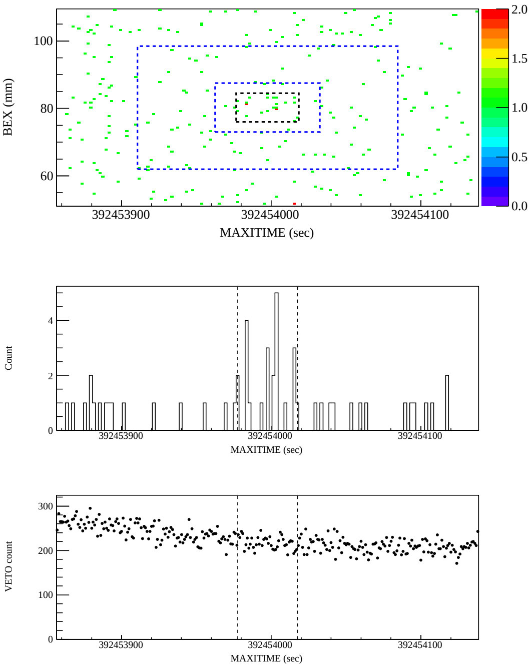

FIGURE B.121: Event map, light curve and VETO count time variability of SXT 120608 with $\log P_{\text{null}} = -10.0$.

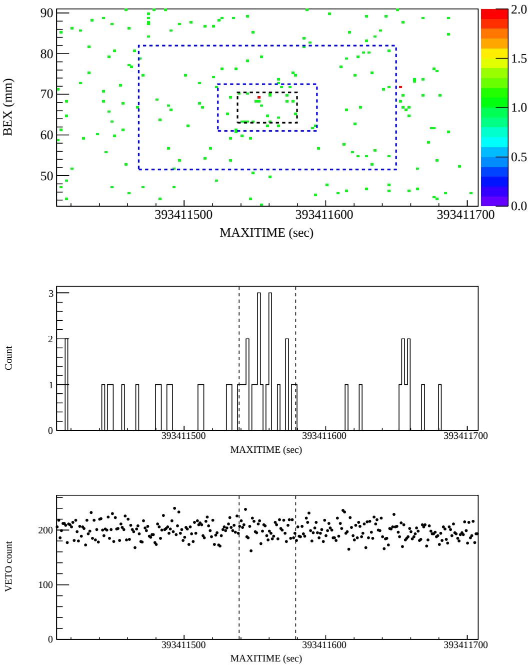

FIGURE B.122: Event map, light curve and VETO count time variability of SXT 120619 with $\log P_{\text{null}} = -9.7$.

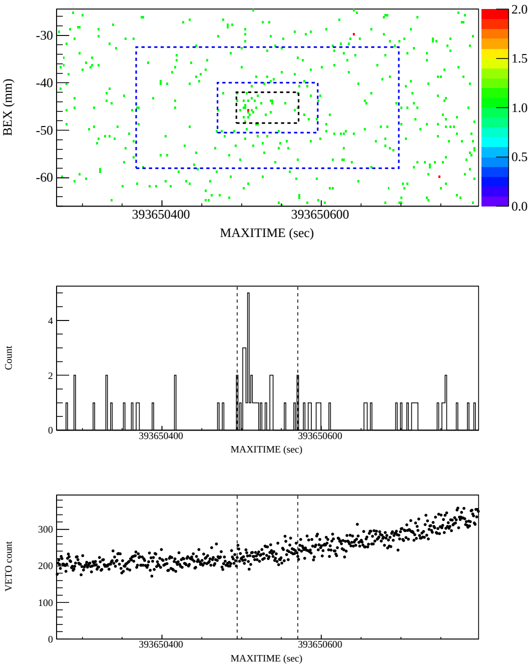

FIGURE B.123: Event map, light curve and VETO count time variability of SXT 120622 with $\log P_{\text{null}} = -11.3$.

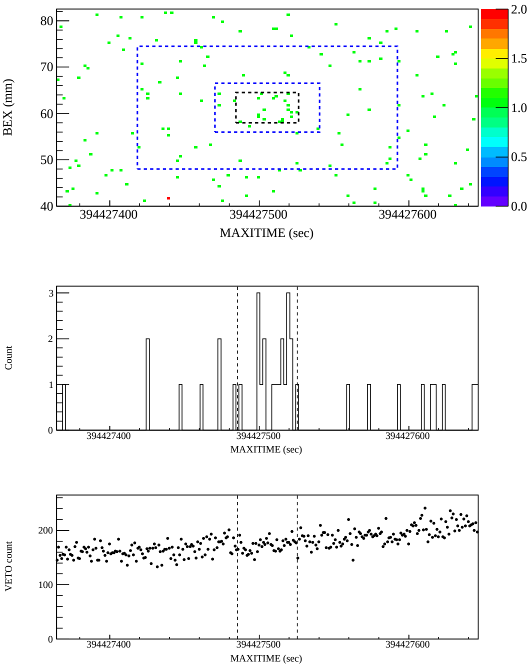

FIGURE B.124: Event map, light curve and VETO count time variability of SXT 120701 with $\log P_{\text{null}} = -10.2$.

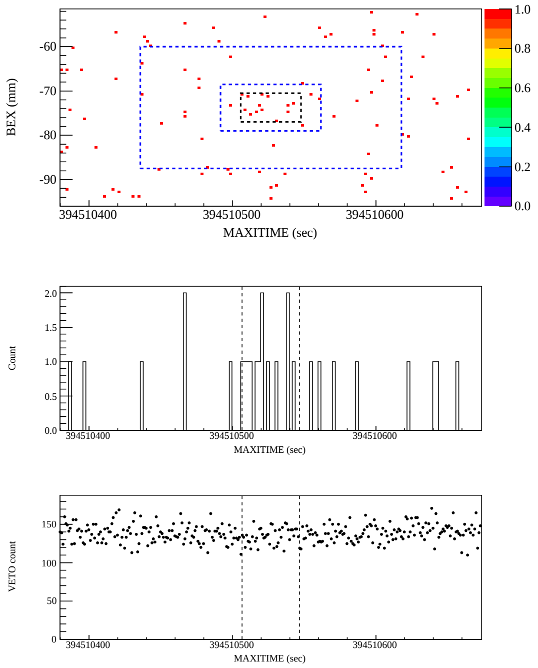

FIGURE B.125: Event map, light curve and VETO count time variability of SXT 120702 with $\log P_{\rm null} = -9.7$.

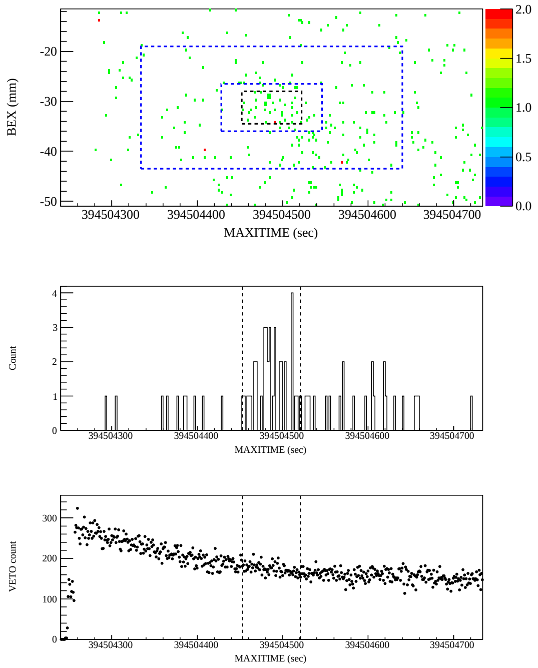

FIGURE B.126: Event map, light curve and VETO count time variability of SXT 120702 with $\log P_{\rm null} = -14.1$.

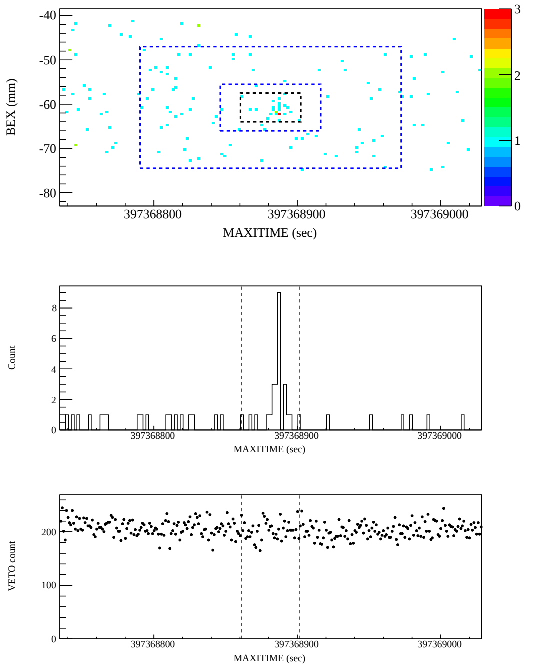

FIGURE B.127: Event map, light curve and VETO count time variability of SXT 120804 with $\log P_{\rm null} = -13.0$.

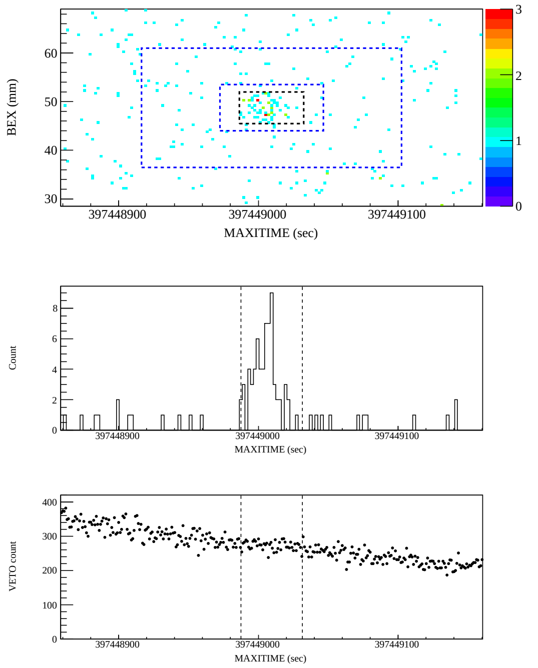

FIGURE B.128: Event map, light curve and VETO count time variability of SXT 120805 with $\log P_{\rm null} = -47.6$.

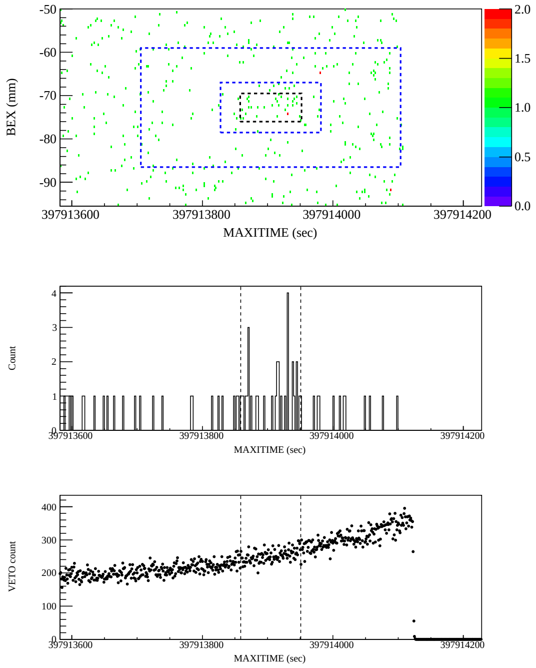

FIGURE B.129: Event map, light curve and VETO count time variability of SXT 120810 with $\log P_{\rm null} = -10.2$.

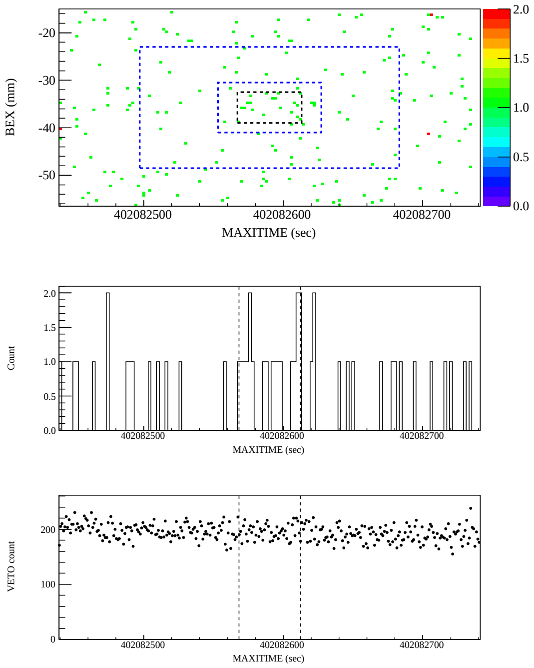

FIGURE B.130: Event map, light curve and VETO count time variability of SXT 120927 with $\log P_{\rm null} = -9.5$.

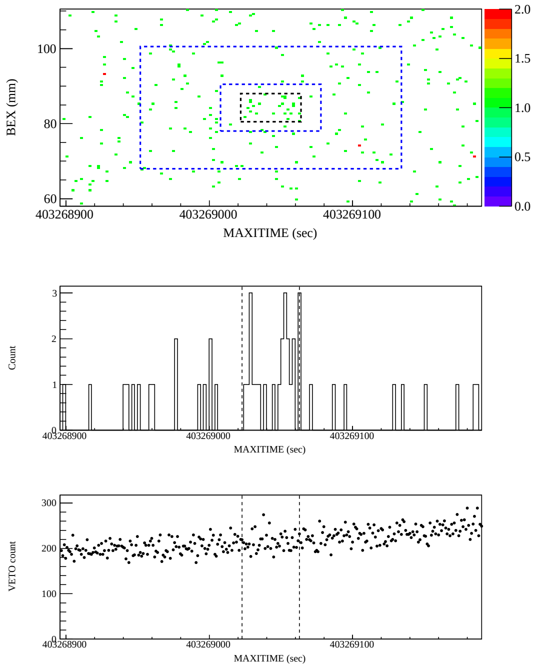

FIGURE B.131: Event map, light curve and VETO count time variability of SXT 121011 with $\log P_{\rm null} = -9.1$.

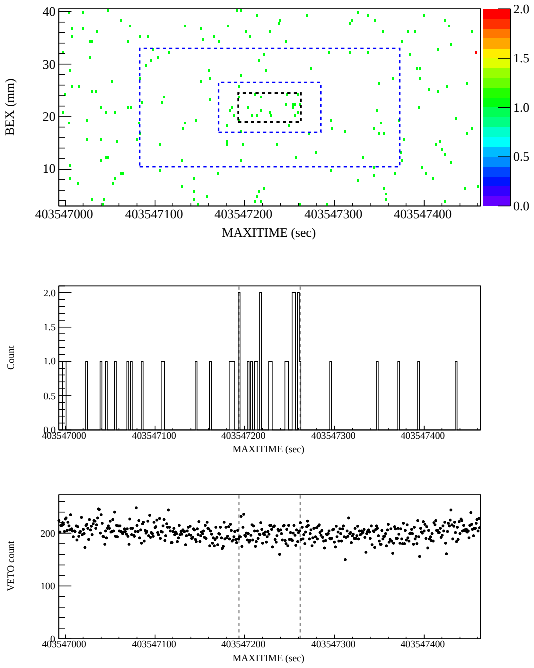

FIGURE B.132: Event map, light curve and VETO count time variability of SXT 121014 with $\log P_{\rm null} = -9.3$.

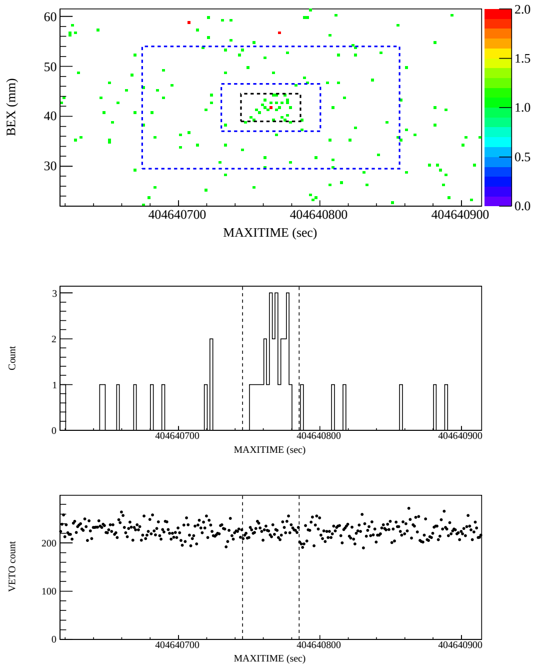

FIGURE B.133: Event map, light curve and VETO count time variability of SXT 121027 with log $P_{\mathrm{null}} = -15.1$.

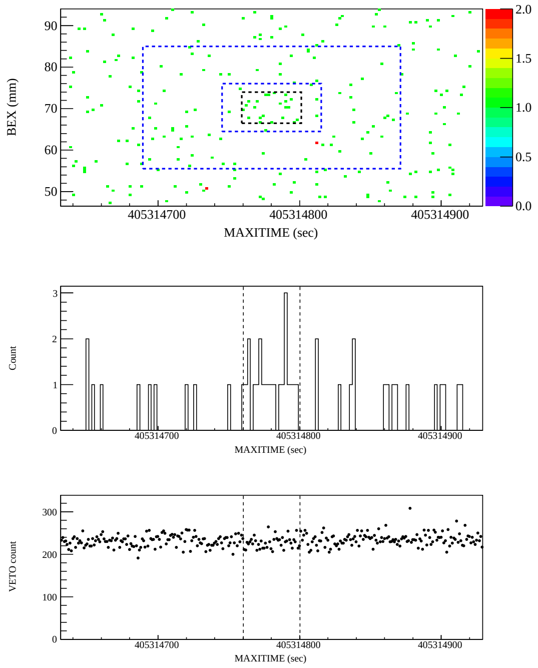

FIGURE B.134: Event map, light curve and VETO count time variability of SXT 121104 with log $P_{\mathrm{null}} = -9.4$.

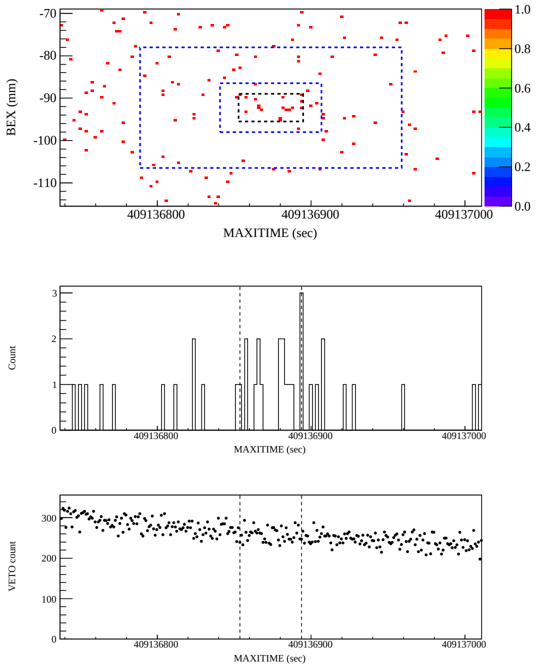

FIGURE B.135: Event map, light curve and VETO count time variability of SXT 121218 with log $P_{\mathrm{null}} = -9.7$.

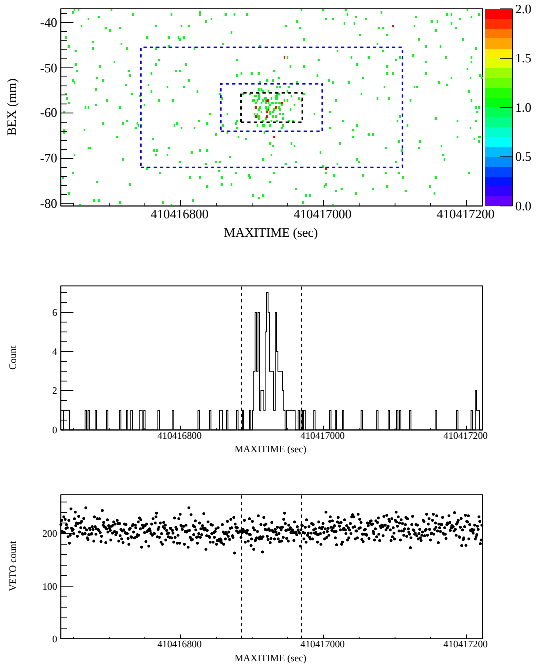

FIGURE B.136: Event map, light curve and VETO count time variability of SXT 130102 with log $P_{\mathrm{null}} = -57.8$.

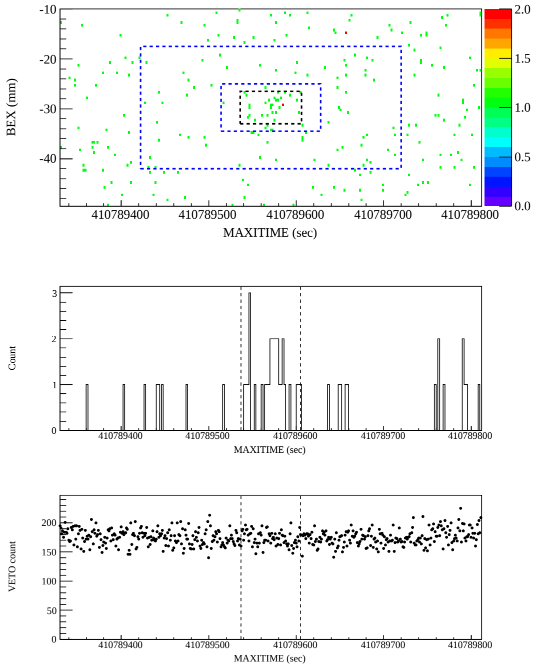

FIGURE B.137: Event map, light curve and VETO count time variability of SXT 130106 with $\log P_{\rm null} = -14.6$.

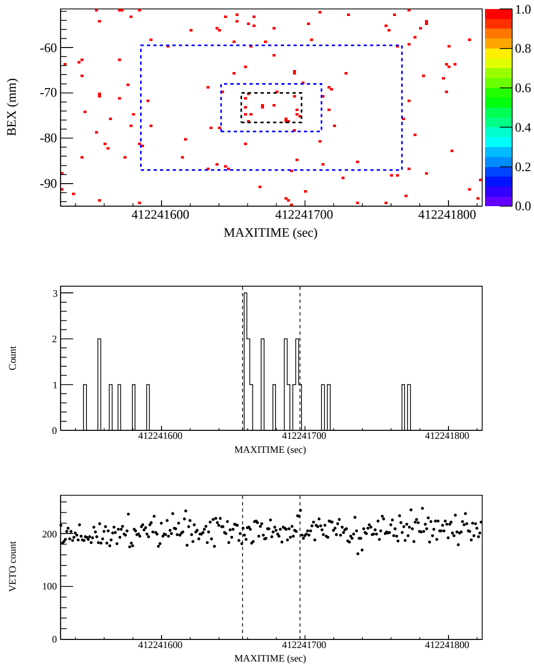

FIGURE B.138: Event map, light curve and VETO count time variability of SXT 130123 with $\log P_{\rm null} = -10.1$.

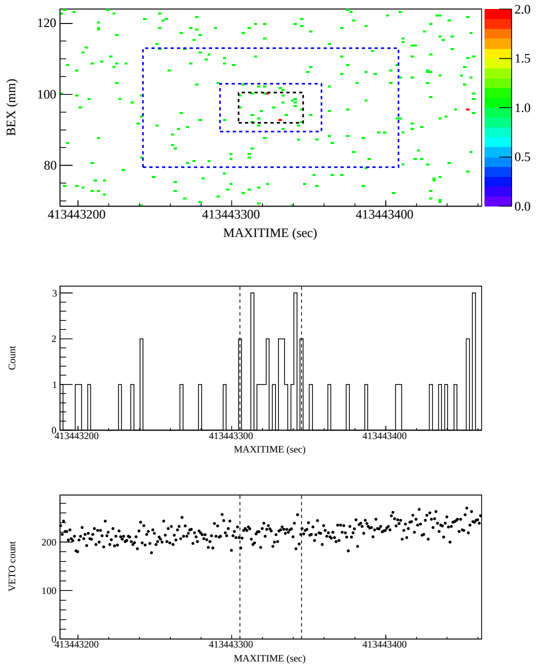

FIGURE B.139: Event map, light curve and VETO count time variability of SXT 130206 with $\log P_{\rm null} = -9.5$.

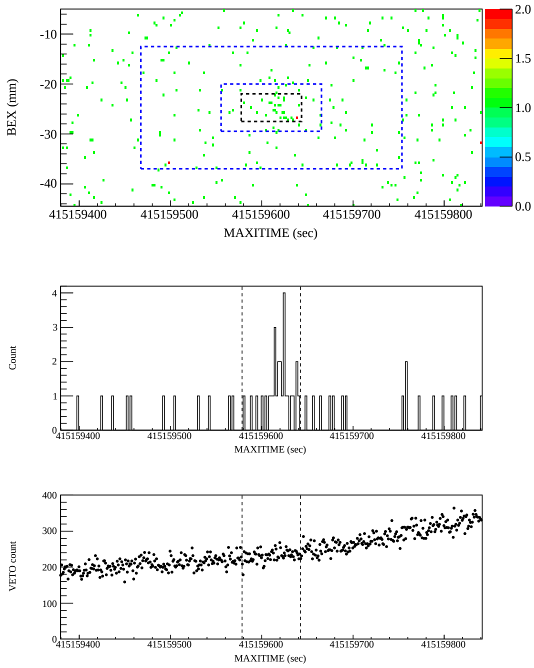

FIGURE B.140: Event map, light curve and VETO count time variability of SXT 130226 with $\log P_{\rm null} = -12.5$.

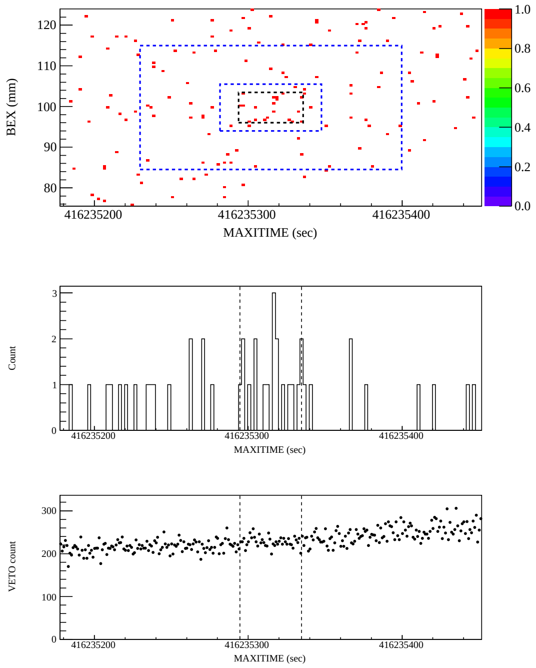

FIGURE B.141: Event map, light curve and VETO count time variability of SXT 130310 with log $P_{\rm null} = -9.4$.

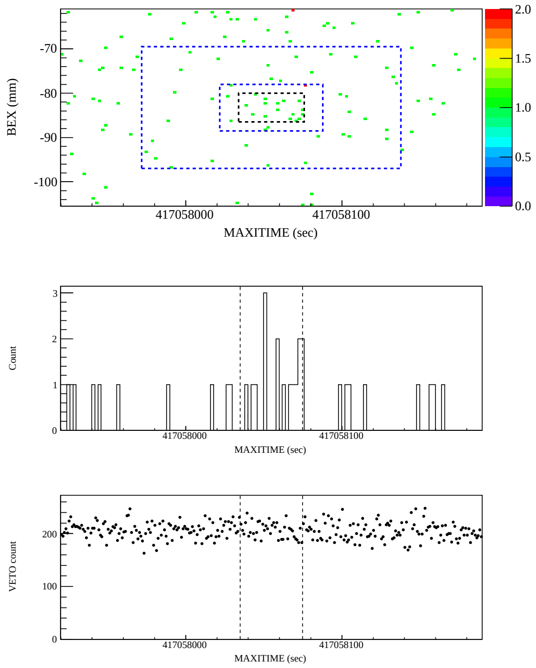

FIGURE B.142: Event map, light curve and VETO count time variability of SXT 130320 with log $P_{\rm null} = -9.3$.

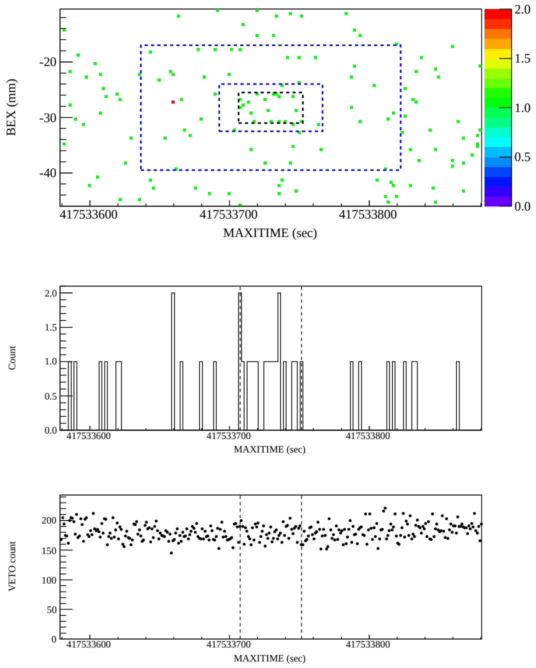

FIGURE B.143: Event map, light curve and VETO count time variability of SXT 130325 with log $P_{\rm null} = -10.2$.

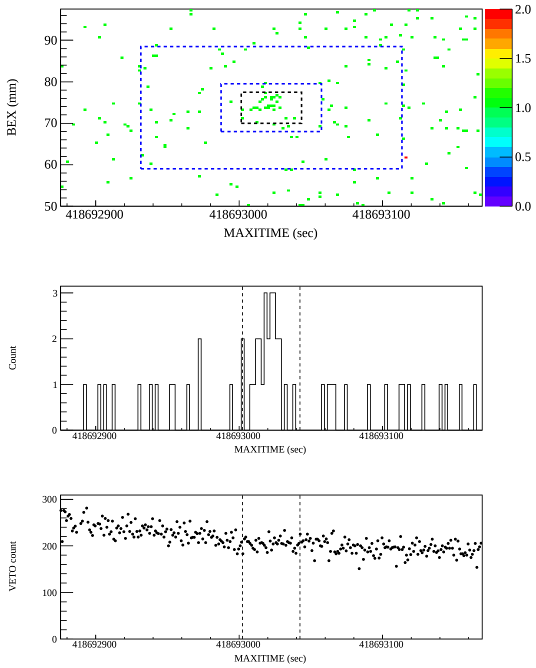

FIGURE B.144: Event map, light curve and VETO count time variability of SXT 130407 with log $P_{\rm null} = -14.8$.

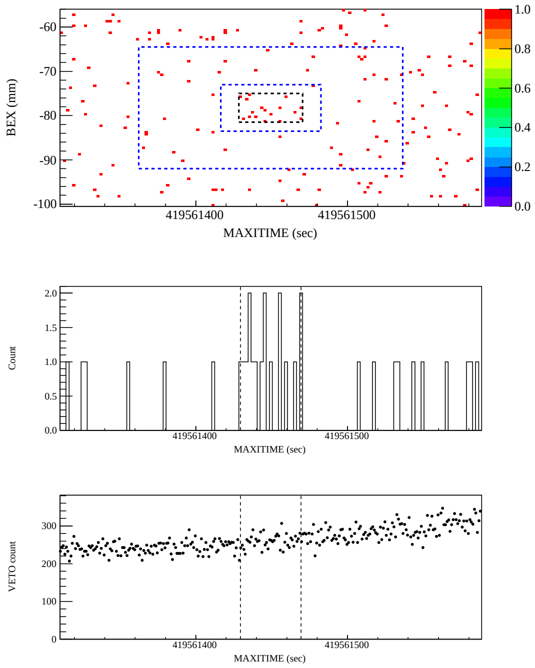

FIGURE B.145: Event map, light curve and VETO count time variability of SXT 130418 with $\log P_{\mathrm{null}} = -9.1$.

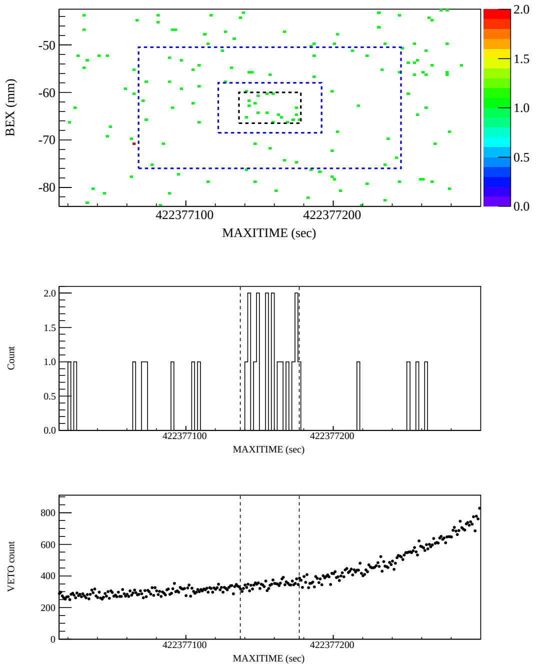

FIGURE B.146: Event map, light curve and VETO count time variability of SXT 130520 with $\log P_{\mathrm{null}} = -9.1$.

Bibliography

[1] Ambruster, C. W., & Wood, K. S. 1986, ApJ, 311, 258

[2] Arefiev, V. A., Priedhorsky, W. C., & Borozdin, K. N. 2003, ApJ, 586, 1238

[3] Bartoli, B., Bernardini, P., Bi, X. J., et al. 2012, ApJ, 758, 2

[4] Baumgartner, W. H., Tueller, J., Markwardt, C. B., et al. 2013, ApJS, 207, 19

[5] Bloom, J. S., Giannios, D., Metzger, B. D., et al. 2011, Science, 333, 203

[6] Briggs, M. S., Paciesas, W. S., Pendleton, G. N., et al. 1996, ApJ, 459, 40

[7] Burrows, D. N., Kennea, J. A., Ghisellini, G., et al. 2011, Nature, 476, 421

[8] Castro-Tirado, A. J., Brandt, S., Lund, N., & Sunyaev, R. 1999, A&A, 347, 927

[9] Colgate, S. A. 1974, ApJ, 187, 333

[10] Connors, A., Serlemitsos, P. J., & Swank, J. H. 1986, ApJ, 303, 769

[11] Costa, E., Frontera, F., Heise, J., et al. 1997, Nature, 387, 783

[12] Djorgovski, S. G., Metzger, M. R., Kulkarni, S. R., et al. 1997, Nature, 387, 876

[13] Eker, Z., Ak, N. F., Bilir, S., et al. 2008, MNRAS, 389, 1722

[14] Evans, C. R., & Kochanek, C. S. 1989, ApJL, 346, L13

[15] Fiocchi, M., Bazzano, A., Natalucci, L., Landi, R., & Ubertini, P. 2011, MNRAS, 414, L41

[16] Forman, W., Jones, C., Cominsky, L., et al. 1978, ApJS, 38, 357

[17] Galama, T. J., Vreeswijk, P. M., van Paradijs, J., et al. 1998, Nature, 395, 670

[18] Galloway, D. K., Muno, M. P., Hartman, J. M., Psaltis, D., & Chakrabarty, D. 2008, ApJS, 179, 360

[19] Giacconi, R., Gursky, H., Paolini, F. R., & Rossi, B. B. 1962, Physical Review Letters, 9, 439

[20] Giacconi, R., Branduardi, G., Briel, U., et al. 1979, ApJ, 230, 540

[21] Gotthelf, E. V., Hamilton, T. T., & Helfand, D. J. 1996, ApJ, 466, 779

[22] Greiner, J., Hartmann, D. H., Voges, W., et al. 2000, A&A, 353, 998

[23] Hall, D. S. 1976, in Astrophysics and Space Science Library, Vol. 60, IAU Colloq. 29: Multiple Periodic Variable Stars, ed. W. S. Fitch, 287

[24] Halpern, J. P., Gezari, S., & Komossa, S. 2004, ApJ, 604, 572

[25] Harris, W. E. 1996, AJ, 112, 1487

[26] Hartmann, D., & Epstein, R. I. 1989, ApJ, 346, 960

[27] Heise, J., Zand, J. I., Kippen, R. M., & Woods, P. M. 2001, in Gamma-ray Bursts in the Afterglow Era, ed. E. Costa, F. Frontera, & J. Hjorth, 16

[28] Hiroi, K., Ueda, Y., Hayashida, M., et al. 2013, ApJS, 207, 36

[29] Hjorth, J., Sollerman, J., Møller, P., et al. 2003, Nature, 423, 847

[30] Hoffman, J. A., Lewin, W. H. G., Doty, J., et al. 1978, ApJL, 221, L57

[31] Isobe, N., Sugimori, K., Kawai, N., et al. 2010, PASJ, 62, L55

[32] Kalamkar, M., Homan, J., Altamirano, D., et al. 2011, ApJL, 731, L2

[33] Kataoka, J., Takahashi, T., Wagner, S. J., et al. 2001, ApJ, 560, 659

[34] Kennea, J. A., Altamirano, D., Evans, P. A., et al. 2012, The Astronomer's Telegram, 4192, 1

[35] Kimura, M., Tsunemi, H., Tomida, H., et al. 2013, PASJ, 65, 14

[36] Klebesadel, R. W., Strong, I. B., & Olson, R. A. 1973, ApJL, 182, L85

[37] Klein, R. I., & Chevalier, R. A. 1978, ApJL, 223, L109

[38] Komossa, S., & Bade, N. 1999, A&A, 343, 775

[39] Kong, A. K. H., Homer, L., Kuulkers, E., Charles, P. A., & Smale, A. P. 2000, MNRAS, 311, 405

[40] Kouveliotou, C., Meegan, C. A., Fishman, G. J., et al. 1993, ApJL, 413, L101

[41] Krimm, H. A., Holland, S. T., Corbet, R. H. D., et al. 2013, ApJS, 209, 14

[42] Levine, A. M., Bradt, H., Cui, W., et al. 1996, ApJL, 469, L33

[43] Lodato, G., King, A. R., & Pringle, J. E. 2009, MNRAS, 392, 332

[44] López-Santiago, J., Montes, D., Crespo-Chacón, I., & Fernández-Figueroa, M. J. 2006, ApJ, 643, 1160

[45] Maccarone, T. J., Long, K. S., Knigge, C., Dieball, A., & Zurek, D. R. 2010, MNRAS, 406, 2087

[46] Maselli, A., Melandri, A., Nava, L., et al. 2013, ArXiv e-prints, arXiv:1311.5254

[47] Matsuoka, M., Kawasaki, K., Ueno, S., et al. 2009, PASJ, 61, 999

[48] Metzger, M. R., Djorgovski, S. G., Kulkarni, S. R., et al. 1997, Nature, 387, 878

[49] Mihara, T., Nakajima, M., Sugizaki, M., et al. 2011, PASJ, 63, 623

[50] Moretti, A., Vattakunnel, S., Tozzi, P., et al. 2012, A&A, 548, A87

[51] Morii, M., Sugimori, K., Kawai, N., & MAXI Team. 2011, Physica E Low-Dimensional Systems and Nanostructures, 43, 692

[52] Morii, M., Tomida, H., Kimura, M., et al. 2013, ArXiv e-prints, arXiv:1310.1175

[53] Negoro, H., Nakahira, S., Tsuboi, Y., et al. 2012, The Astronomer's Telegram, 4175, 1

[54] Nolan, P. L., Abdo, A. A., Ackermann, M., et al. 2012, ApJS, 199, 31

[55] Paciesas, W. S., Meegan, C. A., Pendleton, G. N., et al. 1999, ApJS, 122, 465

[56] Paciesas, W. S., Meegan, C. A., von Kienlin, A., et al. 2012, ApJS, 199, 18

[57] Panaitescu, A., & Kumar, P. 2001, ApJL, 560, L49

[58] Pélangeon, A., Atteia, J.-L., Nakagawa, Y. E., et al. 2008, A&A, 491, 157

[59] Pendleton, G. N., Mallozzi, R. S., Paciesas, W. S., et al. 1996, ApJ, 464, 606

[60] Pye, J. P., & McHardy, I. M. 1983, MNRAS, 205, 875

[61] Revnivtsev, M., Sazonov, S., Jahoda, K., & Gilfanov, M. 2004, A&A, 418, 927

[62] Sakamoto, T., Lamb, D. Q., Graziani, C., et al. 2004, ApJ, 602, 875

[63] Sakamoto, T., Lamb, D. Q., Kawai, N., et al. 2005, ApJ, 629, 311

[64] Sakamoto, T., Hill, J. E., Yamazaki, R., et al. 2007, ApJ, 669, 1115

[65] Sakamoto, T., Hullinger, D., Sato, G., et al. 2008, ApJ, 679, 570

[66] Sakamoto, T., Barthelmy, S. D., Baumgartner, W. H., et al. 2011, ApJS, 195, 2

[67] Schmidt, M., Higdon, J. C., & Hueter, G. 1988, ApJL, 329, L85

[68] Serino, M. 2014, in prep.

[69] Serino, M., Uzawa, A., Tsuboi, Y., et al. 2011, The Astronomer's Telegram, 3211, 1

[70] Setti, G., & Woltjer, L. 1989, A&A, 224, L21

[71] Smith, D. A., Levine, A., Bradt, H., et al. 2002, ApJS, 141, 415

[72] Soderberg, A. M., Berger, E., Page, K. L., et al. 2008, Nature, 453, 469

[73] Strohmayer, T., & Bildsten, L. 2006, New views of thermonuclear bursts, ed. W. H. G. Lewin & M. van der Klis, 113–156

[74] Sugizaki, M., Mihara, T., Serino, M., et al. 2011, ArXiv e-prints, arXiv:1102.0891

[75] Toizumi, T. 2011, PhD thesis, Tokyo Institute of Technology

[76] Tomida, H., Tsunemi, H., Kimura, M., et al. 2011, PASJ, 63, 397

[77] Torres, C. A. O., Quast, G. R., da Silva, L., et al. 2006, A&A, 460, 695

[78] Tsunemi, H., Tomida, H., Katayama, H., et al. 2010, PASJ, 62, 1371

[79] Ukwatta, T. N., Linnemann, J. T., Tollefson, K., et al. 2011, ArXiv e-prints, arXiv:1112.0622

[80] van Paradijs, J., Groot, P. J., Galama, T., et al. 1997, Nature, 386, 686

[81] Véron-Cetty, M.-P., & Véron, P. 2010, A&A, 518, A10

[82] Wijers, R. A. M. J., Rees, M. J., & Meszaros, P. 1997, MNRAS, 288, L51

[83] Wu, X.-F., Hou, S.-J., & Lei, W.-H. 2013, ApJL, 767, L36

[84] Yoshida, A., Murakami, T., Itoh, M., et al. 1989, PASJ, 41, 509

[85] Zauderer, B. A., Berger, E., Soderberg, A. M., et al. 2011, Nature, 476, 425